DNAPL SOURCE ZONE DEPLETION DURING IN SITU CHEMICAL OXIDATION (ISCO): EXPERIMENTAL AND MODELING STUDIES

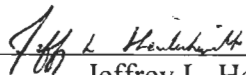by
Jeffrey L. Heiderscheidt

Report Documentation Page

1. REPORT DATE	2. REPORT TYPE	3. DATES COVERED
OCT 2005	**N/A**	**-**

4. TITLE AND SUBTITLE	5a. CONTRACT NUMBER
DNAPL Source Depletion During In Situ Chemical Oxidation (ISCO): Experimental and Modeling Studies	5b. GRANT NUMBER
	5c. PROGRAM ELEMENT NUMBER

6. AUTHOR(S)	5d. PROJECT NUMBER
	5e. TASK NUMBER
	5f. WORK UNIT NUMBER

7. PERFORMING ORGANIZATION NAME(S) AND ADDRESS(ES)	8. PERFORMING ORGANIZATION REPORT NUMBER
Colorado School of Mines	

9. SPONSORING/MONITORING AGENCY NAME(S) AND ADDRESS(ES)	10. SPONSOR/MONITOR'S ACRONYM(S)
The Department of the Air force AFIT/CIA WPAFB, OH 45433	11. SPONSOR/MONITOR'S REPORT NUMBER(S) **CI04-1682**

12. DISTRIBUTION/AVAILABILITY STATEMENT
Approved for public release, distribution unlimited

13. SUPPLEMENTARY NOTES
See also ADM001839., The original document contains color images.

14. ABSTRACT

15. SUBJECT TERMS

16. SECURITY CLASSIFICATION OF:			17. LIMITATION OF ABSTRACT	18. NUMBER OF PAGES	19a. NAME OF RESPONSIBLE PERSON
a. REPORT **unclassified**	b. ABSTRACT **unclassified**	c. THIS PAGE **unclassified**	**UU**	**355**	
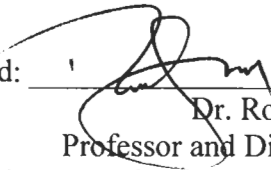
A thesis submitted to the Faculty and Board of Trustees of the Colorado School of Mines in partial fulfillment of the requirements for the degree of Doctor of Philosophy (*Environmental Science and Engineering*).

Golden, Colorado

Date: __22 Aug 05__
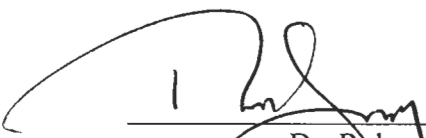
Signed: _____
Jeffrey L. Heiderscheidt

Approved: _____
Dr. Tissa H. Illangasekare
AMAX Distinguished Chair and
Professor of Environmental Science and Engineering
Thesis Advisor

Approved: _____
Dr. Robert L. Siegrist
Professor and Division Director
Division of Environmental Science and Engineering
Thesis Advisor

Golden, Colorado

Date: __8-22-05__

_____
Dr. Robert L. Siegrist
Professor and Division Director
Division of Environmental Science and Engineering

ABSTRACT

In situ chemical oxidation (ISCO) using permanganate is a promising technology for remediating groundwater and soil contaminated by chlorinated solvents present as dense non-aqueous phase liquids (DNAPLs). However, there remain gaps in knowledge about ISCO effects on mass depletion from complex DNAPL source zones and effects of $MnO_{2(s)}$ formation, impacting field application of the technology. Further, a simulation tool is needed for studying ISCO under typical complex field conditions.

A 2D experiment was performed investigating oxidation of a complex DNAPL source zone composed of tetrachloroethylene (PCE) within a simulated aquifer, to qualitatively understand ISCO effects on mass depletion and permeability, and generate quantitative data for ISCO model testing. Hydraulic head and aqueous concentrations were monitored and soil cores were analyzed to evaluate permeability effects and mass depletion rate changes due to changes in DNAPL saturation and $MnO_{2(s)}$ formation. For this experiment, $MnO_{2(s)}$ formation depended partly on source configuration, and did not noticeably reduce permeability or alter flow patterns until exceeding 0.1g $MnO_{2(s)}$/kg soil. Oxidation effects on mass depletion depended on source configuration (ganglia versus pool and location of ganglia related to pool); effects were dramatically different for a complex source zone than a lone pool or residual source, highlighting the importance of source architecture characterization to performance of an ISCO field application.

The Chemical Oxidation Reactive Transport in 3D (CORT3D) model code was developed as a decision tool for simulating ISCO, and tested by modeling experiments focusing on important ISCO processes. Simulations confirmed the importance of accounting for changing permeability and multiple natural oxidant demand (NOD) fractions. Simulations also verified oxidation can increase mass depletion from a PCE DNAPL source more than can be attributed solely to increased concentration gradient.

CORT3D was used to investigate interaction of aquifer NOD, oxidant delivery rate, and oxidant concentration on oxidant transport at the Navy Training Center in Orlando, Florida. Permanganate transport was simulated under a variety of delivery scenarios and NOD conditions. For this high NOD site, lower oxidant concentration delivered at high flow rate can provide more optimal oxidant delivery effectiveness by limiting unproductive oxidant consumption (and accompanying permeability reduction) by NOD.

TABLE OF CONTENTS

LIST OF FIGURES

LIST OF TABLES

ACKNOWLEDGEMENTS

DEDICATION

To my wife, daughter, and son.

Chapter 1

INTRODUCTION

1.1   Problem Description

Chlorinated solvents such as trichloroethylene (TCE) and tetrachloroethylene (PCE) are contaminants of concern in groundwater at many contaminated sites (each present at about 60% of National Priority List sites), ranking 16th and 30th respectively on the 2003 CERCLA Priority List of Hazardous Substances (ATSDR 2003). These chemicals have been used extensively since the early 20th century as cleaning solvents in the dry-cleaning, metal cleaning, vapor degreasing, and textile processing industries (ATSDR 2004, USHHS 2002). They have also been used to a large extent as intermediate chemicals in the production of pesticides, gums, resins, paints, and other chemicals such as refrigerants (USEPA 2004a). A consequence of their widespread use is that they have been leaked, spilled, and improperly disposed of at many sites. The State Coalition for Remediation of Drycleaners (SCRD 2004), representing eleven states, estimates that over 80% of U.S. dry-cleaning operations use PCE and that 75% of the 36,000 dry-cleaning sites in the U.S. have some level of soil and groundwater contamination.

As contaminants, these chlorinated solvents are frequently present in the form of dense non-aqueous phase liquid (DNAPL) primary source zones, or as dissolved and/or sorbed contaminant in low permeability media (LPM) secondary source regions (Johnson and Pankow 1992, Pankow and Cherry 1996, USEPA 1993, USEPA 2004b). These contaminants are termed non-aqueous because they are present as a separate immiscible liquid phase having low solubilities in water, typically on the order of 10^2 - 10^3 mg/L or parts-per-million (ppm). On the other hand, the drinking water maximum contaminant levels (MCLs) of these contaminants are typically on the order of 10^0 - 10^2 µg/L or parts-

per-billion (ppb). The combined result is that aqueous phase concentrations exceed MCLs by several order of magnitude, and the DNAPL source can persist for decades.

DNAPLs present a challenging source zone because of the complex nature of their movement through the subsurface. Because DNAPLs have a density greater than that of water, they tend to migrate downward through the unsaturated and saturated zones. However, the interplay of viscous, gravitational, and capillary forces, in conjunction with physical soil heterogeneities (large and small), results in a non-uniform and unpredictable migration vertically and laterally (Illangasekare et al. 1995a, Illangasekare et al. 1995b, Kueper and Frind 1991, Schwille 1988). The unstable distribution behavior (e.g., fingering), even in a relatively homogeneous porous media, was demonstrated in 3D tank experiments by Held and Illangasekare (1995a, b). As the main body of DNAPL migrates, residual DNAPL is left behind as disconnected blobs and ganglia partially filling the pore space. Capillary forces hold this DNAPL residual in place, such that even relatively large hydraulic gradients can not further mobilize it (Kueper et al. 2003). Additionally, there may be regions of pooled or high saturation DNAPL where the DNAPL fills a large fraction of the soil pore space.

In recent years, there has been increased emphasis and research into DNAPL source depletion. Traditional pump-and-treat systems are not able to substantially reduce the source mass and become long-term containment systems. Source depletion technologies like surfactant/co-solvent flushing, thermal treatment, and chemical oxidation offer the potential to drastically reduce DNAPL source mass, decreasing mass flux of contaminant into the aqueous phase and decreasing the lifetime of the contamination (Stroo et al. 2003, USEPA 2003). Unfortunately, source depletion efforts can be challenged by subsurface heterogeneities, imprecise knowledge of source locations, and effects of the effort on source zone distribution or subsurface hydrogeologic conditions (Freeze and McWhorter 1997, ITRC 2002, Marvin et al. 2002, Siegrist and Lowe 1996, USEPA 2003).

Feenstra and Cherry (1996) pointed out that actual free-phase DNAPL has not been found at most sites strongly suspected of having DNAPL contamination. In many cases, the existence of a DNAPL source can only be inferred from indirect evidence such as aqueous contaminant concentrations exceeding 1% of the aqueous solubility of the chemical (USEPA 1992, USEPA 2003). Parker et al. (2003) demonstrated the difficulty in locating actual subsurface DNAPL sources by performing extensive soil coring and water sampling at five sites (three that had free-phase DNAPL in monitoring wells) with DNAPL contaminated sandy aquifers. They found the DNAPL to be present in sporadic, thin layers only identifiable by taking continuous soil cores, sub-sampling them on small (5 cm or less) vertical intervals, and applying a hydrophobic red dye (Sudan IV) to the cores.

As alluded to before, lenses of LPM provide additional challenges as secondary sources. Mackay and Cherry (1989) pointed out that sand aquifers contaminated by DNAPLs frequently have silty or clayey LPM strata below or within them, with permeabilities 10^3 - 10^6 times lower than surrounding sand. Diffusion of aqueous phase components into LPM, and subsequent diffusion out of the LPM after the DNAPL source is depleted is a particularly challenging remediation problem (Liu and Ball 2002). In many cases, pure-phase contaminant entered the aquifer and has had several to many years of close contact with LPM, resulting in diffusion of a substantial mass of dissolved contaminant into the LPM. For example, Freeze and McWhorter (1997) show that for a typical fractured clay LPM, 50-100% of the original DNAPL mass can end up in the LPM matrix, depending on the fracture sizes, either dissolved or sorbed to soil particles. Subsequently, even if the pure-phase contaminant is removed from the aquifer, the dissolved contaminant in the LPM will continue to diffuse out and remain a source of groundwater contamination, potentially well above MCLs, for years to come (Johnson and Pankow 1992, Lee and Chrysikopoulos 1998, Wilking 2004).

1.2   Motivation

The complete literature review can be found in Chapter 2.   However, an abbreviated version, focusing on the need for this research is provided here.

Chemical oxidation, specifically with permanganate, has been used to treat water and waste water for over 50 years. In the last fifteen years or so, chemical oxidation has become a promising in situ remediation technique for sites whose groundwater and soil are contaminated by chlorinated solvents, especially where contaminants are not present in DNAPL form.   Field-scale pilot tests have shown encouraging results for sites contaminated with low levels of chlorinated solvents (Cline et al. 1997, Hood 2000, Lowe et al. 2002, Schnarr et al. 1998, Siegrist et al. 1999).   Additionally, laboratory research has provided an understanding of many fundamental details of the technology. The reaction pathways and kinetics of permanganate oxidation of alkenyl halides, specifically chlorinated ethenes such as PCE and TCE have been elucidated (Huang et al. 1999, Huang et al. 2001, Huang et al. 2002, Schnarr et al. 1998, Yan and Schwartz 1999, Yan and Schwartz 2000). Struse et al. (2002) demonstrated the ability of permanganate to diffuse into LPM, destroying DNAPL TCE and preventing diffusion of aqueous TCE from the LPM.   A number of researchers have also studied the impacts of water chemistry and porous media constituents on the reaction (Gates-Anderson et al. 2001, Glaze and Kang 1988, Li and Schwartz 2000, Urynowicz 2000, Vella and Veronda 1994). However, limited research of chemical oxidation in the presence of greater than residual DNAPL saturation has shown inconclusive results (MacKinnon and Thomson 2002, NATO/CCMS 2003, Rietsma and Marshall 2000, Schroth et al. 2001, Siegrist et. al. 1999, Urynowicz and Siegrist 2000, USEPA 1998).

Studies of the effects of permanganate oxidation on porous media permeability have to-date been largely qualitative (Conrad et al. 2002, Lee et al. 2003, Li and Schwartz 2000, Reitsma and Randhawa 2002, Siegrist et al. 2002).   For example, research has shown that oxidation of a high DNAPL saturation source using permanganate can result in permeability reductions at the DNAPL perimeter due to

precipitation of manganese dioxide thereby reducing the ability for oxidant to be transported to the source, but also possibly reducing the mass flux of aqueous contaminant from the DNAPL source (Lee et al. 2003, Siegrist et al. 2002). On the other hand, research into permeability effects from permanganate oxidation of DNAPL source zones at lower saturations is more ambiguous. Nelson et al. (2001) concluded that the manganese oxides produced during oxidation of a PCE DNAPL present at approximately 4-7% saturation had negligible effect on the permeability in a system under neutral pH conditions. However, Lee et al. (2003) found that permanganate oxidation of a TCE DNAPL source zone at 8% saturation, under slightly acidic conditions, resulted in generation of up to 4900 mg $MnO_2(s)$/kg of porous media, with a six-fold decrease in velocity of the oxidation front over the two-month experiment, attributed to reductions in permeability. Further research is necessary to better understand how well ISCO will work under different site and source conditions, including the effects of ISCO on source zone porous media (Ibaraki and Schwartz 2001, Seol et al. 2003, Stroo et al. 2003).

A goal of ISCO is to speed up remediation of a contaminant source zone by inducing increased mass transfer (and subsequent destruction) from the source. Based on experimental results, Schnarr et al. (1998) suggest that NAPL dissolution and oxidation are processes that occur in parallel with increased mass transfer during oxidation occurring primarily as a result of an increased aqueous concentration gradient. Reitsma and Dai (2001) performed a theoretical study to estimate the maximum expected NAPL mass transfer enhancement resulting from chemical oxidation. They estimated a maximum five times increase in dispersive mass transport from a PCE NAPL pool resulting from the increased concentration gradient; however, they predict little enhancement in local-scale mass transfer from NAPL to aqueous phase suggesting no change in dissolution mass transfer parameters. Further, they suggest that actual enhancement is likely to be less, because permeability reduction and decreased interfacial contact area were not accounted for in the estimate. On the contrary, MacKinnon and Thomson (2002) calculated a ten times initial increase in PCE mass transfer from a

NAPL pool during a 2D oxidation experiment, with decreasing mass flux over time attributed to $MnO_2(s)$ formation. Additional research is necessary to further quantify the expected changes in NAPL mass transfer during and after oxidation, especially with consideration to changing NAPL architecture and $MnO_2(s)$ formation.

Site conditions such as NAPL architecture, soil heterogeneity, oxidant delivery, and soil natural oxidant demand are critical factors affecting ISCO implementation. In order to implement ISCO effectively, it is important to consider the interaction of these factors under realistic conditions. Field-scale investigations provide realistic conditions, but do not allow for complete control of experimental conditions. Additionally, they generally allow only limited monitoring, preventing a full understanding of how site and source conditions are affecting the chemical oxidation. For example, even at the Canadian Forces Base Borden, Ontario, Canada (with extensive monitoring and site characterization), researchers were not able to fully characterize the DNAPL source distribution before or after oxidation (Nelson et al. 2000, Nelson et al. 2001). Large tanks provide an alternative with near-complete control, as a means to improve qualitative understanding as well as generate accurate data on individual or combined processes. Unfortunately, large-scale tank experiments are costly, time-consuming, and difficult to set up, so only a limited number can be performed. Further, it is simply not possible to perform experiments for all possible field scenarios. Because of these challenges posed by large-tank lab and field-scale experiments, a computer model code is needed for simulating chemical oxidation and related processes under a wide range of hydrogeologic and source conditions. Such a modeling code allows simulation of field conditions that are not possible to study in an experiment.

However, a search of published literature turned up only two efforts at developing a computer model code for site remediation by ISCO using permanganate (Hood 2000, Hood and Thomson 2000, Zhang and Schwartz 2000). While both models incorporate second order oxidation, rate-limited or kinetic sorption, and Gilland-Sherwood type dissolution mass transfer correlations, neither model code is in the public domain, nor are

they readily available for use or modification. Additionally, although both models are said to incorporate kinetic NOD oxidation, published simulations have treated NOD as an instantaneous sink. In essence this means oxidant within a model cell is not available for destroying contaminant until all NOD within that cell has been oxidized. Further, it is important to note neither model code tracks $MnO_2(s)$ generation or incorporates changing permeability as a result; however both studies pointed to this as an area for further research. Finally, neither modeling effort attempted to capture diffusion as an important transport process in the application of ISCO using permanganate.

1.3 Research Goals

Based on a review of available literature, there remain gaps in knowledge about ISCO effects on mass depletion from complex DNAPL source zones and effects on permeability, impacting field application of the technology. The goals of this research were to expand understanding of in situ chemical oxidation, and provide knowledge and tools to improve the field application of the technology. These objectives were achieved by examining the following hypotheses:

(1) In situ chemical oxidation using permanganate will result in decreased DNAPL source mass depletion rates and down-gradient plume concentrations, compared to pre-oxidation.

(2) The effects of ISCO using permanganate on DNAPL source depletion depends on the complexity of the DNAPL entrapment architecture.

(3) A numerical computer modeling code for simulating ISCO of DNAPL source zones comprised of chlorinated ethenes using permanganate can capture important processes, including: DNAPL mass transfer or dissolution, potentially increased DNAPL mass transfer due to chemical reaction during oxidation, kinetic oxidation of contaminant and multiple NOD components, competition of contaminant and NOD for available oxidant, and permeability reduction due to precipitation of $MnO_2(s)$ during oxidation.

1.4 Thesis Outline

This dissertation is divided into six chapters and five appendices. Introduction to the problem, along with motivation and research goals are presented in Chapter 1. Chapter 2 contains background on the main aspects of this research, including summaries of previous studies. Contributions of this dissertation are organized in stand-alone manuscript format in the following chapters:

Chapter 3   Chemical Oxidation Reactive Transport in 3D (CORT3D) model development and testing.

Chapter 4   Experimental investigation of in situ chemical oxidation of complex DNAPL source zones by permanganate.

Chapter 5   Optimizing permanganate transport to overcome high natural oxidant demand at Navy Training Center, Orlando, Florida – a numerical study

Chapter 6 discusses the conclusions and research findings. It also identifies potential areas for further research. Appendix A describes methods and materials used for experimental work. Appendix B provides user instructions and example input and output files for the developed computer model. Appendix C is a summary of preliminary intermediate-scale 2D experiments performed prior to the work described in Chapter 4. Appendix D is a summary of large-scale 2D experiments where chemical oxidation of a complex PCE DNAPL spill in a heterogeneous soil followed surfactant flushing. Finally, Appendix E (found on the included CD) contains the full set of simulation results from the field site modeling of Chapter 5.

1.5 References

ATSDR. (2003). "2003 CERCLA Priority List of Hazardous Substances." Agency for Toxic Substances and Disease Registry, Division of Toxicology, U.S. Dept. of Health and Human Services. Oct. 2003. http://www.atsdr.cdc.gov/clist.html.

ATSDR. (2004). "Medical management guidelines (MMGs) for tetrachloroethylene." Agency for Toxic Substances and Disease Registry, Division of Toxicology, U.S.

Dept. of Health and Human Services. May 2004. http://www.atsdr.cdc.gov/MHMI/mmg18.html.

Cline, S.R., West, O.R., Korte, N.E., Gardner, F.G., Siegrist, R.L., and Baker, J.L. (1997). "KMnO4 chemical oxidation and deep soil mixing for soil treatment." *Geotech. News*, 15 (5): 25-28.

Conrad, S.H., Glass, R.J., and Peplinski, W.J. (2002). "Bench-scale visualization of DNAPL remediation processes in analog heterogeneous aquifers: surfactant floods and in situ oxidation using permanganate." *J. Contam. Hydrol.*, 58 (1-2): 13-49.

Feenstra, S. and Cherry, J.A. (1996). "Diagnosis and assessment of DNAPL sites." In: J.F. Pankow and J.A. Cherry (Eds) *Dense chlorinated solvents and other DNAPLs in groundwater: history, behavior, and remediation*. Waterloo Press, Portland, OR, pp. 395-473.

Freeze, R.A. and McWhorter, D.B. (1997). "A framework for assessing risk reduction due to DNAPL mass removal from low-permeability soils." *Ground Water*, 35 (1): 111-123.

Gates-Anderson, D.D., Siegrist, R.L., and Cline, S.R. (2001). "Comparison of potassium permanganate and hydrogen peroxide as chemical oxidants for organically contaminated soils." *J. Environ. Eng.*, 127 (4): 337-347.

Glaze, W.H. and Kang, J.-W. (1988). "Advanced oxidation processes for treating groundwater contaminated with TCE and PCE: laboratory studies." *J. AWWA*, 88 (5): 57-63.

Held, R.J. and Illangasekare, T.H. (1995a). Fingering of dense non-aqueous phase liquids in porous media: 1. Experimental investigation. *Water Resour. Res.*, 31 (5): 1213-1222.

Held, R.J. and Illangasekare, T.H. (1995b). Fingering of dense non-aqueous phase liquids in porous media: 2. Analysis and classification. *Water Resour. Res.*, 31 (5): 1223-1231.

Hood, E. (2000). *Permanganate Flushing of DNAPL Source Zones: Experimental and Numerical Investigation*. Ph.D. Dissertation, University of Waterloo, Waterloo, ON. 243 pp.

Hood, E. and Thomson, N.R. (2000). "Numerical simulation of in situ chemical oxidation." In: *Chemical Oxidation and Reactive Barriers*, Wickramanayake,

G.B., Gavaskar, A.R., Chen, A.S.C. (Eds.). Battelle Press, Columbus, OH, pp. 83-90.

Huang, K., Hoag, G.E., Chheda, P., Woody, B.A., and Dobbs, G.M. (1999). "Kinetic study of oxidation of trichloroethylene by potassium permanganate." *Environ. Eng. Sci.*, 16 (4): 265-274.

Huang, K., Hoag, G.E., Chheda, P., Woody, B.A., and Dobbs, G.M. (2001). "Oxidation of chlorinated ethenes by potassium permanganate: a kinetics study." *J. Haz. Mater.*, 87 (1-3): 155-169.

Huang, K., Hoag, G.E., Chheda, P., Woody, B.A., and Dobbs, G.M. (2002). "Kinetics and mechanism of oxidation of tetrachloroethylene with permanganate." *Chemosphere*, 46 (6): 815-825.

Ibaraki, M. and Schwartz , F.W. (2001). "Influence of Natural Heterogeneity on the Efficiency of Chemical Floods in Source Zones." *Ground Water*; 39 (5): 660-666.

Illangasekare, T.H., Armbruster, E.J. III, and Yates, D.N. (1995a). Non-aqueous-phase fluids in heterogeneous aquifer—experimental study. *J. Environ. Eng.*, 121 (8): 571-579.

Illangasekare, T.H., Ramsey, J.L., Jensen, K.H., and Butts, M. (1995b). "Experimental study of movement and distribution of dense organic contaminants in heterogeneous aquifers: an experimental study." *J. Contam. Hydrol.*, 20 (1-2): 1-25.

ITRC. (2002). "Regulatory overview--DNAPL source reduction: Facing the challenge." Interstate Technology and Regulatory Cooperation Work Group (ITRC), Dense Non-aqueous Phase Liquids Team, Washington D.C. Apr 2002, 42 pp. http://www.itrcweb.org/user/DNAPL-2.pdf.

Johnson, R.L. and Pankow, J.F. (1992). "Dissolution of dense chlorinated solvents into groundwater. 2. Source functions for pools of solvent." *Environ. Sci. & Technol.*, 26 (5): 896-901.

Kueper, B.H., and Frind, E.O. (1991). "Two-phase flow in heterogeneous porous media, 1, Model development." *Water Resour. Res.*, 27 (6): 1049-1057.

Kueper, B.H., Wealthall, G.P., Smith, J.W.N., Leharne, S.A., and Lerner, D.N. (2003). *An illustrated handbook of DNAPL transport and fate in the subsurface.*

Environment Agency R&D Publication 133, Environmental Agency, Almondsbury, Bristol, U.K. 67 pp.

Lee, K.Y. and Chrysikopoulos, C.V. (1998). "NAPL pool dissolution in stratified and anisotropic porous formations." *J. Environ. Eng.*, 124 (9): 851-862.

Lee, E.S., Seol, Y., Fang, Y.C., and Schwartz, F.W. (2003). "Destruction efficiencies and dynamics of reaction fronts associated with the permanganate oxidation of trichloroethylene." *Environ. Sci. Technol.*, 37 (11): 2540-2546.

Li, X.D. and Schwartz, F.W. (2000). Efficiency problems related to permanganate oxidation schemes. In: Wickramanayake, G.B., Gavaskar, A.R., Chen, A.S.C. (Eds), *Chemical Oxidation and Reactive Barriers*. Battelle Press, Columbus, OH, pp. 41-48.

Liu, C. and Ball, W.P. (2002). "Back Diffusion of Chlorinated Solvent Contaminants from a Natural Aquitard to a Remediated Aquifer Under Well-Controlled Field Conditions: Predictions and Measurements." *Ground Water*, 40 (2): 175-184.

Lowe, K.S., Gardner, F.G., and Siegrist, R.L. (2002). "Field evaluation of in situ chemical oxidation through vertical well-to-well recirculation of $NaMnO_4$." *Ground Water Monit. Rem.*, 22 (1): 106-115.

Mackay, D.M. and Cherry, J.A. (1989). "Groundwater contamination: Pump-and-treat remediation." *Environ. Sci. & Technol.*, 23 (6): 630-636.

MacKinnon, L.L. and Thomson, N.R. (2002). "Laboratory-scale in situ chemical oxidation of a perchloroethylene pool using permanganate." *J. Contam. Hydrol.*, 56 (1-2): 49-74.

Marvin, B.K., Chambers, J., Leavitt, A., and Schreier, C.G. (2002). "Chemical and engineering challenges to in situ permanganate remediation." *Proc., 3rd Int. Conf. on Remediation of Chlorinated and Recalcitrant Compounds*, Monterey CA, May 2002. Battelle Press, Columbus, OH. 2C-04 (8pp.).

NATO/CCMS (North Atlantic Treaty Organization/Committee on the Challenges of Modern Society). (2003). "Evaluation of demonstrated and emerging technologies for the treatment and clean up of contaminated land and groundwater (phase III)." U.S. EPA Rep. No. EPA/542/R-02/010, U.S. EPA, Washington D.C. 291 pp.

Nelson, M.D., Parker, B.L., and Cherry, J.A. (2000). "Passive destruction of PCE DNAPL by potassium permanganate in a sandy aquifer." In: Wickramanayake,

G.B., Gavaskar, A.R., Chen, A.S.C. (Eds), *Chemical Oxidation and Reactive Barriers.* Battelle Press, Columbus, OH. pp. 135-143.

Nelson, M.D., Parker, B.L., Al, T.A., Cherry, J.A., and Loomer, D. (2001). "Geochemical Reactions Resulting from In Situ Oxidation of PCE-DNAPL by KMnO4 in a Sandy Aquifer." *Environ. Sci. Technol.*, 35 (6): 1266-1275.

Pankow, J.F. and Cherry, J.A. (Eds). (1996). Dense Chlorinated Solvents and Other DNAPLs in Groundwater: History, Behavior, and Remediation. Waterloo Press, Portland, OR, 525 pp.

Parker, B.L., Cherry, J.A., Chapman, S.W., and Guilbeault, M.A. (2003). "Review and analysis of chlorinated solvent dense non-aqueous phase liquid distributions in five sandy aquifers." *Vadose Zone J.*, 2 (2): 116-137.

Reitsma, S. and Marshall, M. (2000). "Experimental study of oxidation of pooled NAPL." In: Wickramanayake, G.B., Gavaskar, A.R., and Chen, A.S.C. (ed.). *Chemical Oxidation and Reactive Barriers*. Battelle Press, Columbus, OH. pp. 25-32.

Reitsma, S. and Dai, Q.L. (2001). Reaction-enhanced mass transfer and transport from non-aqueous phase liquid source zones. *J. Contam. Hydrol.*, 49: 49-66.

Reitsma, S. and Randhawa, J. (2002). "Experimental investigation of manganese dioxide plugging in porous media." In: Gavaskar, A.R. and Chen, A.S.C. (Eds), *Proc., 3rd Int. Conf. on Remediation of Chlorinated and Recalcitrant Compounds*, Monterey CA, May 2002. Battelle Press, Columbus, OH. 2C-39 (8pp.).

Schnarr, M., Truax, C., Farquhar, G., Hood, E., Gonully, T., and Stickney, B. (1998). "Laboratory and controlled field experimentation using potassium permanganate to remediate trichloroethylene and perchloroethylene DNAPLs in porous media." *J. Contam. Hydrol.*, 29 (3): 205-224.

Schroth, M.H, Oostrom, M., Wietsma, T.W., and Istok, J.D. (2001). "In situ oxidation of trichloroethene by permanganate: effects on porous medium hydraulic properties." *J. Contam. Hydrol.*, 50 (1-2): 79-98.

Schwille, F. (1988). *Dense Chlorinated Solvents in Porous and Fractured Media*. Lewis Publishers, Chelsea, MI. Translated by J.F. Pankow, 146 pp.

SCRD. (2004). *Conducting Contamination Assessment Work at Drycleaning Sites*. State Coalition for Remediation of Drycleaners, Mar 2004, 52 pp. http://www.drycleancoalition.org/download/assessment.pdf.

Seol, Y., Zhang, H., and Schwartz, F.W. (2003). "A review of in situ chemical oxidation and heterogeneity." *Environ. & Eng. Geosci.*, 9 (1): 37-49.

Siegrist, R.L. and Lowe, K.S. (Eds). (1996). "In situ remediation of DNAPL compounds in low permeability media: Fate/transport, in situ control technologies, and risk reduction," *Oak Ridge National Laboratory Rep. No. ORNL/TM-13305* for the DOE Office of Science and Technology.

Siegrist, R.L., Lowe, K.S., Murdoch, L.C., Case, T.L., and Pickering, D.A. (1999). "In situ oxidation by fracture emplaced reactive solids." *J. Environ. Eng.*, 125 (5): 429-440.

Siegrist, R.L., Urynowicz, M.A., Crimi, M.L., and Lowe, K.S. (2002). "Genesis and effects of particles produced during in situ chemical oxidation using permanganate." *J. Environ. Eng.*, 128 (11): 1068-1079.

Stewart, R. (1965). "Oxidation by permanganate." In: Wiberg, K.B. (Ed.), *Oxidation in Organic Chemistry*, Part A, Chap. 1. Academic Press, New York, NY. pp. 1-68.

Stroo, H.F., Unger, M., Ward, C.H., Kavanaugh, M.C., Vogel, C., Leeson, A., Marqusee, J.A., and Smith, B.P. (2003). "Remediating chlorinated solvent source zones." *Environ. Sci. Technol.*, 37 (11): 224A-230A.

Struse, A.M., Siegrist, R.L., Dawson, H.E., and Urynowicz, M.A. (2002). "Diffusive transport of permanganate during in situ oxidation." *J. Environ. Eng.*, 128(4): 327-334.

Urynowicz, M.A. (2000). *Dense non-aqueous phase trichloroethene degradation with permanganate ion*. Ph.D. Dissertation, Colorado School of Mines, Golden CO. 166 pp.

Urynowicz, M.A. and Siegrist, R.L. (2000). "Chemical degradation of TCE DNAPL by permanganate." In: Wickramanayake, G.B., Gavaskar, A.R., and Chen, A.S.C. (ed.). *Chemical Oxidation and Reactive Barriers*. Battelle Press, Columbus, OH. pp. 75-82.

USEPA. (1992). "Dense non-aqueous phase liquids—A workshop summary". U.S. EPA Rep. No. EPA/600/R-92/030, Office of Research and Development, Washington D.C., 78 pp.

USEPA. (1993). "Evaluation of the likelihood of DNAPL presence at NPL sites." U.S. EPA Rep. No. EPA/540/R-93/073, Office of Solid Waste and Emergency

Response, Washington D.C. 114 pp.,
http://www.epa.gov/superfund/resources/remedy/pdf/540r-93073-s.pdf.

USEPA. (1998). "In Situ Remediation Technology: In situ chemical oxidation." U.S. EPA Rep. No. EPA/542/R96/005, Office of Solid Waste and Emergency Response, Washington D.C. 39 pp.

USEPA. (2003). "The DNAPL remediation challenge: Is there a case for source depletion?." U.S. EPA Rep. No. EPA/600/R-03/143, Office of Research and Development, Washington D.C., 129 pp., http://www.epa.gov/ada/download/reports/600R03143/600R03143-fm.pdf.

USEPA. (2004a). "Contaminant focus-trichloroethylene." U.S. EPA, Technology Innovation Program, Washington D.C. http://www.clu-in.org/ contaminantfocus/default.focus/sec/Trichloroethylene_(TCE)/cat/Overview/.

USEPA. (2004b). "Discussion paper--Cleanup goals appropriate for DNAPL source zones." U.S. EPA, Office of Solid Waste and Emergency Response, Washington D.C., 16 pp., http://gwtf.cluin.org/docs/options/dnapl_goals_paper.pdf.

USHHS. (2002). "Report on Carcinogens, Tenth Edition" U.S. Department of Health and Human Services, Public Health Service, National Toxicology Program, December 2002. http://ehp.niehs.nih.gov/roc/toc10.html.

Vella, P.A. and Veronda, B. (1994). "Oxidation of trichloroethylene: A comparison of potassium permanganate and Fenton's Reagent." In: Proc., 3rd Intl. Symposium, *Chemical Oxidation: Technologies for the Nineties, Vol 3*. Vanderbilt University, Nashville, TN, Feb 1993. Technomic Publishing, Lancaster, PA. pp. 62-73.

Wilking, B. (2004) *Factors controlling matrix storage during DNAPL mass depletion in heterogeneous porous media*. Master's thesis, Colorado School of Mines, Golden, CO. 183 pp.

Yan, E.Y. and Schwartz, F.W. (1999). "Oxidative degradation and kinetics of chlorinated ethylenes by potassium permanganate." *J. Contam. Hydrol*., 37 (3): 343-365.

Yan, E.Y. and Schwartz, F.W. (2000). "Kinetics and mechanisms for TCE oxidation by permanganate." *Environ. Sci. Technol*., 34 (12): 2535-2541.

Zhang, H. and Schwartz, F.W. (2000). "Simulating the in situ oxidative treatment of chlorinated ethylenes by potassium permanganate." *Water Resour. Res*., 36 (10): 3031-3042.

Chapter 2

BACKGROUND AND LITERATURE REVIEW

2.1 Introduction

This chapter expands on the problem description and motivation introduced in Chapter 1. It reviews past research related to implementation of in situ chemical oxidation (ISCO) of DNAPL sources using permanganate. The challenges of DNAPL sources, as well as subsurface heterogeneity, are discussed. This is followed by a review of the important processes related to ISCO including DNAPL mass transfer, diffusion, oxidation kinetics, natural oxidant demand (NOD), and effects of manganese oxide solid formation. Next, a review of past efforts to develop an ISCO modeling code is provided. Given last is a summary of the problem and gaps in current knowledge.

2.2 DNAPL Contamination

Chlorinated solvents such as trichloroethylene (TCE) and tetrachloroethylene (PCE) are frequently present in the form of dense non-aqueous phase liquid (DNAPL) primary source zones, or as dissolved and/or sorbed contaminant in low permeability media (LPM) secondary source regions (Johnson and Pankow 1992, Pankow and Cherry 1996, USEPA 1993, USEPA 2004b). These contaminants are termed non-aqueous because they are present as a separate immiscible liquid phase having low solubilities in water, typically on the order of 10^2 - 10^3 mg/L or parts-per-million (ppm). On the other hand, the drinking water maximum contaminant levels (MCLs) of these contaminants are typically on the order of 10^0 - 10^2 μg/L or parts-per-billion (ppb). The combined result is that aqueous phase concentrations exceed MCLs by several order of magnitude, and the DNAPL source can persist for decades.

DNAPLs present a challenging source zone because of the complex nature of their movement through the subsurface. Because DNAPLs have a density greater than that of water, they tend to migrate downward through the unsaturated and saturated zones. However, the interplay of viscous, gravitational, and capillary forces, in conjunction with physical soil heterogeneities (large and small), results in a non-uniform and unpredictable migration vertically and laterally (Illangasekare et al. 1995a, Illangasekare et al. 1995b, Kueper and Frind 1991, Schwille 1988). The unstable distribution behavior (e.g., fingering), even in a relatively homogeneous porous media, was demonstrated in 3D tank experiments by Held and Illangasekare (1995a, b). As the main body of DNAPL migrates, residual DNAPL is left behind as disconnected blobs and ganglia partially filling the pore space. Additionally, there may be regions of pooled or high saturation DNAPL where the DNAPL fills a large fraction of the soil pore space. Further, actual DNAPL sources are difficult to locate and often have not been located at sites strongly suspected of having DNAPL contamination (Feenstra and Cherry 1996, USEPA 1992, USEPA 2003, Parker et al. 2003)

Lenses of low permeability media (LPM) provide additional challenges as secondary sources. Diffusion of aqueous phase components into LPM, and subsequent diffusion out of the LPM after the DNAPL source is depleted is a particularly challenging remediation problem (Liu and Ball 2002). In many cases, pure-phase contaminant entered the aquifer and has had several to many years of close contact with LPM, resulting in diffusion of a substantial mass of dissolved contaminant into the LPM (Freeze and McWhorter 1997). Subsequently, even if the pure-phase contaminant is removed from the aquifer, the dissolved contaminant in the LPM will continue to diffuse out and remain a source of groundwater contamination, potentially well above MCLs, for years to come (Johnson and Pankow 1992, Lee and Chrysikopoulos 1998, Wilking 2004).

2.3   Challenges of Low Permeability Media and Site Heterogeneity

Schwille (1988) presented experimental and modeling results demonstrating the significant effect that site heterogeneity has on DNAPL migration and trapping resulting in complex, persistent source zones. Figure 2.1 depicts a generic site conceptual model of a groundwater system contaminated by DNAPLs. Even in a relatively homogeneous soil (light color in Figure 2.1) micro-scale heterogeneities typically exist, resulting in large zones of residual saturation (Dekker and Abriola 2000a, USEPA 2004). When initially released into the environment, DNAPLs sink below the water table, spreading laterally upon contact with finer grained layers (Illangasekare et al. 1995a, Illangasekare et al. 1995b, Kueper et al. 1989, Pinder and Abriola 1986). Lateral spreading results from the finer grained layer forming a capillary barrier with a higher entry pressure. In addition to this lateral spreading on top of finer grained layers, some DNAPL may enter the finer grained material as a result of fingering due to pore-scale heterogeneities at the interface of the two layers (Held and Illangasekare 1995a, Held and Illangasekare 1995b, Kueper and Frind 1991a, Kueper and Frind 1991b, Poulson and Kueper 1992). On the other hand, the presence of coarser grained lenses, especially when overlying LPM lenses, can act as a trap of sorts, resulting in high DNAPL saturations or pooling (Illangasekare et al. 1995b).
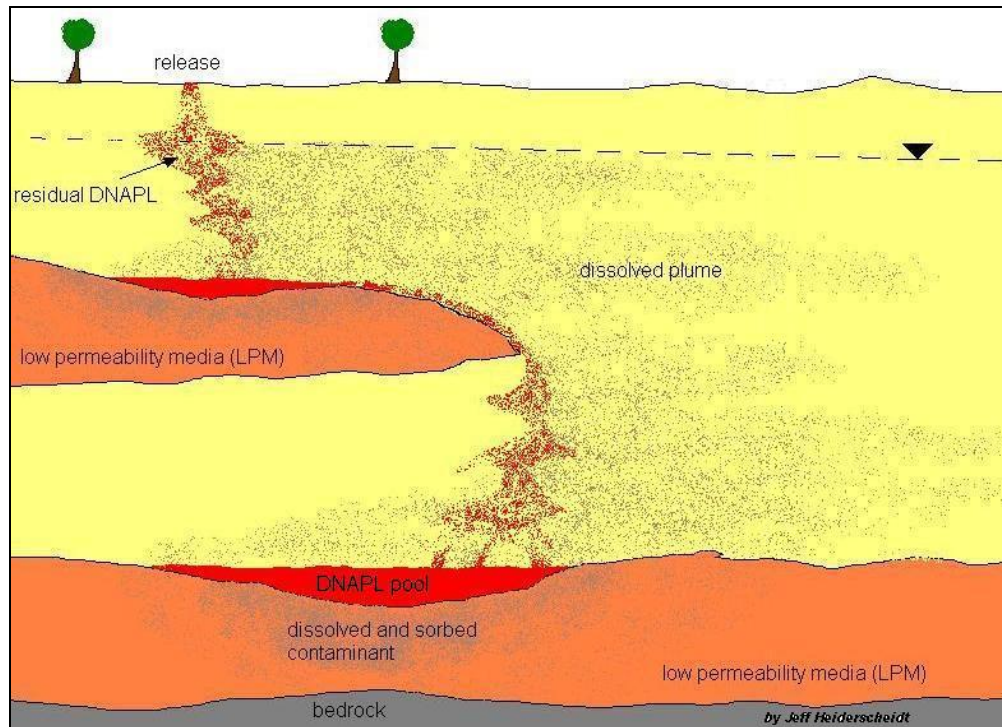
Figure 2.1: Generic Contaminated Site Conceptual Model

A field experiment at the Borden site by Kueper et al. (1993) confirmed that PCE DNAPL released into soil generated a complex source zone. Further, in that case when the PCE encountered grain size variations causing lateral migration, the resulting horizontal pools tended to be relatively thin. Parker et al. (2003) carried out extensive soil coring and water sampling at five sites with DNAPL contaminated sandy aquifers. The five sites were typical of many DNAPL contaminated sites in that the contamination occurred several decades or more ago. Three of the sites actually had free phase DNAPL in monitoring wells. Results of the sampling by Parker et al. (2003) demonstrated the difficulty in locating actual subsurface DNAPL source zones, and showed that remaining DNAPL in these aged sites occurs in sporadic, thin layers. The thin layers of DNAPL were only reliably identifiable by taking continuous soil cores, sub-sampling them on

small (5 cm or less) vertical intervals, and applying a hydrophobic red dye (Sudan IV) to the cores which gave a visual indicator that DNAPL was present.

Another challenge is that sand aquifers frequently have silty or clayey LPM below or within them (Mackay and Cherry 1989). These confining or low permeability layers may contain or develop fractures which facilitate DNAPL migration into or through the layer. DNAPL within these fractures can dissolve and diffuse into the layer matrix relatively quickly (Siegrist and Lowe 1996). Observations at sites contaminated with DNAPL products suggest a significant fraction of dissolved chemical may diffuse into LPM which acts as a sink for relatively high amounts of contaminant mass in the dissolved and sorbed phases (Ball et al. 1997, Johnson and Pankow 1992, Liu and Ball 2002, Mackay and Cherry 1989). Johnson et al. (1989) studied an extremely low permeability clay liner beneath a 5-year old hazardous waste dump containing DNAPLs and found that organic contaminants (including TCE) had diffused 15-20 cm into the liner in only five years. LPM consisting of or containing clay can be especially challenging because clays tend to have higher porosity and greater potential for organic contaminants to sorb to the soil particles than the surrounding aquifer (Mackay and Cherry 1989).

In addition to creating complex distribution of contaminant mass that is difficult to locate and characterize, site heterogeneity also makes removal of the contaminant source more challenging. Traditional source removal techniques often rely on groundwater flow to remove the contaminant. However, groundwater flow through source zones of high DNAPL saturation is greatly reduced by the reduction in effective permeability due to DNAPL filling most of the pore space (Powers et al. 1998, Saba and Illangasekare 2000). Oostrum et al. (1999) and Taylor et al. (2001) both performed 2D tank experiments of surfactant flushing of DNAPLs in heterogeneous systems. Results from both studies showed that surfactants can be effective for residuals and entrapped ganglia, but did not considerably reduce DNAPL mass from highly saturated DNAPL pools overlying LPM due to flow bypassing. Similarly, the modeling work of Saenton et

al. (2002) showed that the effectiveness of mass removal by surfactant flushing depends on the aquifer heterogeneity, which controls the DNAPL entrapment and surfactant delivery to the locations of entrapped DNAPLs. Flow bypassing reduces the delivery efficiency of the surfactant, prolonging the time to achieve the desired remediation end-point. In some extreme cases, the injected surfactant completely bypassed the NAPL source zones. Further, Soga et al. (2004) reviewed source depletion technologies and performed numerical simulations demonstrating that soil heterogeneity and complexity of DNAPL source zone morphology are critical factors controlling source reduction effectiveness.

Similarly, ground water flow through regions or strata of LPM is often negligible compared to flow around the LPM. Diffusion is the dominant transport mechanism in LPM, so groundwater carrying the treating chemicals can not easily access the LPM zones (Dekker and Abriola 2000b, Stroo et al. 2003). Consequently, once the DNAPL phase source is depleted by an aggressive source removal technology (or even by natural dissolution), plume concentrations are likely to rebound as diffused mass is returned from the LPM regions back into the surrounding, higher permeability flow zone (Freeze and McWhorter 1997, Liu and Ball 2002, Parker et al. 1994, Parker et al. 1997, Polak et al. 2003, Reynolds and Kueper 2002).

2.4   Kinetics of Chemical Oxidation with Permanganate

Research into the kinetics of permanganate oxidation of a wide variety of chemicals has been going on for many years. Ladbury and Cullis (1958) reviewed and summarized the various reaction pathways and kinetics for permanganate oxidation of aromatic hydrocarbons, phenols, aromatic alcohols, sugars, aliphatic acids, aldehydes, ketones, as well as a number of inorganic compounds. More recently, research has elucidated the reaction pathways and kinetics of permanganate oxidation of alkenyl halides, specifically chlorinated ethenes, such as PCE and TCE (Huang et al. 1999, Huang et al. 2001, Huang et al. 2002, Schnarr et al. 1998, Yan and Schwartz 1999, Yan

and Schwartz 2000).   Although this research is applicable to oxidation of any chlorinated ethene by permanganate (Huang et al. 2001, Siegrist et al. 2001, Yan and Schwartz 1999), only the PCE oxidation kinetics are discussed here because only PCE will be used in experiments of the proposed research. For the oxidation of PCE by permanganate (in the pH range 3.5 – 12), the following half-cell reactions apply:

$$4MnO_4^- + 16H^+ + 12e^- \rightarrow 4MnO_{2\ (s)} + 8H_2O \tag{2.1}$$

$$3C_2Cl_4 + 12H_2O \rightarrow 6CO_2 + 24H^+ + 12Cl^- + 12e^- \tag{2.2}$$

which, when combined, produce the following stoichiometric reaction

$$4MnO_4^- + 3C_2Cl_4 + 4H_2O \rightarrow 6CO_2 + 4MnO_{2\ (s)} + 8H^+ + 12Cl^- \tag{2.3}$$
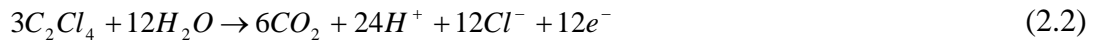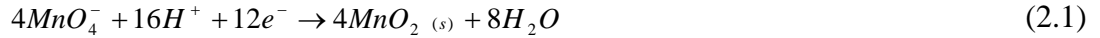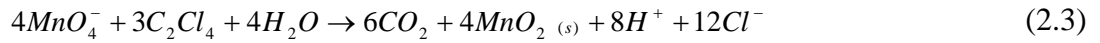
This is a simplification of the series of reactions involved. For example, Schnarr et al. (1998) proposed that Cl_2 is formed as an intermediate product that is quickly and completely changed to $2Cl^-$, based on thermodynamic considerations.

At lower pH levels (<3.5), the permanganate half-cell reaction becomes (Stewart 1965, Yan and Schwartz 1999)

$$4MnO_4^- + 32H^+ + 20e^- \rightarrow 4Mn^{2+} + 16H_2O \tag{2.4}$$

which, when combined with Equation 2, produces the following stoichiometric reaction

$$4MnO_4^- + 5C_2Cl_4 + 4H_2O \rightarrow 10CO_2 + 4Mn^{2+} + 8H^+ + 20Cl^- \tag{2.5}$$
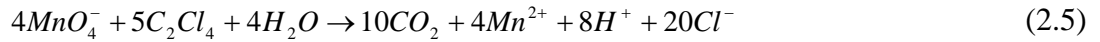
Equation 2.5 suggests that, for low pH, more PCE mass can be destroyed per mass of permanganate with reduced precipitation of manganese oxides. However, there will be a large increase in the amount of CO_2 generated. In fact, Huang et al. (2002) found that while CO_2 generation greatly increased at a pH of 3, the rate of PCE oxidation did not significantly change over a pH range of 3 – 10. This supports and expands on previous research by Yan and Schwartz (1999) showing the oxidation rate for PCE by permanganate was independent of pH in the range of 4 – 8. Further, Huang et al. (2002) found that the reaction rate was independent of ionic strength over the range of 0 – 0.2 M that is commonly encountered in natural groundwater. However, they did find the reaction rate increased with increasing temperature.

The oxidation of PCE by permanganate has been found to be first-order with respect to both PCE and permanganate, making the reaction second-order overall (Hood et al. 2000, Huang et al. 2002, Zhang and Schwartz 2000) with a reaction rate (k_2) ranging from 0.035 – 0.045 L/mol-sec at 20°C. A number of in situ field applications of ISCO using permanganate, performed by Chambers et al. 2000, Clayton et al. 2000, Lowe et al. 2002, Moes et al. 2000, and Siegrist et al. 1999, were reviewed to see how field oxidation reaction rates compare to those determined from lab studies. However, reaction rates have not been estimated from field data, presumably because contact time can not be reliably estimated and/or because aqueous concentrations drop to non-detect before the first sampling round so that the time for a given concentration decrease can not be determined.

The rate law describing the irreversible oxidation of PCE by permanganate is

$$\frac{d[PCE]}{dt} = -k_2[PCE][MnO_4^-] \tag{2.6}$$

where $d[PCE]/dt$ is rate of change in PCE concentration per unit time (T^{-1}), [*PCE*] is the concentration of PCE (ML^{-3}), [MnO_4^-] is the concentration of permanganate (ML^{-3}), and k_2 is the second-order reaction rate ($L^3M^{-1}T^{-1}$). If permanganate is present in excess, such that its concentration remains essentially constant throughout oxidation of the PCE, the reaction can be treated as pseudo-first-order using Equation 2.7

$$k_1 = -k_2[MnO_4^-] \tag{2.7}$$

where k_1 is the pseudo-first-order rate constant (1/sec). In the case of permanganate oxidation of other chlorinated ethenes (TCE, 1,1-DCE, cis-DCE, trans-DCE, VC), the ratio of moles permanganate consumed per mole contaminant oxidized will change based on the appropriate reaction stoichiometry (Equations 2.8-2.10), as will the second order rate constant (k_2) and pseudo-first-order rate constant (k_1).

$$2MnO_4^- + C_2HCl_3 \rightarrow 2CO_2 + 2MnO_{2\ (s)} + H^+ + 3Cl^- \qquad \text{(for TCE)} \tag{2.8}$$

$$8MnO_4^- + 3C_2H_2Cl_2 \rightarrow 6CO_2 + 8MnO_{2\ (s)} + 2OH^- + 6Cl^- + 2H_2O \quad \text{(for DCE)} \tag{2.9}$$

$$10MnO_4^- + 3C_2H_3Cl \rightarrow 6CO_2 + 10MnO_{2\ (s)} + 7OH^- + 3Cl^- + H_2O \qquad \text{(for VC)} \qquad (2.10)$$

2.5   Natural Oxidant Demand

Field soils and aquifer sediments typically contain natural organic matter (NOM), reduced metals, and other reductants that can be readily oxidized. These soil constituents are referred to collectively as natural oxidant demand (NOD), or sometimes soil oxidant demand (SOD), and compete with target contaminants for available oxidant. Zhang and Schwartz (2000) proposed that components comprising the NOD have a much faster reaction rate with MnO_4^- than do chlorinated contaminants, in order to explain delayed breakthrough of MnO_4^- in column experiments by Schnarr et al. (1998). This conceptual model of NOD oxidation corresponds to an instantaneous sink (Figure 2.2a). Under this concept, all of the NOD must be oxidized before any PCE oxidation occurs; thus, in order to oxidize a given mass of PCE, the mass of MnO_4^- needed will be equal to the NOD plus the demand determined from the reaction stoichiometry.

On the other hand, there is evidence that not all NOD components are oxidized faster than the contaminant (Mumford et al. 2002, Mumford et al. 2005, Siegrist et al. 1999, Struse et al. 2002, Yan and Schwartz 1999). Because NOD is generally a complex mixture of components whose surface area available for oxidant contact varies, it seems likely that NOD oxidation will be a kinetic process as depicted in Figure 2.2b. This means that oxidation of NOD and PCE occur simultaneously, with relative rates of oxidation controlling depletion of each.
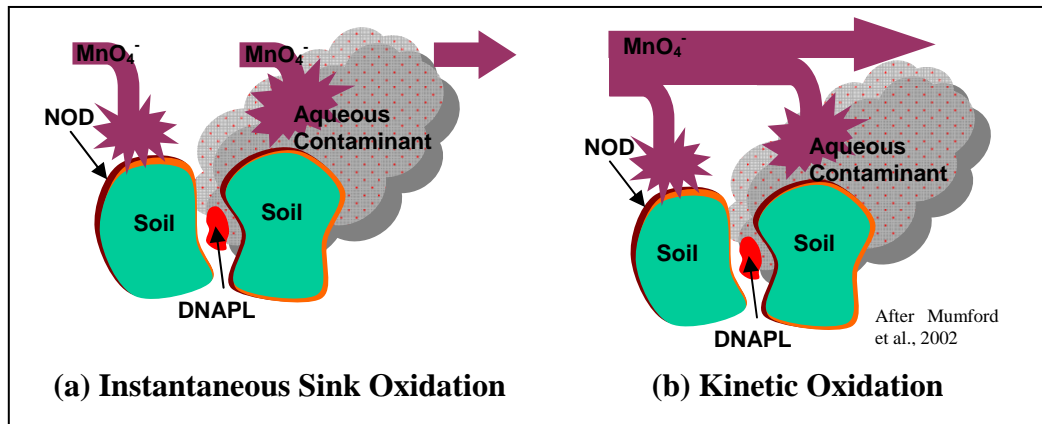
Figure 2.2: NOD Oxidation Conceptual Models

Further, because NOD results from a mixture of constituents, the kinetic rate for oxidation of NOD can vary widely for different soils. While the kinetic rates for some NOD constituents of a particular soil are often higher than that of the target contaminant, preliminary results related to this research, and that of others, suggests NOD frequently consists of at least two components with markedly different oxidation rates (Crimi and Siegrist 2004, Jackson 2004, Mumford et al. 2005). As an example, Chambers et al. (2000) found two distinct NOD oxidation rates for each of three different field soils in batch tests. The rate during the first 24 hours was 10 – 20 times faster than the rate during the next 13 days. They also found that the slower rate for the three soils was virtually the same, while the initial fast rate varied by soil type with silt and clay being about twice that of sand. Similar results are shown in Figure 2.3, for a field soil taken from the Mines Park test site near the Colorado School of Mines in Golden CO (Seitz 2004). Because the graph is natural log of oxidant concentration over initial concentration versus time, the slope can be taken directly as a kinetic oxidation rate. From the figure, it can be seen that during the first day, the fraction of NOD oxidized has a high oxidation rate; after the first day, the remaining NOD is oxidized at a much lower

rate. The addition of site groundwater increased the overall amount of NOD slightly, but did not change the NOD oxidation rates.
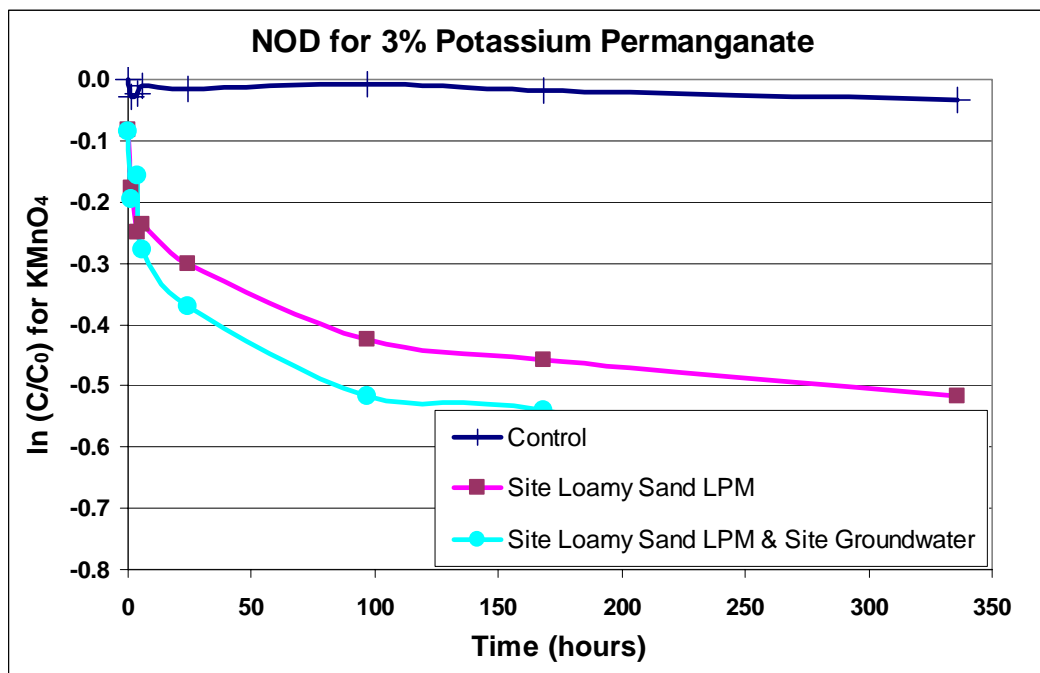
Figure 2.3: NOD Oxidation Rates for Mines Park Soil (Seitz 2004)

Mumford et al. (2005) considered the possibility that the multiple rates could be a result of organic carbon located within soil grain micropores being more difficult for oxidant to access. They performed batch NOD studies on native coarse sand from the Borden test site (grain size greater than 0.42mm), as well as on coarse Borden sand that had first been crushed (grain size less than 0.074mm). Results from the one week NOD tests showed no significant difference, suggesting that either the proposed geometric configuration is not a rate-limiting factor or that reduced species in micropores are still unavailable even after crushing (Mumford et al. 2005).

The research on kinetic rates for NOD oxidation to date has not determined the overall reaction order. The results from the studies already mentioned suggest that it is first-order with respect to NOD, but there has been little study of the effect of MnO_4^-

concentration. The work of Crimi and Siegrist (2004) did utilize two MnO_4^- concentrations, and provided some indication that at least the NOD fraction with the slower kinetic rate is also first-order with respect to MnO_4^- (second-order overall), because increasing the oxidant concentration by a factor of four resulted in a doubling of the oxidation rate for the slow fraction of NOD.

Additionally, research is limited on how NOD values determined from batch tests will compare to actual NOD affects in a real-world groundwater system. The results of Huang et al. (2000) suggest that batch NOD tests will over-estimate real-world NOD, as represented by NOD determination from a 1D flow column, by as much as 300 times. However, their batch tests were conducted with unusually high water to solids ratio of 10:1 and their batch tests were vigorously mixed. Crimi and Siegrist (2004) independently varied both water to solids ratio and degree of mixing (static, gentle stirring, completely mixing) to quantify the effects on NOD determination for a field soil. Their results indicate that (for the field soil studied) a water to solids ratio of one or slightly more, combined with static or gently stirred conditions, results in an NOD determination within 10% of that from a 1D flow column. If the solid to liquid ratio is too high, oxidant is depleted before reaching the actual NOD value. On the other hand, if the solid to liquid ratio is too low, too much oxidant is depleted and oxidant demand is over-estimated because the batch tests typically continue until all or nearly all the oxidant is gone (Crimi and Siegrist 2004). NOD mass fraction estimates determined from batch-scale tests may need to be adjusted or "up-scaled" to be effective in predicting field-scale performance.

Along these lines, Mumford et al. (2004) developed an in situ push-pull technique for estimating the NOD mass fraction for a field soil. They injected oxidant and a conservative tracer at three locations of uncontaminated soil within the Borden site, allowed two days for the oxidant to react with aquifer material, and extracted the oxidant and tracer. They also performed batch tests on field soil taken from the site, duplicating conditions of the push-pull tests and found the push-pull tests and the two-day batch tests

provided similar results. Mumford et al. (2004) concluded that the in situ push-pull technique is viable, with the advantage that it provides a measurement representative of a much larger aquifer volume. Conversely, batch tests can provide NOD estimates representative of actual in situ field performance, provided that the batch tests are not simply carried out as ultimate NOD tests (i.e., run until all oxidizable material is gone) but instead stopped at a representative time. Mumford et al. (2004) also found that the variability between replicate batch test results decreased as the soil mass was increased, with least variability when the water to solids ratio was approximately one. Finally, the increased variability for small batch test soil masses, along with the 30% variation in NOD values estimated from the push-pull tests for the three locations, highlight the variability and site-specific nature of NOD values even for a relatively homogeneous site like Borden (Mumford et al. 2004).

2.6   Permeability Effects of Oxidation by Permanganate

Research has shown that oxidation of a high DNAPL saturation source using permanganate may result in permeability reductions due to precipitation of manganese oxides thereby reducing the ability for oxidant to be transported to the source (Lee et al. 2003, Schroth et al. 2001, Siegrist et al. 2002). On the other hand, research into permeability effects from permanganate oxidation of DNAPL source zones at lower saturations is a bit more ambiguous. Nelson et al. (2001) concluded that the manganese oxides produced during oxidation of a PCE DNAPL present at approximately 4-7% saturation had negligible effect on the permeability, despite the system remaining at a neutral pH due to natural buffering from the carbonate mineral-containing sands. On the contrary, Lee et al. (2003) found that permanganate oxidation of a TCE DNAPL source zone at 8% saturation resulted in generation of up to 4900 mg $MnO_2(s)$/kg porous media, in an unbuffered silica sand system utilizing de-ionized water. Further, they witnessed a six-fold decrease in velocity of the oxidation front over the two-month experiment. They

attributed this decrease in oxidation front velocity to decreased oxidation delivery resulting from reductions in permeability.

There are several methods to relate permeability reductions to reductions in porosity resulting from immobile components in porous media pore spaces. These may take the form of power law models as in Equations 2.11 (Wyllie 1962) and 2.12 (Reis and Acock 1994) or capillary-tube models like the Kozeny-Carman equation in Equation 2.13 (Bear 1972)

$$k_{r,w} = \left(\frac{1 - S_n - S_{r,w}}{1 - S_{r,w}} \right)^3 \tag{2.11}$$

$$k_{r,w} = \left(1 - \frac{\phi - \phi_{eff}}{\phi} \right)^b \tag{2.12}$$

$$k_{r,w} = \frac{\phi^3}{K_s (1-\phi)^2} \left(\frac{d_{50}^2}{180} \right) \tag{2.13}$$

where $k_{r,w}$ is the relative water permeability, S_n is the saturation of immobile component in the pore space, $S_{r,w}$ is the residual water saturation for the porous media, ϕ is the soil porosity, ϕ_{eff} is the effective soil porosity, b is an empirical exponent related to the type of porous media, K_s is the saturated hydraulic conductivity (LT^{-1}) and d_{50} is the representative (median) grain size (L).

Saenton (2003) found Equation 2.11 to provide good agreement to experimentally derived permeability data (Saba 1999) for DNAPL in silica sands like those that are being used in this research. Additionally, Clement et al. (1996) proposed Equation 2.12 (with b = 19/6) for pore-clogging due to microbial growth. However, Reis and Acock (1994) concluded that the various forms of the Kozeny-Carman equation are not generally a good model for the reduction in permeability following chemical precipitation in a porous media because they significantly under-predict permeability reductions. They also pointed out that power law models suffer from under-prediction of permeability reductions, especially at high levels of plugging. This can be seen in the research by Lee

et al. (2003). Converting the mass of $MnO_2(s)$ generated to a volume, using a $MnO_2(s)$ density of 5040 g/L (CRC 2001) and either Equation 2.11 or Equation 2.12 (with b=3.5, the average value determined from three studies using similar sand, Reis and Acock 1994), the mass of $MnO_2(s)$ generated in the experiment of Lee et al. (2003) results in an estimated 1.6% reduction in permeability. However, the CRC (2001) density is for a dry, aged mineral pyrolusite form of $MnO_2(s)$. Li and Schwartz (2004) determined the precipitated $MnO_2(s)$ is a hydrous birnessite-like form expected to have a lower density. Unfortunately, no values for the density of this precipitated form have been determined. Using a lower estimated density (e.g., 1000 g/L) to estimate the volume of $MnO_2(s)$, and Equation 2.11 or 2.12, results in an estimated permeability reduction of 7.5%. However, a much greater reduction would be needed to account for the experimental results, such as would occur if manganese oxides block the pore throats before the entire pore space is filled.

Reitsma and Randhawa (2002) performed 1D column experiments oxidizing aqueous PCE at approximately 50 mg/L with 2000 mg/L $KMnO_4$ (Darcy velocity of 3.0 m/day) in silica sand. They found that with $MnO_2(s)$ filling as little as 1% of pore space (assuming solid $MnO_2(s)$ with density of 5040 g/L), permeability was reduced by 98%. Even if the density of the precipitated $MnO_2(s)$ is taken as 1000 g/L the predicted permeability reduction (by Equation 2.11 or 2.12) would only be 15%. Reitsma and Randhawa (2000) concluded that the increased permeability reduction must be due to pore-clogging. They also found higher flow rates resulted in slower permeability reduction, possibly because the higher flow rate dislodges some $MnO_2(s)$ particles as they begin to get lodged in pore throats.

Similarly, Schroth et al. (2001) performed 1D column experiments to study the effects of $MnO_2(s)$ formation on permeability. Their study differed from that of Reitsma and Randhawa (2002) in that residual DNAPL TCE was emplaced in 2/3 of the column length, the $KMnO_4$ concentration was 790 mg/L, and the Darcy velocity was 15.8 m/day. They estimated a permeability reduction of 96% in 24 hours. Based on the mass of TCE

destroyed, the mass of $MnO_2(s)$ generated can be estimated as 66.2 g. Assuming it was evenly distributed throughout the DNAPL source zone, with a $MnO_2(s)$ density of 5040 mg/L, the estimated permeability reduction (by Equation 2.11 or 2.12) would only be 10%. However, if the $MnO_2(s)$ is considered to be located primarily in the first 25% of the source zone as visually observed by Schroth et al. (2001), the estimated permeability reduction becomes 33.6%. Further, if the precipitated $MnO_2(s)$ density is again taken as 1000 mg/L, and it is considered to be located in the first 25% of the source zone, the estimated permeability reduction (at 95.2%) is quite close to the observed reduction. The column used by Schroth et al. (2001) had twice the cross-sectional area and 33 times the length of that used by Reitsma and Randhawa (2002), suggesting that even if throat clogging is occurring at the pore scale, the permeability relations of Equations 2.11 and 2.12 may still be effective at larger scales, as long as an appropriate density is used for the precipitated $MnO_2(s)$.

While permeability reductions in and around the source zone, generated by oxidation using permanganate, are quite possible, they may not be entirely bad. Although flow of additional oxidant through the source zone may be reduced, so would water flow in general. This reduction or blockage of flow through the source zone could act to chemo-stabilize a DNAPL source effectively cutting off the flux of dissolved contaminant from the DNAPL (MacKinnon and Thomson 2002). However, Conrad et al. (2002) found that, while a $MnO_2(s)$ shell or rind did indeed form around a DNAPL pool during oxidation with permanganate, three months after oxidation the shell failed and DNAPL fingers emerged through it indicating that chemo-stabilization may not be a long term benefit/solution. As alluded to in the previous discussion about the oxidation kinetics, system chemistry impacts the $MnO_2(s)$ generation and subsequent effects on porous media permeability. For example, according to Stewart (1965) and Yan and Schwartz (1999), if the pH drops below 3.5 the kinetics favor production of soluble Mn^{2+} instead of $MnO_2(s)$. Along these lines, in a well-buffered system such as an aquifer of carbonate soils the pH will likely remain more neutral leading to more $MnO_2(s)$

generation. The groundwater flow can also have an effect, such as controlling if and how much $MnO_2(s)$ is transported colloidally instead of being deposited close to the point of generation.

2.7   Diffusion in Porous Media

The subsurface environment frequently contains regions of LPM within, or as an aquitard beneath aquifers. Subsequent to contamination within the aquifer, substantial contaminant mass can make its way into the LPM zones by diffusion. For example, in the case of an extremely low permeability clay liner beneath a 5-year old hazardous waste dump containing DNAPLs, Johnson et al. (1989) found that organic contaminants (including TCE) had diffused 15-20 cm into the liner in only five years. On the other hand, waste-generated chloride had diffused up to 83 cm in that time. The different distances were attributed to different molecular diffusion rates as well as sorption of the organics retarding diffusion. Similarly, Ball et al. (1997) studied a soil core from the aquitard beneath a TCE/PCE plume at Dover Air Force Base (AFB), Delaware. They found that PCE and TCE had diffused approximately 80-100 cm into the aquitard in the estimated 15-20 years since the plume arrived above the core location. In a later field experiment at the Dover AFB site, Liu and Ball (2002) confirmed the validity of their previous diffusion modeling. Their results also appear to provide direct evidence that an underlying confining layer can be contaminated by an overlying plume of aqueous contamination, and the confining layer can subsequently become a source of groundwater contamination through back-diffusion once the primary plume is gone.

On the other hand, LPM may contain fractures large enough to allow DNAPL migration into the LPM fractures. A series of modeling studies have focused on DNAPL migration through such fractures, and the subsequent dissolution and diffusion of contaminant mass into the surrounding matrix. These studies have shown that significant mass of contaminant can end up diffusing into the matrix, in a relatively short time on the

order of only a few years (Parker et al. 1994, Parker et al. 1997, Reynolds and Kueper 2002, Ross and Lu 1999).

As seen by Johnson et al. (1989), different solutes diffuse at different rates through porous media. Millington and Quirk (1959, 1961), proposed that the effective diffusion coefficient, D_e, (L^2T^{-1}) of an aqueous solute through a porous media can be estimated from the molecular diffusion coefficient for a bulk solution of the solute (at an infinitely dilute concentration), D_m, (L^2T^{-1}) and the effective porosity, ϕ_{eff}

$$D_e = D_m \phi_{eff}^{4/3} \tag{2.14}$$

In order to account for the reduced effective porosity of a multiphase system, Jury et al. (1991) modified the Millington-Quirk relationship, relating it to water content (θ_w) as well as effective porosity.

$$D_e = D_m \frac{\theta_w^{10/3}}{\phi_{eff}^2} \tag{2.15}$$

In the fully water-saturated case, the water content (θ_w) is equal to effective porosity (ϕ_{eff}) and Equation 2.15 simplifies to the Millington-Quirk relation of Equation 2.14.

Tidwell et al. (2000) researched the effect of porosity on diffusion of potassium iodide into Culebra dolomite slabs using x-ray absorption imaging at the centimeter-scale. They found that diffusion rates within the slabs indeed varied spatially, and depended on the magnitude of porosity at each location. Conversely, Itakura et al. (2003) performed diffusion experiments using three different organic contaminants, including TCE and three soil configurations (reconstituted and intact kaolin clay as well as reconstituted sandy silt), and determined the relation

$$D_e = D_m \phi \tag{2.16}$$

inadequately fit a combination of their data (19 points) and that from four other studies (6 points). Subsequently, they concluded "there is little correlation between tortuosity and porosity." However, from the data they present (and excluding only two of the six data points from other studies, keeping 23 of 25 data points), it appears that the Millington-

Quirk relation of Equation 15 fits reasonably well. Itakura et al. (2003) also tested different thicknesses of reconstituted clay, and determined that sample thickness, over the range of 1.25 – 2.97 cm, did not significantly affect the effective diffusion coefficient.

Because different chemicals have different molecular diffusion coefficients, and different sorptive properties, it may be possible to exploit these differences in remediating chlorinated solvent mass located in LPM. Based on the small number of studies reported in the literature, ISCO using permanganate appears promising. Struse et al. (2002) studied the transport of permanganate by diffusion through 2.54 cm long, intact cores of low permeability silty clay loam soil. Permanganate diffused through the uncontaminated core in approx. 15 days. When TCE was emplaced in the center of the core, it took twice as long for the permanganate to get all the way through the core; however, nearly all of the TCE was successfully oxidized with none diffusing out of the core despite having only half the distance to travel. These results indicate the permanganate can effectively diffuse into an LPM and oxidize contaminant mass located there. Further, the effective diffusion coefficients correlated well to the porosities, using the Millington-Quirk relation. Similarly, Siegrist et al. (1999) tested the ability of permanganate to diffuse into silty clay LPM at a field site in Ohio. The permanganate was emplaced via hydraulic fracturing, and continuous cores were extracted at several times over 15 months. After 10 months, the permanganate had visibly diffused over 15 cm above and below the emplacement, and batch tests showed that this zone still sustained a high degradation potential. However, few additional studies have been reported in the literature and there has been insufficient study of how LPM configuration will impact the effectiveness of chemical oxidation within an aquifer.

2.8   DNAPL Mass Transfer

Mass transfer or dissolution of the DNAPL into the aqueous phase is generally modeled based on the well-known stagnant film model (Sherwood et al. 1975) utilizing a first-order linear driving force

$$\frac{dc_\infty}{dt} = -k_{La}(c_\infty - c^*) \tag{2.17}$$

where dc_∞/dt is the rate of change of aqueous concentration per time ($ML^{-3}T^{-1}$), c_∞ is the aqueous solute concentration (ML^{-3}) of the bulk solution, c^* is the aqueous solubility limit of the solute (ML^{-3}), and k_{La} is the DNAPL dissolution rate or lumped mass transfer coefficient (T^{-1}). The origin of this model is Fick's First Law of Diffusion that states mass flux of a substance diffusing across a given cross-sectional area per unit time is proportional to the concentration gradient at the surface

$$J_a = -D_m \frac{dc}{dz} \tag{2.18}$$

where J_a is the mass flux per unit area ($ML^{-2}T^{-1}$) and dc/dz is the concentration gradient (ML^{-4}). The change in aqueous concentration per time is then the mass flux per unit area (J_a) times the DNAPL-water interfacial area, A_{nw}, (L^2), divided by the porous media volume of interest, V, (L^3). In the stagnant film model (Figure 2.4), the film is assumed to be very thin such that the concentration gradient is linear and can be approximated by the saturated aqueous concentration on the DNAPL side minus the bulk aqueous concentration on the bulk aqueous side, divided by the film thickness, δ, (L). The molecular diffusion coefficient, D_m, divided by the film thickness, δ, then is the intrinsic mass transfer coefficient, k_L, (LT^{-1}). The lumped mass transfer coefficient is the product of the intrinsic mass transfer coefficient, k_L, times the DNAPL-water interfacial area, A_{nw}, divided by the porous media volume of interest, V.
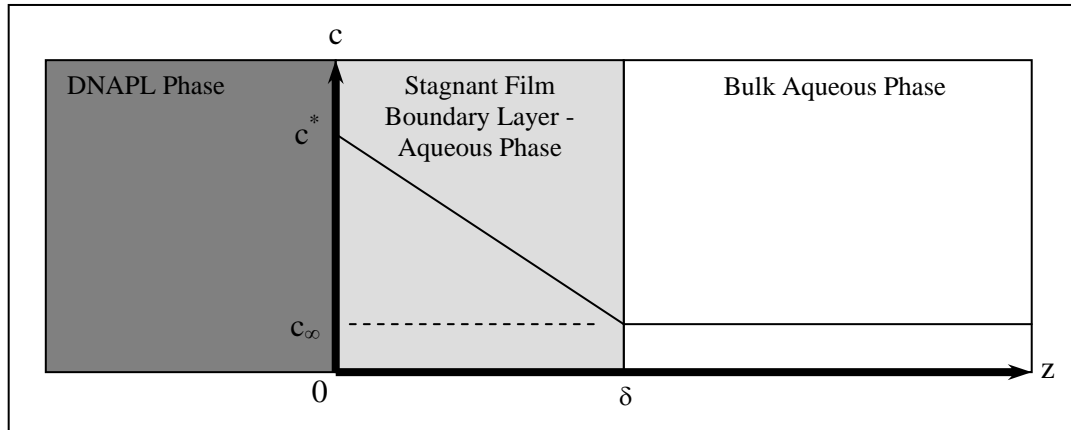
Figure 2.4: Stagnant Film Model for DNAPL Dissolution Mass Transfer

The lumped mass transfer coefficient is used because the complex architecture of DNAPL sources makes A_{nw} too difficult to estimate, and the stagnant film thickness is a theoretical construct that can not be measured. Although k_{La} is still a parameter that can not be measured directly, because it combines parameters that can not be measured, it reduces the unknowns to a single parameter for estimation.

As a result, a considerable amount of research has been devoted to developing methods to estimate k_{La} from measurable system parameters, including pore size and DNAPL saturation which affect the specific interfacial surface area for dissolution (Ewing 1996, Imhoff et al. 1994, Miller et al. 1990, Nambi 1999, Powers et al. 1994a Powers et al. 1994b, Saba and Illangasekare 2000). The general approach is to utilize an empirically determined Gilland-Sherwood correlation as given by Welty et al. (1976)

$$Sh = a + b\,Re^c\,Sc^d \tag{2.19}$$

to estimate the modified Sherwood number (*Sh*) from other dimensionless numbers describing the system (e.g. Reynolds number, *Re*, and Schmidt number, *Sc*), where *a*, *b*, *c*, and *d* are empirically determined constants. The modified Sherwood number relates the mass transport in a system to the diffusive forces, the Reynolds number relates system

inertial forces to viscous forces, and the Schmidt number relates viscous forces to diffusive forces. Mathematical equations for these three dimensionless numbers are

$$Sh = \frac{k_{La}d_{50}^2}{D_m} \tag{2.20}$$

$$Re = \frac{\rho_w \bar{v} d_{50}}{\mu_w} \tag{2.21}$$

$$Sc = \frac{\mu_w}{\rho_w D_m} \tag{2.22}$$

where ρ_w is the aqueous phase density (ML^3), $\bar{v}$ is the average linear groundwater velocity (LT^{-1}), and μ_w is the aqueous phase dynamic viscosity (ML^{-1}T^{-1}). The Sherwood number determined from the empirical correlation is then used in Equation 2.20 to estimate the lumped mass transfer coefficient, k_{La}. Most correlations incorporate volumetric DNAPL content (θ_n) in some form to account for the changing DNAPL-water interfacial area as dissolution proceeds (Miller et al. 1990, Powers et al. 1994b). Example Gilland-Sherwood relations are shown in Table 2.1.

Table 2.1: Gilland-Sherwood Mass Transfer Correlations for NAPL-Water Systems

$Sh = 37.15\left(\dfrac{\theta_n}{n}\right)^{1.24} \text{Re}^{0.61}$ (for $\theta_n/n < 0.35$)	Nambi and Powers (2003)
$Sh = 0.4727\,\text{Re}^{0.2793}\,Sc^{0.33}\left(\dfrac{\theta_n}{1-\theta_n}\right)^{1.642}\left(\dfrac{d_{50}}{\tau L}\right)^{0.1457}$	Saba et al. (2001)
$Sh = 11.34\,\text{Re}^{0.2767}\,Sc^{0.33}\left(\dfrac{\theta_n d_{50}}{\tau L}\right)^{1.037}$	Saba and Illangasekare (2000)
$Sh = 4.84\,\text{Re}^{0.219}\,\theta_n^{1.32}$	Ewing (1996)
$Sh = 36.8\,\text{Re}^{0.654}$	Powers et al. (1994a)
$Sh = 4.13\,\text{Re}^{0.598}\left(\dfrac{d_{50}}{d_M}\right)^{0.673}U^{0.369}\left(\dfrac{\theta_n}{\theta_{n0}}\right)^{\beta}$; $\beta = 0.518 + 0.114\left(\dfrac{d_{50}}{d_M}\right) + 0.10U$	Powers et al. (1994b)
$Sh = 340\theta_n^{0.87}\,\text{Re}^{0.71}\left(\dfrac{d_{50}}{x}\right)^{0.31}$	Imhoff et al. (1994)
$Sh = 12\,\text{Re}^{0.75}\,\theta_n^{0.60}\,Sc^{0.5}$	Miller et al. (1990)

In the relations shown in Table 2.1, L is the characteristic or dissolution length in the flow direction (L), d_M is the diameter of a "medium" sand grain (defined by U.S. Department of Agriculture as 0.05cm), and x is the distance into the residual DNAPL source in the direction of flow (L). Coefficients of the correlations have typically been found to have 95% confidence intervals of approximately $\pm$ 17% for the scaling coefficient at the beginning, $\pm$ 12% for the Reynolds number exponent, and $\pm$ 13% for the NAPL content exponent (Miller et al. 1990, Nambi and Powers 2003, Powers et al. 1994b, Saba and Illangasekare 2000, Saenton 2003). Confidence intervals for other coefficients, when present, have not been reported. Differences in empirical coefficients and formulations are at least partly due to differences in experimental conditions. For example Powers et al. (1994a) used a 1D system with spherical dissolving organic media and Powers et al. (1994b) used a 1D homogeneous system, while Saba and Illangasekare

(2000) were considering a 2D system with heterogeneity-induced flow-bypassing. Miller et al. (1990) and Imhoff et al. (1994) both used 1D systems. Ewing (1996) and Saba et al. (2001) considered a 2D system with surfactant flushing. Nambi and Powers (2003) further expanded the available choices by looking at 2D systems with high DNAPL saturations resulting in slower mass transfer characterized by a significantly increased exponent on the DNAPL saturation term. These correlations have been found to be effective for modified Sherwood numbers ranging from 0.01 to over 25.0 (Imhoff et al. 1994, Miller et al. 1990, Nambi and Powers 2003).

Another useful dimensionless number is the second Damkohler number, *Da(II)*, shown in Equation 2.23, which relates the characteristic time of DNAPL mass transfer or dissolution (τ_m) to the characteristic time of chemical reaction (τ_r). The characteristic time of mass transfer is the inverse of the lumped mass transfer coefficient and the characteristic time of chemical reaction is the inverse of the first-order (or pseudo-first-order) chemical reaction rate. So a working definition of the second Damkohler number is the ratio of chemical reaction rate to mass transfer rate as shown in Equation 2.24.

$$Da(II) = \frac{\tau_m}{\tau_r} \qquad (2.23)$$

$$Da(II) = \frac{k_1}{k_{La}} \qquad (2.24)$$

In the context of DNAPL source depletion by chemical oxidation, the magnitude of *Da(II)* provides an indication of whether the rate of mass depletion is rate-limited by either the mass transfer from the DNAPL to aqueous phase or the chemical reaction rate. A *Da(II)<<1* indicates contaminant mass is transferring into the aqueous phase faster than the chemical reaction can destroy it, while a *Da(II)>>1* suggests that the chemical reaction is faster than the mass transfer. The ideal situation is to adjust system conditions such that the second Damkohler is as near to one as possible.

Similarly, the first Damkohler number, *Da(I)* shown in Equation 2.25 is a dimensionless number relating the characteristic time of fluid motion or hydraulic

retention time (τ_f) to the characteristic time of DNAPL mass transfer or dissolution (τ_m). In the hydrology and contaminant transport setting, the retention time is given by Equation 2.26, where L is the characteristic length or length of interest (L) and $\bar{v}$ is the linear pore velocity of the fluid. Equation 2.27 gives the characteristic time for DNAPL mass transfer or dissolution which is just the inverse of the lumped mass transfer coefficient (k_{La}).

$$Da(I) = \frac{\tau_f}{\tau_m} \tag{2.25}$$

$$\tau_f = \frac{L}{\bar{v}} \tag{2.26}$$

$$\tau_m = \frac{1}{k_{La}} \tag{2.27}$$

Combining Equations 2.25 – 2.27 gives a working definition of the first Damkohler number, Equation 2.28, which is a ratio of the dissolution rate to the fluid transport rate.

$$Da(I) = \frac{k_{La}L}{\bar{v}} \tag{2.28}$$

The magnitude of $Da(I)$ provides an indication of whether dissolution is occurring at or near equilibrium such that the local equilibrium assumption (LEA) would be valid. Under LEA conditions, estimating mass removal rates from a DNAPL source are simplified and can be accomplished assuming the aqueous phase contacting the DNAPL has a contaminant concentration equal to the contaminant's aqueous solubility (Powers et al. 1991). However, deviation from equilibrium dissolution is frequently seen in field situations and is generally a result of rate-limited mass transfer from the DNAPL to aqueous phase, physical heterogeneity, and rate-limited sorption/de-sorption (Brusseau 1992). Generally, Brusseau (1992) found that $Da(I) >= 100$ indicates equilibrium, $10 =< Da(I) < 100$ indicates near equilibrium, and $Da(I) < 10$ indicates rate-limited mass transfer.

Mayer and Miller (1996) performed a series of 2D simulations and confirmed that moderate heterogeneity can significantly impact mass transfer rates away from LEA conditions. Because the mass transfer rate is dependent upon the water velocity as represented by the Reynolds number (typically to a power other than one) in the correlations, the first Damkohler number may be useful in optimizing the mass transfer of a given system depending on what mass transfer correlation best describes the system (Mayer et al. 1999). A caveat from Zhu and Sykes (2000) is that some correlations developed from 1D column data tend to result in simulation of equilibrium dissolution without changing to rate-limited mass transfer as DNAPL saturation gets low, and so may be ill-suited to large-scale problems.

A goal of ISCO is to speed up remediation of a contaminant source zone by inducing increased mass transfer (and subsequent destruction) from a DNAPL source. Based on experimental results, Schnarr et al. (1998) suggest that DNAPL dissolution and oxidation are processes that occur in parallel with increased mass transfer during oxidation occurring primarily as a result of an increased aqueous concentration gradient. Urynowicz (2000) demonstrated the ability for permanganate to increase dissolution of DNAPL TCE in batch and flow-thru experiments without porous media present; however, the rate decreased as a $MnO_2(s)$ film formed at the DNAPL-water interface. Reitsma and Dai (2001) performed a theoretical study to estimate the maximum expected DNAPL mass transfer enhancement resulting from chemical oxidation. They estimated a maximum five times increase in dispersive mass transport from a PCE DNAPL pool resulting from the increased concentration gradient; however, they predict little enhancement in local-scale mass transfer from DNAPL to aqueous phase suggesting no change in dissolution mass transfer parameters. Further, they suggest that actual enhancement is likely to be less because permeability reduction and decreased interfacial contact area were not accounted for in the estimate. On the contrary, MacKinnon and Thomson (2002) calculated a ten times initial increase in PCE mass transfer from a

DNAPL pool during a 2D oxidation experiment, with decreasing mass flux over time attributed to $MnO_2(s)$ formation.

Cussler (1997) presents an equation for adjusting the intrinsic mass transfer coefficient, k_L, to account for irreversible, first-order (or pseudo-first-order) homogeneous chemical reaction

$$k_L^* = (D_m k_1)^{1/2} \coth\left[\left(\frac{k_1}{D_m}\right)^{1/2} \delta\right]$$
(2.29)

where k_L^* is the intrinsic mass transfer coefficient with chemical reaction (MT^{-1}), δ is the theoretical thickness of the stagnant film (L), D_m is the molecular diffusion coefficient (L^2T^{-1}), and k_1 is the first-order or pseudo-first-order kinetic reaction rate constant (T^{-1}). Equation 2.29 was presented by Cussler (1997) for diffusion from a well-mixed gas into a liquid that is not well-mixed, across a thin stagnant liquid film at the interface. The equation was developed from a mass balance across the stagnant film with a constant concentration at the well-mixed gas surface and zero concentration at the liquid surface. Urynowicz (2000) found this equation to be applicable to mass transfer from a TCE DNAPL to the aqueous phase for batch systems with no porous media during oxidation using permanganate, before substantial $MnO_2(s)$ formation at the DNAPL surface. In applying this equation to mass transfer from DNAPL to the aqueous phase, it is assumed that the contaminant concentration at the DNAPL surface remains constant and equal to the solubility limit of the contaminant, regardless of DNAPL thickness, until the DNAPL is depleted. This is the same assumption inherent in the common use of the stagnant film model to describe DNAPL mass transfer under natural (non-reaction-enhanced) dissolution conditions.

According to Cussler (1997) adjustment of the mass transfer coefficient is necessary only if the chemical reaction is fast, with half life on the order of minutes. Because δ can not be measured, it can be replaced with D_m/k_L, where k_L is the intrinsic mass transfer coefficient without chemical reaction (MT-1). Further, k_L is defined as the

molecular diffusion coefficient divided by the stagnant film thickness. Dividing through by k_L gives the change in mass transfer caused by the chemical reaction as given by Cussler (1997)

$$\frac{k_L^*}{k_L} = \left[\frac{D_m k_1}{(k_L)^2}\right]^{1/2} \coth\left[\left(\frac{k_1 D_m}{k_L^2}\right)^{1/2}\right]$$

(2.30)

Unfortunately, this requires knowledge of the intrinsic mass transfer coefficient without chemical reaction, k_L, which can not be determined for DNAPL dissolution in porous media because it is not possible to know the DNAPL-water interfacial area needed to obtain k_L from the lumped mass transfer coefficient, k_{La}, which is determined empirically.

2.9   Modeling of DNAPL Site Remediation by ISCO with Permanganate

A search of published literature turned up only two efforts at developing a computer model for site remediation by ISCO using permanganate (Hood 2000, Hood and Thomson 2000, Zhang and Schwartz 2000). While both models incorporate second order contaminant oxidation, contaminant sorption, and Gilland-Sherwood type DNAPL dissolution mass transfer correlations, neither model is in the public domain, nor are they readily available for use or modification. For dissolution mass transfer, Hood (2000) utilized the correlation of Powers et al. (1994b), while Zhang and Schwartz (2000) used a correlation similar in form to that of Ewing (1996) but with different coefficients.

Both Hood (2000) and Zhang and Schwartz (2000) recognize the importance accounting for NOD reactions in chemical oxidation design and operation, and so both models are said to include kinetic NOD oxidation; however, during published simulations the NOD oxidation rate was set arbitrarily much higher than the contaminant oxidation rate, effectively forcing the model to treat NOD as an instantaneous sink instead of a kinetic reaction. Additionally, it is important to note that neither model tracks $MnO_2(s)$ generation or incorporates changing permeability as a result; however both studies point

to this as an area for further research. Finally, neither modeling effort attempted to capture diffusion as an important transport process in the application of ISCO using permanganate.

2.10 Summary

Chlorinated solvents are a common subsurface contaminant, frequently present as DNAPLs. Subsurface heterogeneity frequently results in a complex DNAPL source zone consisting of regions of residual DNAPL saturation or ganglia as well as regions of high DNAPL saturation or pools. The DNAPL source zone complexity combined with the subsurface heterogeneity challenge source depletion remediation efforts. Previous research has determined the kinetics for ISCO of chlorinated solvents using permanganate, and identified the complex nature and importance of NOD in implementing ISCO. Additionally, research has shown that ISCO using permanganate can result in reduced soil permeability due to precipitation of manganese oxides. When studying ISCO of DNAPL sources, past efforts have largely focused on application to a single pool or residual DNAPL source and have not studied the effect of ISCO on a complex or heterogeneous source zone where there is flow interaction between regions of residual and high saturation. Further, past studies of manganese oxide effects have primarily focused on the resulting permeability reductions, not the changes in mass transfer from the DNAPL source to the aqueous phase caused by the manganese oxide formation. Finally, past efforts to model ISCO using permanganate have not incorporated the complexity of NOD nor the effects of manganese oxide formation and so can not be used to study the interaction of the important processes that occur during ISCO implementation.

44

2.11   References

Ball, W.P., Liu, C., Xia, G., and Young, D.F. (1997). "A diffusion-based interpretation of tetrachloroethene and trichloroethene concentration profiles in a groundwater aquitard." *Water Resour. Res.*, 33 (12): 2741–2757.

Bear, J. (1972). *Dynamics of fluids in porous media*. American Elsevier Publishing Company, Dover, NY, 764 pp.

Brusseau, M.L. (1992). Rate-limited mass transfer and transport of organic solutes in porous media that contain immobile immiscible organic liquid. *Water Resour. Res.*, 28 (1): 33-45.

Chambers, J., Leavitt, A., Waiti, C., Schreier, C.G., Melby, J., and Goldstein, L. (2000). "In situ Destruction of Chorinated Solvents with KMnO4 Oxidizes Chromium." In: Wickramanayake, G.B., Gavaskar, A.R., Chen, A.S.C. (Eds), *Chemical Oxidation and Reactive Barriers*. Battelle Press, Columbus, OH, pp. 49-55.

Clayton, W.S., Marvin, B.K., Pac, T., and Mott-Smith, E. (2000). A multisite field performance evaluation of in situ chemical oxidation using permanganate. In: Wickramanayake, G.B., Gavaskar, A.R., Chen, A.S.C. (Eds), *Chemical Oxidation and Reactive Barriers*. Battelle Press, Columbus, OH, pp. 101-109.

Clement, T.P., Hooker, B.S., and Skeen, R.S. (1996). "Macroscopic models for predicting changes in saturated porous media properties caused by microbial growth." *Ground Water*, 34 (5): 934-942.

Conrad, S.H., Glass, R.J., and Peplinski, W.J. (2002). "Bench-scale visualization of DNAPL remediation processes in analog heterogeneous aquifers: surfactant floods and in situ oxidation using permanganate." *J. Contam. Hydrol*., 58 (1-2): 13-49.

CRC. (2001). CRC Handbook of Chemistry and Physics, 82nd Ed. CRC Press, Cleveland, OH. 2664 pp.

Crimi M. and Siegrist, R.L. (2004). *Experimental Evaluation of In Situ Chemical Oxidation Activities at the Naval Training Center (NTC) Site, Orlando, Florida*. Naval Facilities Engineering Command, Port Hueneme CA. 64 pp.

Cussler, E.L. (1997). *Diffusion: Mass Transfer in Fluid Systems*. Cambridge University Press. 580 pp.

Dekker, T.J. and Abriola, L.M. (2000a). "The influence of field-scale heterogeneity on the infiltration and entrapment of dense non-aqueous phase liquids in saturated formations." *J. Contam. Hydrol.*, 42 (2): 187-218.

Dekker, T.J. and Abriola, L.M. (2000b). "The influence of field-scale heterogeneity on the surfactant-enhanced remediation of entrapped non-aqueous phase liquids." *J. Contam. Hydrol.*, 42 (2): 219-251.

Ewing, J.E. (1996). *Effects of dimensionality and heterogeneity on surfactant-enhanced solubilization of non-aqueous phase liquids in porous media*. MS Thesis, University of Colorado at Boulder, 152 pp.

Freeze, R.A. and McWhorter, D.B. (1997). "A framework for assessing risk reduction due to DNAPL mass removal from low-permeability soils." *Ground Water*, 35 (1): 111-123.

Held, R.J. and Illangasekare, T.H. (1995a). Fingering of dense non-aqueous phase liquids in porous media: 1. Experimental investigation. *Water Resour. Res.*, 31 (5): 1213-1222.

Held, R.J. and Illangasekare, T.H. (1995b). Fingering of dense non-aqueous phase liquids in porous media: 2. Analysis and classification. *Water Resour. Res.*, 31 (5): 1223-1231.

Hood, E. (2000). *Permanganate Flushing of DNAPL Source Zones: Experimental and Numerical Investigation*. Ph.D. Dissertation, University of Waterloo, Waterloo, ON. 243 pp.

Hood, E. and Thomson, N.R. (2000). "Numerical simulation of in situ chemical oxidation." In: *Chemical Oxidation and Reactive Barriers*, Wickramanayake, G.B., Gavaskar, A.R., Chen, A.S.C. (Eds.). Battelle Press, Columbus, OH, pp. 83-90.

Hood, E.D., Thomson, N.R., Grossi, D., and Farquhar, G.J. (2000). "Experimental determination of the kinetic rate law for the oxidation of perchloroethylene by potassium permanganate." *Chemosphere*, 40: 1383-1388.

Huang, K., Hoag, G.E., Chheda, P., Woody, B.A., and Dobbs, G.M. (1999). "Kinetic study of oxidation of trichloroethylene by potassium permanganate." *Environ. Eng. Sci.*, 16 (4): 265-274.

Huang, K.-C., Hoag, G.E., and Chheda, P. (2000). "Soil oxidant demand during chemical oxidation of trichloroethylene by permanganate in soil media." *Proc.,*

46

32nd Mid-Atlantic Industrial and Hazardous Waste Conference, Technomonic Publishing Co, : 617-626.

Huang, K., Hoag, G.E., Chheda, P., Woody, B.A., and Dobbs, G.M. (2001). "Oxidation of chlorinated ethenes by potassium permanganate: a kinetics study." *J. Haz. Mater.*, 87 (1-3): 155-169.

Huang, K., Hoag, G.E., Chheda, P., Woody, B.A., and Dobbs, G.M. (2002). "Kinetics and mechanism of oxidation of tetrachloroethylene with permanganate." *Chemosphere*, 46 (6): 815-825.

Illangasekare, T.H., Armbruster, E.J. III, and Yates, D.N. (1995a). Non-aqueous-phase fluids in heterogeneous aquifer—experimental study. *J. Environ. Eng.*, 121 (8): 571-579.

Illangasekare, T.H., Ramsey, J.L., Jensen, K.H., and Butts, M. (1995b). "Experimental study of movement and distribution of dense organic contaminants in heterogeneous aquifers: an experimental study." *J. Contam. Hydrol.*, 20 (1-2): 1-25.

Imhoff, P.T., Jaffe´, P.R., and Pinder, G. F. (1994). "An experimental study of complete dissolution of a non-aqueous phase liquid in saturated porous media." *Water Resour. Res.*, 30 (2): 307–320.

Itakura, T. , Airey, D. W., and Leo, C. J. (2003). "The diffusion and sorption of volatile organic compounds through kaolinitic clayey soils." *J. Contam. Hydrol.*, 65 (3-4): 219-243.

Jackson, S. (2004). *Comparative evaluation of permanganate and catalyzed hydrogen peroxide during in situ chemical oxidation of DNAPLs*. Master's thesis, Colorado School of Mines, Golden, CO. 132 pp.

Johnson, R.L. and Pankow, J.F. (1992). "Dissolution of dense chlorinated solvents into groundwater. 2. Source functions for pools of solvent." *Environ. Sci. & Technol.*, 26 (5): 896-901.

Johnson, R.L., Cherry, J.A., and Pankow, J.F. (1989). "Diffusive contaminant transport in natural clay: A field example and implications for clay-lined waste disposal sites." *Environ. Sci. Technol.*, 23 (3): 340-349.

Jury, W.A., Gardner, W.R., and Gardner, W.H. (1991). *Soil Physics, 5th ed.*. John Wiley & Sons, New York, NY, 328 pp.

Kueper, B.H., and Frind, E.O. (1991a). "Two-phase flow in heterogeneous porous media, 1, Model development." *Water Resour. Res.*, 27 (6): 1049-1057.

Kueper, B.H., and Frind, E.O. (1991b). "Two-phase flow in heterogeneous porous media, 2, Model application." *Water Resour. Res.*, 27 (6): 1059-1070.

Kueper, B.H., Abbott, W., and Farquhar, G. (1989). "Experimental observations of multiphase flow in heterogeneous porous media." *J. Contam. Hydrol.*, 5 (1): 83-95.

Kueper, B.H., Redman, D., Starr, R.C., Reitsma, S., and Mah. M. (1993). A field experiment to study the behavior of tetrachloroethylene below the water table: Spatial distribution of residual and pooled DNAPL. *Ground Water*, 31 (5): 756–766.

Ladbury, J.W. and Cullis, C.F. (1958). "Kinetics and mechanism of oxidation by permanganate." *Chem. Rev.*, 58 (2): 403-438.

Lee, E.S., Seol, Y., Fang, Y.C., and Schwartz, F.W. (2003). "Destruction efficiencies and dynamics of reaction fronts associated with the permanganate oxidation of trichloroethylene." *Environ. Sci. Technol.*, 37 (11): 2540-2546.

Li, X.D. and Schwartz, F.W. (2004). DNAPL remediation with in situ chemical oxidation using potassium permanganate. Part I. Mineralogy of Mn oxide and its dissolution in organic acids. *J. Contam. Hydrol.*, 68 (1-2): 39-53.

Liu, C. and Ball, W.P. (2002). "Back Diffusion of Chlorinated Solvent Contaminants from a Natural Aquitard to a Remediated Aquifer Under Well-Controlled Field Conditions: Predictions and Measurements." *Ground Water*, 40 (2): 175-184.

Lowe, K.S., Gardner, F.G., and Siegrist, R.L. (2002). "Field evaluation of in situ chemical oxidation through vertical well-to-well recirculation of NaMnO4." *Ground Water Monit. Rem.*, 22 (1): 106-115.

Mackay, D.M. and Cherry, J.A. (1989). "Groundwater contamination: Pump-and-treat remediation." *Environ. Sci. & Technol.*, 23 (6): 630-636.

MacKinnon, L.L. and Thomson, N.R. (2002). "Laboratory-scale in situ chemical oxidation of a perchloroethylene pool using permanganate." *J. Contam. Hydrol.*, 56 (1-2): 49-74.

48

Mayer, A.S. and Miller, C.T. (1996). The influence of mass transfer characteristics and porous media heterogeneity on non-aqueous phase dissolution. *Water Resour. Res.*, 32 (6): 1551-1567.

Mayer, A.S., Zhong, L. ,and Pope, G.A. (1999). Measurement of mass-transfer rates and surfactant-enhanced solubilization of non-aqueous phase liquids. *Environ. Sci. Technol.*, 33 (17): 2965-2972.

Miller, C.T., Poirier-McNeill, M.M., and Mayer, A.S. (1990). "Dissolution of trapped non-aqueous phase liquids: mass transfer characteristics." *Water Resour. Res.*, 26 (11): 2783-2793.

Millington, R.J. and Quirk, J.P. (1959). "Permeability of porous media." *Nature*, 183: 387-388.

Millington, R.J. and Quirk, J.P. (1961). "Permeability of porous solids." *Trans. Faraday Society*, 57: 1200-1207.

Moes, M., Peabody, C., Siegrist, R.L., and Urynowicz, M. (2000). Permanganate injection for source zone treatment of TCE DNAPL. In: Wickramanayake, G.B., Gavaskar, A.R., Chen, A.S.C. (Eds), *Chemical Oxidation and Reactive Barriers*. Battelle Press, Columbus, OH, pp. 117-124.

Mumford, K.G., Thomson, N.R., and Allen-King, R.M. (2002). "Investigating the kinetic nature of natural oxidant demand." In: Gavaskar, A.R. and Chen, A.S.,C (Eds), *Remediation of Chlorinated and Recalcitrant Compounds*. Battelle Press, Columbus, OH. 2C-37 (6 pp.).

Mumford, K.G., Lamarche, C.S., and Thomson, N.R. (2004). Natural oxidant demand of aquifer materials using the push-pull technique. *J. Environ. Eng.*, 130 (10): 1139-1146.

Mumford, K.G., Thomson, N.R., and Allen-King, R.M. (2005). Bench-scale investigation of permanganate natural oxidant demand kinetics. *Environ. Sci. Technol.*, 39 (8): 2835-2840.

Nambi, I.M. (1999). *Dissolution of non-aqueous phase liquids in heterogeneous subsurface systems*. Ph.D. dissertation, Dep. of Civ. and Environ. Eng., Clarkson Univ., Potsdam, NY.

Nambi, I.M. and Powers, S.E. (2003). "Mass transfer correlations for non-aqueous phase liquid dissolution from regions with high initial saturations." *Water Resour. Res.*, 39 (2): 1030, doi:10.1029/2001WR000667.

Nelson, M.D., Parker, B.L., Al, T.A., Cherry, J.A., and Loomer, D. (2001). "Geochemical Reactions Resulting from In Situ Oxidation of PCE-DNAPL by KMnO4 in a Sandy Aquifer." *Environ. Sci. Technol*., 35 (6): 1266-1275.

Oostrom, M., Hofstee, C., Walker, R.C., and Dane, J.H. (1999). "Movement and remediation of trichloroethylene in a saturated, heterogeneous porous medium 2. Pump-and-treat and surfactant flushing." *J. Contam. Hydrol.*, 37 (1-2): 179-197.

Parker, B.L. Gillham, R.W., and Cherry, J.A. (1994). "Diffusive disappearance of immiscible-phase organic liquids in fractured geologic media." *Ground Water*, 32 (5): 805-820.

Parker, B.L., McWhorter, D.B., and Cherry, J.A. (1997). "Diffusive loss of non-aqueous phase organic solvents from idealized fracture networks in geologic media." *Ground Water*, 35 (6): 1077-1087.

Parker, B.L., Cherry, J.A., Chapman, S.W., and Guilbeault, M.A. (2003). "Review and analysis of chlorinated solvent dense non-aqueous phase liquid distributions in five sandy aquifers." *Vadose Zone J*., 2 (2): 116-137.

Pinder, G.F. and Abriola, L.M. (1986). "On the simulation of non-aqueous phase organic compounds in the subsurface." *Water Resour. Res*., 22 (9): 109S-119S.

Polak, A., Grader, A.S., Wallach, R., and Nativ, R. (2003). "Chemical diffusion between a fracture and the surrounding matrix: Measurement by computed tomography and modeling." *Water Resour. Res.*, 39 (4): 1106, doi:10.1029/2001WR000813.

Poulsen, M.M. and Kueper, B.H. (1992). "A field experiment to study the behavior of tetrachloroethylene in unsaturated porous media." *Environ. Sci. Technol*., 26 (5): 889-895.

Powers, S.E., Abriola, L.M., Dunkin, J.S., and Weber, W.J. Jr. (1994a). "Phenomenological models for transient NAPL-water mass-transfer processes." *J. Contam. Hydrol*., 16 (1): 1-33.

Powers, S.E., Abriola, L.M., and Weber Jr., W.J. (1994b). "An experimental investigation of non-aqueous phase liquid dissolution in saturated subsurfacesystems: Transient mass transfer rate." *Water Resour. Res*., 30 (2): 321-332.

Powers, S.E., Nambi, I.M., and Curry, G.W. Jr. (1998). "NAPL dissolution in heterogeneous systems: Mechanisms and a local equilibrium modeling approach." *Water Resour. Res*., 34 (12): 3293– 3302.

Reis, J.C. and Acock, A.M. (1994). "Permeability reduction models for the precipitation of inorganic solids in Berea sandstone." *In Situ*, 18 (3): 347-368.

Reitsma, S. and Dai, Q.L. (2001). Reaction-enhanced mass transfer and transport from non-aqueous phase liquid source zones. *J. Contam. Hydrol.*, 49: 49-66.

Reitsma, S. and Randhawa, J. (2002). "Experimental investigation of manganese dioxide plugging in porous media." In: Gavaskar, A.R. and Chen, A.S.C. (Eds), *Proc., 3rd Int. Conf. on Remediation of Chlorinated and Recalcitrant Compounds*, Monterey CA, May 2002. Battelle Press, Columbus, OH. 2C-39 (8pp.).

Reynolds, D.A. and Kueper, B.H. (2002). "Numerical examination of the factors controlling DNAPL migration through a single fracture." *Ground Water*, 40 (4): 368-377.

Ross, B. and Lu, N. (1999). "Dynamics of DNAPL penetration into fractured porous media." *Ground Water*, 37 (1): 140-147.

Saba, T.A. (1999). *Upscaling of mass transfer from entrapped NAPLs under natural and enhanced conditions.* Ph.D. Dissertation, University of Colorado, Boulder CO. 204 pp.

Saba, T.A. and Illangasekare, T.H. (2000). "Effect of ground-water flow dimensionality on mass transfer from entrapped non-aqueous phase liquid contaminants." *Water Resour. Res.*, 36 (4): 971-979.

Saba, T.A., Illangasekare, T.H., and Ewing, J.E. (2001). "Investigation of surfactant-enhanced dissolution of entrapped non-aqueous phase liquid chemicals in a two dimensional groundwater flow field." *J. Contam. Hydrol.*, 51: 63-82.

Saenton, S. (2003). *Prediction of mass flux from DNAPL source zone with complex entrapment architectur: model development, experimental validation, and up-scaling*. Ph.D. Dissertation, Colorado School of Mines, Golden CO. 246 pp.

Saenton, S., Illangesekare, T.H., Soga, K., and Saba, T.A. (2002). "Effects of source zone heterogeneity on surfactant-enhanced NAPL dissolution and resulting remediation end-points." *J. Contam. Hydrol.*, 59: 27-44.

Schnarr, M., Truax, C., Farquhar, G., Hood, E., Gonully, T., and Stickney, B. (1998). "Laboratory and controlled field experimentation using potassium permangante to remediate trichloroethylene and perchloroethylene DNAPLs in porous media." *J. Contam. Hydrol.*, 29 (3): 205-224.

Schroth, M.H, Oostrom, M., Wietsma, T.W., and Istok, J.D. (2001). "In situ oxidation of trichloroethene by permanganate: effects on porous medium hydraulic properties." *J. Contam. Hydrol.*, 50 (1-2): 79-98.

Schwille, F. (1988). *Dense Chlorinated Solvents in Porous and Fractured Media*. Lewis Publishers, Chelsea, MI. Translated by J.F. Pankow, 146 pp.

Seitz, S. (2004). *Experimental evaluation of mass transfer and matrix interactions during in situ chemical oxidation relying on diffusive transport*. MS Thesis, Colorado School of Mines, Golden, CO, 125 pp.

Sherwood, T.K., Pigford, R.L., and Wilke, C.R. (1975). *Mass Transfer*. McGraw-Hill, New York, NY. 677 pp.

Siegrist, R.L. and Lowe, K.S. (Eds). (1996). "In situ remediation of DNAPL compounds in low permeability media: Fate/transport, in situ control technologies, and risk reduction," *Oak Ridge National Laboratory Rep. No. ORNL/TM-13305* for the DOE Office of Science and Technology.

Siegrist, R.L., Lowe, K.S., Murdoch, L.C., Case, T.L., and Pickering, D.A. (1999). "In situ oxidation by fracture emplaced reactive solids." *J. Environ. Eng.*, 125 (5): 429-440.

Siegrist, R.L., Urynowicz, M.A., West, O.R., Crimi, M.L., and Lowe, K.S. (2001). *Principles and practices of in situ chemical oxidation using permanganate*. Battelle Press, Columbus, OH, 348 pp.

Siegrist, R.L., Urynowicz, M.A., Crimi, M.L., and Lowe, K.S. (2002). "Genesis and effects of particles produced during in situ chemical oxidation using permanganate." *J. Environ. Eng.*, 128 (11): 1068-1079.

Soga, K., Page, J.W.E., and Illangasekare, T.H. (2004). A review of NAPL source zone remediation efficiency and the mass flux approach. *J. Haz. Mater.*, 110 (1-30): 13-27.

Stewart, R. (1965). "Oxidation by permanganate." In: Wiberg, K.B. (Ed.), *Oxidation in Organic Chemistry*, Part A, Chap. 1. Academic Press, New York, NY. pp. 1-68.

Stroo, H.F., Unger, M., Ward, C.H., Kavanaugh, M.C., Vogel, C., Leeson, A., Marqusee, J.A., and Smith, B.P. (2003). "Remediating chlorinated solvent source zones." *Environ. Sci. Technol.*, 37 (11): 224A-230A.

Struse, A.M., Siegrist, R.L., Dawson, H.E., and Urynowicz, M.A. (2002). "Diffusive transport of permanganate during in situ oxidation." *J. Environ. Eng*., 128(4): 327-334.

Taylor, T.P., Pennell, K.D., Abriola, L.M., and Dane, J.H. (2001). "Surfactant enhanced recovery of tetrachloroethylene from a porous medium containing low permeability lenses: 1. Experimental studies." *J. Contam. Hydrol.*, 48 (3-4): 325-350.

Tidwell, V.C., Meigs, L.C., Christian-Frear, T., and Boney, C.M. (2000). "Effects of spatially heterogeneous porosity on matrix diffusion as investigated by X-ray absorption imaging." *J. Contam. Hydrol.*, 42 (2): 285-302.

Urynowicz, M.A. (2000). *Dense non-aqueous phase trichloroethene degradation with permanganate ion*. Ph.D. Dissertation, Colorado School of Mines, Golden CO. 166 pp.

USEPA. (2004). "Discussion paper--Cleanup goals appropriate for DNAPL source zones." U.S. EPA, Office of Solid Waste and Emergency Response, Washington D.C., 16 pp., http://gwtf.cluin.org/docs/options/dnapl_goals_paper.pdf.

Welty, J.R., Wicks, C.E., and Wilson, R.E. (1976). *Fundamentals of momentum, heat, and mass transfer, 2nd ed.*. John Wiley & Sons, New York, NY. 789 pp.

Wyllie, M.R.J. (1962). "Relative permeability." In: *Petroleum Production Handbook, Reservoir Engineering, Vol II*, Frick, T.C. (Ed). McGraw-Hill, New York, NY.

Yan, E.Y. and Schwartz, F.W. (1999). "Oxidative degradation and kinetics of chlorinated ethylenes by potassium permanganate." *J. Contam. Hydrol*., 37 (3): 343-365.

Yan, E.Y. and Schwartz, F.W. (2000). "Kinetics and mechanisms for TCE oxidation by permanganate." *Environ. Sci. Technol*., 34 (12): 2535-2541.

Zhang, H. and Schwartz, F.W. (2000). "Simulating the in situ oxidative treatment of chlorinated ethylenes by potassium permanganate." *Water Resour. Res*., 36 (10): 3031-3042.

Zhu, J. and Sykes, J.F. (2000). The influence of NAPL dissolution characteristics on field-scale contaminant transport in subsurface. *J. Contam. Hydrol.*, 41: 133-154.

Chapter 3

CHEMICAL OXIDATION REACTIVE TRANSPORT IN 3D (CORT3D) MODEL DEVELOPMENT AND TESTING

3.1   Abstract

Laboratory research has provided an understanding of many fundamental details of in situ chemical oxidation (ISCO) of chlorinated ethenes using permanganate such as the reaction pathways and kinetics. A number of researchers have also studied the impacts of water chemistry and porous media constituents on the reaction. However, additional research is necessary to better understand how well ISCO will work under different site and source conditions, including the effects of ISCO on source zone porous media.

Site conditions such as NAPL architecture, soil heterogeneity, oxidant delivery, and soil natural oxidant demand are critical factors affecting ISCO implementation. In order to implement ISCO effectively, it is important to consider the interaction of these factors under realistic conditions. Field-scale investigations provide realistic conditions, but do not allow for complete control of experimental conditions nor are they usually conducive to extensive monitoring. On the other hand, large tank experiments provide an alternative with near-complete control, as a means to improve qualitative understanding as well as generate accurate data on individual or combined processes. Unfortunately, they are costly, time-consuming, and difficult to set up; it is not possible to simulate all possible field scenarios. A model code is needed for simulating ISCO using permanganate, and related processes under realistic hydrogeologic and source conditions, allowing investigation of field scenarios that can not be studied experimentally. Unfortunately, existing codes are incomplete and not readily available. Consequently, a numerical computer modeling code, Chemical Oxidation Reactive Transport in 3D

(CORT3D) has been developed to help fill this need. In addition to processes incorporated by other codes, it includes: multiple natural oxidant demand (NOD) components, kinetic NOD oxidation, and permeability reductions resulting from $MnO_2(s)$ generation.

The model code was verified against analytical solutions or other models to ensure it properly represents important processes related to ISCO. Models of 1D experiments highlighting important ISCO processes were created using the code and tested to demonstrate that the modeling code captures processes and effects observed in the experiments. Where sufficient data was available, the model was calibrated using one set of data and then used to predict observed effects from an independent set of data. The model code was able to reproduce important ISCO-related processes for the conditions tested, including: PCE or TCE, low to moderate DNAPL saturations, and non-existent to fairly high NOD. The model code is an important first attempt to capture permeability changes resulting from permanganate oxidation of PCE. Reductions in permeability may be an important factor in designing oxidant delivery for effective source zone treatment, as well as contributing to reduction of contaminant mass flux from the source zone to meet remediation goals. Simulations confirmed the importance of accounting for changing permeability as well as multiple NOD fractions with differing oxidation rates. Further, simulations verify that, at least for PCE, oxidation increases mass transfer from a DNAPL source by a greater amount than can be attributed solely to an increased concentration gradient. The code has been demonstrated to capture processes important to implementation of ISCO. These processes are identified as important in determining if ISCO is feasible for a particular site and in optimizing oxidant delivery. As a result, the code should be useful for comparing different oxidant delivery scenarios, as well as different possible source configurations, to assist in optimizing remediation design for a specific site.

3.2 Introduction

Chlorinated solvents such as trichloroethylene (TCE) and tetrachloroethylene (PCE) are contaminants of concern in groundwater at many contaminated sites, ranking 16th and 30th respectively on the 2003 CERCLA Priority List of Hazardous Substances (ATSDR 2003). These chemicals have been used extensively since the early 20th century as cleaning solvents and as intermediate chemicals in production of pesticides, paints, refrigerants, and other chemicals (ATSDR 2004, USEPA 2004a, USHHS 2002). As contaminants, they are frequently present in the form of dense non-aqueous phase liquid (DNAPL) primary source zones, or as dissolved and/or sorbed contaminant in low permeability media (LPM) secondary source regions (Johnson and Pankow 1992, Pankow and Cherry 1996, USEPA 1993, USEPA 2004b). Although they typically have solubilities in the parts-per-million range, the drinking water maximum contaminant levels (MCLs) are typically in the parts-per-billion range.

DNAPLs present a challenging source zone because of the complex nature of their movement through the subsurface. The interplay of viscous, gravitational, and capillary forces results in a non-uniform and unpredictable migration vertically and laterally. As the main body of DNAPL migrates, residual DNAPL is left behind as disconnected blobs and ganglia partially filling the pore space. Capillary forces hold this DNAPL residual in place, such that even relatively large hydraulic gradients can not further mobilize it (Kueper et al. 2003). Figure 3.1 illustrates these phenomenon in a generic site conceptual model of a groundwater system contaminated by DNAPLs.
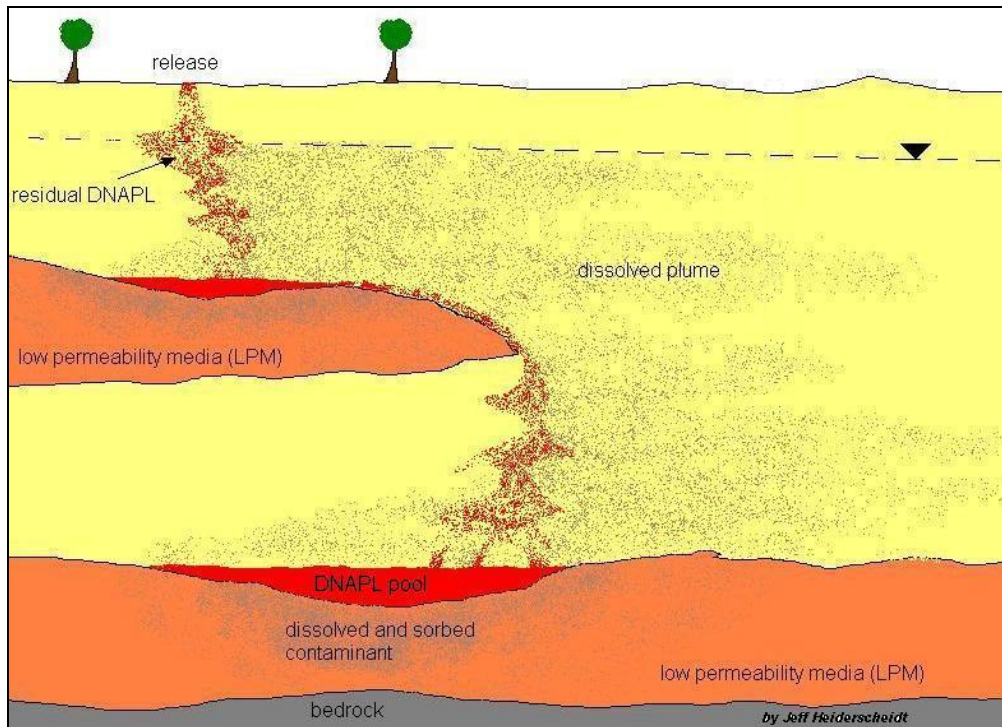
Figure 3.1: Generic Contaminated Site Conceptual Model

A number of remediation technologies are available for reducing the mass of DNAPL present in a primary source zone, such as pump-and-treat or surfactant/co-solvent flushing. However, subsurface heterogeneities and imprecise knowledge of source locations frequently challenge these technologies (Freeze and McWhorter 1997, ITRC 2002, Marvin et al. 2002, Siegrist and Lowe 1996, USEPA 2003). For example, diffusion of aqueous phase components into LPM, and subsequent diffusion out of the LPM after the DNAPL source is depleted is a particularly challenging remediation problem (Liu and Ball 2002). Sand aquifers contaminated by DNAPLs frequently have silty or clayey LPM strata below or within them (Mackay and Cherry 1989). These LPM strata typically have permeabilities of 1000 to 10 million times less than the surrounding sand. In many cases, pure-phase contaminant entered the aquifer and has had several to many years of close contact with LPM, resulting in diffusion of a substantial mass of

dissolved contaminant into the LPM. Subsequently, even if the pure-phase contaminant is removed from the aquifer, the dissolved contaminant in the LPM will continue to diffuse out and remain a source of groundwater contamination, potentially well above MCLs, for years to come (Johnson and Pankow 1992, Lee and Chrysikopoulos 1998, Wilking 2004).

Chemical oxidation, specifically with permanganate, has been used to treat water and waste water for over 50 years. In the last fifteen years or so, chemical oxidation has become a promising in situ remediation technique for sites whose groundwater and soil are contaminated by chlorinated solvents, especially where contaminants are not present in DNAPL form. Field-scale pilot tests have shown encouraging results for sites contaminated with low levels of chlorinated solvents (Cline et al. 1997, Hood 2000, Lowe et al. 2002, Schnarr et al. 1998, Siegrist et al. 1999). A goal of ISCO is to speed up remediation of a contaminant source zone by inducing increased mass transfer (and subsequent destruction) from the source. Based on experimental results, Schnarr et al. (1998) suggest that NAPL dissolution and oxidation are processes that occur in parallel with increased mass transfer during oxidation occurring primarily as a result of an increased aqueous concentration gradient. Reitsma and Dai (2001) performed a theoretical study to estimate the maximum expected NAPL mass transfer enhancement resulting from chemical oxidation. They estimated a maximum five times increase in dispersive mass transport from a PCE NAPL pool resulting from the increased concentration gradient; however, they predict little enhancement in local-scale mass transfer from NAPL to aqueous phase suggesting no change in dissolution mass transfer parameters. Further, they suggest that actual enhancement is likely to be less because permeability reduction and decreased interfacial contact area were not accounted for in the estimate. On the contrary, MacKinnon and Thomson (2002) calculated a ten times initial increase in PCE mass transfer from a NAPL pool during a 2D oxidation experiment, with decreasing mass flux over time attributed to $MnO_2(s)$ formation as a byproduct of oxidation using permanganate.

Laboratory research has provided an understanding of many fundamental details of the technology. The reaction pathways and kinetics of permanganate oxidation of alkenyl halides, specifically chlorinated ethenes such as PCE and TCE have been elucidated (Huang et al. 1999, Huang et al. 2001, Huang et al. 2002, Schnarr et al. 1998, Yan and Schwartz 1999, Yan and Schwartz 2000). A number of researchers have also studied the impacts of water chemistry and porous media constituents on the reaction (Gates-Anderson et al. 2001, Glaze and Kang 1988, Li and Schwartz 2000, Urynowicz 2000, Vella and Veronda 1994). However, additional research is necessary to better understand how well ISCO will work under different site and source conditions, including the effects of ISCO on source zone porous media (Ibaraki and Schwartz 2001, Seol et al. 2003, Stroo et al. 2003).

Site conditions such as NAPL architecture, soil heterogeneity, oxidant delivery, and soil natural oxidant demand are critical factors affecting ISCO implementation. In order to implement ISCO effectively, it is important to consider the interaction of these factors under realistic conditions. Field-scale investigations provide realistic conditions, but do not allow for complete control of experimental conditions. Additionally, they generally allow only limited monitoring, preventing a full understanding of how site and source conditions are affecting the chemical oxidation. For example, even at the Canadian Forces Base Borden, Ontario, Canada (with extensive monitoring and site characterization), researchers were not able to fully characterize the DNAPL source distribution before or after oxidation (Nelson et al. 2000, Nelson et al. 2001). Large tanks provide an alternative with complete control. Unfortunately, large-scale tank experiments are costly, time-consuming, and difficult to set up, so only a limited number can be performed. Because of these challenges posed by large-tank lab and field-scale experiments, a computer model code is needed for simulating chemical oxidation and related processes under a wide range of hydrogeologic and source conditions. Such a model code should incorporate the processes listed in Table 3.1.

Table 3.1: Important Processes to be Captured by an ISCO Model

Advection	2nd Order Contaminant Oxidation
Dispersion	Kinetic NOD oxidation
Sorption	Multiple NOD components
Diffusion	Permeability decrease due to $MnO_2(s)$ formation
DNAPL Dissolution	Permeability Increase due to DNAPL Dissolution

However, there have been few efforts to develop a computer model code to simulate ISCO using permanganate (Hood 2000, Hood and Thomson 2000, Zhang and Schwartz 2000). While previous efforts incorporated some of the important processes (second order oxidation, rate-limited or kinetic sorption, and Gilland-Sherwood type DNAPL dissolution mass transfer correlations), they are not in the public domain, nor are they readily available for use or modification. Additionally, although reported to incorporate kinetic NOD oxidation, published simulations have treated NOD as an instantaneous sink. In essence, this means oxidant within a model cell is not available for destroying contaminant until all NOD within that cell has been oxidized. Further, it is important to note that these previous efforts made no attempt to simulate $MnO_2(s)$ generation or incorporate changing permeability as a result; however they each pointed to this as an area for further research. Finally, they did not attempt to capture diffusion as an important transport process in the application of ISCO using permanganate. The objective of this research is to develop, verify, and test (by modeling experiments of important ISCO processes) a computer model code for simulating ISCO of chlorinated ethenes using permanganate.

3.3   Model Formulation

There are three main applications for a new numerical model code for simulating ISCO using permanganate. The first is as a tool to investigate the interaction of site and source conditions with different transport and reactive processes, providing insight into

how these factors affect oxidation effectiveness. Similarly, the second is as a decision tool that can be used to assess whether ISCO using permanganate is a feasible technology for further consideration at a specific site based on site and source conditions. For example, the model code might be used to assess whether oxidation appears feasible for a site suspected of having a large mass of DNAPL present in a long thick pool where the overlying aquifer is moderately heterogeneous with a high NOD content. The third is as a design tool to assist in determining the optimal oxidant delivery scheme (what oxidant concentration at what flow rate and in what locations?) for a site based on site and source conditions. Although there is typically a large degree of uncertainty in site characterization, the new modeling code will be useful for comparing different scenarios. Further, by performing simulations using the expected upper and lower limits for site parameters, the effect of the uncertainty can be examined; this may provide insight into additional site characterization to perform.

In developing the model code, the goals are that the model be: easily available, readily useable by the average trained environmental modeler, and able to simulate any combination of processes from Table 3.1. The code should utilize input parameters that are typically available or can be estimated by batch or small column studies using field samples. These include: soil characteristics (porosity, saturated hydraulic conductivity, dispersivity, bulk density, median grain size), contaminant characteristics (density, molecular weight, molecular diffusion coefficient), NOD distribution (mass fraction), oxidation reaction information (contaminant oxidation rate, NOD oxidation rates, reaction stoichiometry), DNAPL dissolution parameters (Gilland-Sherwood parameters), and sorption parameters based on the contaminant and soil. Additionally, information about the contaminant source distribution (location, DNAPL saturation) and subsurface flow characteristics will be necessary.

Development of the Chemical Oxidation Reactive Transport in 3D (CORT3D) model code began by selecting the multi-component reactive transport code RT3D version 2.5 (Clement 1997, Clement 2002, Clement et al. 1998) as a point of departure.

For the purposes of chemical oxidation, the interest is not in multi-phase flow but in mass transfer, so a multi-phase code like UTCHEM (Delshad et al. 1996), TOUGH2 (Pruess et al. 1999), or STOMP (Lenhard et al. 1995, White et al. 1995) was not necessary. At many sites, the DNAPL spill occurred years prior to discovery and remediation planning, and the DNAPL is likely no longer migrating. On the other hand, this study is focused on multiple component reactions; MT3DMS, which handles only single-component reactions (Zheng and Wang 1999), was not applicable. Finally, a transport code was desired that is relatively easy to use, easily modifiable, widely available, well-documented, well-tested, and widely used. RT3D met these requirements. The well-documented, widely accepted, and commonly used groundwater flow code MODFLOW-2000, which can simulate the flow regime under both transient and steady-state conditions with a wide variety of boundary conditions and stresses (McDonald and Harbaugh 1988, Harbaugh et al. 2000), was used to generate the underlying spatial and temporal variations in groundwater head distribution.

The formulation of each process represented in the model code follows. The code does not incorporate oxidant auto-decomposition as it is yet to be determined whether this results in a significant reduction in oxidant concentrations. This type of auto-catalytic decomposition of permanganate was suggested by Urynowicz (2000) based on research results indicating that more oxidant mass was consumed in destruction of a given mass of TCE when initial oxidant concentration was increased.

3.3.1   DNAPL Dissolution

Mass transfer or dissolution of the DNAPL into the aqueous phase is implemented using the well-known stagnant film model (Sherwood et al. 1975) utilizing a first-order linear driving force

$$\frac{dX_{napl}}{dt} = -\frac{\phi_{eff}}{\rho_B} k_{La} \left(C_{cont}^* - C_{cont} \right) \tag{3.1}$$

where X_{napl} is the mass fraction of DNAPL in soil (MM^{-1}), ϕ_{eff} is the effective soil porosity available for water flow, ρ_B is the soil bulk density (L^3T^{-1}), C^*_{cont} is the maximum solubility limit of the contaminant (ML^{-3}), C_{cont} is the aqueous concentration of the contaminant (ML^{-3}), and k_{La} is the DNAPL dissolution rate or lumped mass transfer coefficient (T^{-1}). The lumped mass transfer coefficient is the product of the intrinsic mass transfer coefficient, k_L, (LT^{-1}) times the DNAPL-water interfacial area, A_{nw}, (L^2), divided by the porous media volume of interest, V, (L^3). The lumped mass transfer coefficient is used because the complex architecture of DNAPL sources makes A_{nw} virtually impossible to estimate. However, k_{La} is dependent on a number of system parameters, such as pore size and the DNAPL saturation which affect the specific interfacial surface area for dissolution. As a result, mass transfer is a system dependent process, and estimation of k_{La} is system specific and must be done empirically using measurable system parameters (Ewing 1996, Imhoff et al. 1994, Miller et al. 1990, Nambi 1999, Powers et al. 1994a, Powers et al. 1994b, Saba and Illangasekare 2000). The general approach is to utilize an empirically determined Gilland-Sherwood correlation (Welty et al. 1976)

$$Sh = a + b\,Re^c\,Sc^d \tag{3.2}$$

to estimate the modified Sherwood number (Sh) from other dimensionless numbers describing the system (e.g. Reynolds number, Re, and Schmidt number, Sc), where a, b, c, and d are empirically determined constants. The modified Sherwood number relates the mass transport in a system to the diffusive forces, the Reynolds number relates system inertial forces to viscous forces, and the Schmidt number relates viscous forces to diffusive forces. Mathematical equations for these three dimensionless numbers are

$$Sh = \frac{k_{La}d^2_{50}}{D_m} \tag{3.3}$$

$$Re = \frac{\rho_w \bar{v} d_{50}}{\mu_w} \tag{3.4}$$

$$Sc = \frac{\mu_w}{\rho_w D_m} \tag{3.5}$$

where d_{50} is the representative (median) grain size (L), D_m is the molecular diffusion coefficient for a bulk solution of the solute (at an infinitely dilute concentration) (L^2T^{-1}), ρ_w is the aqueous phase density (ML^{-3}), $\bar{v}$ is the average linear groundwater velocity (LT^{-1}), and μ_w is the aqueous phase dynamic viscosity ($ML^{-1}T^{-1}$). The Sherwood number determined from the empirical correlation (Equation 3.2) is then used in Equation 3.3 to estimate the lumped mass transfer coefficient, k_{La}. Most correlations incorporate volumetric DNAPL content (θ_n) in some form to account for the changing DNAPL-water interfacial area as dissolution proceeds (Miller et al. 1990, Powers et al. 1994b). Example Gilland-Sherwood relations are shown in Table 3.1, where L is the characteristic or dissolution length in the flow direction (L), d_M is the diameter of a "medium" sand grain (defined by U.S. Department of Agriculture as 0.05cm), and x is the distance into the residual DNAPL source in the direction of flow (L).

Table 3.2: Gilland-Sherwood Mass Transfer Correlations for NAPL-Water Systems

$Sh = 37.15\left(\dfrac{\theta_n}{n}\right)^{1.24} Re^{0.61}$ (for $\theta_n/n < 0.35$)	Nambi and Powers (2003)
$Sh = 0.4727\, Re^{0.2793}\, Sc^{0.33}\left(\dfrac{\theta_n}{1-\theta_n}\right)^{1.642}\left(\dfrac{d_{50}}{\tau L}\right)^{0.1457}$	Saba et al. (2001)
$Sh = 11.34\, Re^{0.2767}\, Sc^{0.33}\left(\dfrac{\theta_n d_{50}}{\tau L}\right)^{1.037}$	Saba and Illangasekare (2000)
$Sh = 4.84\, Re^{0.219}\, \theta_n^{1.32}$	Ewing (1996)
$Sh = 36.8\, Re^{0.654}$	Powers et al. (1994a)
$Sh = 4.13\, Re^{0.598}\left(\dfrac{d_{50}}{d_M}\right)^{0.673} U^{0.369}\left(\dfrac{\theta_n}{\theta_{n0}}\right)^{\beta}$; $\beta = 0.518 + 0.114\left(\dfrac{d_{50}}{d_M}\right) + 0.10U$	Powers et al. (1994b)
$Sh = 340\theta_n^{0.87}\, Re^{0.71}\left(\dfrac{d_{50}}{x}\right)^{0.31}$	Imhoff et al. (1994)
$Sh = 12\, Re^{0.75}\, \theta_n^{0.60}\, Sc^{0.5}$	Miller et al. (1990)

Differences in empirical coefficients and formulations are at least partly due to differences in experimental conditions. For example Powers et al. (1994a) used a 1D system with spherical dissolving organic media and Powers et al. (1994b) used a 1D homogeneous system, while Saba and Illangasekare (2000) were considering a 2D system with heterogeneity-induced flow-bypassing. Miller et al. (1990) and Imhoff et al. (1994) both used 1D systems. Ewing (1996) and Saba et al. (2001) considered a 2D system with surfactant flushing. Nambi and Powers (2003) further expanded the available choices by looking at 2D systems with high DNAPL saturations resulting in slower mass transfer characterized by a significantly increased exponent on the DNAPL saturation term.

The computer model code being developed as part of this research is written such that any mass transfer correlation can be used. However, a general form of the mass transfer correlation of Saba and Illangasekare (2000) is used in the model code. This

correlation was used by Saenton (2003) for intermediate-scale 2D PCE natural dissolution as well as surfactant enhanced dissolution experiments, and found to be flexible and effective. The generic correlation is

$$Sh = \alpha_1 \, \text{Re}^{\alpha_2} \, Sc^{\alpha_3} \left(\frac{\theta_n d_m}{\tau L} \right)^{\alpha_4} \tag{3.6}$$

where the empirical coefficients α_1, α_2, α_3, α_4, τ are unique for a given system, and are determined through inverse modeling.

The model code does not directly account for ISCO effects on mass transfer when calculating the lumped mass transfer coefficient. One potential course is to use an equation for adjusting the intrinsic mass transfer coefficient, k_L, to account for irreversible, first-order (or pseudo-first-order) homogeneous chemical reaction as given by Cussler (1997)

$$k_L^* = (D_m k_1)^{1/2} \coth\left[\left(\frac{k_1}{D_m} \right)^{1/2} \delta \right] \tag{3.7}$$

where δ is the theoretical stagnant film thickness (L), D_m is the molecular diffusion coefficient (L^2T^{-1}), and k_1 is the first-order (or pseudo-first-order) kinetic reaction rate constant (T^{-1}). According to Cussler (1997) this adjustment is necessary only if the chemical reaction is fast, with a half life on the order of minutes. Because δ can not be measured, it can be replaced with D_m/k_L, where k_L is the intrinsic mass transfer coefficient without chemical reaction (MT^{-1}). Further, k_L is defined as the molecular diffusion coefficient divided by the stagnant film thickness. Dividing through by k_L gives the change in mass transfer caused by the chemical reaction (Cussler 1997)

$$\frac{k_L^*}{k_L} = \left[\frac{D_m k_1}{(k_L)^2} \right]^{1/2} \coth\left[\left(\frac{k_1 D_m}{k_L^2} \right)^{1/2} \right] \tag{3.8}$$

Unfortunately, this requires knowledge of the intrinsic mass transfer coefficient without chemical reaction, k_L, which can not be determined for DNAPL dissolution in porous media because it is not possible to know the DNAPL-water interfacial area

needed to obtain k_L from the lumped mass transfer coefficient, k_{La}, which is determined empirically. In addition to the potential increase in intrinsic mass transfer coefficient due to chemical reaction, ISCO using permanganate results in manganese oxide formation, decreasing the DNAPL-water interfacial area which decreases the lumped mass transfer coefficient. Again, the change in interfacial area is unknown so calculating the resulting change in k_{La}, does not appear possible. On the other hand, the MnO_2(s) formation at the DNAPL surface is indirectly captured in the calculation of k_{La} by the changing Reynolds number which changes as a result of decreasing porosity. As currently implemented, if the intrinsic mass transfer coefficient is expected to increase due to fast chemical reaction, the Gilland-Sherwood parameters need to be estimated for dissolution during chemical reaction thru inverse modeling. A forward simulation is then run in phases, using the appropriate Gilland-Sherwood parameters for each phase. One possibility for incorporating the change in interfacial area is through the tortuosity parameter, τ, in Equation 3.6; however, additional research is necessary to determine if this is possible.

3.3.2   Contaminant Diffusion

Numerical finite difference model codes tend to introduce artificial numerical dispersion under highly diffusion-dominated conditions. Contaminant that enters a model cell during a transport time step is considered to be at the center of the model cell at the start of the next time step, artificially increasing mobile species transport further than it would have diffused in a given time step. However, models using these codes can still be useful for comparing different scenarios. To that end, the original RT3D version 2.5 computer model code has been modified to allow different effective diffusion coefficients to be simulated for each mobile species. Further, the effective diffusion coefficient for each species varies spatially based on soil properties. This modification is important for simulating diffusive transport of permanganate into LPM, where transport is dominated by diffusion (Siegrist et al. 1999, Struse et al. 2002). The original RT3D code used a single effective diffusion coefficient for all species, thereby limiting its

effectiveness at simulating diffusion-dominated transport. In CORT3D, effective diffusion coefficients, D_e, $(L^2 T^{-1})$ are estimated using a modified Millington-Quirk relationship (Jury et al. 1991), relating effective diffusion to water content (θ_w) as well as effective porosity.

$$D_e = D_m \frac{\theta_w^{10/3}}{\phi_{eff}^2} \tag{3.9}$$

In the fully water-saturated case, the water content is equal to effective porosity and Equation 3.9 simplifies to the Millington-Quirk relation (1959, 1961)

$$D_e = D_m \phi_{eff}^{4/3} \tag{3.10}$$

Use of the modified Millington-Quirk relation has been shown effective for a variety of soils. Tidwell et al. (2000) researched the effect of porosity on diffusion of potassium iodide into Culebra dolomite slabs using x-ray absorption imaging at the centimeter-scale. They found that diffusion rates within the slabs indeed varied spatially, and depended on the magnitude of porosity at each location. Conversely, Itakura et al. (2003) performed diffusion experiments using three different organic contaminants, including TCE and three soil configurations (reconstituted and intact kaolin clay as well as reconstituted sandy silt), and determined the relation

$$D_e = D_m \phi_{eff} \tag{3.11}$$

inadequately fit a combination of their data (19 points) and that from four other studies (6 points). Subsequently, they concluded "there is little correlation between tortuosity and porosity." However, from the data they present (and excluding only two of the six data points from other studies, keeping 23 of 25 data points), it appears that the modified Millington-Quirk relation of Equation 3.9 fits the data to some degree with an R^2 of 0.65 compared to an R^2 of 0.40 for Equation 3.11.

3.3.3   Contaminant Oxidation

A new chemical oxidation reaction module or package has been developed for use with the modified RT3D code. The new module tracks a number of mobile and immobile species. The mobile species are: aqueous phase contaminant (cont), permanganate (MnO_4^-), and chloride (Cl^-). Contaminant concentrations (resulting from the oxidation reaction) are calculated using the second order reaction (Huang et al. 1999, Siegrist et al. 2001),

$$\frac{dC_{cont}}{dt} = -k_2 C_{cont} C_{MnO_4^-} \tag{3.12}$$

where C_i is the concentration of component i (ML^{-3}), dC_i/dt is the rate of change in concentration of component i with time, and k_2 is the 2nd-order reaction coefficient for degradation of the contaminant by MnO_4^- ($L^3M^{-1}T^{-1}$).

MnO_4^-, and Cl^- concentrations are calculated based on the reaction stoichiometry, but the MnO_4^- equation also includes NOD terms. Although the reaction module was written so the stoichiometric ratios are adjustable to accommodate modeling oxidation of different contaminants, for oxidation of PCE the stoichiometric reaction given by Equation 3.13 applies. This reaction has been shown to represent the oxidation of PCE by permanganate over the pH range of 3.5-10 expected to be found in the subsurface (Huang et al. 2002, Siegrist et al. 2001, Yan and Schwartz 1999). The reaction equations for permanganate and chloride are shown in Equations 3.14 and 3.15,

$$4MnO_4^- + 3C_2Cl_4 + 4H_2O \rightarrow 6CO_2 + 4MnO_{2\ (s)} + 8H^+ + 12Cl^- \tag{3.13}$$
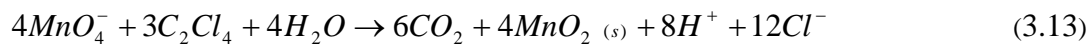
$$\frac{dC_{MnO_4^-}}{dt} = Y_{MnO_4^-/cont} \frac{dC_{cont}}{dt} - \left(k_{NOD_f} X_{NOD_f} + k_{NOD_s} X_{NODs} \right) \frac{\rho_B}{\phi} \tag{3.14}$$

$$\frac{dC_{Cl^-}}{dt} = -Y_{Cl^-/cont} \left(k_2 C_{cont} C_{MnO_4^-} \right) \tag{3.15}$$

where $Y_{i/j}$ is the stoichiometric molar mass ratio of component i to component j from Equation 3.13 and the component molecular weights. In Equation 3.14, X_{NOD_f} is the

mass fraction of NOD sites with a faster oxidation rate (MM^{-1}), X_{NOD_s} is the mass fraction of NOD sites with a slower oxidation rate (MM^{-1}), k_{NOD_f} is the first-order oxidation rate for fast NOD sites (T^{-1}), and k_{NOD_s} is the first-order oxidation rate for slow NOD sites (T^{-1}).

In addition to the specified mobile species, the reaction module also tracks a number of immobile species, including: DNAPL phase contaminant, sorbed contaminant, MnO_2(s), and natural oxidant demand (NOD). Generation of MnO_2(s) occurs via Equation 3.16,

$$\frac{dX_{MnO_2}}{dt} = \frac{\phi}{\rho_B}\left[Y_{MnO_2/MnO_4^-}\left(-\frac{dC_{MnO_4^-}}{dt}\right)\right] \qquad (3.16)$$

where, X_{MnO2} is the mass fraction of MnO_2(s) precipitates in the soil (MM^{-1}) and dX_i/dt is the rate of change in mass fraction for component i with time. The MnO_2(s) precipitates are assumed to be immobile and remain at the location they are generated. Treating all the generated MnO_2(s) as immobile provides a worst-case simulation of generated solids filling pore-space and potentially altering permeability as discussed in Section 3.3.5. The MnO_2(s) formed during oxidation using permanganate may take different forms depending on soil and water conditions as well as where it forms. Much of it is likely to form within the pore space as an amorphous, hydrous, porous form reducing effective porosity available for water flow. The amorphous, hydrous particles of MnO_2(s) that form within the pore space may also become lodged in pore throats blocking flow. Additionally, some may form as a more structured and solid film on soil particle surfaces where it can reduce the pore throat diameter. MnO_2(s) can also form as a film at the DNAPL-water interface reducing the interfacial area for mass transfer from the DNAPL to the aqueous phase (Urynowicz 2000). It is unlikely that MnO_2(s) will form in the same combination of these mechanisms for all conditions.

The reaction module can also simulate either equilibrium or rate-limited sorption of contaminant through the following equation (Haggerty and Gorelick 1994),

$$\frac{dX_{sorb}}{dt} = \frac{\phi}{\rho_B} \xi \left(C_{cont} - \frac{X_{sorb}}{\lambda_{cont}} \right) \tag{3.17}$$

where ξ is the rate-limited sorption mass transfer coefficient (T^{-1}), X_{sorb} is the mass fraction of sorbed contaminant in the soil (MM^{-1}), and λ_{cont} is the linear sorption coefficient (L^3M^{-1}). As ξ gets larger, the non-equilibrium sorption approaches equilibrium sorption; on the other hand, as ξ gets very small sorption becomes negligible.

3.3.4   Natural Oxidant Demand

Field soils and aquifer sediments typically contain natural organic matter (NOM), reduced metals, and other reductants that can be readily oxidized. These soil constituents are referred to collectively as natural oxidant demand (NOD), or sometimes soil oxidant demand (SOD), and compete with target contaminants for available oxidant. Zhang and Schwartz (2000) proposed that components comprising the NOD have a much faster reaction rate with MnO_4^- than do chlorinated contaminants, in order to explain delayed breakthrough of MnO_4^- in column experiments by Schnarr et al. (1998). This conceptual model of NOD oxidation corresponds to an instantaneous sink (Figure 3.2a). Under this concept, all of the NOD must be oxidized before any PCE oxidation occurs; thus, in order to oxidize a given mass of PCE, the mass of MnO_4^- needed will be equal to the NOD plus the mass determined from the reaction stoichiometry.

On the other hand, there is evidence that not all NOD components are oxidized faster than the contaminant (Mumford et al. 2002, Mumford et al. 2005, Siegrist et al. 1999, Struse et al. 2002, Yan and Schwartz 1999). Because NOD is generally a complex mixture of components whose surface area available for oxidant contact varies, it is appropriate to treat NOD oxidation as a kinetic process as depicted in Figure 3.2b. This

means that oxidation of NOD and PCE occur simultaneously, with relative rates of oxidation controlling depletion of each.
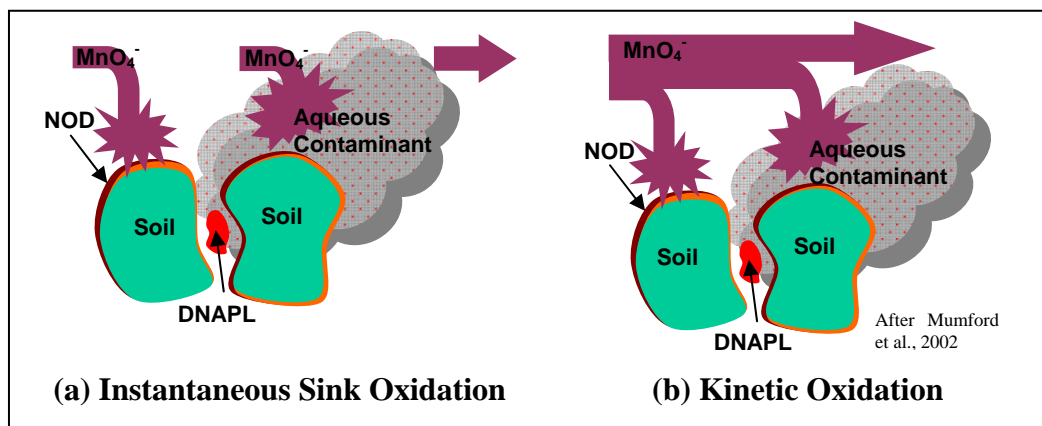
Figure 3.2: NOD Oxidation Conceptual Models

Further, Because NOD results from a mixture of constituents, the kinetic rate for oxidation of NOD can vary widely for different soils. While the kinetic rates for some NOD constituents of a particular soil are often higher than that of the target contaminant, preliminary results related to this research, and that of others, suggests NOD frequently consists of at least two components with markedly different oxidation rates (Crimi and Siegrist 2004, Jackson 2004, Mumford et al. 2005). As an example, Chambers et al. (2000) found two distinct NOD oxidation rates for each of three different field soils in batch tests. The rate during the first 24 hours was 10 – 20 times faster than the rate during the next 13 days. They also found that the slower rate for the three soils was virtually the same, while the initial fast rate varied by soil type with silt and clay being about twice that of sand. Similar results are shown in Figure 3.3, for a field soil taken from the Mines Park test site near the Colorado School of Mines in Golden CO (Seitz 2004). Because the graph is natural log of oxidant concentration over initial

concentration versus time, the slope can be taken directly as a kinetic oxidation rate. From the figure, it can be seen that during the first day, the fraction of NOD oxidized has a high oxidation rate; after the first day, the remaining NOD is oxidized at a much lower rate. The addition of site groundwater increased the overall amount of NOD slightly, but did not change the NOD oxidation rates.
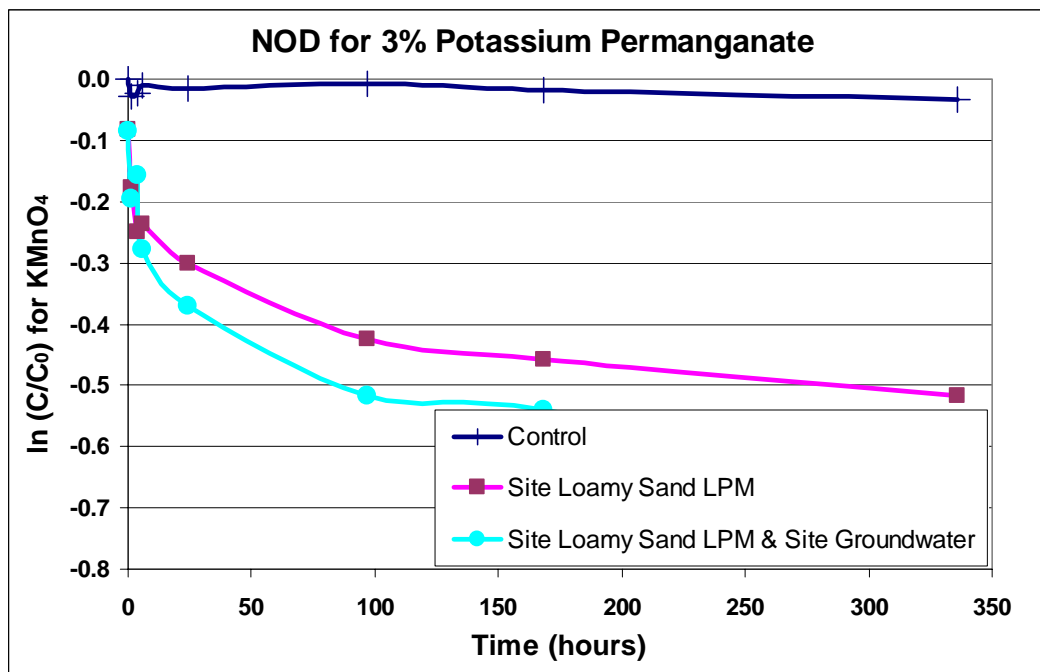
Figure 3.3: NOD Oxidation Rates for Mines Park Soil (Seitz 2004)

Mumford et al. (2005) considered the possibility that the multiple rates could be a result of organic carbon located within soil grain micropores being more difficult for oxidant to access. They performed batch NOD studies on native coarse sand from the Borden test site (grain size greater than 0.42mm), as well as on coarse Borden sand that had first been crushed (grain size less than 0.074mm). Results from the one week NOD tests showed no significant difference, suggesting that either the proposed geometric

configuration is not a rate-limiting factor or that reduced species in micropores are still unavailable even after crushing (Mumford et al. 2005).

The research on kinetic rates for NOD oxidation to date, has not determined the overall reaction order. The results from the studies already mentioned suggest that it is first-order with respect to NOD, but there has been little study of the effect of MnO_4^- concentration. The work of Crimi and Siegrist (2004) utilized two MnO_4^- concentrations, and provided some indication that at least the NOD fraction with the slower kinetic rate is also first-order with respect to MnO_4^- (second-order overall).

In the new model code, NOD is assumed to be immobile, because batch studies so far have suggested the soil NOD is typically far greater than any NOD exerted by dissolved constituents in the groundwater. Further, the volume of NOD oxidized is assumed to be negligible compared to the pore space so that removal of NOD does not increase permeability; however, the oxidation of NOD does consume permanganate generating $MnO_2(s)$ which in turn does reduce permeability. Due to the absence of second-order NOD kinetic data, at locations where oxidant is present, changes to the mass fraction of fast and slow NOD are calculated using first-order Equations 3.18 and 3.19, respectively. If NOD oxidation is actually second order (or some higher order) reaction instead of first-order, treating it as first-order in the model code will result in simulations overestimating permanganate depletion from NOD oxidation. In a higher order reaction, the kinetic constant is dependent on the concentration of the oxidant as well as the amount of NOD so that as oxidant is consumed the rate of NOD oxidation will decrease. Overestimating the permanganate depletion in the simulation would further cause an underestimation in the contaminant oxidation.

$$\frac{dX_{nod_f}}{dt} = -k_{nod_f} X_{nod_f} \tag{3.18}$$

$$\frac{dX_{nod_s}}{dt} = -k_{nod_s} X_{nod_s} \tag{3.19}$$

3.3.5 Permeability Effects

Research has shown that oxidation of a high DNAPL saturation source using permanganate may result in permeability reductions due to precipitation of manganese oxides (Lee et al. 2003, Schroth et al. 2001, Siegrist et al. 2002). On the other hand, research into permeability effects from permanganate oxidation of DNAPL source zones at lower saturations is more ambiguous. Nelson et al. (2001) concluded that the manganese oxides produced during oxidation of a PCE DNAPL present at approximately 4-7% saturation had negligible effect on the permeability, despite the system remaining at a neutral pH due to natural buffering from the carbonate mineral-containing sands. On the contrary, Lee et al. (2003) found that permanganate oxidation of a TCE DNAPL source zone at 8% saturation resulted in generation of up to 4900mg MnO_2(s)/kg porous media, in an unbuffered silica sand system utilizing de-ionized water. Further, they witnessed a six-fold decrease in velocity of the oxidation front over the two-month experiment, attributing this decrease to reductions in permeability. This is especially interesting because less MnO_2(s) is expected to precipitate at low pH where the reaction favors generation of Mn^{2+} instead of MnO_2(s) (Stewart 1965, Yan and Schwartz 1999).

There are various methods to relate permeability changes to changes in porosity resulting from immobile components in porous media pore spaces, such as a power law model as in Equation 3.20 (Wyllie 1962) or capillary-tube model like the Kozeny-Carman equation in Equation 3.21 (Bear 1972)

$$k_{r,w} = \left(\frac{1 - S_n - S_{r,w}}{1 - S_{r,w}} \right)^3 \tag{3.20}$$

$$k_{r,w} = \frac{\phi_{eff}^3}{K_s (1 - \phi_{eff})^2} \left(\frac{d_m^2}{180} \right) \tag{3.21}$$

where $k_{r,w}$ is the relative water permeability, S_n is the saturation of immobile component in the pore space, $S_{r,w}$ is the residual water saturation for the porous media and K_s is the saturated hydraulic conductivity.

Saenton (2003) found Equation 3.20 to provide good agreement to experimentally derived permeability data (Saba 1999) for DNAPL in silica sands like those that are being used in this research. Additionally, Clement et al. (1996) proposed a form of Equation 3.20 for pore-clogging due to microbial growth. These power law and Kozeny-Carman equations may not be perfectly suited to permeability reduction following chemical precipitation in porous media because they significantly under-predict permeability reductions, especially at high levels of plugging (Reis and Acock 1994). However, application of the CORT3D model code is done at a much larger scale than the pore-scale. Although Equations 3.20 and 3.21 may not be applicable to estimating pore-scale permeability reduction due to chemical precipitation, they may be adequate at the much larger modeling scale. For example, Equation 3.20 may estimate a 10% permeability reduction. In reality pores with the smallest throats may see a nearly 100% reduction, while pores with large throats may see virtually no reduction. Because the large throat pores are initially responsible for the greatest transport of water, plugging of the smallest pores has relatively little impact, and the overall change (at a modeling scale) may be well represented by the estimate of Equation 3.20.

Along these lines, CORT3D incorporates a version of Equation 3.20 to estimate permeability changes

$$k_{r,w} = \left(\frac{1 - S_{mno2} - S_n - S_{r,w}}{1 - S_{r,w}} \right)^3 \tag{3.22}$$

where S_{mno2} is a pseudo-saturation representing the volume of total pore space filled with manganese oxide solids. This pseudo-saturation is estimated by converting the mass fraction of solids produced to a volume using an effective manganese oxide precipitate density. The effective density is essentially a fitting parameter, and not an actual density of manganese oxide particles generated. This is because $MnO_2(s)$ formed during oxidation using permanganate may take different forms depending on soil and water conditions as well as where it forms. Much of it is likely to form within the pore space as

an amorphous, hydrous, porous form reducing effective porosity available for water flow; this form is expected to have an undetermined density that is lower than that of dry, solid $MnO_2(s)$. Additionally, the amorphous, hydrous particles of $MnO_2(s)$ that form within the pore space may also become lodged in pore throats blocking flow. Further, some may form as a more structured and solid film on soil particle surfaces where it can reduce the pore throat diameter. The effective density parameter accounts for permeability reductions resulting from all three of these mechanisms. The magnitude of permeability reduction occurring as a result of each mechanism is expected to be site specific, depending on soil and water conditions. As a result, it is expected that the effective density parameter may vary between simulations of different site conditions, but should be a constant for all similar conditions within a single simulation. It should also be noted that the relation represented by Equation 3.22 was generated for unconsolidated sand with well-sorted grains and non-wetting DNAPL (Wyllie 1962). If significantly different conditions are to be modeled, a different relation may be necessary. For example, the exponent is changed from 3 to 4 for cemented sandstone (Wyllie 1962).

Because dissolution and oxidation are transient processes where NAPL saturation decreases with time and manganese oxide solids increase with time (i.e. effective porosity and permeability change), the groundwater flow pattern needs to be updated periodically. The more frequent the update of the flow solution (through changes of effective hydraulic conductivity, porosity, NAPL saturation, and manganese oxide volume) the closer the simulation approaches the transient solution. Because the flow and transport solutions are not coupled in this model code, long (time) simulations are broken down to a number of short steady-state flow and transient transport runs that are executed in sequence. The implementation of simulating changing permeability as a result of DNAPL dissolution and chemical oxidation is depicted in Figure 3.4

Similar to the model code of Saenton (2003) for simulating surfactant enhanced aquifer remediation, effective hydraulic conductivities are used within MODFLOW to generate the velocity field. This velocity field is then used in estimating the DNAPL

dissolution mass transfer coefficient. Then the transport model code simulates the DNAPL dissolution, oxidation, and other relevant reactions over a relatively short time interval. If overall simulation time is not over, the transport results are used to generate new porosities and hydraulic conductivities and the process is repeated.
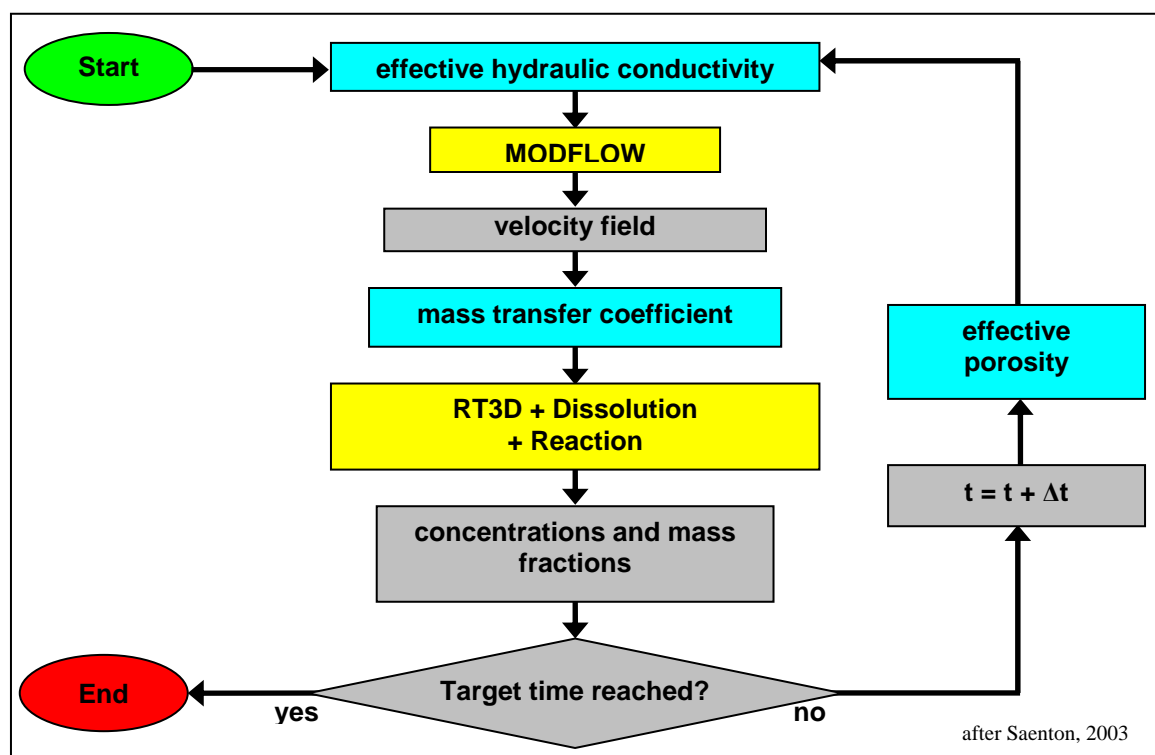
Figure 3.4: CORT3D Permeability Effects Process

3.4   Model Code Verification

An important step in developing new model code is verification comparing results from this model code against analytical solutions and/or other (previously verified) numerical codes. After the code has been verified, the next step is testing to demonstrate that a model (utilizing the code) of specific site or experimental conditions can reproduce important processes and effects after being calibrated with an independen set of

observations (Refsgaard and Henriksen 2004, Refsgaard and Knudsen 1996, Van Waveren et al. 1999). Results of experimental testing of the new code are found in Section 3.5.

3.4.1 Comparison to Analytical Solutions

The chemical oxidation reactions in CORT3D have been verified against analytical solutions. This was done in several steps. First, oxidation of PCE (w/o NOD present) was simulated using a 1D homogeneous system under no-flow conditions, using both the CORT3D model and the analytical solution to the PCE oxidation rate law (given in Equation 3.12) shown below (Hood 2000),

$$[PCE] = \frac{\left\{[MnO_4^-]_0 - Y_{MnO4/pce}[PCE]_0\right\}[PCE]_0}{[MnO_4^-]_0 e^{\left\{[MnO_4^-]_0 - Y_{MnO4/pce}[PCE]_0\right\}k_2 t} - Y_{MnO4/pce}[PCE]_0} \tag{3.23}$$

where, [*component*] is the concentration of the specified component in mg/L at time, t (sec), and [*component*]$_0$ is the initial concentration of the specified component at time zero. The concentrations of the other components (MnO_4^-, MnO_2(s), and Cl^-) are calculated based on the reaction stoichiometry. Figure 3.5 shows the results from the analytical solution (points) and CORT3D model results (line). The agreement indicates that the kinetics of the model are operating correctly.
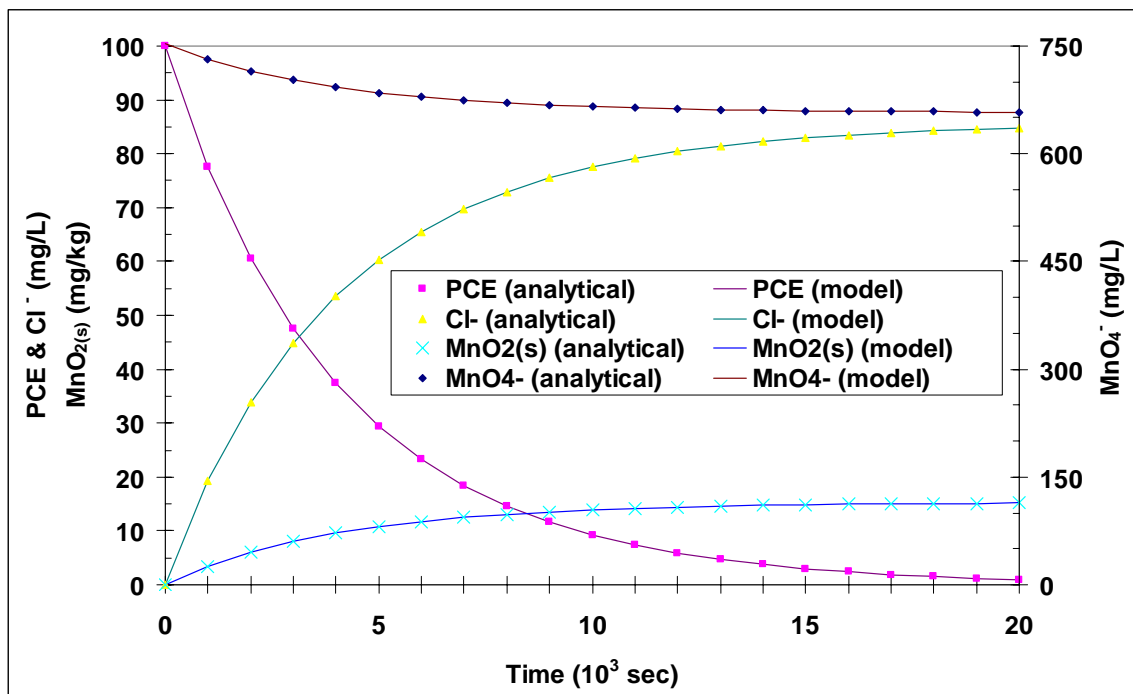
Figure 3.5: Comparison of Analytical and Model Results for PCE Oxidation

The NOD oxidation kinetics were similarly tested, using the model to simulate oxidation of fast NOD (w/o PCE present) under no-flow conditions, and comparing it to the analytical solution for first order degradation in Equation 3.24.

$$[NOD] = [NOD]_0 e^{-kt} \tag{3.24}$$

Figure 3.6 shows the results from the analytical solution (points) and CORT3D model results (line). Results for slow NOD are not shown as they are similar to those for the fast NOD, varying only by the rate of change. Again, the agreement indicates that the model kinetics are operating correctly.
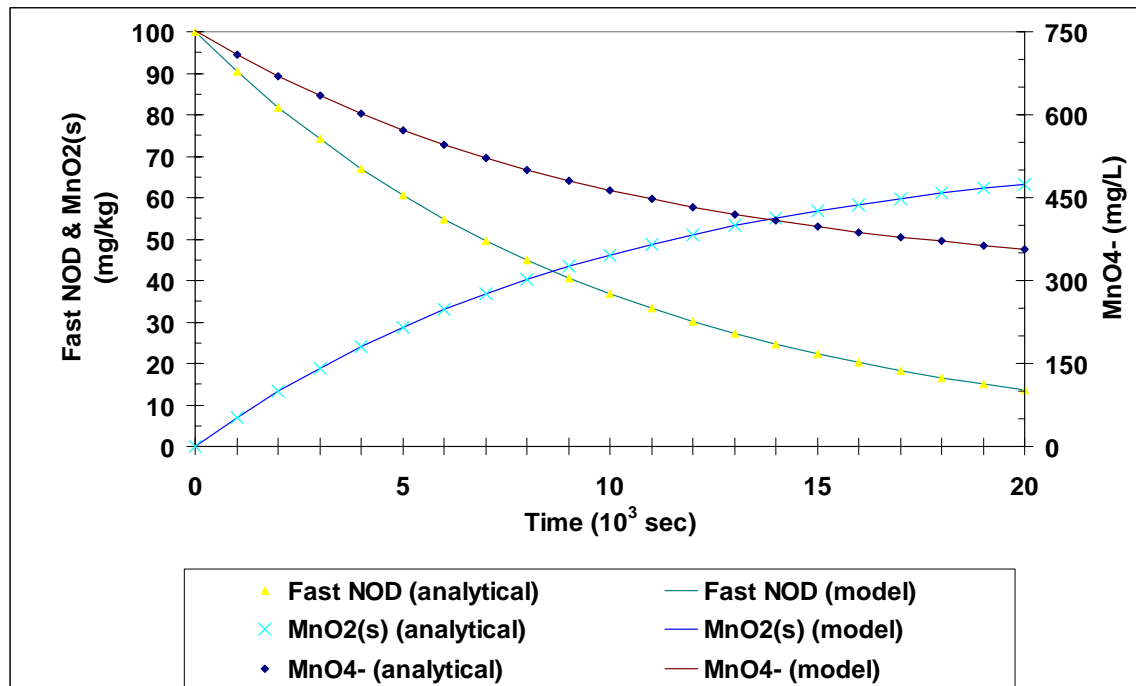
Figure 3.6: Comparison of Analytical and Model Results for NOD Oxidation

The model was also verified against analytical solutions incorporating advection, dispersion, and chemical reaction. Although the CORT3D computer model incorporates second-order chemical oxidation, available analytical solutions only incorporate 1st-order reactions. Additionally, the analytical solutions are for homogeneous systems under uniform flow in the direction of the primary axis.

The CORT3D simulations were set up so that either contaminant or oxidant was present in excess. This means the concentration of the species in excess does not change significantly as the reaction progresses, and the reaction becomes pseudo-first-order with a first-order rate constant (k_1) equal to the second-order rate constant times the molar concentration of the species in excess (Equation 3.25). Equation 3.26 is the 1D solute-transport equation for a finite system with a third-type (or Cauchy) flux boundary at the inlet. Equation 3.27 is the analytical solution from Selim and Mansell (1976), modified

by van Genuchten and Alves (1982) and presented in the USGS *Analytical Solutions for 1D, 2D, and 3D Solute Transport in Ground-water Systems with Uniform Flow* (Wexler, 1992):

$$k_1 = k_2 \left[C_{Excess} \right] \tag{3.25}$$

$$\frac{\partial C}{\partial t} = D_x \frac{\partial^2 C}{\partial x^2} - \bar{v}_x \frac{\partial C}{\partial x} - k_1 C \tag{3.26}$$

$$C(x,t) = C_0 \left\{ \frac{\exp\left[\frac{(\bar{v}_x - U)x}{2D_x} \right] + \frac{(U - \bar{v}_x)}{(U + \bar{v}_x)} \exp\left[\left(\frac{\bar{v}_x + U}{2D_x} \right) x - \frac{UL}{D_x} \right]}{\left[\left[\frac{(U + \bar{v}_x)}{2\bar{v}_x} - \frac{(U - \bar{v}_x)^2}{2\bar{v}_x (U + \bar{v}_x)} \right] \exp\left[\frac{[-UL]}{D_x} \right] \right]} \right.$$

$$- 2 \frac{\bar{v}_x L}{D_x} \exp\left[\frac{\bar{v}_x x}{2D_x} - \frac{\bar{v}_x^2 t}{4D_x} - k_1 t \right]$$

$$\left. \bullet \sum_{i=1}^{\infty} \frac{\beta_i \left[\beta_i \cos\left(\frac{\beta_i x}{L} \right) + \left(\frac{\bar{v}_x L}{2D_x} \right) \sin\left(\frac{\beta_i x}{L} \right) \right]}{\left[\beta_i^2 + \left(\frac{\bar{v}_x L}{2D_x} \right)^2 + \frac{\bar{v}_x L}{2D_x} \right]} \bullet \frac{\exp\left[\frac{-\beta_i^2 D_x t}{L^2} \right]}{\left[\beta_i^2 + \left(\frac{\bar{v}_x L}{2D_x} \right)^2 + \frac{k_1 L^2}{D_x} \right]} \right\} \tag{3.27}$$

with

$$U = \sqrt{\bar{v}_x^2 + 4k_1 D_x} \tag{3.28}$$

where $C(x,t)$ is the concentration at location x and time t, C_o is the concentration of the species of interest entering at the inlet, $\bar{v}_x$ is the linear pore velocity in the x-direction, D_x is the longitudinal dispersion coefficient, L is the column length, and β_i are the roots of the equation

$$\beta \cot \beta - \frac{\beta^2 D_x}{\bar{v}_x L} + \frac{\bar{v}_x L}{4D_x} = 0 \tag{3.29}$$

The outlet boundary is a second type (or Neumann) specified concentration gradient boundary, with the specified gradient equal to zero. The initial condition is that the concentration of the species of interest is zero at all locations in the column.

Two comparisons were performed for a short, 40cm, column—one with oxidant in excess and one with PCE in excess. In each simulation a unit concentration of the species of interest was applied at the inlet. A linear pore velocity of 5.0cm/hr, longitudinal dispersion coefficient of $2.0cm^2/hr$, and pseudo-first order reaction rate constant of 1.362 per hour were used. These parameters are of the same order of magnitude as the PCE oxidation experiment modeled in Section 3.4. Figure 3.7 shows the PCE concentration when oxidant is held constant in excess, while Figure 3.8 shows the oxidant concentration when PCE is artificially held constant in excess. In both cases, the CORT3D model results are identical to the analytical solution indicating the model is working correctly.
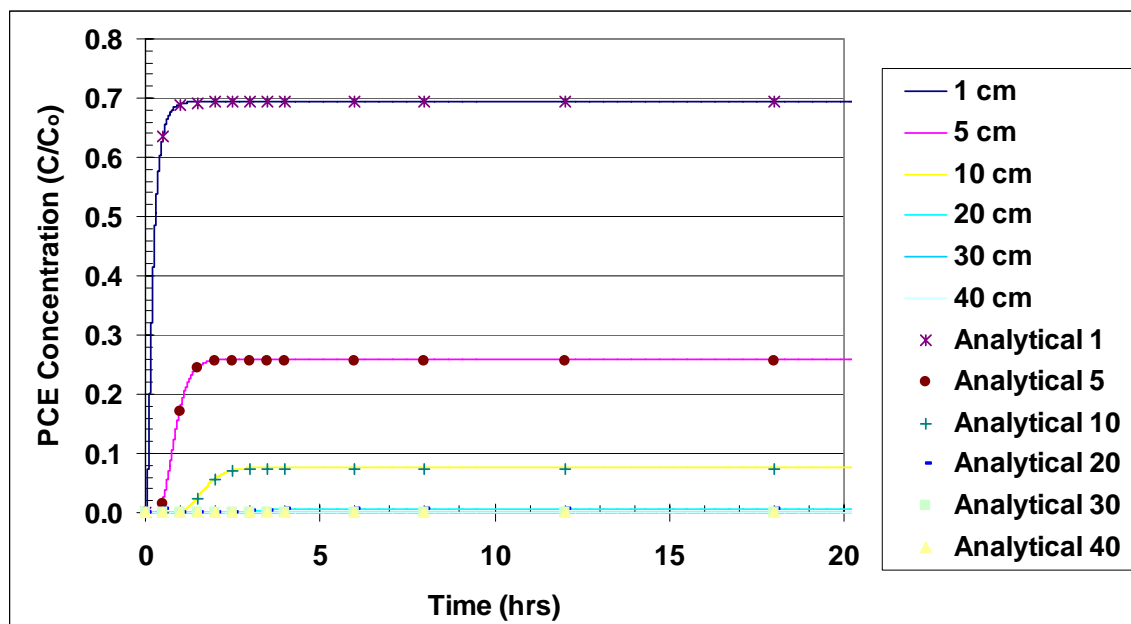
Figure 3.7: Analytical and Model Results for Short 1D Column – PCE
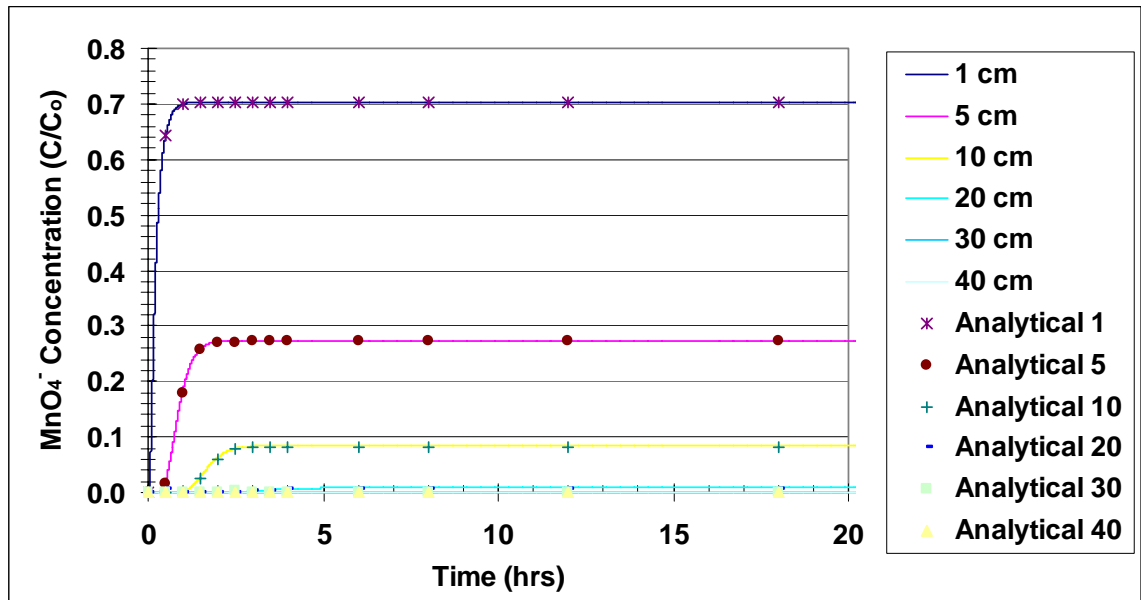
Figure 3.8: Analytical and Model Results for Short 1D Column – MnO$_4$$^-$

An additional comparison was made for a much larger 1D case, with a 40m long column, and different conditions to verify the model code works at larger scales. In this simulation, oxidant was held in excess and a unit concentration of PCE was input at the inlet. The linear pore velocity was 0.6m/hr, the longitudinal dispersion coefficient was 0.6m^2/hr, and the pseudo-first-order reaction rate was 0.001 per hour. Again, the model exactly reproduced the analytical solution results as shown in Figure 3.8.

Figure 3.9: Analytical and Model Results for Long 1D Column – PCE

Next, the model code was verified against a 2D analytical solution for a semi-infinite length, finite width aquifer containing homogenous medium, with constant and uniform groundwater velocity in the x-direction only, and a constant line contaminant source of a finite width at the inlet as illustrated in Figure 3.10. Equation 3.30 shows the governing 2D solute-transport equation. Again the simulation was set up with oxidant in excess to approximate a pseudo-first-order reaction, because the analytical solution is first-order. The analytical solution for this scenario (Equation 3.31) is again from the USGS manual (Wexler, 1992).

$$\frac{\partial C}{\partial t} = D_x \frac{\partial^2 C}{\partial x^2} + D_y \frac{\partial^2 C}{\partial y^2} - \bar{v}_x \frac{\partial C}{\partial x} - k_1 C \qquad (3.30)$$

$$C(x,y,t) = C_0 \sum_{n=0}^{\infty} L_n P_n \cos(\eta y)$$

$$\bullet \left\{ \exp\left[\frac{x(\bar{v}_x - \beta)}{2D_x}\right] erfc\left[\frac{x - \beta t}{2\sqrt{D_x t}}\right] + \exp\left[\frac{x(\bar{v}_x + \beta)}{2D_x}\right] erfc\left[\frac{x + \beta t}{2\sqrt{D_x t}}\right] \right\} \quad (3.31)$$

with

$$L_n = \begin{cases} \frac{1}{2} & ,n = 0 \\ 1 & ,n > 0 \end{cases} \quad (3.32)$$

$$P_n = \begin{cases} \dfrac{Y_2 - Y_1}{W} & ,n = 0 \\ \dfrac{[\sin(\eta Y_2) - \sin(\eta Y_2)]}{n\pi} & ,n > 0 \end{cases} \quad (3.33)$$

$$\eta = \frac{n\pi}{W} \quad ,n = 0,1,2,... \quad (3.34)$$

$$\beta = \sqrt{\bar{v}_x^2 + 4D_x(\eta^2 D_y + k_1)} \quad (3.35)$$

where $C(x,y,t)$ is the concentration at location (x,y) and time t, D_y is the transverse dispersion coefficient, W is the width of the aquifer, Y_1 is the location of the lower edge of the strip source at the inlet, and Y_2 is the location of the upper edge of the strip source. The inlet is a first type (or Dirichlet) constant concentration boundary with concentration equal to C_0 for y between Y_1 and Y_2, and zero elsewhere. The outlet and side boundaries are all second type (or Neumann) specified concentration gradient boundaries, with the specified gradient equal to zero.

For the comparison, an aquifer 50m wide by 100m long, containing a unit concentration PCE source 10m wide, centered at the inlet was used. A linear pore velocity of 0.2m/hr, longitudinal dispersion coefficient of 0.2m^2/hr, transverse dispersion coefficient of 0.02m^2/hr, and pseudo-first order reaction rate constant of $1.36\text{x}10^{-3}$ per hour were used. Figure 3.10 is a schematic of the 2D system being simulated. Figure 3.11 shows the PCE concentration when oxidant is held constant in excess. The numbers in the plot legend refer to the x and y location (m).

Figure 3.10: Schematic of 2D Aquifer Scenario Used in Simulation

Figure 3.11: Analytical and Model Results for 2DAquifer – PCE

Figure 3.12 shows a plot of numerical model results versus analytical solution results for locations along the length of the aquifer at Y=25m (centerline of plume) as well as Y=20 and 30m (near edge of plume). The line on Figure 3.12 represents a 1:1 relation. While the numerical results do not match the analytical results exactly, they are close with an R^2=0.995 for the off-centerline locations and 0.999 for the centerline locations. Considering the numerical model utilized a 1m square cell size to limit the computer run time, the difference is not significant.

Figure 3.12: Analytical to Numerical Correlation for 2D Aquifer – PCE

3.4.2   Comparison to Other Numerical Models

A series of simulations were performed to verify the revised RT3D diffusion code work as expected. The new code was used to simultaneously simulate pure diffusion (without a hydraulic gradient, hence absence of advection and mechanical mixing) of three components (PCE, MnO_4^-, and Cl^-), and the results were compared to those of running the original RT3D code individually for each of the three component diffusion coefficients. Figure 3.13 compares the original RT3D results (left) to the modified RT3D results (right) for each species. The identical results indicate the new effective diffusion code works properly.

**Figure 3.13: Comparison of Original RT3D (left) and Modified RT3D (right)
Diffusion Results**

Simulations were also run testing the new code under combined advective and dispersive/diffusive conditions. Figure 3.14 is a comparison of results from the original RT3D (top) and CORT3D (bottom) under conditions with aqueous PCE initially present in the LPM, and a region of high permeability sand above it. Again, identical results indicate that the new diffusion code in CORT3D is working properly under combined diffusion and advection/mechanical dispersion conditions.

Figure 3.14: Comparison of Codes under Advective Conditions

3.5   Experimental Testing of Models Using New Code

After verifying the model code worked properly, it was used to simulate a series of 1D laboratory experiments, documented in literature, highlighting important ISCO related processes. The goal of these tests was not to universally validate the modeling code for all conditions, since it is recognized that models of specific scenarios must be individually validated for the specific boundary conditions, performance criteria, and application (Refsgaard and Henriksen 2004, Refsgaard and Knudsen 1996, Van Waveren et al. 1999). Instead, the purpose of this testing was to demonstrate that models created using the modeling code capture specific important ISCO-related processes and effects

observed in experiments. Where sufficient data was available, the model was calibrated using one set of data and then used to predict observed effects from an independent set of data.

3.5.1   Simulating Permeability Effects from Oxidizing TCE DNAPL

A significant feature of CORT3D is incorporation of permeability effects resulting from oxidation using permanganate. However, there is no analytical solution to test the model against, so this could only be tested against experimental data. Schroth et al. (2001) performed a set of column experiments specifically to study the effects of oxidizing TCE DNAPL on porous media permeability. In these experiments, a 95cm x 5.1cm diameter column was packed with high purity silica sand and then a residual TCE DNAPL source zone was created in the first 65cm. TCE DNAPL saturation was measured to be approximately 17% throughout the entire source zone using dual-energy gamma radiation attenuation. Once the flushing experiment began, water head drop throughout the column was monitored regularly, using a computerized pressure data gathering system with ceramic tensiometers ($\pm$0.2cm) inserted in the column, to assess changes in permeability. The first experiment was natural dissolution only. The second experiment included flushing with potassium permanganate (790mg/L as $KMnO_4$), but ended after only 30 hours due to a pump failure. As a result, the CORT3D model code could not be utilized in a prediction scenario. All that could be done was to determine if the model captured the general change in permeability observed in the experiment. On the other hand, simulating the experiments by Schroth et al. (2001) provided the additional benefit of testing the model for use in simulating TCE oxidation.

Figure 3.15 shows the heads observed at three locations (8cm, 18cm, and 38cm from the column inlet) during the experiment. Before simulating the experiment, the experimental head data require some discussion. Because this was a 1D experiment, flow bypassing was not able to occur as pores became blocked due to $MnO_2(s)$ precipitation. As a result, pressures in the column increased quickly as more pores became blocked.

Subsequently, after only a day, water head within the column exceeded the upper limits of the tensiometers and data beyond that time are not reliable. Further, since flow bypassing could not occur, it appears from the data that as water head increased some pore blockages were physically dislodged due to sufficiently high hydraulic gradients at the pore throat. Similar behavior was reported for 1D experiments by Reitsma and Randhawa (2002). Such physical dislodgement could have transported manganese oxides further along the column ahead of the oxidation reaction front to begin blocking pores that otherwise would not have started to. This is suggested by the data where head gradually increases at T1 between 10-15 hours and then roughly levels off as head begins to gradually increase at T2. The head at T2 initially increases at the same rate that T1 initially increased, and again leveled off. Again, as T2 began to level off, head and T4 began increasing. The leveling off at each location may be to preferential channeling that resulted from hydraulic gradients not allowing further blockage of some pores. Development of preferential flow channels may also have advanced the oxidation reaction front (along the channels) faster than if the reaction front advanced uniformly. Finally, although the head data beyond 25 hours is not reliable, it does indicate a substantial increase in hydraulic head occurred. This may be partly due to $MnO_2(s)$ blocking occurring at the stainless steel column outlet screen. The screen size was unspecified, but openings were smaller than the soil grains to keep soil within the column. Consequently, the openings were approximately pore size or smaller and any $MnO_2(s)$ transported through the sand may have collected at the screen.

Despite limitations on the experimental data, the overall permeability reduction process can be discerned. Permeability reductions begin later for down-gradient locations as the reaction front propagates through the column. Further, the rate of permeability reduction can be estimated from the data prior to apparent dislodgement of pore blockages.

Figure 3.15: Actual Water Head for 1D TCE Oxidation Column

A finite difference 1D model was created using 1cm cell spacing. Boundary conditions consisted of a constant flow inlet (Q = 21.72ml/min for the dissolution experiment and 21.63 mL/min for the oxidation experiment) and constant head outlet (5cm). The flow model was calibrated to determine the initial hydraulic conductivity (5.85cm/min) using provided head data from the end of the dissolution experiment. Next the dissolution experiment (no oxidant) data was used to obtain the NAPL dissolution parameters by inverse modeling using the inverse modeling code PEST (Doherty 2003). PEST performs a non-linear least squares regression comparing model output to observed experimental values, to estimate point-scale parameter values for the dissolution mass transfer relation of Equation 3.6 (τ= 2.22, α_1= 59.73, α_2= 6.26, α_3= 0.50, α_4= 0.13). Figure 3-16 shows the experimental and simulated (a) effluent TCE concentration versus time and (b) TCE mass remaining in the column versus time.

Figure 3.16: Calibration of 1D TCE Dissolution Experiment

The calibrated dissolution parameters were used, along with second-order chemical oxidation kinetic rate for TCE taken from literature (39 L/mol-min from Zhang and Schwartz 2000), to simulate the oxidation experiment. As discussed previously, the model utilizes the relative water permeability relation shown in Equation 3.22 (adapted from Wyllie 1962) to relate changes in effective porosity to relative permeability. Further, the model code treats all $MnO_2(s)$ as immobile; once generated, the solids remain in the same location. As discussed previously, the model code converts mass of

generated $MnO_2(s)$ in a model cell to volume based on the effective density of precipitated manganese oxide. However, this effective density is a fitting parameter because the precipitated manganese oxides are a porous, hydrous form having an undetermined density expected to be considerably lower than that of dry, consolidated, manganese oxide solids. Additionally, the effective density parameter is not an actual density of the precipitated solids as it also accounts for permeability reductions resulting from additional mechanisms including formation of manganese oxide film on the soil particle surfaces reducing pore throat diameter and blockage of some pore throats without significantly reducing pore volume. The optimal $MnO_2(s)$ effective density for these experimental conditions was found to be 105mg/mL (approximately 48 times less than the density of dry, solid $MnO_2(s)$). Figure 3.17 shows the simulated water head (above the effluent) for the same three locations along the column as in Figure 3.15. The simulation was able to capture the general experimental trends including permeability reduction near inlet occurring first with down-gradient reductions occurring later and rate of permeability reductions at each location similar to initial rates seen in the experiment.

Figure 3.17: Simulated Water Head for 1D TCE Oxidation Column

Additionally, the model was able to capture the oxidation of TCE using dissolution parameters from a separate experiment and kinetic rates from literature. Figure 3.18 shows the experimental and simulated (a) effluent TCE concentration versus time and (b) TCE mass remaining in the column versus time.

**Figure 3.18: Comparison of Simulated and Observed Results for 1D TCE
Oxidation**

For this 1D experiment, the simulation was able to reproduce TCE oxidation even
though it did not match exact head values. This should not be surprising since the
experiment was a 1D column under constant flow conditions; flow rate through the
DNAPL source did not depend on hydraulic gradient. In a 2D or 3D system, where flow
bypassing can occur and where flow rate through a source depends on hydraulic gradient,

it is expected that the ability of a simulation to capture oxidation results will be more dependent on also capturing hydraulic head changes.

3.5.2   Simulating Oxidation of PCE DNAPL

Next, the model was tested using column experiments investigating the oxidation of residual PCE DNAPL using potassium permanganate, performed by Schnarr et al. (1998). The columns were 30cm long, with a diameter of 5.2cm, and were filled with fine-grained sand from the Borden test site, Ontario. Although Schnarr et al. (1998) determined the Borden site soil exerted some degree of natural oxidant demand (NOD), possibly partly due to the 0.027 wt. % fraction of organic content, they did not specifically try to determine how much. Approximately one milliliter of PCE was distributed throughout the last 10cm of the column to achieve approximately 1% saturation. Two columns received oxidant at 7500mg/L (as $KMnO_4$) and two received oxidant at 10,000mg/L. One column of each flow rate had a Darcy velocity of approximately 42 cm/day, while the other had a Darcy velocity of approximately 65cm/day. A fifth column received no oxidant and had a Darcy velocity of 61cm/day. Schnarr et al. (1998) said that although constant flow rates were desired, actual flow rates varied during the experiments and no further details were provided. Only the high flow rate experiments (61-65cm/day) were simulated in the work reported here.

The goal in simulating these experiments was not to reproduce results from the entire experiments, but again to determine if specific processes and effects could be captured by models created using the new modeling code. Additional information about the experiments would be needed to try and exactly reproduce results, such as details about PCE source emplacement, variability of flow rate, and possible sorption of PCE to the Borden site soil. The specific processes to be captured in these simulations included: increased mass transfer from the DNAPL to aqueous phase during oxidation, effect of fast NOD on PCE oxidation and permanganate breakthrough, effect of slow NOD on PCE oxidation and permanganate breakthrough, simultaneous existence of aqueous PCE

and permanganate in effluent, rebound in aqueous PCE concentrations following conclusion of permanganate flushing, and generation of chloride as PCE is destroyed.

A 1D model was created using 1cm cell spacing. Boundary conditions consisted of a constant flow inlet and constant head outlet. The fifth (natural dissolution) column data was used to obtain the NAPL dissolution parameters by inverse modeling, again using the inverse modeling code PEST (Doherty 2003): $\tau = 2.25$, $\alpha_1 = 76.51$, $\alpha_2 = 0.98$, $\alpha_3 = 0.49$, $\alpha_4 = 0.75$. Figure 3.19 shows experimental and simulated (a) effluent PCE concentration versus time and (b) PCE mass remaining in the column versus time.

The calibrated dissolution parameters were used, along with second-order kinetic rates taken from literature for PCE (2.7 L/mol-min from Zhang and Schwartz 2000), to simulate the fourth (low oxidant, high flow rate) column experiment and calibrate the NOD parameters (amount and kinetic rates). Finally, the third column experiment (high oxidant concentration, high flow rate) was simulated. However, it was found that for both experiments, the mass transfer fitting parameter (α_1) had to be increased during the oxidation phase of the simulation compared to natural dissolution (a factor of four for the high concentration experiment and a factor of three for the low).

Figure 3.19: Calibration of 1D PCE Dissolution Experiment

The need to increase α_1 during oxidation may be because oxidation increased mass transfer from the DNAPL to water phase by more than could be accounted for by just the increased concentration gradient. At first glance, it would seem that α_1 was relegated into a fitting parameter. However, based on an analysis of experimental conditions, it can be shown that the increase (and difference in magnitude between experiments) can likely be attributed to the chemical oxidation reaction through Equation

3.8. As discussed previously, lack of knowledge about the DNAPL-water interfacial area makes direct application of Equation 3.8 to predict increased mass transfer impossible, so several assumptions are necessary. First, assume the PCE is uniformly distributed throughout the column source zone with one spherical droplet in each soil pore with one-half of its surface area in contact with flowing water. Then, if the soil grains are assumed spherical, with a median diameter of 0.013cm, with a given porosity of 0.41, the number of pore spaces can be estimated. Next, the exposed surface area of each PCE droplet can be estimated from the emplaced volume of PCE, number of pores, and equations for volume and surface area of a sphere. Finally, take the volume of the source area as the volume of interest (V), the estimated number of pores times the estimated exposed PCE droplet surface area as the DNAPL-water interfacial area (A_{nw}), and utilize Equation 3.36 to estimate the intrinsic mass transfer rate (k_L) from the lumped mass transfer coefficient (k_{La}). Once an estimate for k_L is obtained, Equation 3.8 can be used to estimate the increase in mass transfer. Table 3.3 contains the k_{La} computed by CORT3D at the beginning of the simulation (using natural dissolution mass transfer parameters), the estimated initial k_L, and the expected mass transfer increase computed based on pseudo-first-order kinetic rates for each experiment (from the PCE oxidation rate and permanganate concentration). The magnitude of the increase in α_1 during simulation of oxidation was not dramatically different than the estimated increase from this analysis, supporting the idea that the increase in α_1 is not simply a fitting parameter but has a basis in the actual physical process. However, additional research is needed to define a method of predicting the increase so it does not have to be experimentally determined through inverse modeling.

$$k_L = \frac{k_{La}V}{A_{nw}}$$
(3.36)

Table 3.3: Estimation of Expected Mass Transfer Increase due to Oxidation

	Experiment 3 (high oxidant concentration)	Experiment 4 (low oxidant concentration)
k_{La} from CORT3D (hr^{-1})	0.80	0.81
Estimated k_L (cm-hr^{-1})	0.153	0.155
Expected Mass Transfer Increase	3.71	3.18

Observed and simulated results of the PCE oxidation experiments with low and high oxidant concentrations are shown in Figures 3.20 and 3.21, respectively: (a) effluent PCE concentration versus time, (b) effluent MnO_4^- concentration versus time, (c) effluent Cl$^-$ versus time, and (d) PCE mass remaining in the column versus time. The simulations were able to capture desired experimental processes and effects in both cases, including the delay before PCE concentrations dropped and Cl$^-$ concentrations began to increase (suggesting initial preferential oxidation of fast NOD), as well as the gradual increase (due to partial oxidant consumption by slow NOD and oxidation of PCE) in oxidant concentration once it began appearing at the effluent. Additionally, the simulations resulted in similar aqueous PCE concentrations in the effluent during oxidation even though permanganate was also present in the effluent, presumably because the PCE DNAPL was at the end of the column so that travel time from DNAPL source to column effluent was less than the reaction time necessary for complete aqueous PCE oxidation. The simulations also reproduced the generation of chloride observed as PCE was destroyed. Finally, the simulations showed aqueous concentration rebounds following oxidation similar to those observed in the experiments, especially for the low oxidant concentration experiment.
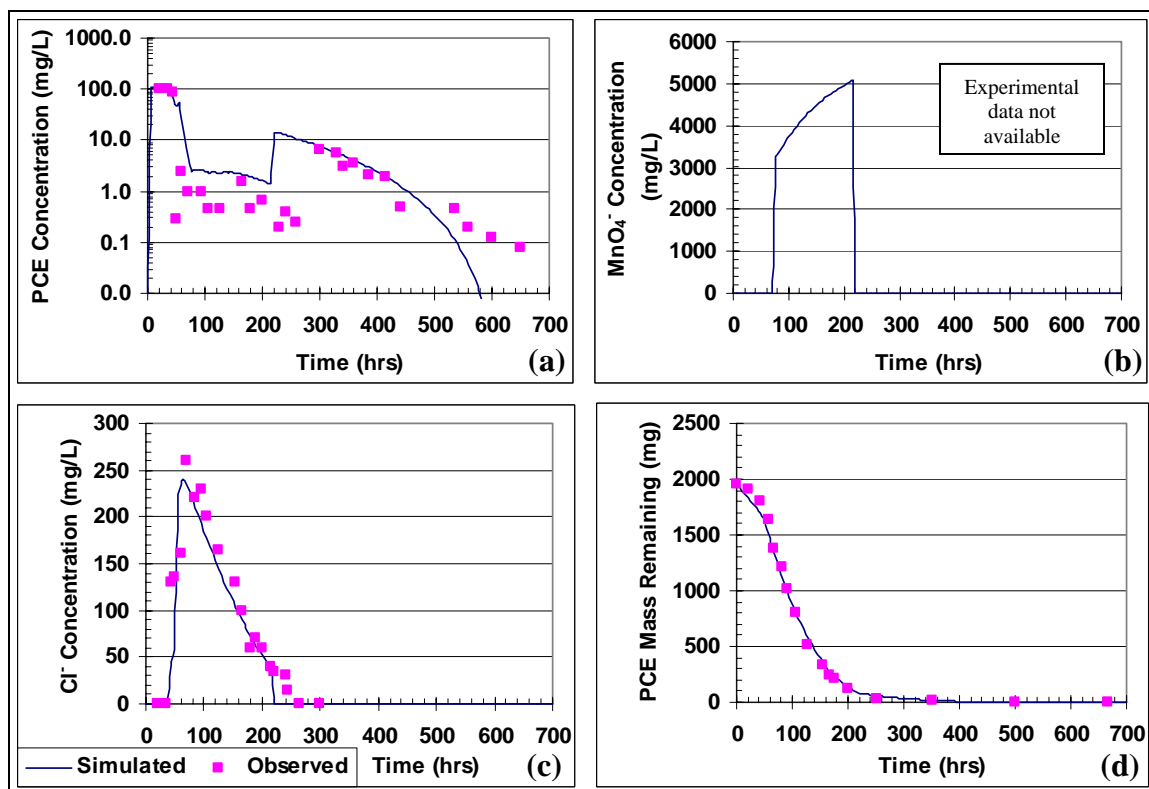
Figure 3.20: Comparison of Simulated and Observed Results for 1D PCE Oxidation – Low Oxidant Concentration
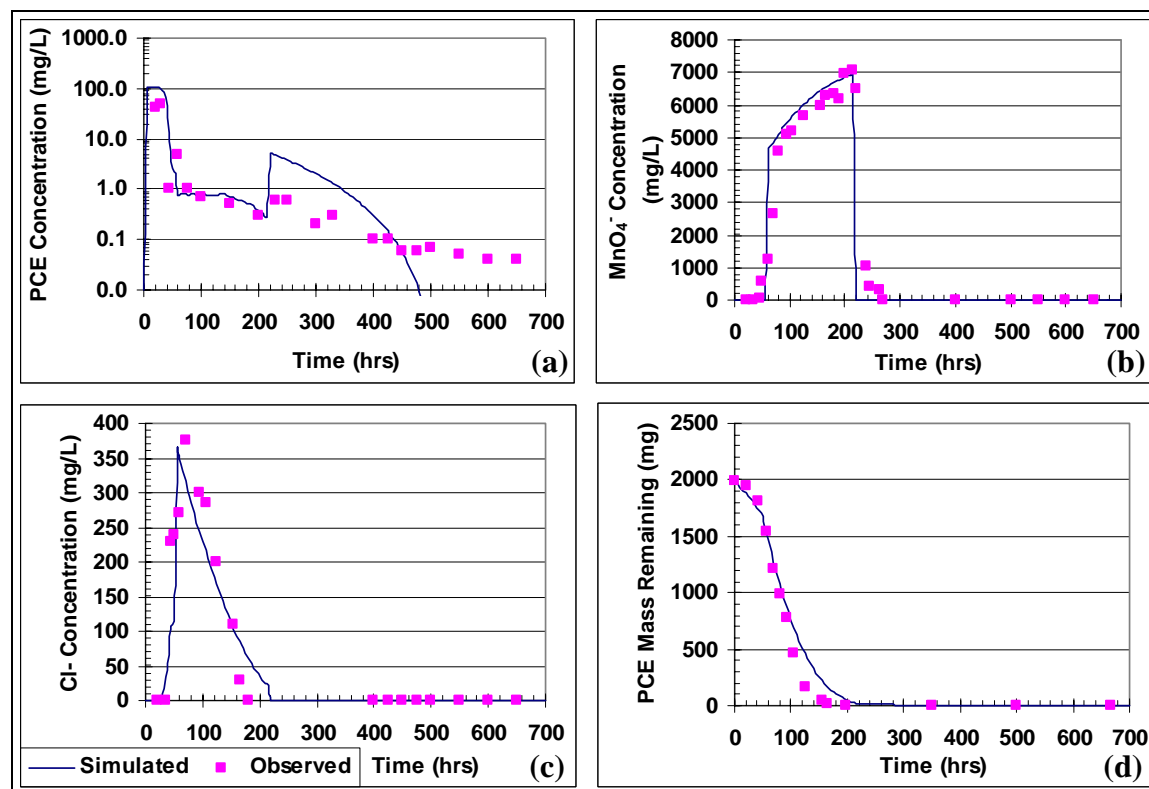
Figure 3.21: Comparison of Simulated and Observed Results for 1D PCE Oxidation – High Oxidant Concentration

It can be seen that both experiments resulted in tails of PCE concentrations which simulations did not reproduce, and the simulations didn't exactly reproduce observed rebounds. As mentioned previously, the goal was not to reproduce entire experimental results; however there are several potential reasons for departures. First, there may have been differences in the configuration of the DNAPL source between columns. Schnarr et al. (1998) do not describe how the PCE was emplaced, and experimental results suggest the initial mass may not have been equal. As a result, there may have been variations in saturation between experiments that is not captured by the model where saturation is assumed uniform throughout the source. Next, it may be a result of sorption of PCE to the field soil and subsequently desorbing after the oxidant flush. The simulations did not

incorporate sorption as no sorption data was provided; however, Borden site soil has been shown to sorb PCE (Ball and Roberts 1991, Mackay et al. 1986, Rivett and Allen-King 2003). Finally, differences may have resulted from fluctuations in the experimental flow rate mentioned by Schnarr et al. (1998) but not quantified.

The need to increase the mass transfer α_1 parameter for simulation of the oxidation experiments may be partially due to slight differences between experiments such as NAPL distribution or small-scale micro-heterogeneities in the column packing generating differing flow fields. However, it seems likely that most of the increase is due to enhanced mass transfer at the NAPL-water interface (greater than merely resulting from the increased concentration gradient) as a result of oxidation. This conclusion is supported by modeling results, which only utilized the increased α_1 while oxidation of PCE was occurring. The original α_1 determined from the natural dissolution experiment was used during the initial period of oxidation (approximately 35 hours) while NOD was being oxidized instead of PCE and during the post-oxidation flushing.

Figure 3.22 shows how the high oxidant concentration simulation results would change if the increased α_1 parameter is used during the entire simulation. In this case, the simulation would predict a much higher initial aqueous PCE concentration (before NOD is consumed and oxidation of PCE begins). Correspondingly, the simulation predicts much greater mass reduction during the initial 50 hours, accompanied by lower chloride concentrations during oxidation (because less PCE remains to be oxidized) and a drastically shortened time to PCE depletion. It appears that utilizing a uniformly increased mass transfer α_1 coefficient for the entire experiment to account for differences in physical experimental conditions does not capture experimental processes and effects as well as utilizing an increased mass transfer coefficient only during oxidation.
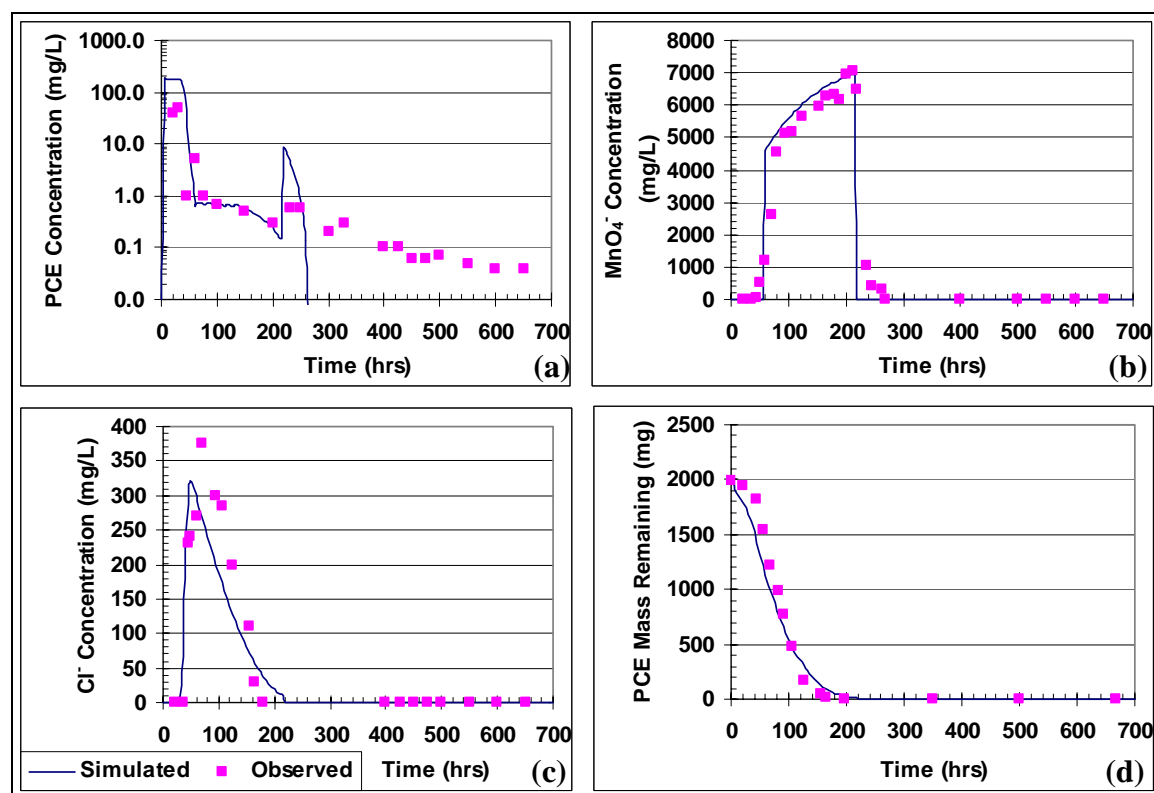
Figure 3.22: Comparison of Simulated and Observed Results for 1D PCE Oxidation (using increased mass transfer parameter for entire simulation)

Conversely, Figure 3.23 shows simulation results if the original natural dissolution α_1 is used for the entire simulation. In this case, the simulation seriously overestimates PCE concentrations during and after oxidation, predicts a much longer tail in the PCE mass removal, and drastically underestimates the chloride concentrations. Clearly, utilizing the same natural dissolution mass transfer parameters for all phases of the experiment, including oxidation, does not capture the processes and effects observed in the experiment.
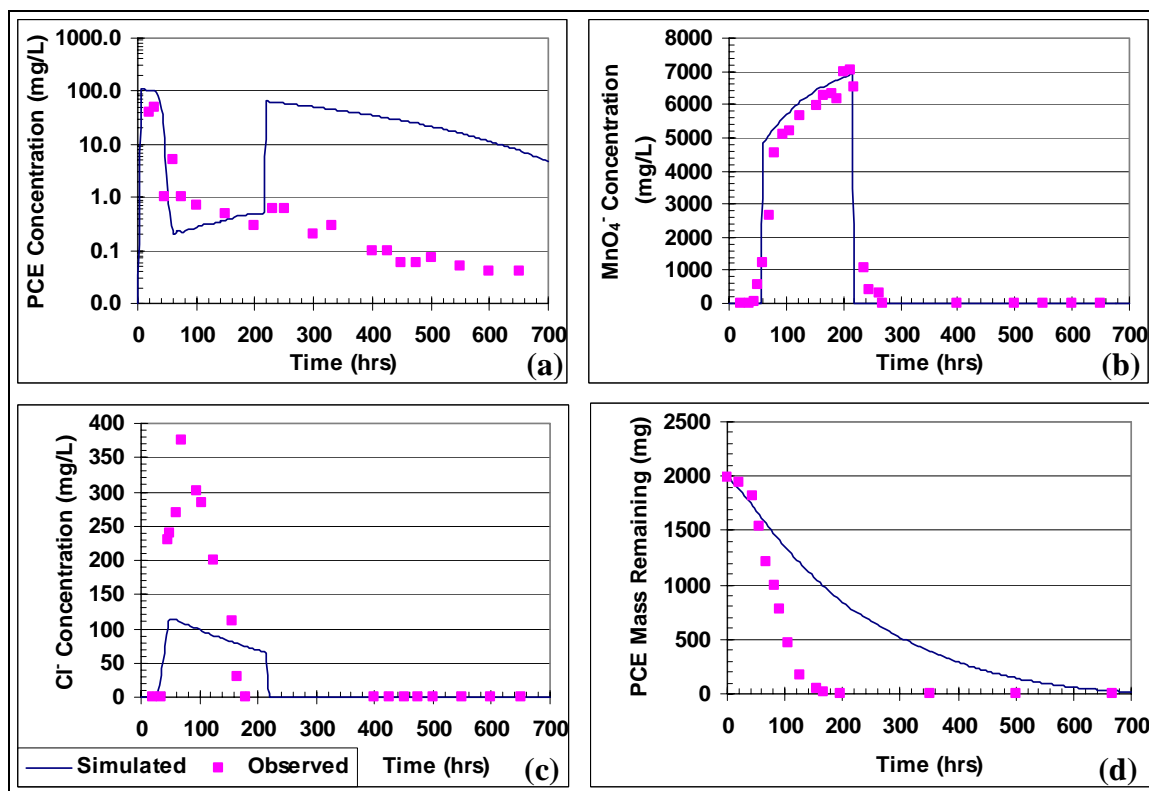
Figure 3.23: Comparison of Simulated and Observed Results for 1D PCE Oxidation (ignoring increased mass transfer during oxidation)

This modeling effort also confirmed the importance of accounting for manganese oxide precipitation in the pore space and treating NOD as multiple fractions in effectively simulating chemical oxidation using permanganate. Figure 3.24 shows simulation results if all conditions are left the same, except that the effective porosity (and therefore permeability) is not altered as manganese oxides are generated. The primary difference is that the model then significantly under predicts PCE concentrations during oxidation. When $MnO_2(s)$ precipitation is simulated, the generation of manganese oxide reduces effective porosity and consequently permeability. In a 1D column, under constant flow conditions, a reduction in permeability is not expected to substantially affect dissolution as flow-bypassing is not possible. However, reductions in effective porosity cause an

increase in linear pore velocity and therefore a reduction in travel time through the column to the outlet. As travel time is reduced, the residence time for aqueous PCE in contact with permanganate is reduced, decreasing the amount of PCE that can be oxidized and increasing effluent PCE concentrations. This is demonstrated in Figure 3.24 where the difference between the observed and simulated concentrations during oxidation increases time elapses, because the simulation (ignoring $MnO_2(s)$ formation) is not capturing the decreasing travel time as $MnO_2(s)$ reduces porosity in the experiment.
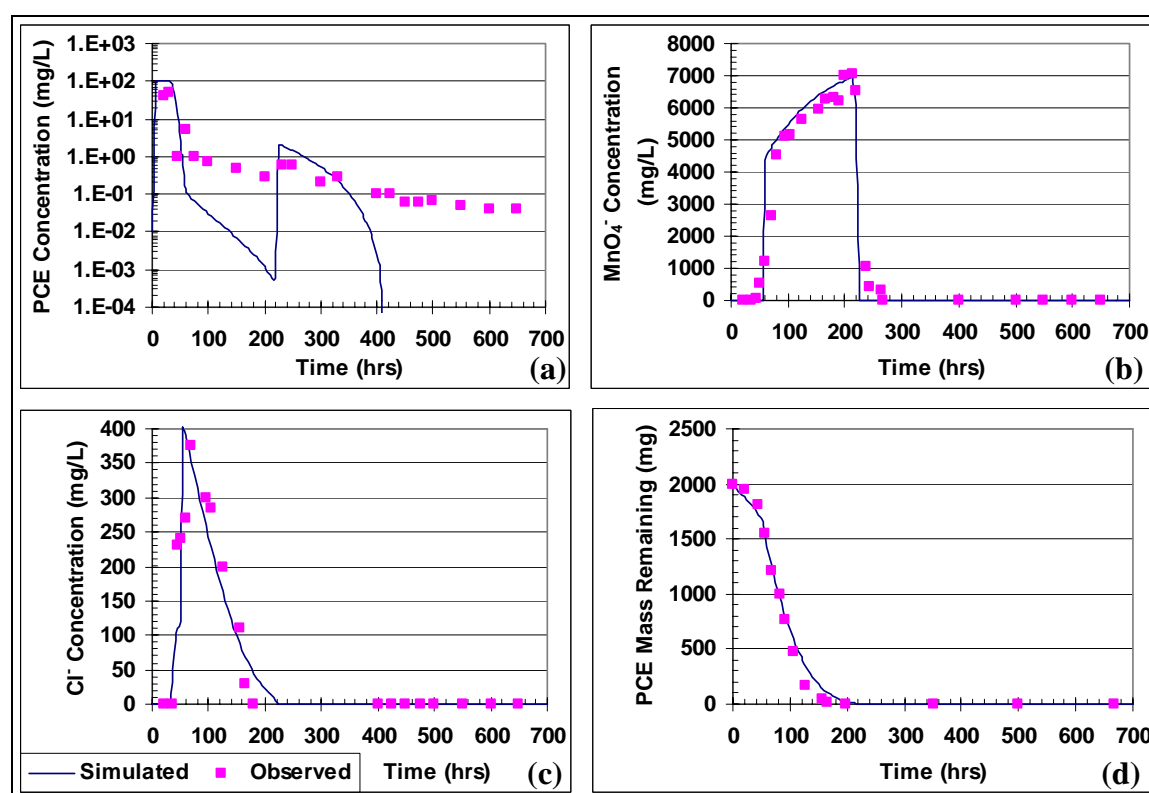
Figure 3.24: Comparison of Simulated and Observed Results for 1D PCE Oxidation (ignoring $MnO_{2(s)}$ precipitation)

As discussed earlier, the existence of some NOD with a very fast kinetic rate accounts for the delayed reduction in PCE concentration and appearance of chloride. However, neither oxidation of this fast NOD nor oxidation of the PCE can account for the delayed increase in oxidant concentrations to the injection concentration. This suggests the existence of a fraction of NOD with a much lower kinetic rate than that which is initially oxidized. This is demonstrated in Figure 3.25 by simulating the experiment without any slow fraction of NOD present. In this case, the oxidant concentration jumps up to near injection concentrations as soon as the fast NOD fraction is consumed and PCE concentrations during oxidation are under-predicted as available oxidant is not being reduced due to oxidation of slow NOD. No combination of changing mass transfer parameters, longitudinal dispersivity, or contaminant oxidation rate was able to reproduce the delayed increase in oxidant concentration except for introduction of a slow NOD fraction.
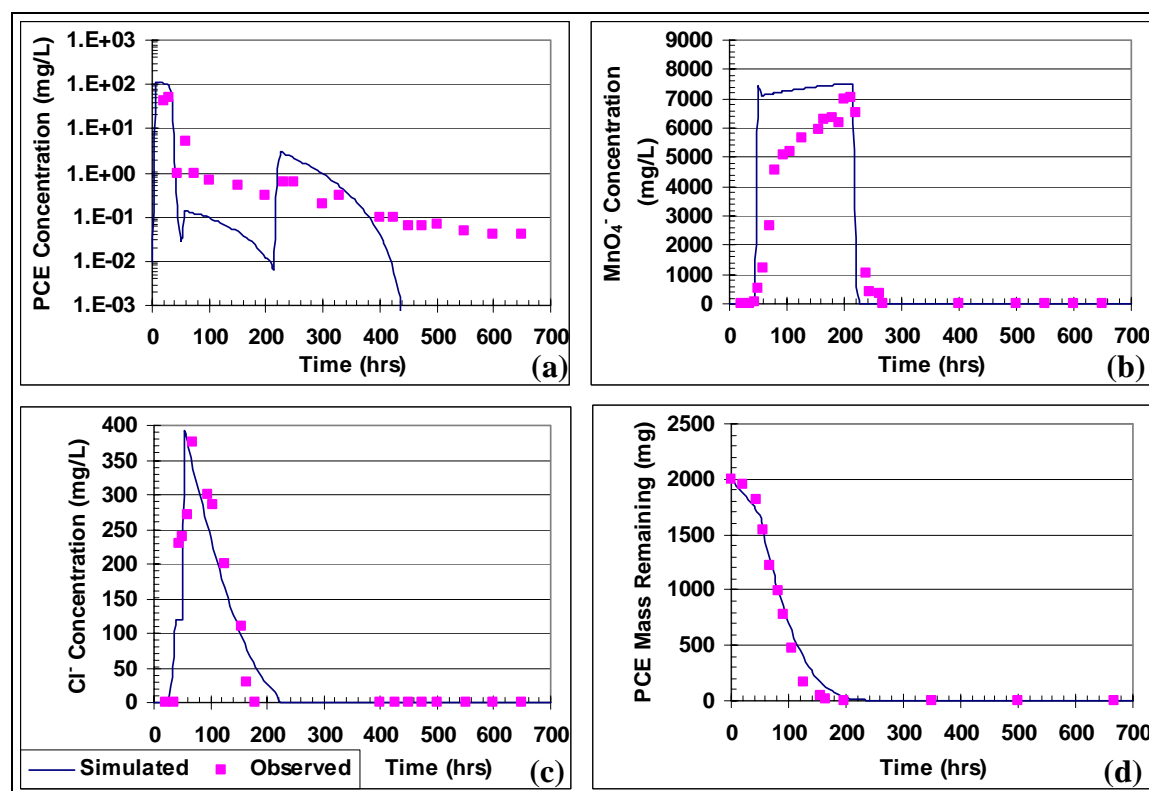
Figure 3.25: Comparison of Simulated and Observed Results for 1D PCE Oxidation (ignoring slow NOD fraction)

3.5.3 Simulating Oxidation of NOD

As alluded to before, NOD is and important factor in chemical oxidation. As such, it was desired to further test the capability of the new model to effectively capture oxidation of NOD. Because the amount of NOD in the columns of Schnarr et al. (1998) was unknown, the model was tested against an experimental NOD column study performed by Crimi and Siegrist (2004). In the study, duplicate columns (2.45cm dia x 7.65cm) were packed with clean soil from the NTC site. A constant concentration of potassium permanganate was injected at a flow rate of 3 mL/min for 54 minutes. The concentration of permanganate exiting the column was monitored to determine the NOD of the soil. Two different concentrations (1000 mg/L and 4000 mg/L as $KMnO_4$) were

used. The soil bulk density, as packed in the columns, was 1830 mg/cm^3 and the porosity was 0.31.

A 1D simulation of the high concentration experiment was set up using CORT3D with 0.5cm cell spacing. The mass fractions of fast and slow NOD, as well as the first-order oxidation rates for each, were calibrated using the average permanganate concentration and cumulative NOD data from the high concentration experiment. Calibration was again performed through inverse modeling using the inverse modeling code PEST (Doherty 2003). It was determined that the NOD consisted of approximately 34% of the fast rate component, with a first order kinetic oxidation rate of 2.0 min^{-1}. The slow component NOD kinetic rate was determined to be 4.3x10^{-2} min^{-1}. Figure 3.26a shows the experimental results for the duplicate columns using the high oxidant concentration as well as the simulated effluent concentration of MnO_4^- versus time. Figure 3.26b shows the mass of NOD remaining in the column. The simulation achieved an R^2 of 0.88 for permanganate concentrations and an R^2 of 0.95 for NOD remaining. Differences between the observed and simulated results may result from slight heterogeneities in column packing, non-uniform distribution of NOD components, and the possibility that the actual NOD is a complex mixture of more than just two components. Additionally, some components of the NOD may effectively shield other components until the first component is depleted. For example, in the NTC soil, a third NOD component with a fast kinetic rate may have become accessible to the oxidant late in the experiment (after a slower rate component coating it was depleted) to result in the relatively fast loss of NOD mass in the last 20 minutes.
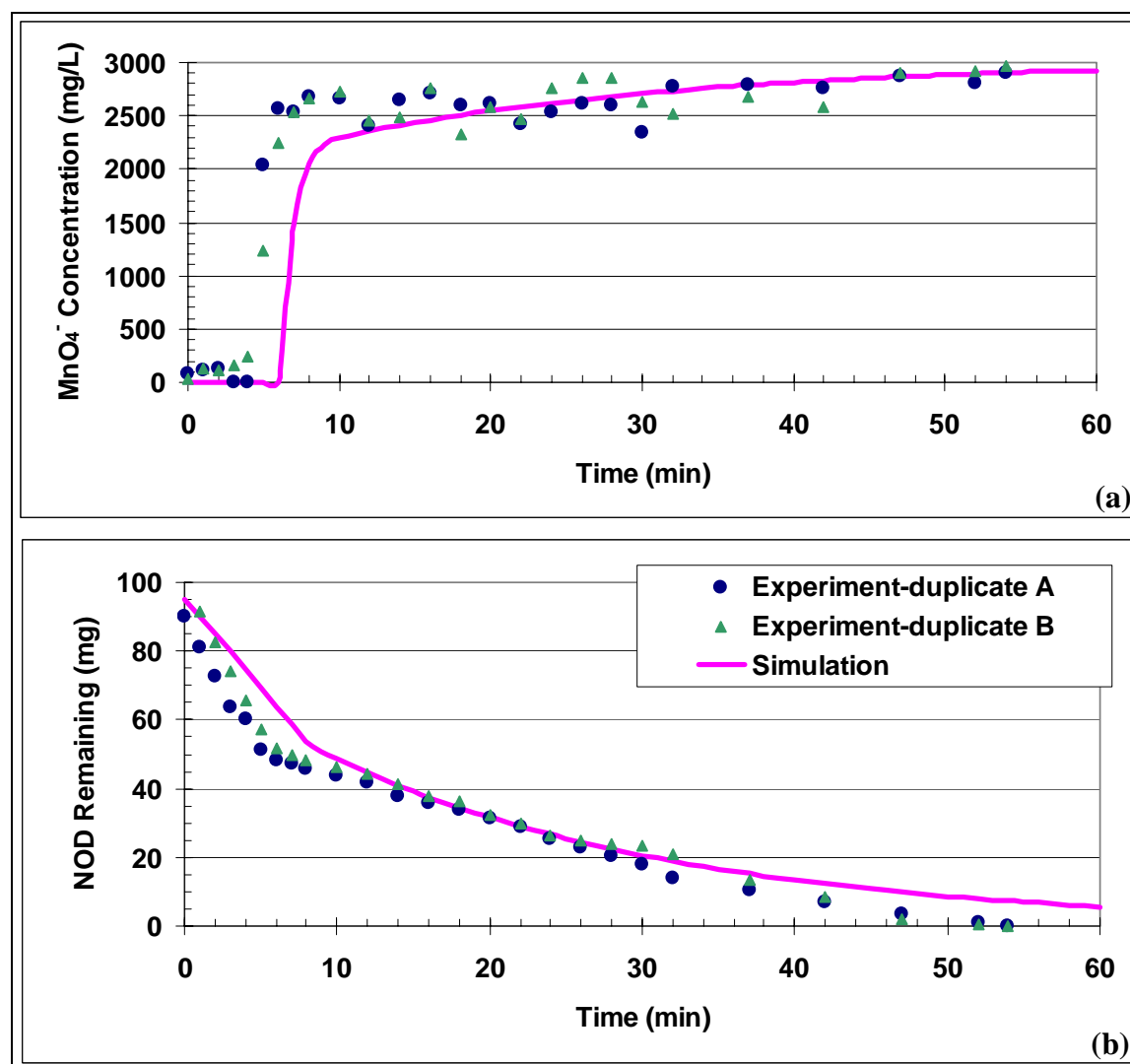
Figure 3.26: Experimental and Model Results for NOD Oxidation – High Oxidant Concentration

The next step in testing the model of this experiment was to use the ratio of slow to fast NOD mass fraction and kinetic rates, determined through calibration of the high oxidant concentration experiment, in simulating the low oxidant concentration column. The only inputs changed for this model run were the initial mass of NOD and the oxidant concentration. As shown in Figure 3.27, the model captured the oxidation of two

different NOD fractions and delay in permanganate breakthrough, achieving an R^2 of 0.93 for both permanganate concentration and NOD remaining.
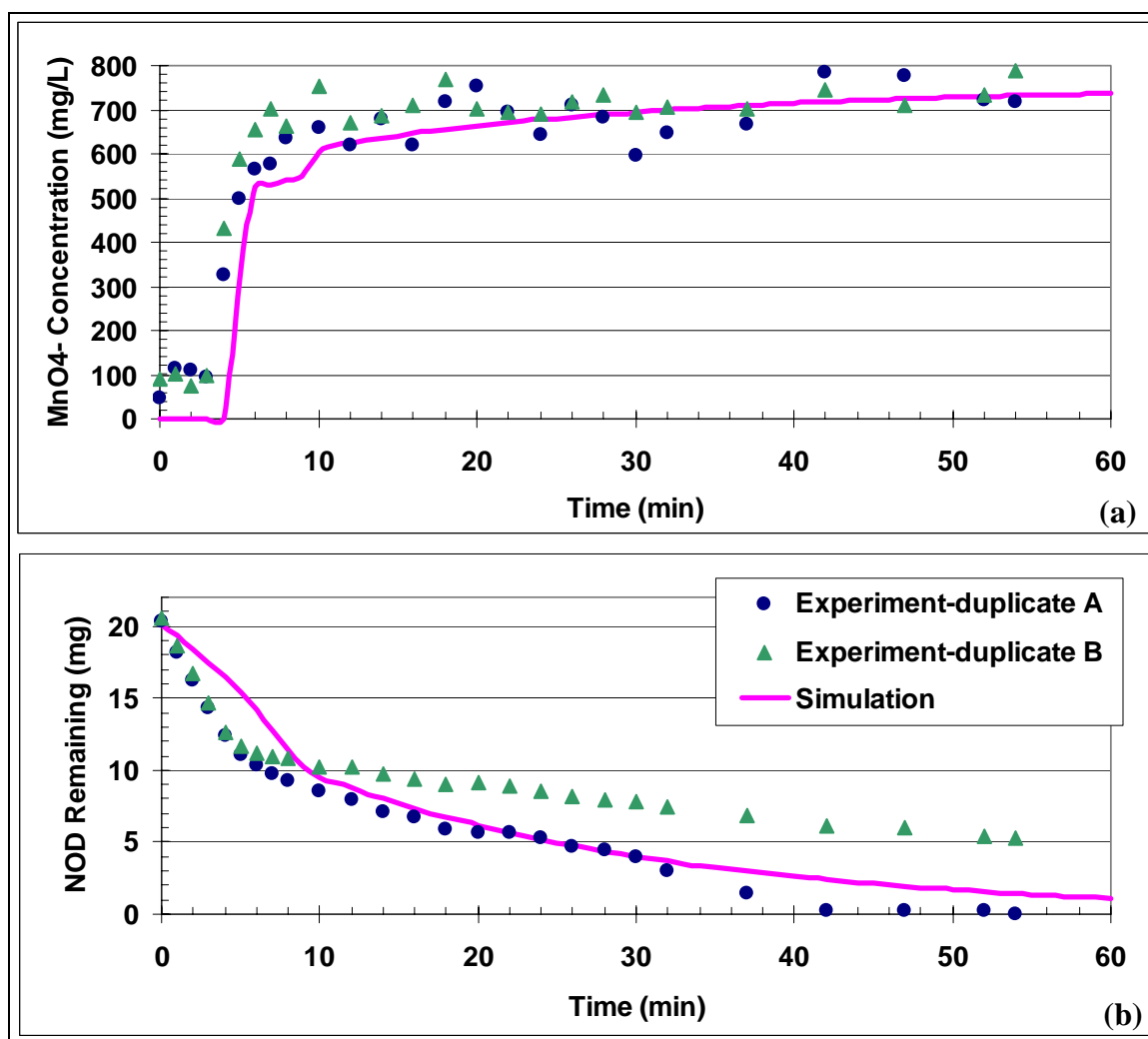
Figure 3.27: Experimental and Model Results for NOD Oxidation – Low Oxidant Concentration

3.6 Concluding Remarks

The new CORT3D model code has been verified against analytical solutions where available, to verify that it functions properly and represents important processes involved with in situ chemical oxidation. Models of experiments highlighting important ISCO processes were created using the code and tested to demonstrate that important ISCO-related process processes were captured. The model code was able to reproduce important ISCO-related processes for the conditions tested, including: PCE or TCE, low to moderate DNAPL saturations, and nonexistent to fairly high NOD content. The model code is challenged by the same numerical dispersion under highly diffusion-controlled conditions, inherent in any finite difference numerical model. However, it is still useful for qualitative comparison of oxidant transport and effectiveness under these conditions and provides direct comparison of the relative transport for the aqueous contaminant as well as the oxidant.

On the other hand, the code is an important first attempt to capture effects of manganese oxide formation resulting from permanganate oxidation of chlorinated ethenes. Manganese oxide formation causing reductions in permeability may be an important factor in designing oxidant delivery for effective source zone treatment, as well as contributing to reduction of contaminant mass flux from the source zone to meet remediation goals. Simulations of the experiments by Schnarr et al. (1998) pointed out the importance of accounting for manganese oxide formation as well as multiple NOD fractions with differing oxidation rates. Those simulations also confirmed that, at least for PCE and the experimental conditions simulated, oxidation can increase mass transfer and source depletion from a DNAPL source by a greater amount than can be attributed solely to an increased concentration gradient. This was demonstrated by the need to increase the lumped mass transfer coefficient during the oxidation phase of the simulation in order to capture experimental results. The code will be useful to compare different oxidant delivery scenarios, as well as different possible source configurations, to optimize remediation design for a specific site.

3.7 References

ATSDR. (2003). "2003 CERCLA Priority List of Hazardous Substances." Agency for Toxic Substances and Disease Registry, Division of Toxicology, U.S. Dept. of Health and Human Services. Oct. 2003. http://www.atsdr.cdc.gov/clist.html.

ATSDR. (2004). "Medical management guidelines (MMGs) for tetrachloroethylene." Agency for Toxic Substances and Disease Registry, Division of Toxicology, U.S. Dept. of Health and Human Services. May 2004. http://www.atsdr.cdc.gov/MHMI/mmg18.html.

Ball, W.P. and Roberts, P.V. (1991). Long term sorption of halogenated organic chemicals by aquifer materials: 1. Equilibrium. *Environ. Sci. Technol.*, 25 (7): 1223-1236.

Bear, J. (1972). *Dynamics of fluids in porous media*. American Elsevier Publishing Company, Dover, NY, 764 pp.

Chambers, J., Leavitt, A., Waiti, C., Schreier, C.G., Melby, J., and Goldstein, L. (2000). "In situ Destruction of Chorinated Solvents with KMnO4 Oxidizes Chromium." In: Wickramanayake, G.B., Gavaskar, A.R., Chen, A.S.C. (Eds), *Chemical Oxidation and Reactive Barriers*. Battelle Press, Columbus, OH, pp. 49-55.

Clement, T.P. (1997). *A modular computer code for simulating reactive multi-species transport in 3-D groundwater systems*. PNNL-11720, Pacific Northwest National Laboratory, Richland WA, 1997. 59 pp.

Clement, T.P. (2002). *What's new in RT3D verstion 2.5*. Pacific Northwest National Laboratory, Richland WA, 2002. 20 pp.

Clement, T.P., Hooker, B.S., and Skeen, R.S. (1996). "Macroscopic models for predicting changes in saturated porous media properties caused by microbial growth." *Ground Water*, 34 (5): 934-942.

Clement, T.P., Sun, Y., Hooker, B.S., and Petersen, J.N. (1998). "Modeling multispecies reactive transport in ground water." *Ground Water Monit. Rem.*; 18 (2): 79-92.

Cline, S.R., West, O.R., Korte, N.E., Gardner, F.G., Siegrist, R.L., and Baker, J.L. (1997). "KMnO4 chemical oxidation and deep soil mixing for soil treatment." *Geotech. News*, 15 (5): 25-28.

116

Crimi M. and Siegrist, R.L. (2004). *Experimental Evaluation of In Situ Chemical Oxidation Activities at the Naval Training Center (NTC) Site, Orlando, Florida*. Naval Facilities Engineering Command, Port Hueneme CA. 64 pp.

Cussler, E.L. (1997). *Diffusion: Mass Transfer in Fluid Systems*. Cambridge University Press. 580 pp.

Delshad, M., Pope, G.A., and Sephrenoori, K. (1996). "A compositional simulator for modeling surfactant enhanced aquifer remediation: 1. Formulation." *J. Contam. Hydrol*., 23 (4): 303-327.

Doherty, J. (2003). *Manual for PEST 7.0*. Watermark Numerical Computing, Brisbane Australia, 279 pp. http://www.sspa.com/pest.

Ewing, J.E. (1996). *Effects of dimensionality and heterogeneity on surfactant-enhanced solubilization of non-aqueous phase liquids in porous media*. MS Thesis, University of Colorado at Boulder, 152 pp.

Freeze R.A. and McWhorter, D.B. (1997). "A framework for assessing risk reduction due to DNAPL mass removal from low-permeability soils." *Ground Water*; 35 (1): 111-123.

Gates-Anderson, D.D., Siegrist, R.L., and Cline, S.R. (2001). "Comparison of potassium permanganate and hydrogen peroxide as chemical oxidants for organically contaminated soils." *J. Environ. Eng.*, 127 (4): 337-347.

Glaze, W.H. and Kang, J.-W. (1988). "Advanced oxidation processes for treating groundwater contaminated with TCE and PCE: laboratory studies." *J. AWWA*, 88 (5): 57-63.

Haggerty, R., and Gorelick, S.M. (1994). "Design of multiple contaminant remediation: Sensitivity to rate-limited mass transfer." *Water Resour. Res*.; 30(2): 435-446.

Harbaugh, A.W., Banta, E.R., Hill, M.C., and McDonald, M.G. (2000). *MODFLOW-2000, the U.S. Geological Survey modular ground-water model—User guide to modularization concepts and the ground-water flow process model*: U.S. Geological Survey Open-File Report 00-92, 130 pp.

Hood, E. (2000). *Permanganate Flushing of DNAPL Source Zones: Experimental and Numerical Investigation*. Ph.D. Dissertation, University of Waterloo, Waterloo, ON. 243 pp.

Hood, E.D. and Thomson, N.R. (2000). "Numerical simulation of in situ chemical oxidation." In: *Chemical Oxidation and Reactive Barriers*, Wickramanayake, G.B., Gavaskar, A.R., Chen, A.S.C. (Eds) . Battelle Press, Columbus, OH. pp. 83-90.

Huang, K., Hoag, G.E., Chheda, P., Woody, B.A., and Dobbs, G.M. (1999). "Kinetic study of oxidation of trichloroethylene by potassium permanganate." *Environ. Eng. Sci*., 16 (4): 265-274.

Huang, K., Hoag, G.E., Chheda, P., Woody, B.A., and Dobbs, G.M. (2001). "Oxidation of chlorinated ethenes by potassium permanganate: a kinetics study." *J. Haz. Mater*., 87 (1-3): 155-169.

Huang, K., Hoag, G.E., Chheda, P., Woody, B.A., and Dobbs, G.M. (2002). "Kinetics and mechanism of oxidation of tetrachloroethylene with permanganate." *Chemosphere*, 46 (6): 815-825.

Ibaraki, M. and Schwartz , F.W. (2001). "Influence of Natural Heterogeneity on the Efficiency of Chemical Floods in Source Zones." *Ground Water*; 39 (5): 660-666.

Imhoff, P.T., Jaffe´, P.R., and Pinder, G. F. (1994). "An experimental study of complete dissolution of a non-aqueous phase liquid in saturated porous media." *Water Resour. Res*., 30 (2): 307–320.

ITRC. (2002). "Regulatory overview--DNAPL source reduction: Facing the challenge." Interstate Technology and Regulatory Cooperation Work Group (ITRC), Dense Non-aqueous Phase Liquids Team, Washington D.C. Apr 2002, 42 pp. http://www.itrcweb.org/user/DNAPL-2.pdf.

Jackson, S. (2004). *Comparative evaluation of permanganate and catalyzed hydrogen peroxide during in situ chemical oxidation of DNAPLs*. Master's thesis, Colorado School of Mines, Golden, CO. 132 pp.

Johnson, R.L. and Pankow, J.F. (1992). "Dissolution of dense chlorinated solvents into groundwater. 2. Source functions for pools of solvent." *Environ. Sci. & Technol*., 26 (5): 896-901.

Jury, W.A., Gardner, W.R., and Gardner, W.H. (1991). *Soil Physics, 5th ed.*. John Wiley & Sons, New York, NY, 328 pp.

Kueper, B.H., Wealthall, G.P., Smith, J.W.N., Leharne, S.A., and Lerner, D.N. (2003). *An illustrated handbook of DNAPL transport and fate in the subsurface*.

Environment Agency R&D Publication 133, Environmental Agency, Almondsbury, Bristol, U.K. 67 pp.

Lee, E.S., Seol, Y., Fang, Y.C., and Schwartz, F.W. (2003). "Destruction efficiencies and dynamics of reaction fronts associated with the permanganate oxidation of trichloroethylene." *Environ. Sci. Technol*., 37 (11): 2540-2546.

Lee, K.Y. and Chrysikopoulos, C.V. (1998). "NAPL pool dissolution in stratified and anisotropic porous formations." *J. Environ. Eng*., 124 (9): 851-862.

Lenhard, R.J., Oostrom, M., and White, M.D. (1995). "Modeling fluid flow and transport in variably saturated porous media with the STOMP simulator. 2. Verification and validation exercises." *Adv. Water Resour*., 18 (6): 365-373.

Li, X.D. and Schwartz, F.W. (2000). Efficiency problems related to permanganate oxidation schemes. In: Wickramanayake, G.B., Gavaskar, A.R., Chen, A.S.C. (Eds), *Chemical Oxidation and Reactive Barriers*. Battelle Press, Columbus, OH, pp. 41-48.

Liu, C. and Ball, W.P. (2002). "Back Diffusion of Chlorinated Solvent Contaminants from a Natural Aquitard to a Remediated Aquifer Under Well-Controlled Field Conditions: Predictions and Measurements." *Ground Water*, 40 (2): 175-184.

Lowe, K.S., Gardner, F.G., and Siegrist, R.L. (2002). "Field evaluation of in situ chemical oxidation through vertical well-to-well recirculation of NaMnO4." *Ground Water Monit. Rem.*, 22 (1): 106-115.

Mackay, D.M. and Cherry, J.A. (1989). "Groundwater contamination: Pump-and-treat remediation." *Environ. Sci. & Technol*., 23 (6): 630-636.

Mackay, D.M., Freyberg, D.L., Roberts, P.V., and Cherry, J.A. (1986). A natural gradient experiment on solute transport in a sand aquifer: 1. Approach and overview of plume movement. *Water Resour. Res.*, 22 (13): 2017-2029.

MacKinnon, L.L. and Thomson, N.R. (2002). "Laboratory-scale in situ chemical oxidation of a perchloroethylene pool using permanganate." *J. Contam. Hydrol*., 56 (1-2): 49-74.

Marvin, B.K., Chambers, J., Leavitt, A., and Schreier, C.G. (2002). "Chemical and engineering challenges to in situ permanganate remediation." *Proc., 3rd Int. Conf. on Remediation of Chlorinated and Recalcitrant Compounds*, Monterey CA, May 2002. Battelle Press, Columbus, OH. 2C-04 (8pp.).

McDonald, M.G., and Harbaugh, A.W. (1988). A modular three-dimensional finite-difference ground-water flow model: U.S. Geological Survey Techniques of Water-Resources Investigations, book 6, chap. A1, 586 pp.

Miller, C.T., Poirier-McNeill, M.M., and Mayer, A.S. (1990). "Dissolution of trapped non-aqueous phase liquids: mass transfer characteristics." *Water Resour. Res.*, 26 (11): 2783-2793.

Millington, R.J. and Quirk, J.P. (1959). "Permeability of porous media." *Nature*, 183: 387-388.

Millington, R.J. and Quirk, J.P. (1961). "Permeability of porous solids." *Trans. Faraday Society*, 57: 1200-1207.

Mumford, K.G., Thomson, N.R., and Allen-King, R.M. (2002). "Investigating the kinetic nature of natural oxidant demand." In: Gavaskar, A.R. and Chen, A.S.,C (Eds), *Remediation of Chlorinated and Recalcitrant Compounds*. Battelle Press, Columbus, OH. 2C-37 (6 pp.).

Mumford, K.G., Thomson, N.R., and Allen-King, R.M. (2005). Bench-scale investigation of permanganate natural oxidant demand kinetics. *Environ. Sci. Technol.*, 39 (8): 2835-2840.

Nambi, I.M. (1999). *Dissolution of non-aqueous phase liquids in heterogeneous subsurface systems*. Ph.D. dissertation, Dep. of Civ. and Environ. Eng., Clarkson Univ., Potsdam, NY.

Nambi, I.M. and Powers, S.E. (2003). "Mass transfer correlations for non-aqueous phase liquid dissolution from regions with high initial saturations." *Water Resour. Res.*, 39 (2): 1030, doi:10.1029/2001WR000667.

Nelson, M.D., Parker, B.L., Al, T.A., Cherry, J.A., and Loomer, D. (2001). "Geochemical Reactions Resulting from In Situ Oxidation of PCE-DNAPL by KMnO4 in a Sandy Aquifer." *Environ. Sci. Technol.*, 35 (6): 1266-1275.

Nelson, M.D., Parker, B.L., and Cherry, J.A. (2000). "Passive destruction of PCE DNAPL by potassium permanganate in a sandy aquifer." In: Wickramanayake, G.B., Gavaskar, A.R., Chen, A.S.C. (Eds), *Chemical Oxidation and Reactive Barriers.* Battelle Press, Columbus, OH. pp. 135-143.

Pankow, J.F. and Cherry, J.A. (Eds). (1996). Dense Chlorinated Solvents and Other DNAPLs in Groundwater: History, Behavior, and Remediation. Waterloo Press, Portland, OR, 525 pp.

Powers, S.E., Abriola, L.M., and Weber Jr., W.J. (1994b). "An experimental investigation of non-aqueous phase liquid dissolution in saturated subsurfacesystems: Transient mass transfer rate." *Water Resour. Res.*, 30 (2): 321-332.

Powers, S.E., Abriola, L.M., Dunkin, J.S., and Weber, W.J. Jr. (1994a). "Phenomenological models for transient NAPL-water mass-transfer processes." *J. Contam. Hydrol.*, 16 (1): 1-33.

Pruess, K., Oldenburg, C., and Moridis, G. (1999). *TOUGH2 User's Guide, Version 2.0*, Lawrence Berkeley National Laboratory Report LBNL-43134, Berkeley, CA, November 1999.

Refsgaard, J.C. and Knudsen, J. (1996). Operational validation and intercomparison of different types of hydrological models. *Water Resour. Res.*, 32 (7): 2189-2202.

Refsgaard, J.C. and Henriksen, H.J. (2004). Modelling guidelines—terminology and guiding principles. *Adv. Water Resour.*, 27 (1): 71-82.

Reis, J.C. and Acock, A.M. (1994). "Permeability reduction models for the precipitation of inorganic solids in Berea sandstone." *In Situ*, 18 (3): 347-368.

Reitsma, S. and Dai, Q.L. (2001). Reaction-enhanced mass transfer and transport from non-aqueous phase liquid source zones. *J. Contam. Hydrol.*, 49: 49-66.

Reitsma, S. and Randhawa, J. (2002). "Experimental investigation of manganese dioxide plugging in porous media." In: Gavaskar, A.R. and Chen, A.S.C. (Eds), *Proc., 3rd Int. Conf. on Remediation of Chlorinated and Recalcitrant Compounds*, Monterey CA, May 2002. Battelle Press, Columbus, OH. 2C-39 (8pp.).

Rivett, M.O. and Allen-King, R.M. (2003). A controlled field experiment on groundwater contamination by a multicomponent DNAPL: dissolved-plume retardation. *J. Contam. Hydrol.*, 66 (1-2): 117-146.

Saba, T.A. (1999). *Upscaling of mass transfer from entrapped NAPLs under natural and enhanced conditions.* Ph.D. Dissertation, University of Colorado, Boulder CO. 204 pp.

Saba, T.A. and Illangasekare, T.H. (2000). "Effect of ground-water flow dimensionality on mass transfer from entrapped non-aqueous phase liquid contaminants." *Water Resour. Res.*, 36 (4): 971-979.

Saba, T.A., Illangasekare, T.H., and Ewing, J.E. (2001). "Investigation of surfactant-enhanced dissolution of entrapped non-aqueous phase liquid chemicals in a two dimensional groundwater flow field." *J. Contam. Hydrol.*, 51: 63-82.

Saenton, S. (2003). *Prediction of mass flux from DNAPL source zone with complex entrapment architectur: model development, experimental validation, and up-scaling*. Ph.D. Dissertation, Colorado School of Mines, Golden CO. 246 pp.

Schnarr, M., Truax, C., Farquhar, G., Hood, E., Gonully, T., and Stickney, B. (1998). "Laboratory and controlled field experimentation using potassium permangante to remediate trichloroethylene and perchloroethylene DNAPLs in porous media." *J. Contam. Hydrol.*, 29 (3): 205-224.

Schroth, M.H, Oostrom, M., Wietsma, T.W., and Istok, J.D. (2001). "In situ oxidation of trichloroethene by permanganate: effects on porous medium hydraulic properties." *J. Contam. Hydrol.*, 50 (1-2): 79-98.

Seitz, S. (2004). *Experimental evaluation of mass transfer and matrix interactions during in situ chemical oxidation relying on diffusive transport*. MS Thesis, Colorado School of Mines, Golden, CO, 125 pp.

Selim, H.M. and Mansell, R.S. (1976). Analytical solutions of the equation for transport of reactive solutes through soils. *Water Resour. Res.*, 12 (3): 528-532.

Seol, Y., Zhang, H., and Schwartz, F.W. (2003). "A review of in situ chemical oxidation and heterogeneity." *Environ. & Eng. Geosci.*; 9 (1): 37-49.

Sherwood, T.K., Pigford, R.L., and Wilke, C.R. (1975). *Mass Transfer*. McGraw-Hill, New York, NY. 677 pp.

Siegrist, R.L. and Lowe, K.S.; eds. (1996). "In situ remediation of DNAPL compounds in low permeability media: Fate/transport, in situ control technologies, and risk reduction," *Oak Ridge National Laboratory Rep. No. ORNL/TM-13305* for the DOE Office of Science and Technology.

Siegrist, R.L., Lowe, K.S., Murdoch, L.C., Case, T.L., and Pickering, D.A. (1999). "In situ oxidation by fracture emplaced reactive solids." *J. Environ. Eng.*, 125 (5): 429-440.

Siegrist, R.L., Urynowicz, M.A., Crimi, M.L., and Lowe, K.S. (2002). "Genesis and effects of particles produced during in situ chemical oxidation using permanganate." *J. Environ. Eng.*, 128 (11): 1068-1079.

122

Siegrist, R.L., Urynowicz, M.A., West, O.R., Crimi, M.L., and Lowe, K.S. (2001). *Principles and practices of in situ chemical oxidation using permanganate*. Battelle Press, Columbus, OH, 348 pp.

Stewart, R. (1965). "Oxidation by permanganate." In: Wiberg, K.B. (Ed.), *Oxidation in Organic Chemistry*, Part A, Chap. 1. Academic Press, New York, NY. pp. 1-68.

Stroo, H.F., Unger, M., Ward, C.H., Kavanaugh, M.C., Vogel, C., Leeson, A., Marqusee, J.A., and Smith, B.P. (2003). "Remediating chlorinated solvent source zones." *Environ. Sci. Technol.*, 37 (11): 224A-230A.

Struse, A.M., Siegrist, R.L., Dawson, H.E., and Urynowicz, M.A. (2002). "Diffusive transport of permanganate during in situ oxidation." *J. Environ. Eng.*, 128(4): 327-334.

Tidwell, V.C., Meigs, L.C., Christian-Frear, T., and Boney, C.M. (2000). "Effects of spatially heterogeneous porosity on matrix diffusion as investigated by X-ray absorption imaging." *J. Contam. Hydrol.*, 42 (2): 285-302.

Urynowicz, M.A. (2000). *Dense non-aqueous phase trichloroethene degradation with permanganate ion*. Ph.D. Dissertation, Colorado School of Mines, Golden CO. 166 pp.

USEPA. (1993). *Evaluation of the likelihood of DNAPL presence at NPL sites*. U.S. EPA Rep. No. EPA/540/R-93/073, Office of Solid Waste and Emergency Response, Washington D.C. 114 pp., http://www.epa.gov/superfund/resources/remedy/pdf/540r-93073-s.pdf.

USEPA. (2003). *The DNAPL remediation challenge: Is there a case for source depletion?*. U.S. EPA Rep. No. EPA/600/R-03/143, Office of Research and Development, Washington D.C., 129 pp., http://www.epa.gov/ada/download/reports/600R03143/600R03143-fm.pdf.

USEPA. (2004a). *Contaminant focus-trichloroethylene*. U.S. EPA, Technology Innovation Program, Washington D.C. http://www.clu-in.org/contaminantfocus/default.focus/sec/Trichloroethylene_(TCE)/cat/Overview/.

USEPA. (2004b). *Discussion paper--Cleanup goals appropriate for DNAPL source zones*. U.S. EPA, Office of Solid Waste and Emergency Response, Washington D.C., 16 pp., http://gwtf.cluin.org/docs/options/dnapl_goals_paper.pdf.

USHHS. (2002). *Report on Carcinogens, Tenth Edition*. U.S. Department of Health and Human Services, Public Health Service, National Toxicology Program, December 2002. http://ehp.niehs.nih.gov/roc/toc10.html.

van Genuchten, M.T. and Alves, W.J. (1982), *Analytical solutions of the one-dimensional convective-dispersive solute t.ransport equation.* U.S. Department of Agriculture Technical Bulletin 1661. 151 pp.

Van Waveren, R.H., Groot, S., Scholten, H., Van Geer, F.C. Wosten, J.H.M., Koeze, R.D., Noort, J.J. (1999). *Good Modeling Practice Handbook*. STOWA Report 99-05, Utrecht, RWS-RIZA, Lelystad, The Netherlands. http://www.info.wau.nl/research%20projects/pub-pdf/gmp.pdf.

Vella, P.A. and Veronda, B. (1994). "Oxidation of trichloroethylene: A comparison of potassium permanganate and Fenton's Reagent." In: Proc., 3rd Intl. Symposium, *Chemical Oxidation: Technologies for the Nineties, Vol 3*. Vanderbilt University, Nashville, TN, Feb 1993. Technomic Publishing, Lancaster, PA. pp. 62-73.

Welty, J.R., Wicks, C.E., and Wilson, R.E. (1976). *Fundamentals of momentum, heat, and mass transfer, 2nd ed..* John Wiley & Sons, New York, NY. 789 pp.

Wexler, E. (1992). "Analytical solutions for one-, two-, and thre-dimensional solute transport in ground-water systems with uniform flow." In: *U.S. Geological Survey Techniques of Water-Resources Investigations*, vol. 3, chap. B7.. U.S. Geological Survey, Denver CO., 198 pp.

White, M.D., Oostrom, M., and Lenhard, R.J. (1995). "Modeling fluid flow and transport in variably saturated porous media with the STOMP simulator. 1. Nonvolatile three-phase model description." *Adv. Water Resour.*, 18 (6): *353-364*.

Wilking, B. (2004) *Factors controlling matrix storage during DNAPL mass depletion in heterogeneous porous media*. Master's thesis, Colorado School of Mines, Golden, CO. 183 pp.

Wyllie, M.R.J. (1962). "Relative permeability." In: *Petroleum Production Handbook, Reservoir Engineering, Vol II*, Frick, T.C. (Ed). McGraw-Hill, New York, NY.

Yan, E.Y. and Schwartz, F.W. (1999). "Oxidative degradation and kinetics of chlorinated ethylenes by potassium permanganate." *J. Contam. Hydrol.*, 37 (3): 343-365.

Yan, E.Y. and Schwartz, F.W. (2000). "Kinetics and mechanisms for TCE oxidation by permanganate." *Environ. Sci. Technol.*, 34 (12): 2535-2541.

Zhang, H. and Schwartz, F.W. (2000). "Simulating the in situ oxidative treatment of chlorinated ethylenes by potassium permanganate." *Water Resour. Res.*, 36 (10): 3031-3042.

Zheng, C. and Wang, P.P. (1999). *MT3DMS: A modular three-dimensional multispecies transport model for simulation of advection, dispersion, and chemical reactions of contaminants in groundwater systems; documentation and user's guide*. Contract Report SERDP-99-1, U.S. Army Engineer Research and Development Center, Vicksburg, MS.

Chapter 4

EXPERIMENTAL INVESTIGATION OF IN SITU CHEMICAL OXIDATION OF COMPLEX DNAPL SOURCE ZONES BY PERMANGANATE

4.1   Abstract

One application of in situ chemical oxidation can be to speed up remediation of a contaminant source zone, consisting of one or more DNAPL sources, by inducing increased mass transfer from the DNAPL sources into the aqueous phase for subsequent destruction.   Individual sources may be present as an interconnected pool of high saturation, as a region of disconnected ganglia at residual saturation, or something in between.

A byproduct of oxidation of contaminant and/or oxidizable aquifer materials using permanganate is the production of manganese oxide ($MnO_2(s)$) solids. Research has shown that these manganese oxide solids may result in permeability reductions in the bulk source zone reducing the ability for oxidant to be transported to individual sources. It can also occur at the DNAPL-water interface, decreasing contact of the oxidant with the DNAPL source. Additionally, it can occur at or within the filter pack or well screen of injection or extraction wells further challenging oxidant delivery.   Permeability reduction is not solely a byproduct of ISCO using permanganate. It can occur with other remedial technologies as well (e.g., bio-fouling from growth of microbiological organisms during bioremediation).   Additionally, $MnO_2(s)$ formation at the DNAPL-water interface, and/or flow bypassing as a result of permeability reductions around the source, may alter the mass transfer rate from the DNAPL into the aqueous phase, diminishing the magnitude of any mass depletion increase induced by oxidation.

A 2D tank experiment was performed, enabling spatial monitoring of permeability changes and relating them to $MnO_2(s)$ distribution measured through post-oxidation soil coring. Additionally, spatial and temporal sampling of aqueous PCE, chloride, and permanganate concentrations was used to relate changes in mass flux from DNAPL residual and pool source zones to $MnO_2(s)$ formation.

For the 2D conditions of this experiment, using clean silica sands, $MnO_2(s)$ formation was found to reduce aqueous permeability in and around DNAPL source zones resulting in changes to the flow pattern, with source zone configuration and soil property contrasts partly determining the effects. A pool with little or no residual around it, in a relatively homogeneous flow field, appeared to benefit from resulting $MnO_2(s)$ pore-blocking that substantially reduced mass transfer from the pool with relatively little mass removed from the pool. On the other hand, a pool with residual around it (in a more complex heterogeneous flow field) appeared to undergo increased mass transfer as $MnO_2(s)$ reduced permeability, complicating flow, and increasing mixing at the DNAPL-water interface. Further, the magnitude of increased PCE mass depletion during oxidation appeared to depend on the PCE configuration (pool versus ganglia) and decreased as $MnO_2(s)$ was formed and deposited at the DNAPL-water interface. Overall, the oxidation of PCE mass appeared to be rate-limited by the mass transfer from the DNAPL to aqueous phase.

It was found that modeling and predicting the effects of $MnO_2(s)$ formation on permeability is possible, using a relatively simple power law model relating the change in porosity resulting from $MnO_2(s)$ formation to changing permeability. Further, it was found that $MnO_2(s)$ levels had to exceed a threshold level before they began to affect permeability. This threshold was determined to be 0.1g $MnO_2(s)$/kg soil for the conditions of this experiment. It is likely that the effective $MnO_2(s)$ density as well as the threshold will vary depending on system conditions. Higher flow rates, smaller pore sizes, or less uniform soil particle sizes are expected to impact the values of these parameters for a particular system.

4.2   Introduction

Chlorinated solvents such as trichloroethylene (TCE) and tetrachloroethylene (PCE) are contaminants of concern in groundwater at many contaminated sites, ranking 16th and 30th respectively on the 2003 CERCLA Priority List of Hazardous Substances (ATSDR 2003). These chemicals have been used extensively since the early 20th century as cleaning solvents and as intermediate chemicals in production of pesticides, paints, refrigerants, and other chemicals (ATSDR 2004, USEPA 2004a, USHHS 2002). As contaminants, they are frequently present in the form of dense non-aqueous phase liquid (DNAPL) primary source zones, or as dissolved and/or sorbed contaminant in low permeability media (LPM) secondary source regions (Johnson and Pankow 1992, Pankow and Cherry 1996, USEPA 1993, USEPA 2004b). Although they typically have solubilities in the parts-per-million range, the drinking water maximum contaminant levels (MCLs) are typically in the parts-per-billion range.

DNAPLs present a challenging source zone because of the complex nature of their movement through the subsurface, as Kueper et al. (1993) demonstrated in a field experiment at the Borden site. When initially released into the environment, DNAPLs sink below the water table, spreading laterally upon contact with finer grained layers (Illangasekare et al. 1995a, Illangasekare et al. 1995b, Kueper et al. 1989, Pinder and Abriola 1986). Lateral spreading results from the finer grained layer forming a capillary barrier with a higher entry pressure. In addition to this lateral spreading on top of finer grained layers, some DNAPL may enter the finer grained material as a result of fingering due to pore-scale heterogeneities at the interface of the two layers (Held and Illangasekare 1995, Kueper and Frind 1991a, Kueper and Frind 1991b, Poulson and Kueper 1992). As the main body of DNAPL migrates, residual DNAPL is left behind as disconnected blobs and ganglia partially filling the pore space. On the other hand, the presence of coarser grained lenses, especially when overlying LPM lenses, can act as a trap of sorts, resulting in high DNAPL saturations or pooling (Illangasekare et al. 1995b).

A number of remediation technologies are available for reducing the mass of DNAPL present in a primary source zone, such as pump-and-treat, surfactant/co-solvent flushing, and ISCO. However, subsurface heterogeneities and imprecise knowledge of source locations frequently challenge these technologies (Freeze and McWhorter 1997, ITRC 2002, Marvin et al. 2002, Siegrist and Lowe 1996, USEPA 2003). Even in a relatively homogeneous soil, micro-scale heterogeneities typically exist, resulting in large zones of residual saturation (Dekker and Abriola 2000a, USEPA 2004). Parker et al. (2003) demonstrated the difficulty in locating DNAPL source zones when they carried out extensive soil coring and water sampling at five typical sites with DNAPL contaminated sandy aquifers where initial contamination occurred decades ago. The thin layers of DNAPL were only reliably identifiable by taking continuous soil cores, sub-sampling them on small (5 cm or less) vertical intervals, and applying a hydrophobic red dye (Sudan IV) to the cores which gave a visual indicator that DNAPL was present.

Chemical oxidation, specifically with permanganate, has been used to treat water and waste water for over 50 years. In the last fifteen years or so, chemical oxidation has become a promising in situ remediation technique for sites whose groundwater and soil are contaminated by chlorinated solvents. Field-scale pilot tests have shown encouraging results for sites contaminated with low levels of chlorinated solvents (Cline et al. 1997, Hood 2000, Lowe et al. 2002, Schnarr et al. 1998, Siegrist et al. 1999).

Laboratory research has provided an understanding of many fundamental details of the technology. The reaction pathways and kinetics of permanganate oxidation of alkenyl halides, specifically chlorinated ethenes, such as PCE and TCE have been elucidated (Huang et al. 1999, Huang et al. 2001, Huang et al. 2002, Schnarr et al. 1998, Yan and Schwartz 1999, Yan and Schwartz 2000). For example, in the oxidation of PCE by permanganate (in the pH range 3.5 – 12), the following half-cell reactions apply:

$$4MnO_4^- + 16H^+ + 12e^- \rightarrow 4MnO_{2\ (s)} + 8H_2O \qquad (4.1)$$

$$3C_2Cl_4 + 12H_2O \rightarrow 6CO_2 + 24H^+ + 12Cl^- + 12e^- \qquad (4.2)$$
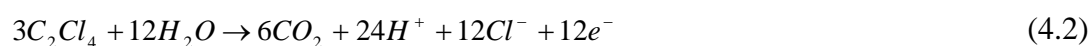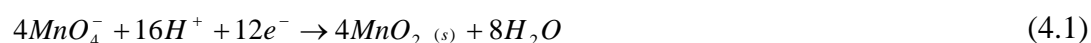
which when combined, produce the following overall stoichiometric reaction
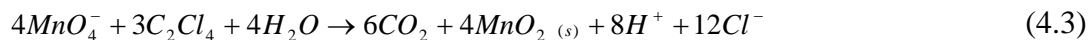
$$4MnO_4^- + 3C_2Cl_4 + 4H_2O \rightarrow 6CO_2 + 4MnO_{2\ (s)} + 8H^+ + 12Cl^- \qquad (4.3)$$

This reaction has been shown to represent the oxidation of PCE by permanganate over the pH range of 3.5-10 expected to be found in the subsurface (Huang et al. 2002, Siegrist et al. 2001, Yan and Schwartz 1999). The oxidation of PCE by permanganate has been found to be first-order with respect to both PCE and permanganate, making the reaction second-order overall (Hood et al. 2000, Huang et al. 2002, Zhang and Schwartz 2000) with a reaction rate (k_2) ranging from 0.035 – 0.045 L/mol-sec at 20°C. The rate law describing the irreversible oxidation of PCE by permanganate is

$$\frac{d[PCE]}{dt} = -k_2[PCE][MnO_4^-] \qquad (4.4)$$

where $d[PCE]/dt$ is rate of change in PCE concentration per unit time (T^{-1}), $[PCE]$ is the concentration of PCE (ML^{-3}), $[MnO_4^-]$ is the concentration of permanganate (ML^{-3}), and k_2 is the second-order reaction rate ($L^3M^{-1}T^{-1}$).

Researchers have also studied the impacts of water chemistry and porous media constituents on the reaction (Gates-Anderson et al. 2001, Glaze and Kang 1988, Li and Schwartz 2000, Urynowicz 2000, Vella and Veronda 1994). Whether contaminant is present or not, field soils and aquifer sediments typically contain natural organic matter (NOM) and other reductants that can be readily oxidized. These soil constituents are referred to collectively as natural oxidant demand (NOD), or sometimes soil oxidant demand (SOD), and compete with target contaminants for available oxidant. Because NOD is generally a complex mixture of components whose surface area available for oxidant contact varies, its oxidation will be a kinetic process. While the kinetic rates for some NOD constituents of a particular soil are often higher than that of the target contaminant, preliminary results related to this research, and that of others, suggests NOD frequently consists of at least two components with markedly different oxidation rates (Crimi and Siegrist 2004, Jackson 2004, Mumford et al. 2005). Further, the amount of NOD present and the kinetic rate for its oxidation can vary widely for different soils.

One goal of ISCO is to speed up remediation of a contaminant source zone by inducing increased mass transfer (and subsequent destruction) from a DNAPL source. Based on experimental results, Schnarr et al. (1998) suggest that DNAPL dissolution and oxidation are processes that occur in parallel with increased mass transfer during oxidation occurring primarily as a result of an increased aqueous concentration gradient. Subsequently, Reitsma and Dai (2001) performed a theoretical study to estimate the maximum expected DNAPL mass transfer enhancement resulting from chemical oxidation. They estimated a maximum five times increase in dispersive mass transport from a PCE DNAPL pool resulting from the increased concentration gradient; however, they predict little enhancement in local-scale mass transfer from DNAPL to aqueous phase suggesting no change in dissolution mass transfer parameters. Further, they suggest that actual enhancement is likely to be less because permeability reduction and decreased interfacial contact area were not accounted for in the estimate. On the contrary, MacKinnon and Thomson (2002) calculated a ten times initial increase in PCE mass transfer from a DNAPL pool during a 2D oxidation experiment, with decreasing mass flux over time attributed to $MnO_2(s)$ formation.

Mass transfer or dissolution of the DNAPL into the aqueous phase is generally defined using the well-known stagnant film model (Sherwood et al. 1975) utilizing a first-order linear driving force

$$\frac{dC_{NAPL}}{dt} = -\frac{D_m A_{NW}}{\delta V}(c_\infty - c^*) \tag{4.5}$$

where dC_{NAPL}/dt is the rate of change of aqueous concentration per time ($ML^{-3}T^{-1}$), c_∞ is the aqueous solute concentration (ML^{-3}) of the bulk solution, c^* is the aqueous solubility limit of the solute (ML^{-3}), D_m is the molecular diffusion coefficient of the contaminant (L^2T^{-1}), A_{NW} is the DNAPL-water interfacial area (L^2), δ is the thickness of the stagnant film (L), and V is the porous media volume of interest (L^3). The stagnant film model originates from Fick's First Law of Diffusion which states the mass flux of a substance diffusing across a given surface area per unit time is proportional to the concentration

gradient at the surface; however, the molecular diffusion coefficient is divided by the stagnant film thickness which is assumed very thin such that the concentration gradient is linear. Because the complex architecture of DNAPL sources makes A_{nw} too difficult to estimate, and the stagnant film thickness is a theoretical construct that can not be measured, the lumped mass transfer coefficient, k_{La} (T^{-1}) is usually used to replace $\frac{D_m A_{nw}}{\delta V}$ so there is a single parameter to estimate. Oxidation using permanganate will certainly increase mass transfer from the DNAPL to the aqueous phase (for subsequent oxidation) by increasing the concentration gradient. However, it may also alter the lumped mass transfer coefficient. For example, it may increase the lumped mass transfer coefficient due to the chemical reaction (Cussler 1997). Alternately, generation of manganese oxides at the DNAPL-water interface may reduce the interfacial area, thereby reducing the lumped mass transfer coefficient (Urynowicz 2000).

Additionally, generation of these manganese oxide solids may result in permeability reductions at several key regions of the subsurface as shown in Figure 4.1. It can occur in the bulk source zone changing the flow field and reducing the ability for oxidant to be transported to individual sources. It can also occur at the DNAPL-water interface, decreasing contact of the oxidant with the DNAPL source. Additionally, it can occur at or within the filter pack or well screen of injection or extraction wells further challenging oxidant delivery. In addition to deposition in different regions, it may be deposited by two different processes. First, the $MnO_2(s)$ may form as a coating on soil surfaces or DNAPL-water interfaces. As a coating on soil surfaces, permeability reductions will result from decreased pore diameters. Alternately, it may form as suspended particles that flocculate together until the aggregate particle becomes too large and blocks the pore throat. It should be pointed out that permeability reduction is not solely a byproduct of ISCO using permanganate. It can occur with other remedial technologies as well (e.g., bio-fouling from growth of microbiological organisms during bioremediation).
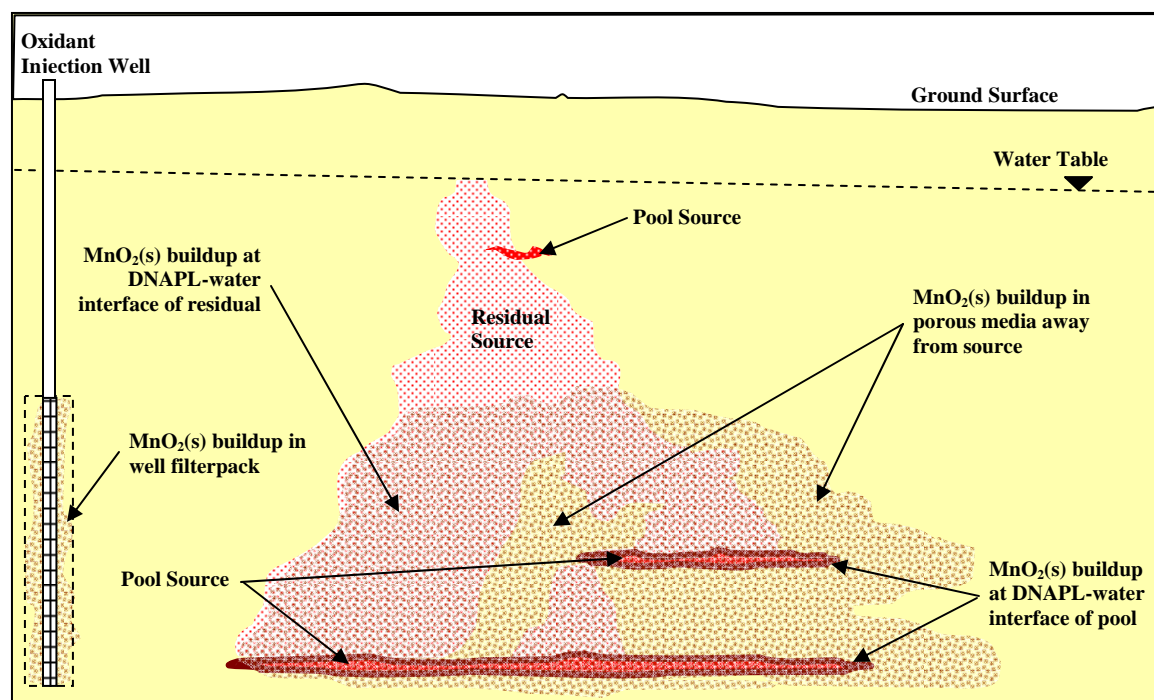
Figure 4.1: Regions of Potential Permeability Reduction

Several researchers have investigated permeability effects resulting from DNAPL oxidation using permanganate. Schroth et al. (2001) performed 1D column experiments to study the effects of $MnO_2(s)$ formation on permeability. Residual DNAPL TCE was emplaced in the first 65cm of the 95cm column length and the column was flushed with 790 mg/L $KMnO_4$ at a Darcy velocity of 15.8 m/day. They saw a permeability reduction of 96% in 24 hours, but did not measure $MnO_2(s)$ deposition. Similarly, MacKinnon and Thomson (2002) performed a 2D experiment, flushing the 2.5m long by 0.45m high tank with $KMnO_4$ (10,000mg/L) at approximately 8.4cm/day Darcy velocity for 146 days. They estimated an 80% reduction in permeability based on tank inlet and outlet water head, attributed to $MnO_2(s)$ deposition in and along the pool, as well as in the effluent endwell screen. Analysis of soil cores showed a 3cm layer above the PCE pool with about 20g $MnO_2(s)$/kg soil and one location (coinciding with a PCE injection point) with

70g $MnO_2(s)$/kg soil through the bottom 19cm of the tank. Lee et al. (2003) performed a 3D experiment oxidizing a residual TCE DNAPL source with 1660mg/L $KMnO_4$ at a Darcy velocity of 9.4cm/day for 63 days. By the end of the experiment, they visually estimated the rate of oxidation advancement had reduced by 83% from $MnO_2(s)$ formation (1-2g $MnO_2(s)$/kg soil); however, permeability reduction was not directly measured.

These experiments, as well as more qualitative ones like the 1D column studies by Siegrist et al. (2002) and 2D tank studies by Conrad et al. (2002), show that $MnO_2(s)$ formation and deposition undoubtedly leads to permeability reductions. However, more quantitative information is needed in order to relate $MnO_2(s)$ formation to permeability reduction in a manner that can be used to better understand and implement ISCO using permanganate. The goal of this research is to fill this need by performing a 2D tank experiment, spatially monitoring permeability changes and relating them to $MnO_2(s)$ distribution measured through post-oxidation soil coring. Another goal was to relate changes in mass flux from DNAPL residual and pool source zones to $MnO_2(s)$ formation.

4.3   Experimental Design

A preliminary set of intermediate-scale experiments were conducted as summarized in Appendix C. The first experiment involved dissolution of a small PCE DNAPL residual zone overlying a pool. The second experiment duplicated the DNAPL source configuration, but added an LPM layer beneath the source to look at diffusion of aqueous PCE into the LPM. The third experiment involved flushing the experiment two tank with permanganate after residual PCE DNAPL was depleted. Preliminary experiments utilized a single rectangular PCE DNAPL source. The purpose of these experiments was to examine interaction of PCE dissolution, aqueous PCE diffusion, permanganate diffusion, and oxidation by systematically adding each process to an otherwise duplicated system. These experiments served to refine tank assembly and sampling protocols, as well as pointing out the value of using a larger, complex,

constructed source zone for this research. They also demonstrated the need to have tapered ends on the sources to prevent abrupt hydraulic conductivity changes resulting in significant vertical flow. A final experiment was then completed as described below.

The experimental design for this research involved assembling a 2D intermediate-scale tank containing a PCE DNAPL source zone within a homogenous flow field. A constant flow was maintained through the tank, and a period of natural dissolution was followed by flushing the tank with potassium permanganate to oxidize the PCE DNAPL source zone containing six sources. A post-oxidation dissolution period followed the oxidant flush. Aqueous samples were collected regularly during each phase from throughout the tank to monitor the effects of oxidation on DNAPL mass depletion. Water head was monitored around each source as well as throughout the tank to determine permeability changes resulting from oxidation. Upon completion of the experiment, the soil cores were obtained from the sources and from throughout the tank to determine the distribution of manganese oxides and remaining mass of DNAPL PCE.

4.3.1 Materials

The experiment was conducted using clean white #8 and #70 silica sand obtained from Unimin Corporation. Additionally, bentonite clay (from Wyo-Ben, Inc.) was used as a confining layer at the top of the 2D tank. Table 4.1 lists the properties of the sands and bentonite. The saturated hydraulic conductivities, K_s, of the sands are approximate values, because the hydraulic conductivity can vary greatly depending on packing procedure. The parameters d_{50} and U are the median grain diameter and uniformity index, respectively. $S_{r,w}$ is the residual or irreducible saturation of water, ρ_B is the dry bulk density, and TOC is the total organic carbon. Natural oxidant demand (NOD) for the silica sands, measured by batch studies, was found by S. Jackson to be below detection levels (personal communication, Oct 2003). Typical chemical analysis data for the silica sands can be found in Appendix A.

Table 4.1: Properties of Porous Media Used in Experiment

Property	#8 sand[1]	#70 sand[2]	Clay[3]
Material	silica	silica	bentonite
K_s **(cm/min)**	101.3	1.458	n/a
d_{50} **(cm)**	0.125	0.019	0.0045
U **(-)**	1.56	1.86	n/a
$S_{r,w}$ **(-)**	0.11	0.30	n/a
pH	7.39	7.39	9.1
TOC[4] (g/kg dry soil)	0.019	0.019	n/a
ρ_B **(g/mL)**	1.6	1.6	0.83
Grain density (g/mL)	2.65	2.65	2.55

[1]Saenton et al. (2001), [2]Barth et al. (2001), Wyo-Ben (1999), [4]Seitz (2004)

Ordinary tap water was de-aired and used to provide water flow through the tank. See Table 4.2 for relevant tap water properties (a more detailed list of tap water properties can be found in Appendix A). Technical grade potassium permanganate (Carus Chemical) was the oxidant used. Analytical grade PCE (>99% purity) from Mallinckrodt Chemicals, colored with 50mg/L Sudan IV hydrophobic organic red dye (analytical grade, Aldrich Chemicals) was used as the DNAPL. See Table 4.3 for PCE properties.   Sodium bromide (analytical grade, Fisher Scientific) was used as a conservative tracer. Additional chemicals used for sample analysis included: hexane (HPLC grade, Mallinckrodt Chemicals), sodium bisulfite ($NaHSO_3$, certified ACS grade, Fisher Scientific), hydroxylamine hydrochloride ($NH_2OH \bullet OH$, reagent grade, J.T. Baker), nitric acid (HNO_3, 70%, Mallinckrodt Chemicals). All aqueous solutions, except oxidant and water flowing through tank, were prepared using DI water (>18.2MΩ-cm). Oxidant was mixed in tap water instead of DI water, so that background chloride levels in the tank remained constant during the oxidation flush and subsequent post-oxidation phase. If DI water was used during oxidation, the background chloride levels would vary spatially and temporally as flushing was changed from oxidant (in DI water) back to tap

water; this would make it difficult to account for background chloride levels when estimating PCE destruction based on chloride concentrations.

Table 4.2: Relevant Tap Water Properties

Property	Value
pH	7.41
Alkalinity (mg/L as CaCO$_3$)	35.2
TOC (mg/L)	1.14
Chloride (mg/L)	25.0
Total Dissolved Solids (mg/L)	185

Table 4.3: PCE Properties

Property	Value
Density (mg/mL)	1620.0
Solubility (mg/L)	200.0
Diffusion Coefficient (cm^2/s)	8.7×10^{-6}
Molecular Weight (g/mol)	165.83
2nd Order Oxidation Rate (L/mol-sec)[*]	4.5×10^{-2}

[*](Zhang and Schwartz, 2000)

4.3.2   2D Intermediate-Scale PCE Dissolution and Oxidation

An intermediate-scale 2D tank was constructed (L x W x H = 243.5cm x 8.0cm x 45.5cm) of clear acrylic, with 1.5mm diameter sampling ports (sealed with rubber septa) distributed throughout the tank.   The tank includes influent and effluent end wells (approximately 8.0cm x 8.0cm x 45.5cm) filled with clean pea gravel to promote mixing. The end wells are separated from the rest of the tank with 200 mesh stainless steel screen. Figure 4.2a shows a photo of the packed tank and Figure 4.2b shows a diagram labeling sources and sampling locations.
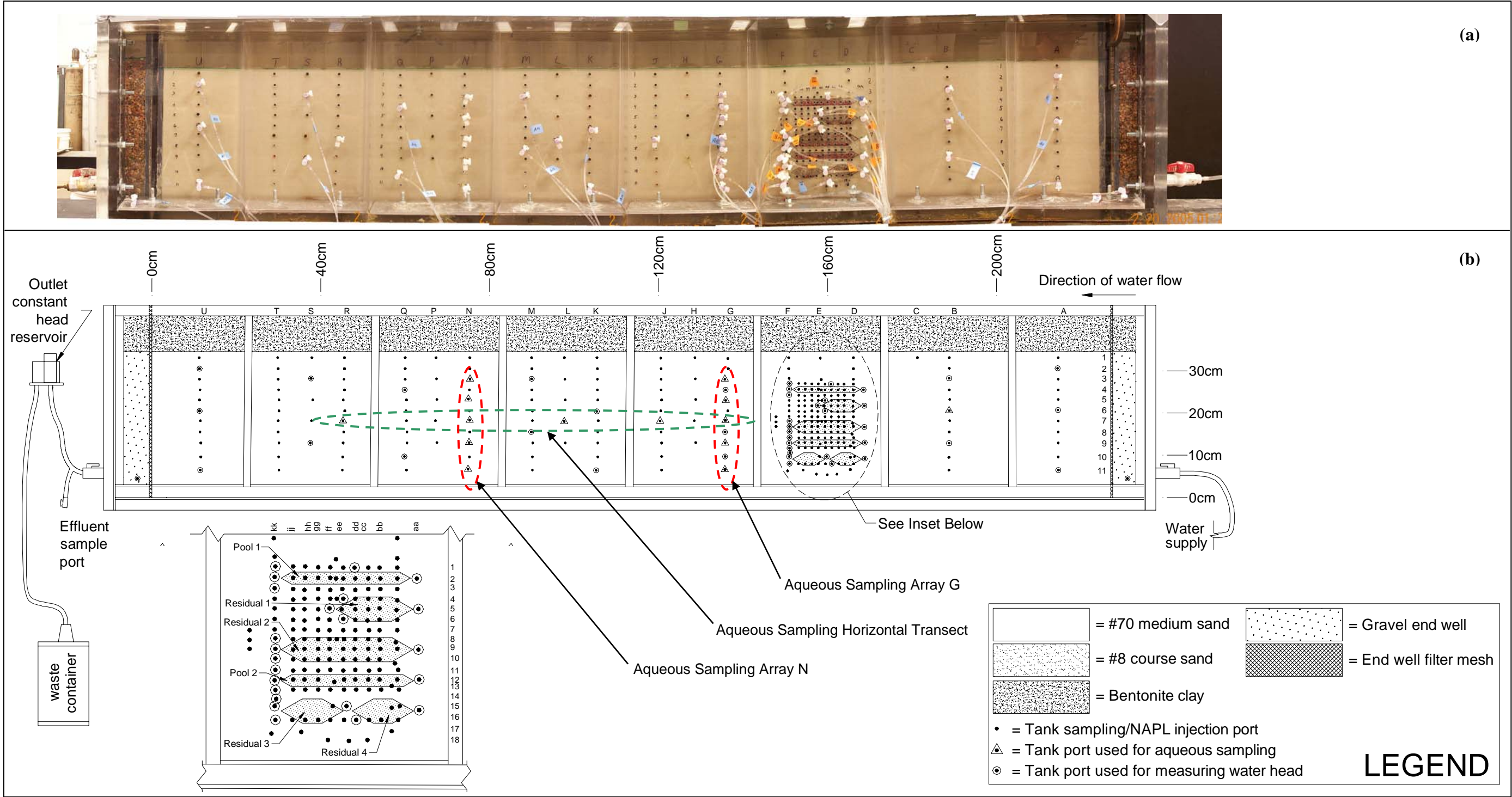
Figure 4.2: (a) Photo and (b) Diagram of 2D Experimental Tank

The tank was wet-packed by hand, to prevent air entrapment, with 91.7kg of clean #70 silica sand, to an approximate bulk density of 1510mg/mL and porosity of 0.41, except for the DNAPL source cells. Each source cell was wet-packed with clean #8 silica sand (1.7kg total) to an approximate bulk density of 1570mg/mL and porosity of 0.41 for each source. The fine-grained sand surrounding the coarse-grained source lens creates a capillary barrier to keep the PCE DNAPL within the well-defined source lens. Wet-packing was performed in 2cm lifts, keeping the water level approximately 2cm above the current sand level adding water, as needed, through the inlet. Each lift was placed, 25cm^3 at a time, progressing from one end of the tank to the other and back. Placement of each portion of sand was accomplished by slowly pouring the sand while briskly moving the container back and forth over roughly a 15cm distance. This back and forth movement maintained a slow and even sand deposition rate as the sand settled through the water layer. After placing each lift, it was tamped twice from above, moving from one end of the tank to the other using an acrylic bar (3mm x 45mm). During the first pass the 45mm side was parallel to the tank length, and during the second it was perpendicular to the tank length. Tamping helped settle the sand to ensure a uniform porosity and bulk density; it also ensured a uniform hydraulic conductivity. If a lift contained a source, the lift was completed, then the source lens excavated so the ends sloped 30° from horizontal. Coarse sand was emplaced, followed by gentle tamping, and the next lift emplaced. Packing the tank took approximately 40 hours, with another 40 hours to instrument the tank and setup ancillary equipment including pump and constant head device.

The source zone consisted of six different discrete sources—two configured as pools and four at near-residual saturation. The layout of the sources (Figure 4.3 and inset of Figure 4.2b) was chosen so that oxidation of DNAPL sources under a variety of conditions could be investigated. Specifically, pool 1 and residual 1 were expected to be mostly unaffected by each other or any other source. Residual 2 and pool 2 were expected to show the interaction of a residual source overlying a pool. Residuals 3 and 4 were

expected to show the interaction that occurs as oxidant passes through successive residual sources.

Ambient air temperature of the lab was $22 \pm 3°C$. A constant flow rate into the tank was provided by a MasterFlex 7523-20 digital pump drive and HV-7013-20 peristaltic pump head from Cole-Parmer. Before entering the tank, water passed through a 5gal holding tank, sediment and carbon filters, and a Degassit A6342 inline de-gassing unit from Varian, Inc. A constant head reservoir was connected to the outlet of the tank. The tank was flushed with water for five days before PCE emplacement, to ensure removal of fines or air bubbles that may have been trapped despite wet-packing. During this period, a dye tracer test was performed, injecting water with red food dye into the inlet to visually determine that the flow front of injected dye was uniform from the tank bottom to top, and that flow accessed all areas of the tank from inlet to outlet. The test verified there were no preferential flow paths or stagnant zones. Following the dye tracer test, no residual red dye was visible in the tank. However, if a small amount remained it was expected to have no impact on the subsequent oxidant injection based on batch studies by Dugan (personal communication, Jan 2005).

After five days, flow through the tank was interrupted for emplacement of the PCE sources. Emplacement was performed by slowly (<1mL/min) injecting PCE into each source using a glass syringe through injection ports at the bottom of each source. PCE was injected until it nearly filled the entire coarse-grained source cell without breaching the capillary barrier. Once source cells were all full, the process was reversed for the four residual zones, except that PCE was withdrawn even more slowly (<0.5mL/min) pausing for 5-10minutes every 5mL. A total of 87.9mL (143.3g) of PCE was emplaced. Table 4.4 describes each source and Figure 4.3 shows them after PCE emplacement. The ganglia-to-pool (GTP) ratio describes the architecture of the source. It is a ratio of the mass of DNAPL present at less than residual saturation to the mass present at residual or greater saturation (Lemke et al. 2004). This ratio was estimated visually because no method to directly measure the DNAPL distribution was available.

Table 0.1: Description of Source Zones

Source		PCE Vol (mL)	Avg Sat (S_n)	GTP Ratio	Initial PCE Mass (g)	Mass as Ganglia (g)
Name	Volume (cm^3)					
Pool 1	174.20	29.93	0.43	0.00	48.78	0.0
Pool 2	178.95	28.79	0.40	0.00	46.92	0.0
Residual 1	163.58	6.79	0.10	0.36	11.07	2.93
Residual 2	324.74	15.79	0.12	0.11	25.73	2.55
Residual 3	118.55	2.79	0.06	1.05	4.55	2.33
Residual 4	120.92	3.85	0.08	0.33	6.28	1.56
TOTAL	1080.94	87.94	-	-	143.33	9.37
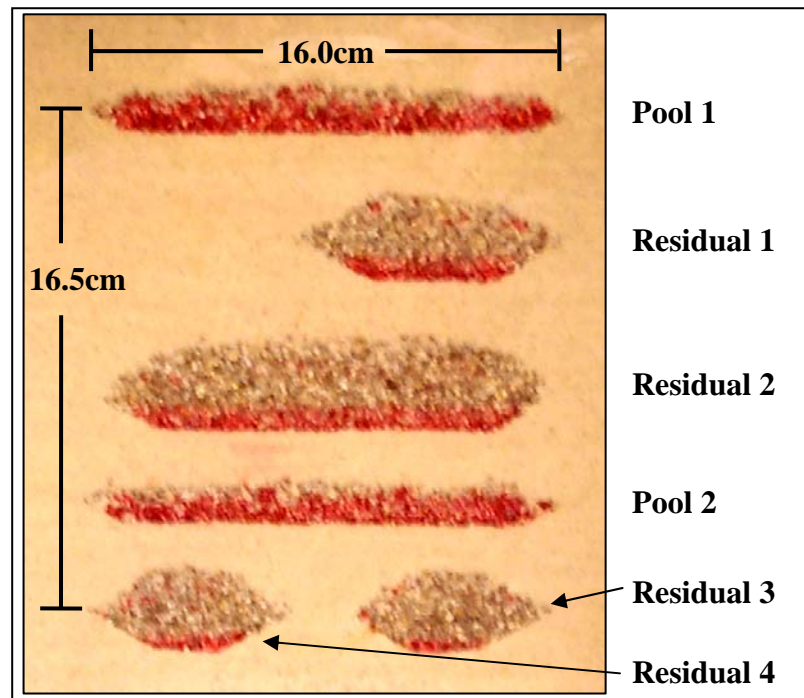
Figure 0.1: Sources with PCE

Once PCE emplacement was complete, flow was resumed through the tank, at a constant flow of 14.6mL/min providing a Darcy velocity of 77.14cm/day. This Darcy

velocity was chosen to represent the flow that might be expected near the center of a source zone, halfway between an injection and extraction well. For example, at the Navy Training Center in Orlando FL (discussed in Chapter 5), the ambient groundwater has a Darcy velocity of approximately 7.5cm/day. Under an injection/extraction scenario, the flow in the center of the treatment area could be expected to increase by an order of magnitude. On the other hand, the selected velocity could also represent ambient groundwater flow conditions in an aquifer with a moderately fast flow rate. At this flow rate it took about 29 hours for fluid to transit the tank. After resuming flow, the eight day natural dissolution phase of the experiment was underway. On the second day of the natural dissolution phase, a transient conservative tracer test using bromide was performed by changing the influent to a solution containing sodium bromide (200.0mg/L as Br^-) for one hour. During the natural dissolution phase, tank effluent was captured and then treated by granular activated carbon (GAC) to remove PCE.

After eight days of natural PCE dissolution, the oxidation phase began and the tank influent was changed to a solution of potassium permanganate (2120mg/L as MnO_4^-) for 59 hours. A total mass of 110.4g of MnO_4^- was flushed through the tank. As a result, the maximum mass of PCE that could be oxidized (assuming 100% of the added MnO_4^- was consumed in PCE oxidation) was 115.5g. However, because only about 50% of the fluid entering the tank was expected to travel through sources, the maximum PCE that could be oxidized was expected to be about 57.8g. A sub-maximal amount of oxidant was added in this experiment because the goal was not to destroy all the PCE. Instead, the goal was to destroy enough PCE and generate enough $MnO_2(s)$ to result in measurable changes in permeability and mass depletion rates, while leaving enough DNAPL PCE so that post-oxidation dissolution could be compared to pre-oxidation. During and following oxidant flushing, until permanganate was no longer present in the effluent, tank effluent was drummed for disposal because the permit for GAC treatment did not include waste containing permanganate.

Following the oxidant flush, the post-oxidation dissolution phase began and continued for another eleven days with effluent again being treated by GAC. Following the experiment, flow was maintained at a reduced rate for another 19 days until tank shutdown and soil coring, with effluent samples taken and flow rate measured every several days to track continued dissolution. Table 4.5 summarizes the chronology of the experiment.

Table 4.5: Experiment Chronology

Phase	Duration (hrs)	Tank Pore Volumes
Pre-DNAPL Emplacement Flushing	117	4.0
Pre-Oxidation Natural Dissolution	199	6.9
Oxidant Flushing	59	2.0
Post-Oxidation Dissolution	245	8.4
Reduced Flow until Shutdown and Coring	472	9.4

4.3.3   Hydraulic Head Monitoring and Data Acquisition

Throughout all phases of the experiment, water head was monitored at 44 locations (21 concentrated around the sources and 23 dispersed across the entire tank) shown on Figure 4.2. This monitoring was performed using a custom-built automated, scanning head measurement device, shown in Figure 4.4. The device consisted of a mechanical multiplexer (DSS24, Scanivalve Corp.) connected to two digitally compensated, high precision, variable reluctance differential pressure transducers (P855D-20 and P855D-22, Validyne Engineering). The pressure scanning system was controlled by a PC running LabView 7.1 (National Instruments) and custom-written virtual interface software. The DSS could be cycled through up to 24 positions at a selectable rate of up to 10 positions per minute; each position connected one head measurement location to each transducer (using 1/16" ID flexible polypropylene tubing from Cole-Parmer) providing monitoring of up to 48 locations. The P855D-20 had a full-

scale range of 88mm (±0.088mm) and the P855D-22 had a full-scale range of 140mm (±0.14mm). This system facilitated monitoring head change in and around the source as oxidation occurred, to quantify changes in permeability.
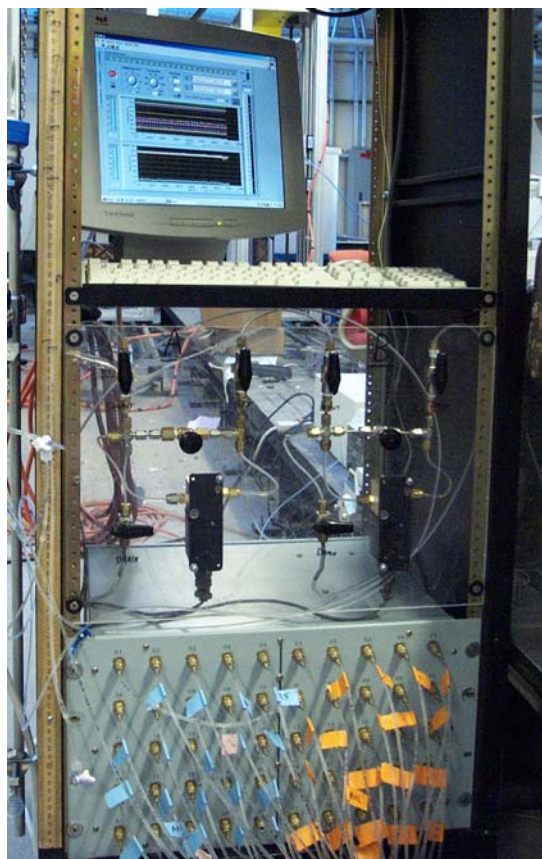
Figure 4.4: Water Head Measurement System

Flow rate through the tank was monitored at least daily to ensure the designed rate was maintained. Flow measurement was accomplished by weighing the tank effluent volume generated over a period of at least 30 minutes.

4.3.4 Sampling and Analytical Methods

Aqueous samples were collected at eight locations within the tank (two vertical transects down-gradient of the source area) during the bromide tracer test. During natural dissolution, chemical oxidation, and post-oxidation dissolution, aqueous samples were obtained from 14 locations within the tank (two vertical transects, and along the horizontal tank centerline as shown in Figure 4.2) as well as the tank effluent. Before collecting an aqueous sample, approximately 0.1mL was purged from the sampling port to eliminate stagnant water from the last sampling episode. All aqueous samples were collected in 1.5mL glass vials and capped with a Teflon-lined septa cap and then analyzed immediately if possible, or refrigerated until analytical equipment was available. In all cases, samples held for volatile organic analysis by GC were analyzed within seven days. Samples held for inorganic analysis by IC and ICP were analyzed within 30 and 90 days, respectively.

Bromide tracer samples were analyzed on a Dionex AS50 ion chromatograph/high performance liquid chromatograph (IC/HPLC) with Dionex IonPac AS-14A ion exchange analytical (4mm x 150mm) and IonPac AG-14A (4mm x 50mm) guard columns, AS50 auto-sampler, AS50 gradient pump, and CD25 conductivity detector. A sodium carbonate (8.0 mM) and sodium bicarbonate (1.0 mM) eluent, at a flow rate of 1.2mL/min, was used with this carbonate-selective anion exchange column. Calibration was performed with an 8-point calibration curve.

Aqueous PCE samples during the natural dissolution and post-oxidation phases were collected with zero-headspace and capped. Samples were analyzed on a Hewlett-Packard (HP) 6890 gas chromatograph (GC) equipped with an HP7683 auto-sampler/injector and DB-624 column, utilizing a flame ionization detector (FID), and a 6-point calibration curve.

During oxidation, aqueous samples were collected and then sub-sampled for a variety of analyses. Immediately after collection, 0.1mL was placed into 1.0mL of hexane and capped, shaken for one minute, and allowed to settle for at least 60 minutes

prior to analysis for PCE using an HP GC equipped with an HP7683 auto-sampler/injector and DB-5 GC column, utilizing an electron capture detector (ECD), and a 6-point calibration curve. Another 0.1mL was placed into a 15mL glass tubes (Hach) containing 4.5mL of DI water, capped, shaken, and analyzed on a HACH DR/4000 spectrophotometer for MnO_4^- at an absorbance of 525 nm within three hours, using a 6-point calibration curve. A third 0.1mL sub-sample was added to 1.0mL of sodium bisulfite (to stop the oxidation reaction by reducing any permanganate in the sample), capped, shaken, and manganese oxides allowed to settle out for six hours prior to analysis for chloride using the same IC and method described for bromide samples (except a 7-point calibration curve was used). Next, (for the aqueous samples obtained from the vertical transects, the final horizontal location, and the effluent), a 0.75mL sub-sample was added to a 15mL polypropylene conical vial containing 4.5mL of DI water and acidified with nitric acid to pH<2, capped, shaken, and analyzed for Mn^{+2} using inductively coupled plasma-atomic emission spectroscopy (Perkin Elmer Optima 3000 ICP-AES). It was assumed that manganese measured by ICP-AES was present in the aqueous sample as either MnO_4^- or $MnO_2(s)$. Therefore, the amount of manganese present as MnO_4^- (measured by spectrophotometry) was subtracted from the ICP-AES results to determine the amount of $MnO_2(s)$ present in the aqueous sample. Finally, pH was measured in the remaining original sample using an Orion 98-63BN micro-pH probe and Orion 420A+ meter. A 3-point calibration was performed daily.

Upon completion of the experiment, soil cores were obtained from throughout the tank (168 from sources and 44 from rest of tank) using a 15mL polypropylene conical vial (with the conical end cut off) or stainless steel grid as shown in Figure 4.5. The soil coring grids were used to core the sources such that the entire source could be extracted while subdividing it into rectangular 2.0cm x 2.6cm cores. The 15mL cylindrical coring tubes were used to obtain 1.3cm diameter cores at representative locations, along the tank centerline, through the rest of the tank. When obtaining a core, the water level was lowered to the desired core level, and the tank was excavated to that point. The coring

device was then pushed into the soil at the desired location and sand was excavated around the device. The device was then removed and the soil sample pushed out into a 50mL polypropylene conical vial containing hexane (36mL for source zone cores, 18mL for other cores). The vial was capped and shaken for 30 seconds, then let sit quiescently for 24 hours before transferring some of the hexane into a glass vial for PCE analysis using the FID detector on the GC. After analyzing for PCE, the hexane remaining in the soil core vials was allowed to evaporate for 48 hours under an exhaust hood. Then 30mL of hydroxylamine hydrochloride (0.2M) and nitric acid (0.1M) were added to the vials to reduce and dissolve any $MnO_2(s)$ (this was assumed to be the dominant species of manganese present so other extractions to identify exchangeable cations were not performed). This is reasonable as there was no visible MnO_4^- present in the pore water from the cores, so MnO_4^- was less than 1mg/L and would be negligible compared to the concentrations of Mn^{+2} in ICP-AES samples from $MnO_2(s)$. The vials were placed on a wrist-action shaker (60rpm) for two hours and then centrifuged for 10min at 1150G before transferring 6mL of liquid into 15mL polypropylene conical vials to be analyzed for Mn^{+2} by ICP-AES. Following ICP-AES analysis, the remaining liquid was drained and the core dried at $103^\circ C$ for four hours before determining the dry weight, so PCE and $MnO_2(s)$ content could be expressed as mass fractions.

Figure 4.5: Soil Coring Devices

4.4   Results and Discussion

The experiment and subsequent data analysis provided insight into several important aspects of chemical oxidation.   Overall oxidation performance will be discussed first, followed by the effects on source depletion.   Last, will be a discussion about manganese oxide formation and subsequent permeability reductions.

4.4.1   Oxidation Performance

Aqueous PCE concentrations were measured at a vertical transect (array G) about 16cm down-gradient of the source zone, at a vertical transect (array N) about 77cm down-gradient, along the tank centerline (about every 15-30cm), and at the tank outlet as indicated in Figure 4.2. PCE concentrations versus time are shown in Figures 4.6 – 4.8. Aqueous PCE concentrations reached a steady state throughout the tank within approximately 40 hours (as little as 10 hours at array G).   Predictably, the PCE concentrations drop below the method detection level (0.05mg/L) during the oxidant flush.   Although rebound was expected because the mass of MnO_4^- added was

insufficient to destroy all the PCE as described in Section 4.3.2, the degree of rebound differed by port. Because of the complex nature of the source zone, varying rebound is not surprising; however, it is interesting that the PCE concentration down-gradient of pool 1 and pool 2 rebounded differently. Concentrations in port G3 and N3 (down-gradient of pool 1) returned to only 10% of their pre-oxidation levels while concentrations in ports G9 and N9 (down-gradient of pool 2) rebounded to 117% of their pre-oxidation levels. This is likely because pool 1 was at the top of the source zone and did not interact with any other sources, whereas pool 2 was purposely located to have residual sources around it to interact with (see Figure 4.3).
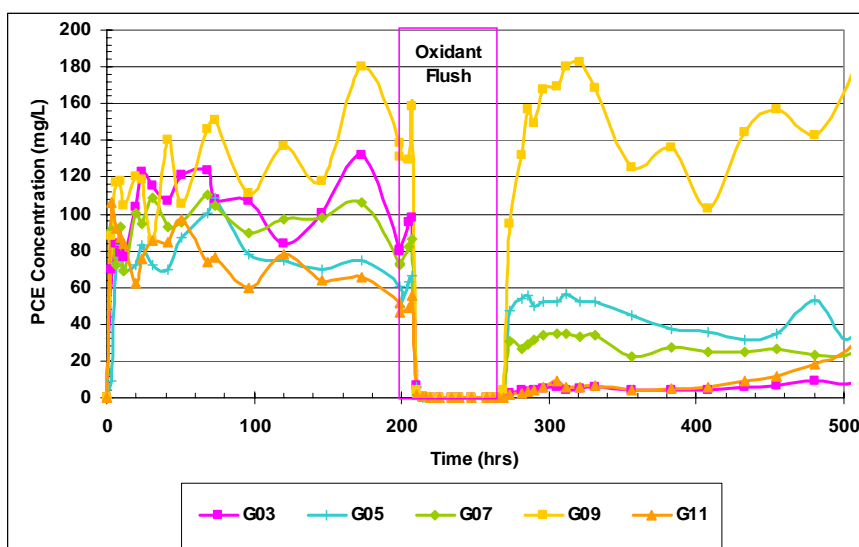
Figure 4.6: PCE Concentrations at Vertical Sampling Array G (located 16cm down-gradient of source zone)
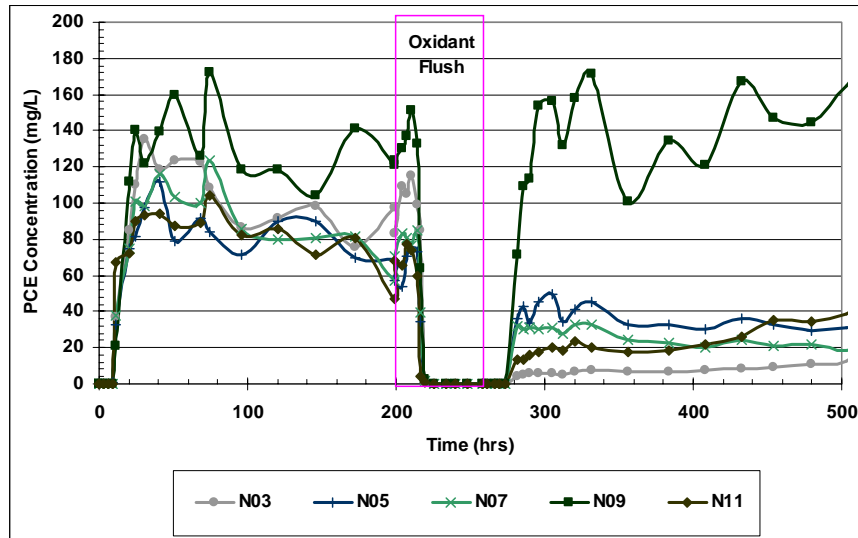
Figure 4.7: PCE Concentrations at Vertical Sampling Array N (located 77cm down-gradient of source zone)
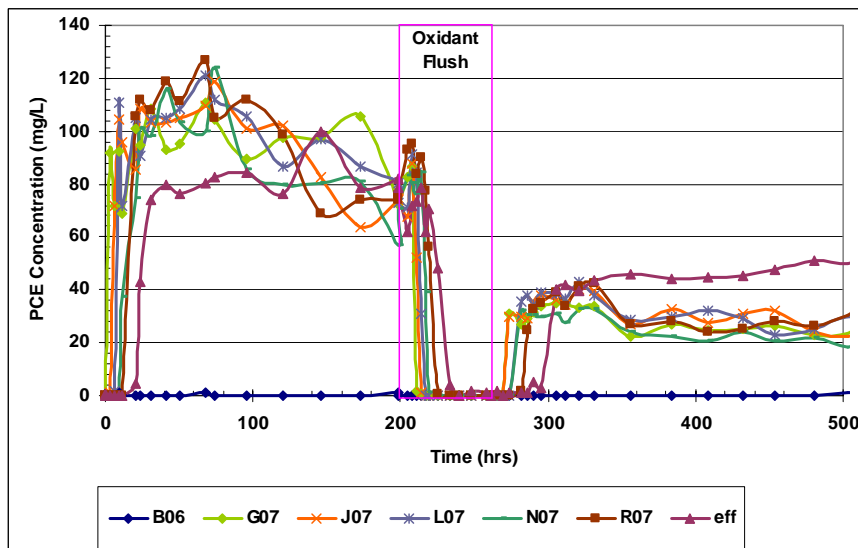
Figure 4.8: PCE Concentrations along Horizontal Centerline

The PCE concentration data was used to generate contour maps of aqueous PCE concentrations in the tank from array G to the outlet end well during each of the three

experiment phases: pre-oxidation (Figure 4.9), oxidation (Figure 4.10), and post-oxidation (Figure 4.11). Each figure has four maps depicting the generation of steady-state concentration conditions through the tank. Maps were generated using the Surfer 8.0 software package to interpolate sample data using the natural neighbor method, honoring observed sample values, with an anisotropy ratio of 5:1. The anisotropy ratio accounts for the larger spacing between the horizontal sample locations and greater variability in the vertical direction. The contour maps only extend from array G to the down-gradient end well because no concentration data between the source zone and array G is available. The only sample data up-gradient of array G was from port B6 up-gradient of the source zone. Because this port always saw zero PCE concentration, it would result in interpolated results through the source zone that are unnaturally low.

Once steady-state conditions were reached during pre-oxidation, the bottom half of the tank (down-gradient of pool 2, as well as residuals 2, 3, and 4) had concentrations roughly 50% higher than the top half of the tank. During oxidation, aqueous PCE concentrations throughout the tank dropped to zero indicating the oxidant was destroying PCE as fast as it could transfer from the DNAPL to the aqueous phase. When the post-oxidation phase reached steady-state conditions, concentrations in the top half of the tank had dropped by roughly 75% compared to pre-oxidation. However, the bottom half of the tank had concentrations higher than during pre-oxidation. Despite adding less oxidant than estimated for complete destruction, ISCO succeeded in substantially decreasing plume concentrations down-gradient of pool 1 and residual 1. On the other hand, it appears to have created a hotspot down-gradient of pool 2. Again, the different effect on pool 1 and pool 2 appears to be a result source zone configuration (see Figure 4.3). Pool 1 was at the top of the source zone without interacting with other sources so that $MnO_2(s)$ was generated at the DNAPL-water interface effectively cutting off mass flux from pool 1. Conversely, pool 2 had residual sources around it that resulted in more complex flow patterns increasing mixing and maintaining flow in contact with pool 2.

152
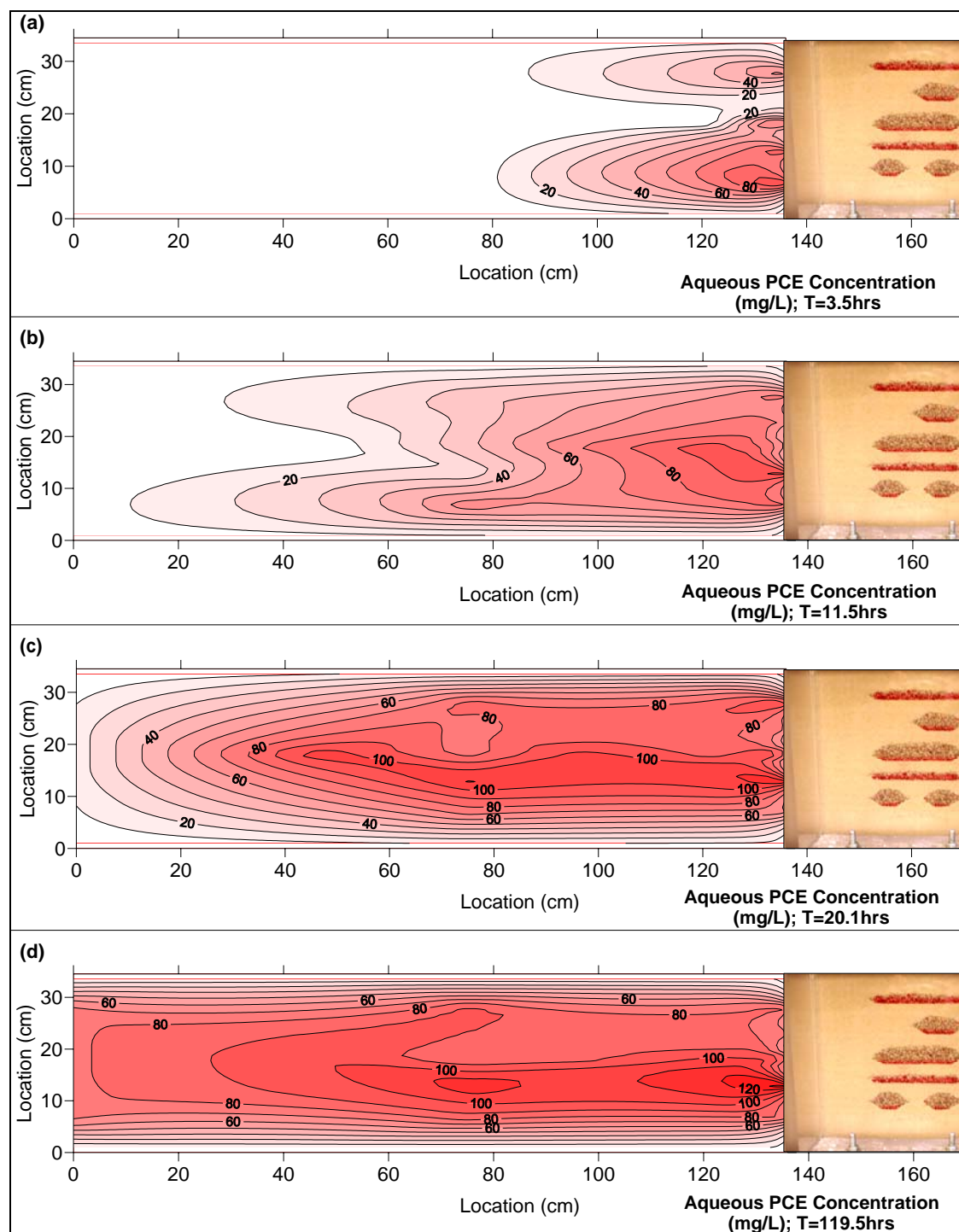
Figure 4.9: Aqueous PCE Distribution Down-gradient of Array G during Pre-Oxidation Natural Dissolution (see Figure 4.2 for tank features)
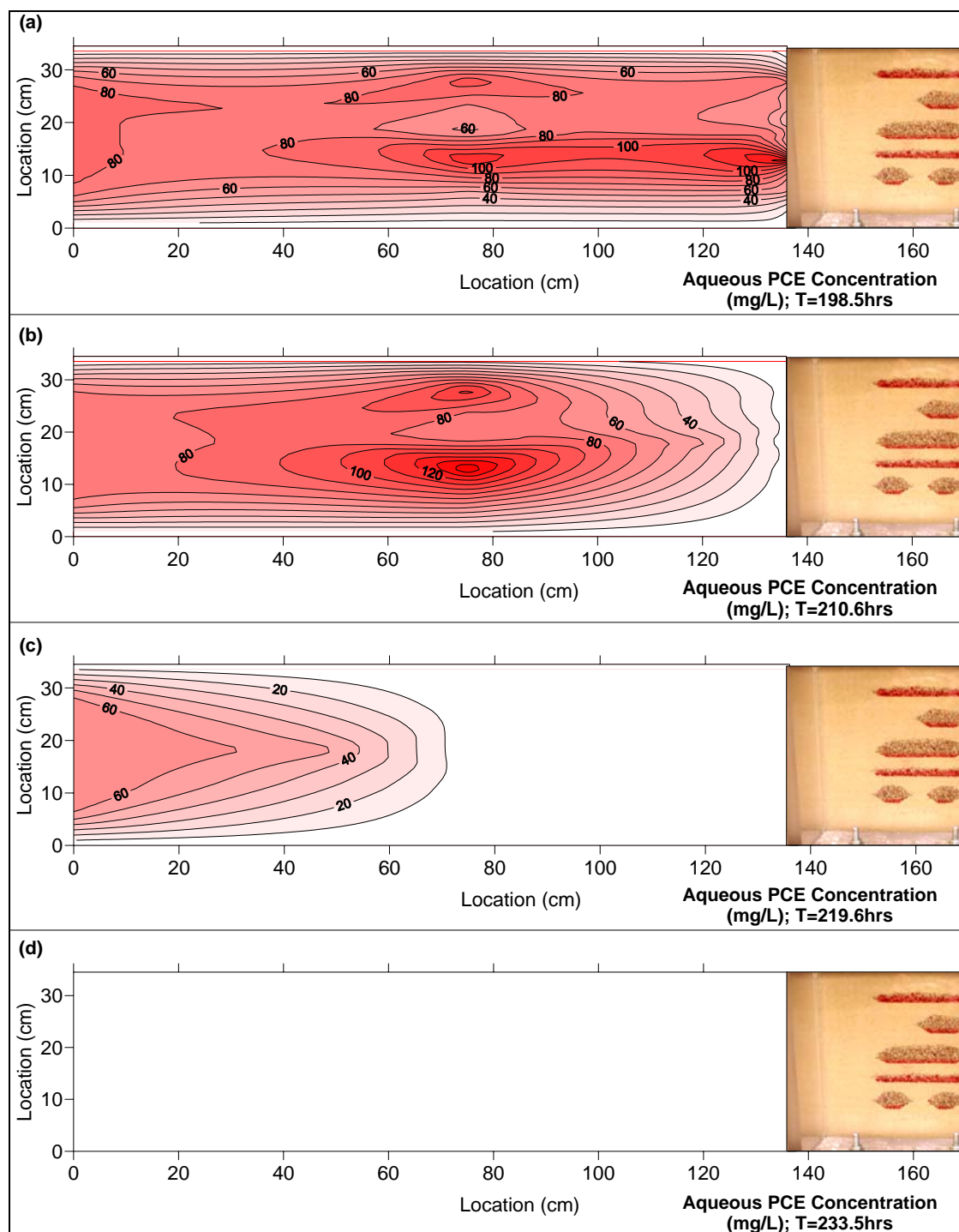
Figure 4.10: Aqueous PCE Distribution Down-gradient of Array G during Oxidation Flush (see Figure 4.2 for tank features)

154
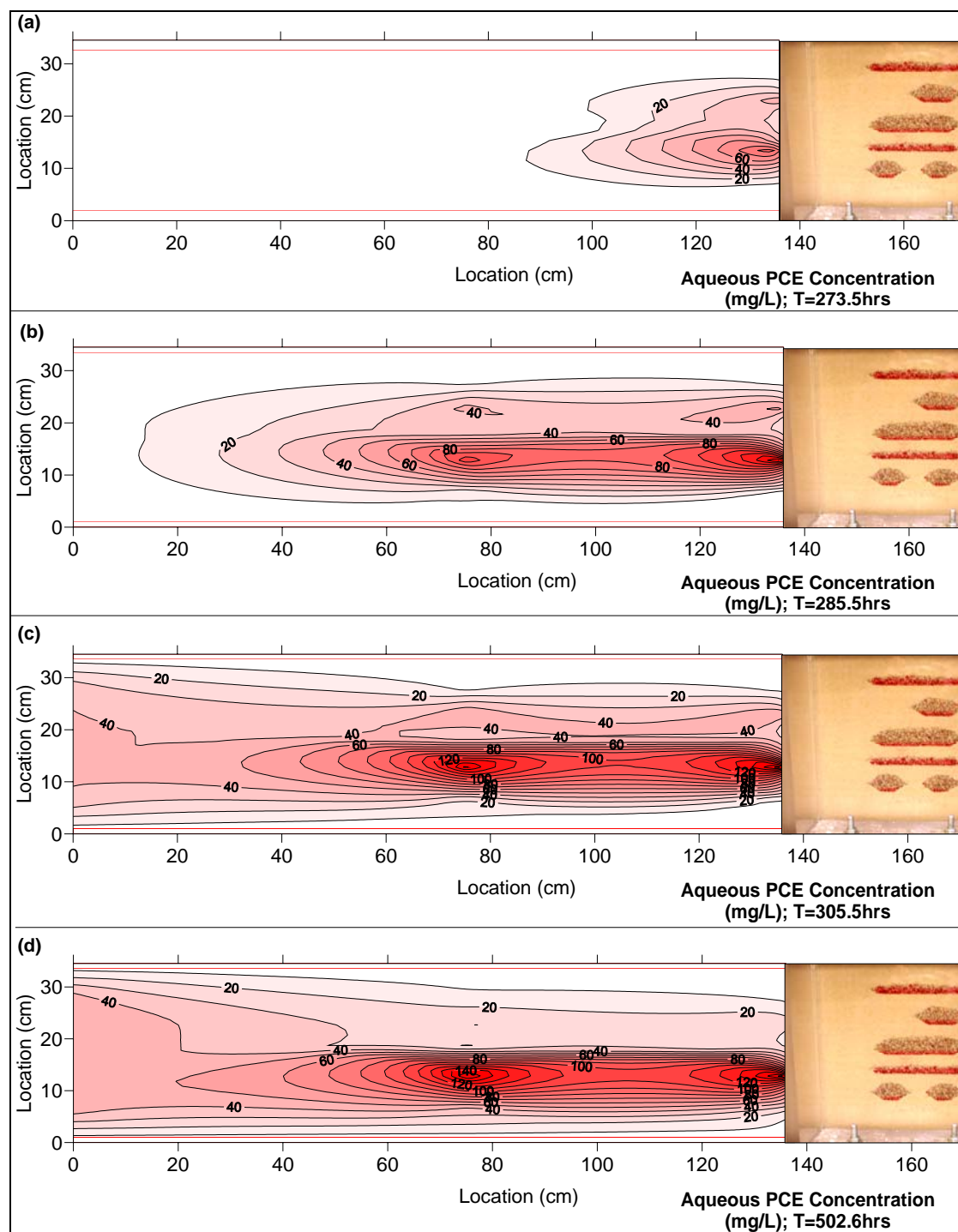
Figure 4.11: Aqueous PCE Distribution Down-gradient of Array G during Post-Oxidation Natural Dissolution (see Figure 4.2 for tank features)

Changes in plume concentration following oxidation are the result of a combination of depletion of source mass as well changes in source mass depletion rates. Changes in mass depletion rates could have resulted from manganese oxide formation at the DNAPL-water interface reducing the interfacial contact area for mass transfer from the DNAPL to aqueous phases. Alternately, mass depletion rates could have changed as a result of manganese oxide induced flow bypassing decreasing the flow of water in direct contact with DNAPL.

4.4.2   Source Depletion Effects

As a next step it was useful to evaluate how the DNAPL PCE mass was depleted during oxidation. Chloride concentrations were measured, at the same locations as aqueous PCE, during and following oxidation as an indirect measure of PCE oxidation because oxidized PCE was the only source of chloride except for background levels in the tap water. The tap water being flushed through the tank had a background chloride level of 25mg/L, as confirmed each sampling round by a sample obtained at port B6 (20cm up-gradient of the source zone), which was subtracted from all sample data. The chloride concentrations were converted to effective oxidized PCE concentrations based on the stoichiometric mole ratio (four moles of chloride equal one mole of PCE) and molecular weights. This assumed any oxidized PCE was completely oxidized to chloride and carbon dioxide. The effective concentration then provided a measure of how much PCE was oxidized.

Figure 4.12 shows cumulative mass of PCE depleted from the tank, based on flow rate and effluent concentrations of PCE and chloride. The shaded region indicates injection of oxidant at the tank inlet and the dashed line represents the time period during which measurable chloride (indicating PCE oxidation) was present in effluent. Because flow rate was constant throughout the experiment, the line slope represents an average mass depletion rate from the source zone. Slopes of "Total PCE Removed" during pre-oxidation, post-oxidation, the first half of oxidation, and second half of oxidation are

listed on Figure 4.12. During oxidation, the mass depletion rate as dissolved aqueous (unoxidized) PCE dropped to zero. On the other hand, during the first half of oxidation, the average total mass depletion rate was greater than either before or after oxidation. The average mass depletion rate increased most significantly at the beginning of the oxidant flush, indicated by the increased slope of the "Total PCE Removed" line, and diminished as the flush continued so by the end of oxidation it returned approximately to pre-oxidation levels.

Variation in mass depletion rate as oxidation progresses can be seen more clearly in Figure 4.13 which shows mass depletion rate versus time, estimated from effluent concentrations and flow rate. The shaded region and dashed line are the same as in Figure 4.12. Shortly after oxidation began (indicated by chloride arrival at the effluent), the mass depletion rate increased to nearly three times the natural dissolution rate. However, this rate was only sustained for 10-15 hours before quickly dropping to just two times pre-oxidation and continued to drop more slowly until reaching pre-oxidation levels. Following conclusion of the oxidant flush (i.e., permanganate no longer present in effluent), the mass depletion rate dropped further to about 80% of pre-oxidation levels and by the end of the experiment it had dropped to about 50%. Similar behavior was also seen in two large-scale 2D experiments utilizing heterogeneous flow fields and even more complex source zones. ISCO was just one portion of each of these large-scale experiments, and data analysis is still underway. However, a summary can be found at Appendix D.
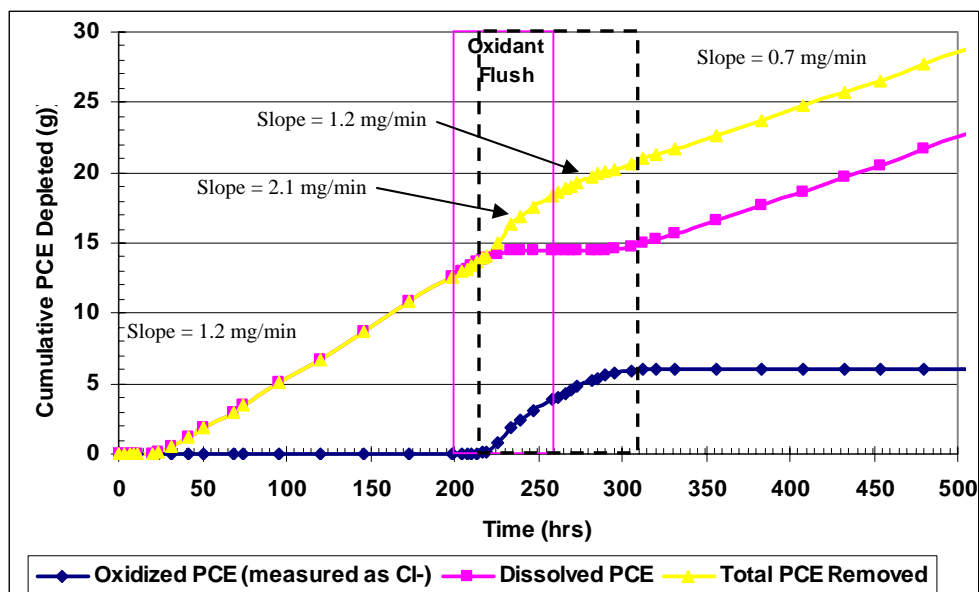
Figure 4.12: Cumulative PCE Mass Depleted from Tank (determined from effluent) – Note: shaded region represents oxidant injection, dashed region represents chloride in effluent
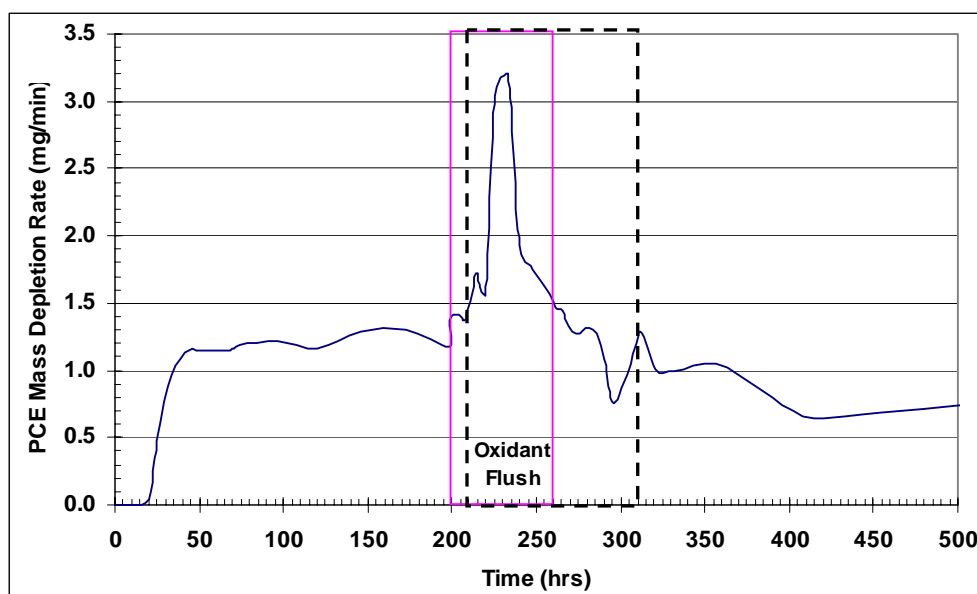
**Figure 4.13: PCE Mass Depletion Rate from Tank (determined from effluent) –
Note: shaded region represents oxidant injection, dashed region represents chloride
in effluent**

The drop off in PCE mass depletion rate while still undergoing oxidation suggests
a change in mass transfer characteristics of the sources. This could be a result of
depletion of PCE originally present as ganglia or deposition of $MnO_2(s)$ at the DNAPL-
water interface. Either of these would decrease the interfacial contact area, thereby
reducing mass transfer of PCE from the DNAPL to aqueous phase for subsequent
oxidation. Alternately, or additionally, permeability reductions from $MnO_2(s)$ deposition
could have caused flow to bypass some of the sources; decreased flow would be expected
to decrease mass transfer from DNAPL to aqueous phase as well.

In order to gain insight into what was limiting the overall oxidation mass
depletion rate for the whole tank, mass depletion rates for each source were estimated
next. The vertical sampling arrays were essentially multilevel samplers, with the port at
each level roughly corresponding to a particular source zone. As such, the concentration
profiles provided an indication as to what was happening at each source. Mass depletion

rates from each source were estimated from concentrations of PCE and oxidized PCE (estimated from chloride data) at the array G port corresponding to the source multiplied by the approximate flow rate through the source, based on the cross-sectional area (to flow) of each source. While these estimated source mass depletion rates are not exact, they are useful approximations for comparative purposes.

Generating these estimated rates required several assumptions. First, that the concentration (of PCE or chloride) at the array G sampling port located at roughly the same tank height as the given source was primarily coming from that source. Further, that this array G port concentration represented the average concentration across a cross-sectional area of tank at, array G, whose flow was comprised of fluid that had been primarily in contact only with the given source. These first two assumptions are supported by visual observations of flow from each source during the initial red dye tracer test and subsequently during oxidation. The dye test indicated that flow through the tank is horizontal and quite uniform with little apparent vertical mixing before array G, and that array G sampling ports fall near, but slightly off-center of the dye plume leaving each source. This can be seen in Figure 4.14 which shows permanganate (a) shortly after arriving at the sources, (b) leaving the sources, and (c) arriving at array G. However, Figure 4.18 (in Section 4.4.3) shows visible $MnO_2(s)$ formed down-gradient of pool 1 that is heaviest about 1-1.5cm below the sampling port corresponding to pool 1. As a result, concentrations measured at port G3 may underestimate down-gradient concentrations from pool 1. On the other hand, concentrations measured at array N were very similar to those at array G, although port N3 appears closer to the centerline of the $MnO_2(s)$ formation visible at array N in Figure 4.17 (in Section 4.4.3), suggesting the port G3 measurements are representing flow leaving pool 1. Additionally, the reduction in effluent concentration and overall mass depletion rate following oxidation support the decreased concentrations observed down-gradient of pool 1 and residual 1.

The third assumption was that the flow rates through each source, normalized to a volumetric flow rate per cross-sectional area, were equal so that the portion of total tank

flow that contacted a given source was only relative to the cross-sectional area (perpendicular to overall tank flow) of the source. This assumption can not be readily verified except to note that the leading edge of the permanganate plumes exiting sources of the same length are nearly even with heights approximately proportional to source height.
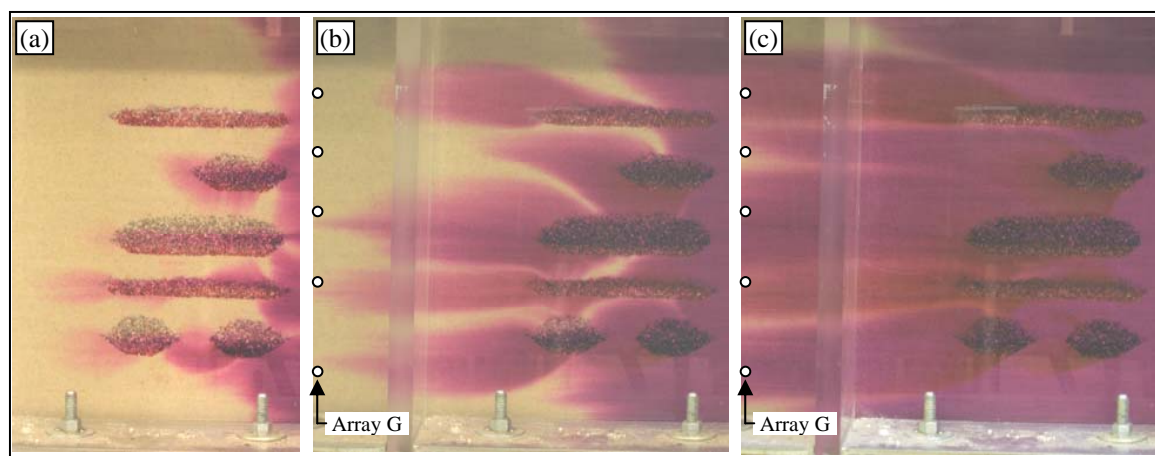
Figure 0.2: Oxidant (a) Arriving at Sources, (b) Leaving Sources, and (c) Arriving at Array G (darkest zones are permanganate, lighter zones within darker zones are manganese oxide, lightest zones are soil that has not received permanganate)

Figure 4.15 shows the estimated PCE mass depletion rate from each source versus time, except that residual sources 4 and 5 are combined into a single mass depletion rate. This was necessary because no samples were obtained from between these two sources, so there was no method to determine how much of each of them contributed to the concentrations measured at array G. The shaded region indicates injection of oxidant at the tank inlet, the dotted line represents the time period during which measurable chloride (indicating PCE oxidation) was present in array G samples. Estimated cumulative mass depleted from each source was then estimated by summing the area under the mass depletion rate curve for each source. Figure 4.16 shows the cumulative PCE mass

depleted from each source (again residual sources 4 and 5 are combined) and Table 4.6 summarizes the PCE mass depleted from each source, during each phase. The shaded region and dotted line are the same as for Figure 4.15.
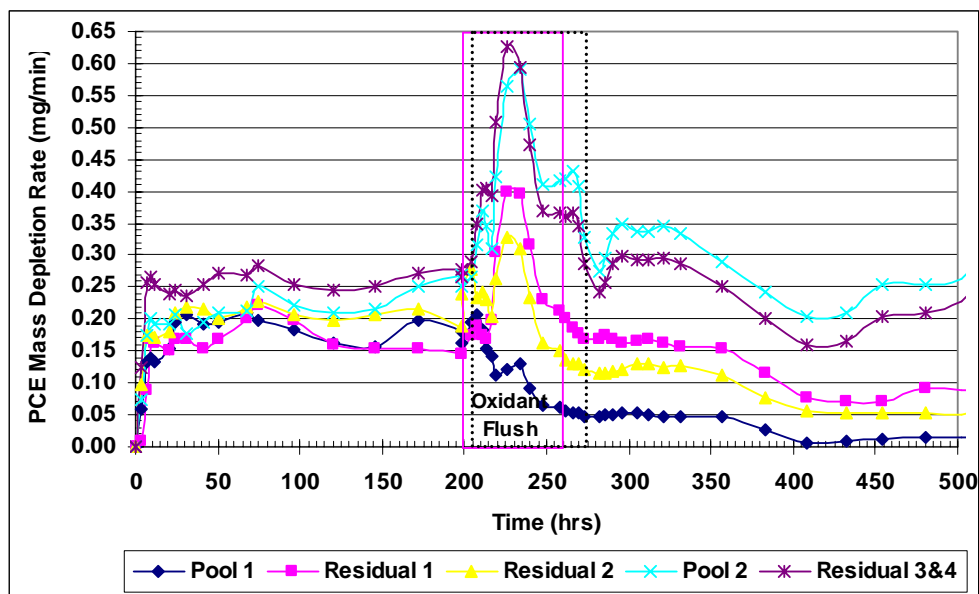
Figure 4.15: Estimated PCE Mass Depletion Rate from Each Source (determined from Array G) – Note: shaded region represents oxidant injection, dotted region represents chloride at array
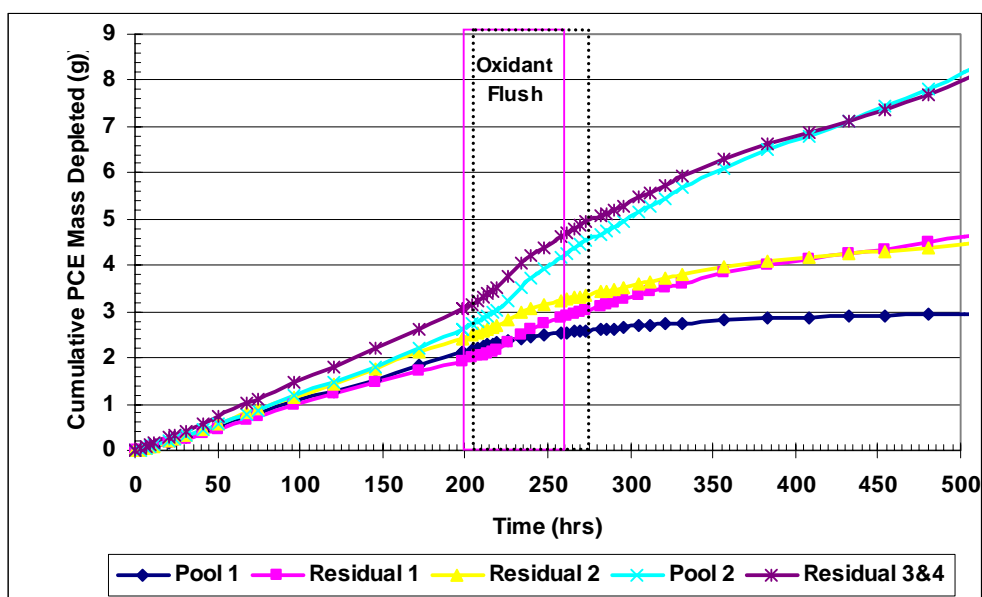
Figure 4.16: Estimated Cumulative PCE Mass Depleted from Each Source (determined from Array G) – Note: shaded region represents oxidant injection, dotted region represents chloride at array

Table 4.6: Estimated PCE Mass Removal from Sources during Each Phase

Source	Initial PCE Mass (g)	Mass as Ganglia (g)	Mass Removed (g)		
			Pre-Ox	Oxidation	Total
Pool 1	48.78	0.0	2.1	0.5	3.09
Pool 2	46.92	0.0	2.6	1.5	8.14
Residual 1	11.07	2.9	1.9	1.0	4.47
Residual 2	25.73	2.5	2.4	0.9	4.48
Residual 3	4.55	2.3	3.0	1.6	8.02
Residual 4	6.28	1.6			
TOTAL	143.33	9.3	12.0	5.5	28.2

All the sources apparently experienced a large increase in mass depletion rate following start of the oxidation flush, except pool 1. The mass depletion rate for pool 1 began to steadily decrease when the other sources began to increase. Because there was

little or no PCE present as ganglia in this source, the decrease is likely due to $MnO_2(s)$ formation at the DNAPL-water interface combined with development of flow bypassing around pool 1 as $MnO_2(s)$ formed and reduced permeability through the pool 1 source. Conversely, it was interesting to note that the mass depletion rate from pool 2 had one of the highest increases during oxidation, roughly equaling that of combined residual 3 and 4. The sudden drop in mass depletion rate from the other sources midway through oxidation appears to occur when mass present as ganglia was depleted. From Table 4.6, if the mass depleted during pre-oxidation is assumed to come from ganglia (except for pools 1 and 2), there were about 2g of PCE mass present as ganglia at the beginning of oxidation. Based on the initially increased oxidation mass depletion rate of 3.2mg/min, oxidation of the ganglia PCE mass would take about 10.4 hours which was approximately the length of the time period before the sudden drop in mass depletion rate occurred. The more gradual decrease following the sudden drop appears similar to the decrease for pool 1 suggesting that the continued decrease was a result of $MnO_2(s)$ formation.

Once the oxidation flush was completed, the mass depletion rates from pool 1 and residual 2 both decreased to less then pre-oxidation levels, while the mass depletion rates from residual 1 and combined residual 3 and 4 returned to pre-oxidation levels. The mass depletion rate from pool 2 remained higher following oxidation than during pre-oxidation. Because residuals 3 and 4 had the greatest GTP ratio, it is not surprising that they had a large increase in mass depletion rates during oxidation; however, their rebound after oxidation to pre-oxidation levels may be a little surprising because they had the largest estimated percent removal as shown in Table 4.6. Based on soil coring results, as well as visual observations of the source zone following oxidation, it appears that the PCE mass in residual source 3 was nearly completely depleted during oxidation and the rebound of mass flux was a result of PCE remaining as ganglia in residual source 4. Similarly the rebound of residual 1, when residual 2 did not rebound, may be because residual 1 had a larger mass originally present as ganglia and more $MnO_2(s)$ appears to have formed around residual 2. It appears the ganglia mass in residual 1 was not quite

completely removed during oxidation allowing the mass depletion rate to return to pre-oxidation levels. The decreased mass depletion rate in pool 1 following oxidation appears to be due to flow by-passing and decreased interfacial DNAPL-water contact area that resulted from high levels of manganese oxide formed at the NAPL-water boundary. The formation of manganese oxides may also partly account for the rebounds in mass depletion rates for residual 1 and combined residual 3 and 4. As shown in Figure 4.17 (next section), $MnO_2(s)$ formation was most prevalent in pools 1 and 2 followed by residual 2. As a result some flow initially through these sources is expected to have been re-directed through residuals 1, 3 and 4, increasing mass depletion rates from them.

Another observation was the dramatic increase in the mass depletion rate from pool 2 during oxidation, followed by increased post-oxidation mass depletion rate compared to pre-oxidation. This was probably partly an artifact of PCE emplacement. Following emplacement, pool 2 appeared to have a thicker transition zone above it that was at a lower saturation than the majority of the source, but still higher than residual saturation. The other possible explanation appears to lay in the configuration of the source zones. Specifically, pool 2 was positioned with a residual source above it to be more realistic. Additionally, it had two residual sources below it. A more complex flow pattern resulted around pool 2 because each source was constructed of coarse sand with a higher hydraulic conductivity than the surrounding sand. As manganese oxides formed in each of the sources, it is likely that flow patterns became even more complex resulting in increased mixing in and around pool 2 enhancing the mass depletion rate.

Regarding overall mass depletion, as Table 4.6 indicates, only 5.5g of DNAPL PCE were oxidized. This was less than theoretically possible based on oxidant mass delivered as discussed in Section 4.3.2. This was partly due to oxidant delivery. In this 2D tank, it was estimated that at most 50% of injected oxidant would pass through sources because oxidant was flushed through the entire cross-sectional area of the tank while the source zone cross-sectional area was less then 50% that of the tank. This is a factor of any flushing scheme, including field applications; some portion of the injected

solution is expected to bypass sources due to subsurface flow and delivery characteristics. The other factor resulting in lower mass depletion than theoretically possible was that not all of the oxidant passing through the source zone participated in oxidation of PCE. The incomplete reaction of permanganate can be observed in Figure 4.14. This may be due to limitations in mass transfer from the DNAPL to aqueous phase or local flow bypassing within the source zone. A goal in any ISCO flushing scheme is to maximize the amount of oxidant contacting the source that participates in contaminant oxidation.

Although the mass depletion rate varied during oxidation, the overall average mass depletion rate during oxidation was 93.2mg/hr (based on PCE oxidized divided by the duration of oxidation). This was over 50% greater than the 60.3mg/hr pre-oxidation rate, and more than twice the subsequent 43.7mg/hr post-oxidation depletion rate. Assuming oxidation could have maintained approximately this overall mass depletion rate, it would have required another 2300g of MnO_4^- under the same delivery conditions to fully deplete the PCE mass if the oxidation phase had been extended. This amounts to another 56.2 days of oxidant delivery or 46.5 pore volumes. However, this is less than half as long as the 119.9 days or 99.3 pore volumes that flushing with water would be expected to take, following conclusion of the 59 hour oxidation phase.

Once the tank was shut down, it was destructively sampled, obtaining 168 cores from the sources and 44 from the rest of the tank. Soil cores from sources were extracted using hexane to measure remaining DNAPL PCE. Despite every effort to extract intact cores and transfer them into the hexane quickly (less than five minutes), the mass balance suggested that a significant mass of PCE was lost during the coring procedure. Of the 143.34g of PCE initially emplaced, only 42.22g were estimated to have been removed (5.87g oxidized); however, only 13.72g of DNAPL PCE were recovered from the soil cores (13.6% of what was expected). Fortunately, a mass balance on chloride, aqueous PCE, permanganate, and $MnO_2(s)$ was performed and provided good agreement. The soil core results indicate that approximately 3.70g $MnO_2(s)$ were deposited throughout the tank, while ICP-AES analysis of effluent samples showed that 0.38g of $MnO_2(s)$ were

transported from the tank. Based on the reaction stoichiometry and molecular weights, the 4.08g $MnO_2(s)$ generated equates to 5.87g of PCE oxidized. This matches the mass of PCE estimated to have been oxidized based on effluent chloride concentrations. Similarly, 110.4g of permanganate were flushed through the tank, with approximately 5.61g consumed in oxidation of PCE and 97.73g exiting the tank in effluent. That means 93.6% of permanganate is accounted for; the slight difference may be due to a combination of the high dilution factor used for sample analysis on the spectrophotometer as well as oxidation of a small amount of oxidizable material on the pea gravel used at the tank inlet. Although the pea gravel was pre-washed before packing the tank and the end well materials were tested for oxidation resistance, a small amount of $MnO_2(s)$ was visible within the first 10cm of sand adjacent to the inlet end well, as seen in Figure 4.17.

Of the oxidant flushed through the tank only 5.1% was consumed in oxidizing PCE. As alluded to in the preceding discussion, this appears to be due to oxidant bypassing sources and decreased mass transfer resulting from reduced interfacial surface area caused by $MnO_2(s)$ formation at DNAPL-water interfaces. Because aqueous PCE concentrations dropped to zero during oxidation, and oxidant was still visible passing through sources, it seems that mass transfer from the DNAPL to aqueous phase was the limiting step. This may be partly due to the configuration of the sources. The sources were constructed using a much more coarse and permeable sand than the rest of the tank. As a result, the flow rate through each source was much higher than the rest of the tank. Based on visual observations during the dye tracer and oxidant injections, the Darcy velocity through each source was roughly four times that of the rest of the tank, resulting in a linear pore velocity through each source of approximately 750cm/day. This velocity may have exceeded the optimal velocity desired to maximize mass transfer from the DNAPL to the aqueous phase. Additionally, the coarse sand also limited the amount of PCE mass present as ganglia. Less coarse sand with a higher DNAPL residual saturation would have allowed more PCE mass to be present as ganglia, increasing the interfacial DNAPL-water contact area and increasing mass transfer. Because so much excess

oxidant was exiting the system, it suggests that a lower oxidant concentration or lower flow rate may have been suitable. Although a lower concentration would reduce the kinetic rate of PCE oxidation, this would be acceptable as long as the oxidation rate still exceeded the dissolution rate. Further, decreasing the oxidation rate sufficiently may have allowed more of the reaction to occur further down-gradient of the source possibly decreasing the $MnO_2(s)$ buildup at the source.

4.4.3   Permeability Reduction

As discussed earlier, manganese oxides were formed and deposited throughout the tank (Figure 4.17a). A focus of this research was to quantify how $MnO_2(s)$ affected permeability and mass depletion or mass transfer, so the spatial distribution was determined by analyzing soil cores from throughout the tank. Soil core results were interpolated with the Surfer 8.0 software package using the using the natural neighbor method, honoring observed sample values, with a horizontal anisotropy ratio of 3:1 (Figure 4.17b). Figure 4.18 is a close-up and $MnO_2(s)$ contour map of the source zone.
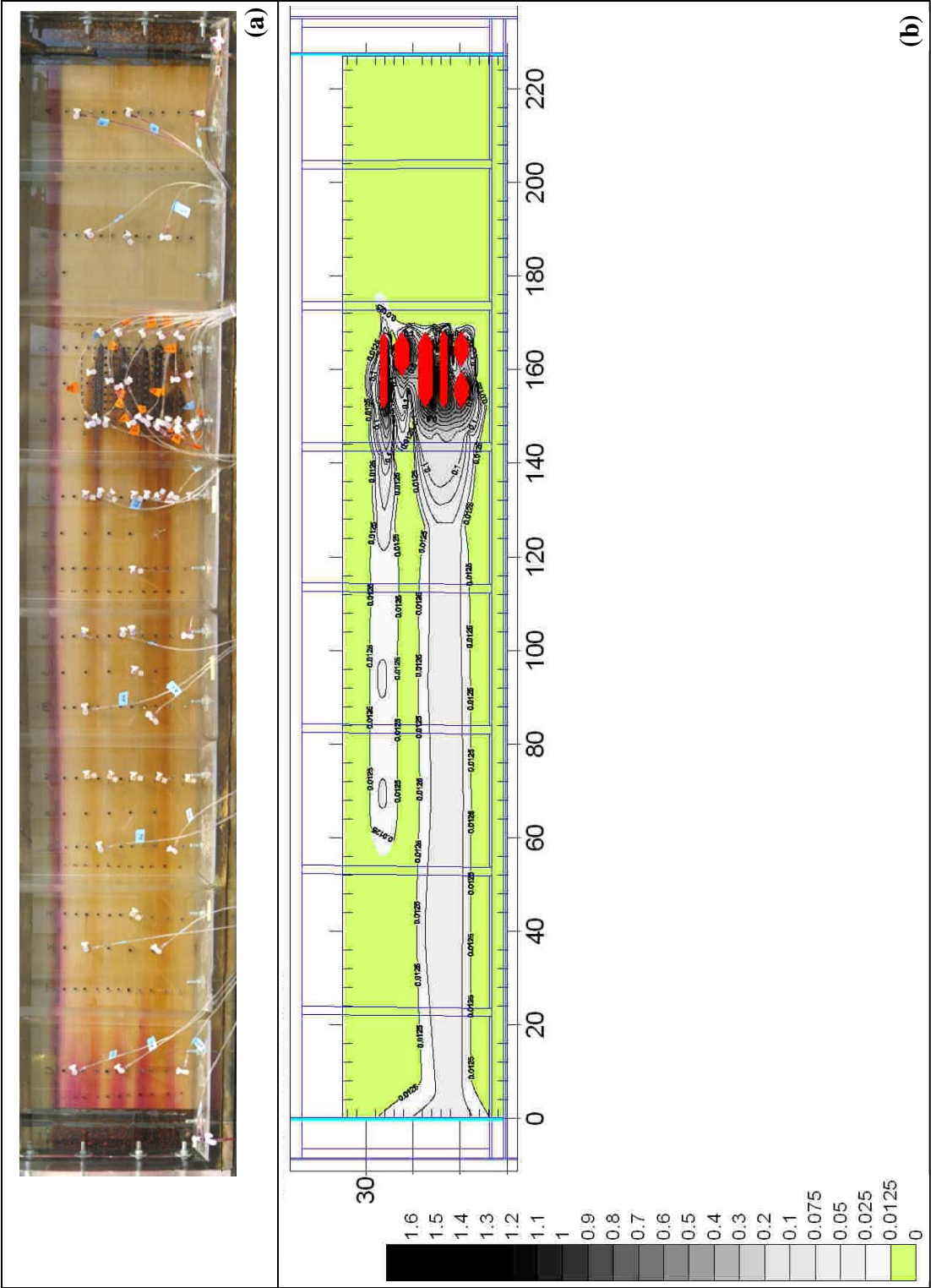
Figure 4.17: MnO$_2$(s) Distribution through Tank (g MnO$_2$(s)/kg soil)
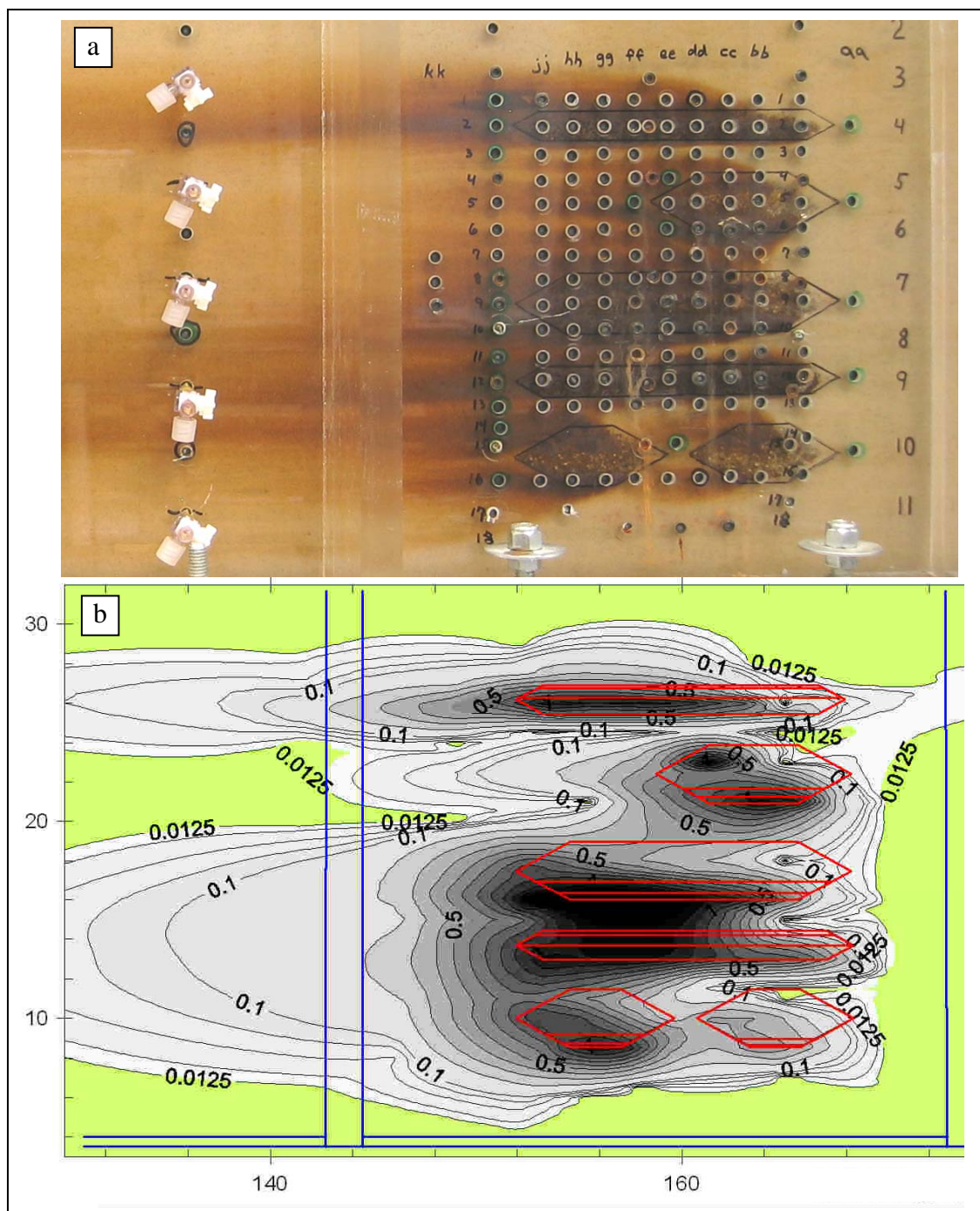
Figure 4.18: MnO$_2$(s) Distribution around Sources (g MnO$_2$(s)/kg soil)

Water head was continuously monitored (approximately every 25 minutes) throughout the tank as a measure of the permeability. Because fluid properties were not changing, and a constant flow was maintained through the tank, any observed changes in water head distribution were a result of changes to the permeability of the porous media. Figure 4.19 shows the measured head at each port during the experiment, note no data is available from approximately 294-340 hours due to an equipment malfunction. The heads fluctuated daily, presumably due to the daily temperature fluctuations in the lab of 4-6°C. The individual ports are not labeled on this graph as it is just meant to provide an overview. However, the tank inlet head, outlet head, and source zone heads have been labeled. It can be seen that during oxidation, the spread of the source zone heads increased so that after oxidation the head drop through the source was approximately double what it had been before oxidation. Further, the heads down-gradient of the source zone did not change, while those up-gradient did. This suggests that while $MnO_2(s)$ was distributed through the length of the tank at various mass fractions, only the higher mass fractions found in and around the sources significantly altered permeability.
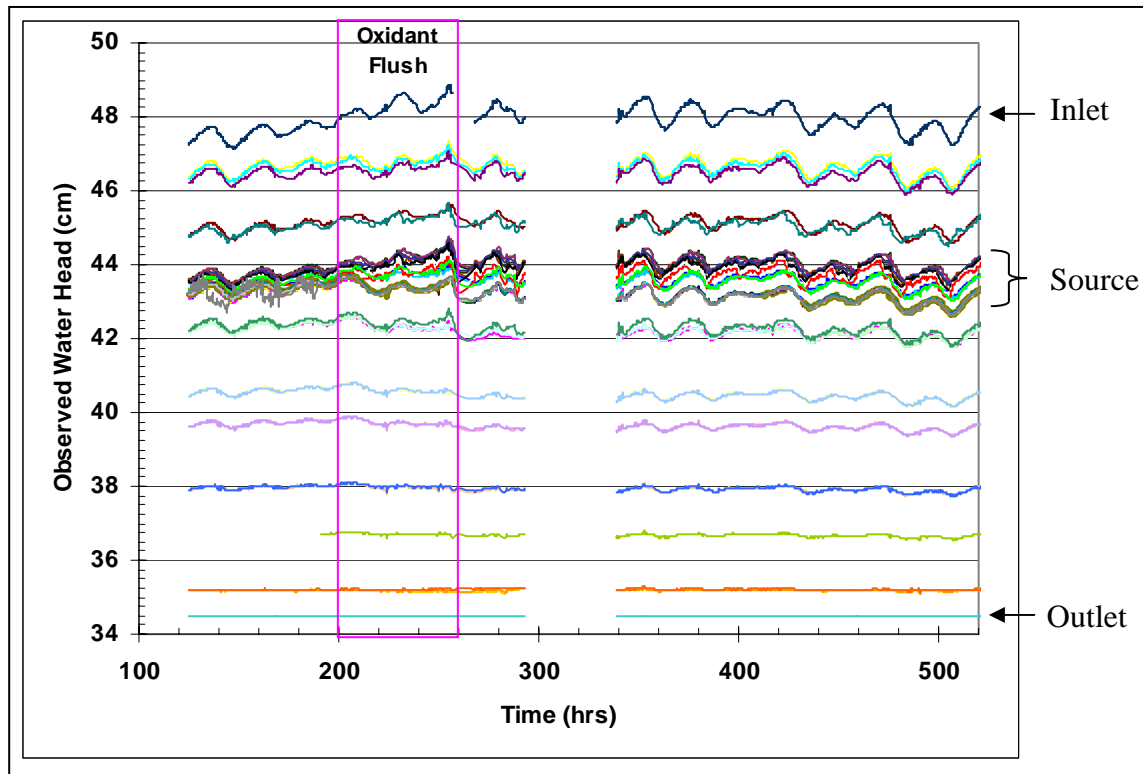
Figure 4.19: Observed Water Head throughout Experiment

The effect of permeability reductions around the sources is clearly visible in Figure 4.20 which graphs the head drop across each source zone over time. The markers are data points selected to eliminate the daily fluctuation effects. The lines represent moving 3-point averages of the data to improve visualization. The greatest increase in head drop (and decrease in permeability) occurred across residual source 2, followed closely by pools 1 and 2. This agrees with visual observations of heavier and darker $MnO_2(s)$ buildup around these sources. It is interesting to see the head drop across residual 4 continue to increase after the oxidation flush has finished. This appears to be a result of $MnO_2(s)$ generated in residual 3 being flushed into residual 4 where it is combining with the high amount of $MnO_2(s)$ already present there
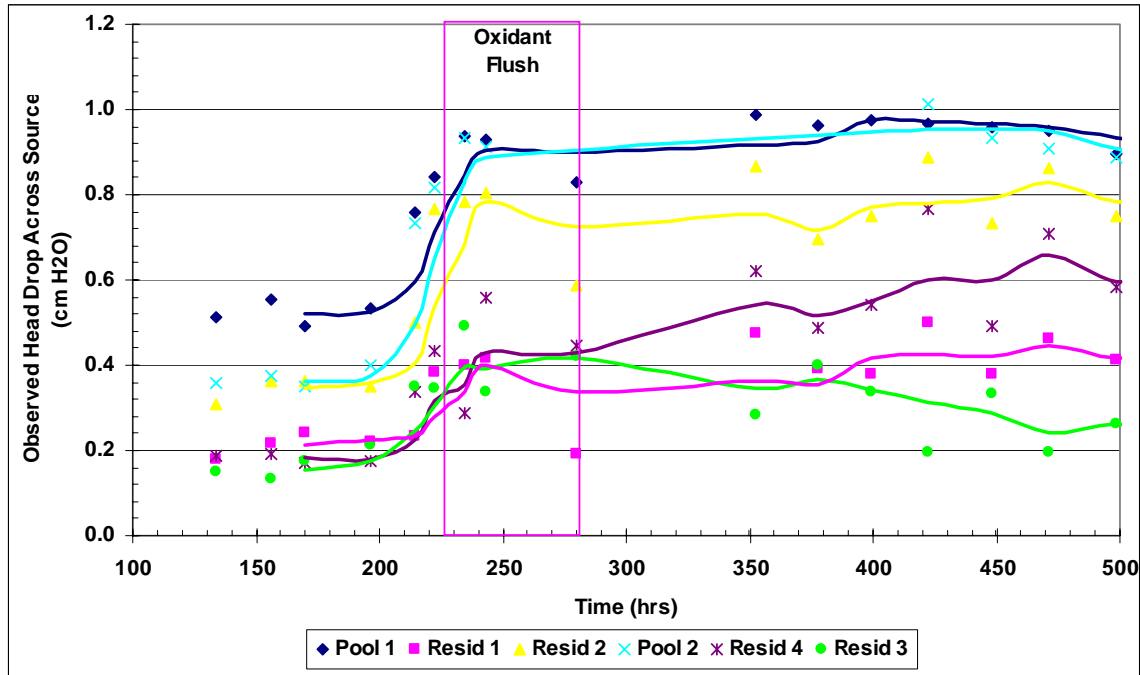
Figure 4.20: Change in Head Drop across Source Zones Following Oxidation

Next, the observed changes in hydraulic head were translated into changes in hydraulic conductivity. The objective was to determine if the buildup of $MnO_2(s)$ could be quantitatively linked to changing hydraulic conductivity in a manner that could be modeled. The newly developed chemical oxidation reactive transport in 3D (CORT3D) computer model, described in detail in Chapter 3, incorporates a modified version of Wyllie's (1962) power law relation of relative aqueous permeability to water saturated pore space

$$k_{r,w} = \left(\frac{1 - S_{mno2} - S_n - S_{r,w}}{1 - S_{r,w}} \right)^3 \tag{4.6}$$

where $k_{r,w}$ is the relative water permeability, S_n is the saturation of DNAPL component in the pore space, $S_{r,w}$ is the residual water saturation for the porous media, and S_{mno2} is a pseudo-saturation representing the volume of total pore space filled with manganese

oxide solids. This pseudo-saturation is estimated by converting the mass fraction of solids produced to a volume using the manganese oxide precipitate density. Because the $MnO_2(s)$ formed is a hydrous form of manganese oxide it is expected to have a density much lower than that of dry, solid manganese oxide. Further, because the density of the generated $MnO_2(s)$ is unknown, it becomes a fitting parameter in determining the pseudo-saturation of $MnO_2(s)$ for Equation 4.6. To be an effective fitting parameter, its value once determined should be constant throughout the experiment or system being considered.

To this end, the CORT3D model was calibrated to observed head and flow rate values for pre-oxidation conditions. Figure 4.21 shows scatter plots of the simulated versus observed head values for (a) locations throughout the tank and (b) locations around the source zones. As indicated by the R^2 values listed for both data sets (>0.94) good calibration was achieved. The apparent variability of Figure 4.21b is a result of the small axes scales magnifying normal daily head fluctuations. Figure 4.22 shows the head drop across each source, with markers (without lines) representing observed values and lines representing simulated values.
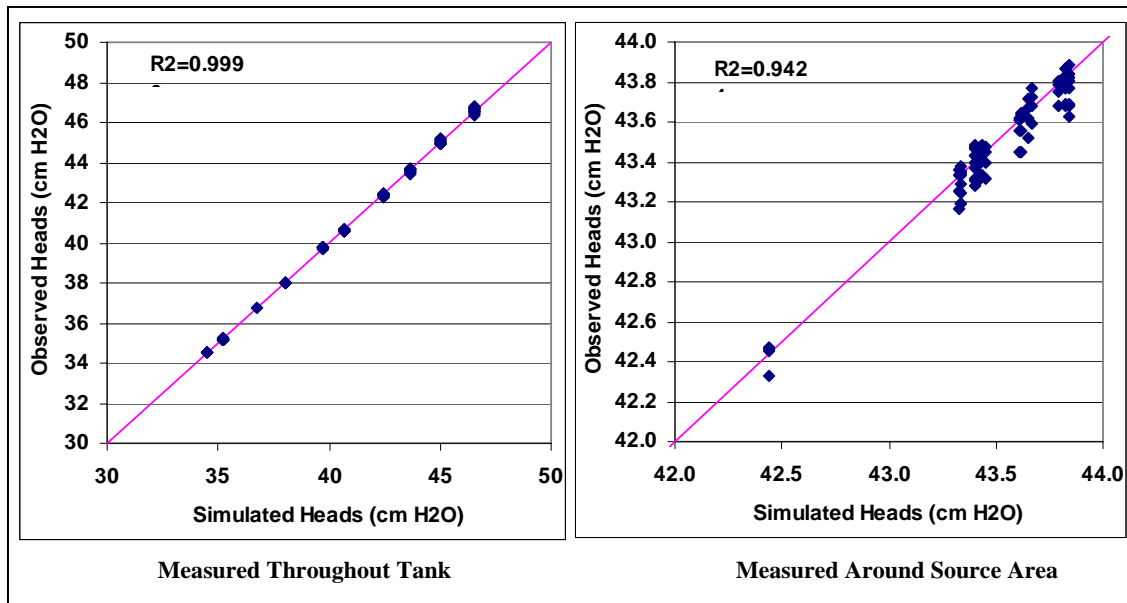
Figure 4.21: Comparison of Model Simulated Heads to Observed Heads – Pre-Oxidation
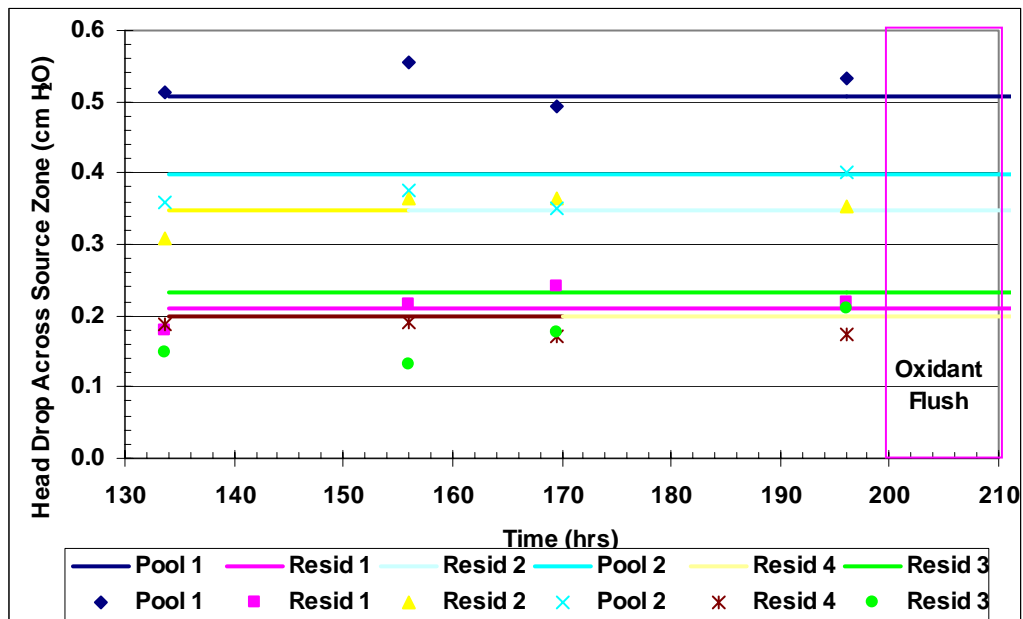
Figure 4.22: Observed and Simulated Head Drop across Sources – Pre-Oxidation

Next, the post-oxidation conditions were simulated using the $MnO_2(s)$ distribution determined from the soil cores (Figure 4.17b). The apparent $MnO_2(s)$ density was varied to achieve the best fit of simulated and observed head values throughout the tank. An apparent density of 9.5mg/mL was found to provide the best fit. Although this value is 530 times less than the density of dry, solid manganese oxide it is not surprising because it represents both the decreased density of the hydrous $MnO_2(s)$ as well as the pore-throat blocking mechanism of permeability reduction. Interestingly, it was found that not all the $MnO_2(s)$ deposited in the tank affected permeability. Only those areas of the tank with $MnO_2(s)$ mass fractions greater than 0.1g $MnO_2(s)$/kg soil (generally in, around, and within 15cm down-gradient of the sources) saw reductions in permeability.

Figure 4.23 again shows scatter plots of the simulated versus observed head measurements. The fit is still good across the entire tank, with reasonably good fit (R^2 >0.88) around the source. The slightly decreased fit in the source area compared to pre-oxidation may be a result of small scale variations in $MnO_2(s)$ or DNAPL PCE mass fractions that could not be measured and incorporated in the modeling effort. Finally, Figure 4.24 shows the head drop across each source, with markers (without lines) representing observed values and lines representing simulated values.
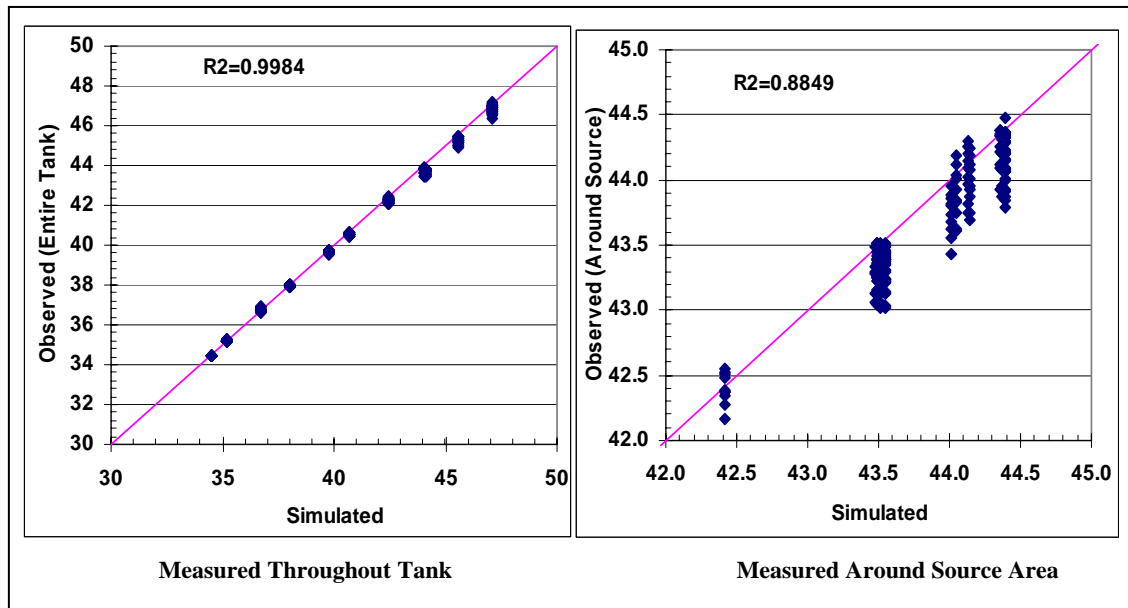
Figure 4.23: Comparison of Model Simulated Heads to Observed Heads – Post-Oxidation
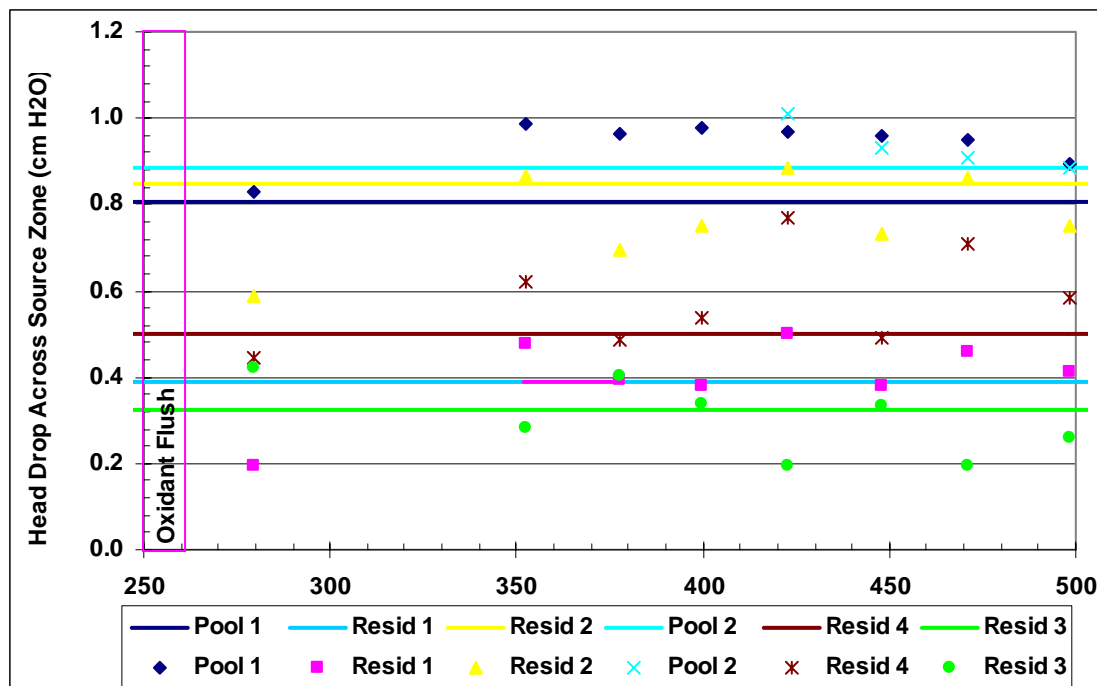
Figure 4.24: Observed and Simulated Head Drop across Sources – Post-Oxidation

4.5   Conclusions

The experiment that was presented in this chapter utilized an intermediate-scale 2D tank filled with clean silica sands and a moderately complex PCE DNAPL source zone, under a single set of flow and oxidant delivery conditions. For the conditions investigated, only a small portion of the injected oxidant mass participated in oxidation of PCE mass. This was partly due to the flushing oxidant delivery scheme; less than 50% of the oxidant flushed through the tank was expected to pass through the source zone. Some degree of source zone bypassing like this is expected for delivery by flushing in the tank experiment, as in field applications. Alternative delivery methods such as probe injection directly into the source zone or subsurface soil mixing to emplace solid $KMnO_4$ or $NaMnO_4$ may reduce source zone bypassing. Another reason only a small portion of injected oxidant mass participated in oxidation of PCE mass is because of limitations on

mass transfer from the DNAPL to aqueous phase within sources or localized flow bypassing within the source zone.

Mass transfer limitations appear to have been partly due to the construction of the sources, using a more coarse sand than in the rest of the tank, having a high hydraulic conductivity and low residual DNAPL saturation. Further, although oxidation initially tripled the mass depletion rate, the rate dropped apparently as PCE ganglia disappeared and as $MnO_2(s)$ formed, decreasing DNAPL-water interfacial area and causing flow-bypassing of sources. In a field situation, DNAPL migrating through a fine subsurface soil may encounter a lens of more coarse sand where it will accumulate as a pool similar to the sources used in this study. In such a situation, if substantial DNAPL mass is present as a pool in the coarse sand, ISCO using permanganate may not be suited to full depletion of the DNAPL source; however, a substantial reduction in mass loading from the DNAPL into the groundwater may be still be achieved.

It is possible that the flow velocity through the sources and/or oxidant concentration could be adjusted to optimize the mass depletion rate and minimize the amount of oxidant mass injected. ISCO effects on mass depletion and mass depletion rates varied by source as a result of source configuration and location. Mass present as ganglia underwent a large increase in mass depletion rate which appeared to drop off upon ganglia depletion. As oxidation continued, mass depletion rates slowly declined apparently due to manganese oxide formation. Pool 1, located so as not to interact with other sources, was the only source not to experience an initial increase in mass depletion rate during oxidation but instead saw a steady decline in mass depletion rate likely due to $MnO_2(s)$ formation at the DNAPL-water interface. On the other hand, the pool located to interact with residual sources above and below it experienced the greatest rebound of mass depletion rate following oxidation. This appears to be a result of the flow field around that pool becoming more complex due to changes in the flow field in and around these sources.

Formation and deposition of $MnO_2(s)$ generated as a result of PCE oxidation using permanganate affected the porous media, reducing the aqueous permeability in and around DNAPL sources resulting in changes to the flow pattern. The configuration of the source zones partly determined the effects. The pool with little or no residual around it, in a relatively homogeneous flow field, appeared to benefit from resulting $MnO_2(s)$ pore-blocking that substantially reduces the mass depletion rate from the pool with relatively little mass removed from the pool. On the other hand, the pool with residual around it (in a more complex heterogeneous flow field) appeared to undergo an increase in mass depletion rate as $MnO_2(s)$ reduced permeability, complicating flow, and increased mixing at the NAPL-water interface. Additionally, sequential residual zones seemed to have a combined effect where some $MnO_2(s)$ generated in the first residual was transported a short distance to the second residual to combine with $MnO_2(s)$ from that source, and magnified impacts in and around the second source. Again, it seems that flow rate and oxidant concentration could be optimized to maximize mass transfer of PCE from the DNAPL to water phase for oxidation, while minimizing the oxidation rate to slow formation of $MnO_2(s)$ and move some of the permeability effects down-gradient of the source.

Modeling and predicting the effects of $MnO_2(s)$ formation on permeability was possible. A relatively simple power law model relating the change in porosity resulting from $MnO_2(s)$ formation to changing permeability was successfully used, with an empirical effective $MnO_2(s)$ density, to simulate conditions used in this research. Further, it was found that $MnO_2(s)$ levels had to exceed a threshold level before they began to affect permeability. This threshold was determined to be 0.1g $MnO_2(s)$/kg soil for the conditions of this experiment. It is likely that the effective $MnO_2(s)$ density as well as the threshold will vary depending on system conditions. Higher flow rates, smaller pore sizes, or less uniform soil particle sizes are expected to impact the values of these parameters for a particular system.

4.6   References

Ball, W.P., Liu, C., Xia, G., and Young, D.F. (1997). "A diffusion-based interpretation of tetrachloroethene and trichloroethene concentration profiles in a groundwater aquitard." *Water Resour. Res.*, 33 (12): 2741–2757.

Bear, J. (1972). *Dynamics of fluids in porous media*. American Elsevier Publishing Company, Dover, NY, 764 pp.

Brusseau, M.L. (1992). Rate-limited mass transfer and transport of organic solutes in porous media that contain immobile immiscible organic liquid. *Water Resour. Res.*, 28 (1): 33-45.

Chambers, J., Leavitt, A., Waiti, C., Schreier, C.G., Melby, J., and Goldstein, L. (2000). "In situ Destruction of Chorinated Solvents with KMnO4 Oxidizes Chromium." In: Wickramanayake, G.B., Gavaskar, A.R., Chen, A.S.C. (Eds), *Chemical Oxidation and Reactive Barriers*. Battelle Press, Columbus, OH, pp. 49-55.

Clayton, W.S., Marvin, B.K., Pac, T., and Mott-Smith, E. (2000). A multisite field performance evaluation of in situ chemical oxidation using permanganate.   In: Wickramanayake, G.B., Gavaskar, A.R., Chen, A.S.C. (Eds), *Chemical Oxidation and Reactive Barriers*. Battelle Press, Columbus, OH, pp. 101-109.

Clement, T.P., Hooker, B.S., and Skeen, R.S. (1996).   "Macroscopic models for predicting changes in saturated porous media properties caused by microbial growth." *Ground Water*, 34 (5): 934-942.

Conrad, S.H., Glass, R.J., and Peplinski, W.J. (2002). "Bench-scale visualization of DNAPL remediation processes in analog heterogeneous aquifers: surfactant floods and in situ oxidation using permanganate." *J. Contam. Hydrol*., 58 (1-2): 13-49.

CRC. (2001). CRC Handbook of Chemistry and Physics, 82nd Ed. CRC Press, Cleveland, OH. 2664 pp.

Crimi M. and Siegrist, R.L. (2004). *Experimental Evaluation of In Situ Chemical Oxidation Activities at the Naval Training Center (NTC) Site, Orlando, Florida*. Naval Facilities Engineering Command, Port Hueneme CA. 64 pp.

Dekker, T.J. and Abriola, L.M. (2000a). "The influence of field-scale heterogeneity on the infiltration and entrapment of dense non-aqueous phase liquids in saturated formations." *J. Contam. Hydrol.*, 42 (2): 187-218.

Dekker, T.J. and Abriola, L.M. (2000b). "The influence of field-scale heterogeneity on the surfactant-enhanced remediation of entrapped non-aqueous phase liquids." *J. Contam. Hydrol.*, 42 (2): 219-251.

Ewing, J.E. (1996). *Effects of dimensionality and heterogeneity on surfactant-enhanced solubilization of non-aqueous phase liquids in porous media*. MS Thesis, University of Colorado at Boulder, 152 pp.

Freeze, R.A. and McWhorter, D.B. (1997). "A framework for assessing risk reduction due to DNAPL mass removal from low-permeability soils." *Ground Water*, 35 (1): 111-123.

Held, R.J. and Illangasekare, T.H. (1995). "Fingering of dense non-aqueous phase liquids in porous media: 2. Analysis and classification." *Water Resour. Res.*, 31 (5): 1223-1231.

Hood, E. (2000). *Permanganate Flushing of DNAPL Source Zones: Experimental and Numerical Investigation*. Ph.D. Dissertation, University of Waterloo, Waterloo, ON. 243 pp.

Hood, E. and Thomson, N.R. (2000). "Numerical simulation of in situ chemical oxidation." In: *Chemical Oxidation and Reactive Barriers*, Wickramanayake, G.B., Gavaskar, A.R., Chen, A.S.C. (Eds.). Battelle Press, Columbus, OH, pp. 83-90.

Hood, E.D., Thomson, N.R., Grossi, D., and Farquhar, G.J. (2000). "Experimental determination of the kinetic rate law for the oxidation of perchloroethylene by potassium permanganate." *Chemosphere*, 40: 1383-1388.

Huang, K., Hoag, G.E., Chheda, P., Woody, B.A., and Dobbs, G.M. (1999). "Kinetic study of oxidation of trichloroethylene by potassium permanganate." *Environ. Eng. Sci.*, 16 (4): 265-274.

Huang, K.-C., Hoag, G.E., and Chheda, P. (2000). "Soil oxidant demand during chemical oxidation of trichloroethylene by permanganate in soil media." *Proc., 32nd Mid-Atlantic Industrial and Hazardous Waste Conference*, Technomonic Publishing Co, : 617-626.

Huang, K., Hoag, G.E., Chheda, P., Woody, B.A., and Dobbs, G.M. (2001). "Oxidation of chlorinated ethenes by potassium permanganate: a kinetics study." *J. Haz. Mater.*, 87 (1-3): 155-169.

Huang, K., Hoag, G.E., Chheda, P., Woody, B.A., and Dobbs, G.M. (2002). "Kinetics and mechanism of oxidation of tetrachloroethylene with permanganate." *Chemosphere*, 46 (6): 815-825.

Illangasekare, T.H., Armbruster, E.J. III, and Yates, D.N. (1995a). Non-aqueous-phase fluids in heterogeneous aquifer—experimental study. *J. Environ. Eng.*, 121 (8): 571-579.

Illangasekare, T.H., Ramsey, J.L., Jensen, K.H., and Butts, M. (1995b). "Experimental study of movement and distribution of dense organic contaminants in heterogeneous aquifers: an experimental study." *J. Contam. Hydrol.*, 20 (1-2): 1-25.

Imhoff, P.T., Jaffe´, P.R., and Pinder, G. F. (1994). "An experimental study of complete dissolution of a non-aqueous phase liquid in saturated porous media." *Water Resour. Res.*, 30 (2): 307–320.

Itakura, T. , Airey, D. W., and Leo, C. J. (2003). "The diffusion and sorption of volatile organic compounds through kaolinitic clayey soils." *J. Contam. Hydrol.*, 65 (3-4): 219-243.

Jackson, S. (2004). *Comparative evaluation of permanganate and catalyzed hydrogen peroxide during in situ chemical oxidation of DNAPLs*. Master's thesis, Colorado School of Mines, Golden, CO. 132 pp.

Johnson, R.L. and Pankow, J.F. (1992). "Dissolution of dense chlorinated solvents into groundwater. 2. Source functions for pools of solvent." *Environ. Sci. & Technol.*, 26 (5): 896-901.

Johnson, R.L., Cherry, J.A., and Pankow, J.F. (1989). "Diffusive contaminant transport in natural clay: A field example and implications for clay-lined waste disposal sites." *Environ. Sci. Technol.*, 23 (3): 340-349.

Jury, W.A., Gardner, W.R., and Gardner, W.H. (1991). *Soil Physics, 5th ed.*. John Wiley & Sons, New York, NY, 328 pp.

Kueper, B.H., and Frind, E.O. (1991a). "Two-phase flow in heterogeneous porous media, 1, Model development." *Water Resour. Res.*, 27 (6): 1049-1057.

Kueper, B.H., and Frind, E.O. (1991b). "Two-phase flow in heterogeneous porous media, 2, Model application." *Water Resour. Res.*, 27 (6): 1059-1070.

Kueper, B.H., Abbott, W., and Farquhar, G. (1989). "Experimental observations of multiphase flow in heterogeneous porous media." *J. Contam. Hydrol.*, 5 (1): 83-95.

Kueper, B.H., Redman, D., Starr, R.C., Reitsma, S., and Mah. M. (1993). A field experiment to study the behavior of tetrachloroethylene below the water table: Spatial distribution of residual and pooled DNAPL. *Ground Water*, 31 (5): 756–766.

Ladbury, J.W. and Cullis, C.F. (1958). "Kinetics and mechanism of oxidation by permanganate." *Chem. Rev.*, 58 (2): 403-438.

Lee, E.S., Seol, Y., Fang, Y.C., and Schwartz, F.W. (2003). "Destruction efficiencies and dynamics of reaction fronts associated with the permanganate oxidation of trichloroethylene." *Environ. Sci. Technol.*, 37 (11): 2540-2546.

Lemke, L.D., Abriola, L.M., and Lang, J.R. (2004). "Influence of Hydraulic Property Correlation on Predicted Dense Non-aqueous Phase Liquid Source Zone Architecture, Mass Recovery and Contaminant Flux." *Water Resour. Res.*, 40, W12417, doi:10.1029/2004WR003061.

Liu, C. and Ball, W.P. (2002). "Back Diffusion of Chlorinated Solvent Contaminants from a Natural Aquitard to a Remediated Aquifer Under Well-Controlled Field Conditions: Predictions and Measurements." *Ground Water*, 40 (2): 175-184.

Lowe, K.S., Gardner, F.G., and Siegrist, R.L. (2002). "Field evaluation of in situ chemical oxidation through vertical well-to-well recirculation of NaMnO4." *Ground Water Monit. Rem.*, 22 (1): 106-115.

Mackay, D.M. and Cherry, J.A. (1989). "Groundwater contamination: Pump-and-treat remediation." *Environ. Sci. & Technol.*, 23 (6): 630-636.

MacKinnon, L.L. and Thomson, N.R. (2002). "Laboratory-scale in situ chemical oxidation of a perchloroethylene pool using permanganate." *J. Contam. Hydrol.*, 56 (1-2): 49-74.

Mayer, A.S. and Miller, C.T. (1996). The influence of mass transfer characteristics and porous media heterogeneity on non-aqueous phase dissolution. *Water Resour. Res.*, 32 (6): 1551-1567.

Mayer, A.S., Zhong, L. ,and Pope, G.A. (1999). Measurement of mass-transfer rates and surfactant-enhanced solubilization of non-aqueous phase liquids. *Environ. Sci. Technol.*, 33 (17): 2965-2972.

184

Miller, C.T., Poirier-McNeill, M.M., and Mayer, A.S. (1990). "Dissolution of trapped non-aqueous phase liquids: mass transfer characteristics." *Water Resour. Res.*, 26 (11): 2783-2793.

Millington, R.J. and Quirk, J.P. (1959). "Permeability of porous media." *Nature*, 183: 387-388.

Millington, R.J. and Quirk, J.P. (1961). "Permeability of porous solids." *Trans. Faraday Society*, 57: 1200-1207.

Moes, M., Peabody, C., Siegrist, R.L., and Urynowicz, M. (2000). Permanganate injection for source zone treatment of TCE DNAPL. In: Wickramanayake, G.B., Gavaskar, A.R., Chen, A.S.C. (Eds), *Chemical Oxidation and Reactive Barriers*. Battelle Press, Columbus, OH, pp. 117-124.

Mumford, K.G., Thomson, N.R., and Allen-King, R.M. (2002). "Investigating the kinetic nature of natural oxidant demand." In: Gavaskar, A.R. and Chen, A.S.,C (Eds), *Remediation of Chlorinated and Recalcitrant Compounds*. Battelle Press, Columbus, OH. 2C-37 (6 pp.).

Mumford, K.G., Lamarche, C.S., and Thomson, N.R. (2004). Natural oxidant demand of aquifer materials using the push-pull technique. *J. Environ. Eng.*, 130 (10): 1139-1146.

Mumford, K.G., Thomson, N.R., and Allen-King, R.M. (2005). Bench-scale investigation of permanganate natural oxidant demand kinetics. *Environ. Sci. Technol.*, 39 (8): 2835-2840.

Nambi, I.M. (1999). *Dissolution of non-aqueous phase liquids in heterogeneous subsurface systems*. Ph.D. dissertation, Dep. of Civ. and Environ. Eng., Clarkson Univ., Potsdam, NY.

Nambi, I.M. and Powers, S.E. (2003). "Mass transfer correlations for non-aqueous phase liquid dissolution from regions with high initial saturations." *Water Resour. Res.*, 39 (2): 1030, doi:10.1029/2001WR000667.

Nelson, M.D., Parker, B.L., Al, T.A., Cherry, J.A., and Loomer, D. (2001). "Geochemical Reactions Resulting from In Situ Oxidation of PCE-DNAPL by KMnO4 in a Sandy Aquifer." *Environ. Sci. Technol.*, 35 (6): 1266-1275.

Oostrom, M., Hofstee, C., Walker, R.C., and Dane, J.H. (1999). "Movement and remediation of trichloroethylene in a saturated, heterogeneous porous medium 2. Pump-and-treat and surfactant flushing." *J. Contam. Hydrol.*, 37 (1-2): 179-197.

Parker, B.L. Gillham, R.W., and Cherry, J.A. (1994). "Diffusive disappearance of immiscible-phase organic liquids in fractured geologic media." *Ground Water*, 32 (5): 805-820.

Parker, B.L., McWhorter, D.B., and Cherry, J.A. (1997). "Diffusive loss of non-aqueous phase organic solvents from idealized fracture networks in geologic media." *Ground Water*, 35 (6): 1077-1087.

Parker, B.L., Cherry, J.A., Chapman, S.W., and Guilbeault, M.A. (2003). "Review and analysis of chlorinated solvent dense non-aqueous phase liquid distributions in five sandy aquifers." *Vadose Zone J*., 2 (2): 116-137.

Pinder, G.F. and Abriola, L.M. (1986). "On the simulation of non-aqueous phase organic compounds in the subsurface." *Water Resour. Res*., 22 (9): 109S-119S.

Polak, A., Grader, A.S., Wallach, R., and Nativ, R. (2003). "Chemical diffusion between a fracture and the surrounding matrix: Measurement by computed tomography and modeling." *Water Resour. Res.*, 39 (4): 1106, doi:10.1029/2001WR000813.

Poulsen, M.M. and Kueper, B.H. (1992). "A field experiment to study the behavior of tetrachloroethylene in unsaturated porous media." *Environ. Sci. Technol*., 26 (5): 889-895.

Powers, S.E., Abriola, L.M., Dunkin, J.S., and Weber, W.J. Jr. (1994a). "Phenomenological models for transient NAPL-water mass-transfer processes." *J. Contam. Hydrol*., 16 (1): 1-33.

Powers, S.E., Abriola, L.M., and Weber Jr., W.J. (1994b). "An experimental investigation of non-aqueous phase liquid dissolution in saturated subsurfacesystems: Transient mass transfer rate." *Water Resour. Res*., 30 (2): 321-332.

Powers, S.E., Nambi, I.M., and Curry, G.W. Jr. (1998). "NAPL dissolution in heterogeneous systems: Mechanisms and a local equilibrium modeling approach." *Water Resour. Res*., 34 (12): 3293– 3302.

Reis, J.C. and Acock, A.M. (1994). "Permeability reduction models for the precipitation of inorganic solids in Berea sandstone." *In Situ*, 18 (3): 347-368.

Reitsma, S. and Dai, Q.L. (2001). Reaction-enhanced mass transfer and transport from non-aqueous phase liquid source zones. *J. Contam. Hydrol.*, 49: 49-66.

Reitsma, S. and Randhawa, J. (2002). "Experimental investigation of manganese dioxide plugging in porous media." In: Gavaskar, A.R. and Chen, A.S.C. (Eds), *Proc., 3rd Int. Conf. on Remediation of Chlorinated and Recalcitrant Compounds*, Monterey CA, May 2002. Battelle Press, Columbus, OH. 2C-39 (8pp.).

Reynolds, D.A. and Kueper, B.H. (2002). "Numerical examination of the factors controlling DNAPL migration through a single fracture." *Ground Water*, 40 (4): 368-377.

Ross, B. and Lu, N. (1999). "Dynamics of DNAPL penetration into fractured porous media." *Ground Water*, 37 (1): 140-147.

Saba, T.A. (1999). *Upscaling of mass transfer from entrapped NAPLs under natural and enhanced conditions.* Ph.D. Dissertation, University of Colorado, Boulder CO. 204 pp.

Saba, T.A. and Illangasekare, T.H. (2000). "Effect of ground-water flow dimensionality on mass transfer from entrapped non-aqueous phase liquid contaminants." *Water Resour. Res.*, 36 (4): 971-979.

Saba, T.A., Illangasekare, T.H., and Ewing, J.E. (2001). "Investigation of surfactant-enhanced dissolution of entrapped non-aqueous phase liquid chemicals in a two dimensional groundwater flow field." *J. Contam. Hydrol.*, 51: 63-82.

Saenton, S. (2003). *Prediction of mass flux from DNAPL source zone with complex entrapment architectur: model development, experimental validation, and up-scaling*. Ph.D. Dissertation, Colorado School of Mines, Golden CO. 246 pp.

Saenton, S., Illangesekare, T.H., Soga, K., and Saba, T.A. (2002). "Effects of source zone heterogeneity on surfactant-enhanced NAPL dissolution and resulting remediation end-points." *J. Contam. Hydrol.*, 59: 27-44.

Schnarr, M., Truax, C., Farquhar, G., Hood, E., Gonully, T., and Stickney, B. (1998). "Laboratory and controlled field experimentation using potassium permangante to remediate trichloroethylene and perchloroethylene DNAPLs in porous media." *J. Contam. Hydrol.*, 29 (3): 205-224.

Schroth, M.H, Oostrom, M., Wietsma, T.W., and Istok, J.D. (2001). "In situ oxidation of trichloroethene by permanganate: effects on porous medium hydraulic properties." *J. Contam. Hydrol.*, 50 (1-2): 79-98.

Schwille, F. (1988). *Dense Chlorinated Solvents in Porous and Fractured Media*. Lewis Publishers, Chelsea, MI. Translated by J.F. Pankow, 146 pp.

Seitz, S. (2004). *Experimental evaluation of mass transfer and matrix interactions during in situ chemical oxidation relying on diffusive transport.* MS Thesis, Colorado School of Mines, Golden, CO, 125 pp.

Sherwood, T.K., Pigford, R.L., and Wilke, C.R. (1975). *Mass Transfer.* McGraw-Hill, New York, NY. 677 pp.

Siegrist, R.L. and Lowe, K.S. (Eds). (1996). "In situ remediation of DNAPL compounds in low permeability media: Fate/transport, in situ control technologies, and risk reduction," *Oak Ridge National Laboratory Rep. No. ORNL/TM-13305* for the DOE Office of Science and Technology.

Siegrist, R.L., Lowe, K.S., Murdoch, L.C., Case, T.L., and Pickering, D.A. (1999). "In situ oxidation by fracture emplaced reactive solids." *J. Environ. Eng*., 125 (5): 429-440.

Siegrist, R.L., Urynowicz, M.A., West, O.R., Crimi, M.L., and Lowe, K.S. (2001). *Principles and practices of in situ chemical oxidation using permanganate.* Battelle Press, Columbus, OH, 348 pp.

Siegrist, R.L., Urynowicz, M.A., Crimi, M.L., and Lowe, K.S. (2002). "Genesis and effects of particles produced during in situ chemical oxidation using permanganate." *J. Environ. Eng.*, 128 (11): 1068-1079.

Stewart, R. (1965). "Oxidation by permanganate." In: Wiberg, K.B. (Ed.), *Oxidation in Organic Chemistry*, Part A, Chap. 1. Academic Press, New York, NY. pp. 1-68.

Stroo, H.F., Unger, M., Ward, C.H., Kavanaugh, M.C., Vogel, C., Leeson, A., Marqusee, J.A., and Smith, B.P. (2003). "Remediating chlorinated solvent source zones." *Environ. Sci. Technol.*, 37 (11): 224A-230A.

Struse, A.M., Siegrist, R.L., Dawson, H.E., and Urynowicz, M.A. (2002). "Diffusive transport of permanganate during in situ oxidation." *J. Environ. Eng*., 128(4): 327-334.

Taylor, T.P., Pennell, K.D., Abriola, L.M., and Dane, J.H. (2001). "Surfactant enhanced recovery of tetrachloroethylene from a porous medium containing low permeability lenses: 1. Experimental studies." *J. Contam. Hydrol.*, 48 (3-4): 325-350.

Tidwell, V.C., Meigs, L.C., Christian-Frear, T., and Boney, C.M. (2000). "Effects of spatially heterogeneous porosity on matrix diffusion as investigated by X-ray absorption imaging." *J. Contam. Hydrol.*, 42 (2): 285-302.

188

USEPA. (2004). "Discussion paper--Cleanup goals appropriate for DNAPL source zones." U.S. EPA, Office of Solid Waste and Emergency Response, Washington D.C., 16 pp., http://gwtf.cluin.org/docs/options/dnapl_goals_paper.pdf.

Urynowicz, M.A. (2000). *Dense non-aqueous phase trichloroethene degradation with permanganate ion*. Ph.D. Dissertation, Colorado School of Mines, Golden CO, 166 pp.

Welty, J.R., Wicks, C.E., and Wilson, R.E. (1976). *Fundamentals of momentum, heat, and mass transfer, 2nd ed.*. John Wiley & Sons, New York, NY. 789 pp.

Wyllie, M.R.J. (1962). "Relative permeability." In: *Petroleum Production Handbook, Reservoir Engineering, Vol II*, Frick, T.C. (Ed). McGraw-Hill, New York, NY.

Yan, E.Y. and Schwartz, F.W. (1999). "Oxidative degradation and kinetics of chlorinated ethylenes by potassium permanganate." *J. Contam. Hydrol*., 37 (3): 343-365.

Yan, E.Y. and Schwartz, F.W. (2000). "Kinetics and mechanisms for TCE oxidation by permanganate." *Environ. Sci. Technol*., 34 (12): 2535-2541.

Zhang, H. and Schwartz, F.W. (2000). "Simulating the in situ oxidative treatment of chlorinated ethylenes by potassium permanganate." *Water Resour. Res*., 36 (10): 3031-3042.

Zhu, J. and Sykes, J.F. (2000). The influence of NAPL dissolution characteristics on field-scale contaminant transport in subsurface. *J. Contam. Hydrol.*, 41: 133-154.

Chapter 5

OPTIMIZING PERMANGANATE TRANSPORT TO OVERCOME HIGH NATURAL OXIDANT DEMAND AT NAVY TRAINING CENTER, ORLANDO, FLORIDA – A NUMERICAL STUDY

5.1 Abstract

Natural oxidant demand (NOD) is a critical parameter that must be considered when designing and implementing an in situ chemical oxidation (ISCO) system. If site aquifer materials have a substantial amount of NOD, the NOD can actually drive the ISCO design even more so than the contaminant, because NOD is typically distributed through the entire site at mass levels greater than the dense non-aqueous phase liquid (DNAPL) mass to be remediated. Further, at least some large portion of the NOD may have a much higher oxidation rate than the contaminant. When using permanganate as the oxidant, NOD becomes even more critical; the oxidant consumption by NOD results in $MnO_2(s)$ formation that may alter the flow field decreasing the oxidant delivery to the source zone. Because of the complex interaction of oxidant consumption and $MnO_2(s)$ formation, optimum oxidant concentration and injection flow rate are not easily determined. Simulation provides a method of estimating NOD effects resulting from various injection flow rates and oxidant concentrations to assist in determining optimum delivery conditions.

Transport simulations were run for a variety of conditions varying the injection/extraction well flow rates and injected oxidant concentration. An additional set of simulations was run keeping the well flow rates and oxidant concentration constant while varying the amount of NOD as well as the NOD oxidation rate. No contaminant was present for any of the simulations, as the goal was to compare oxidant transport

under varying injection schemes and not to predict performance with respect to contaminant destruction.

The optimal oxidant delivery scenario was determined based on comparison of: distance of measurable MnO_4^-, distance of measurable NOD reduction, and extent of significant $MnO_2(s)$ generation. For the purpose of this study, significant $MnO_2(s)$ generation was considered to be a mass fraction of 1000 mg $MnO_2(s)$ /kg soil (shown on the graphs as 0.001 mg/mg). The selected cutoff represents a minimum 2.5% reduction in permeability based on a simple reduction in porosity. However, actual permeability loss may be as much as 10-20 times higher at some locations due to $MnO_2(s)$ clogging of pore throats before significantly filling porespace volume. Ideally, the MnO_4^- transport distance should be maximized while minimizing the $MnO_2(s)$ generation, as the $MnO_2(s)$ has the potential to decrease the permeability, thereby affecting the ability for oxidant to continue flushing through the desired region.

Simulation results showed that increasing the oxidant concentration resulted in a greater increase in the ratio of extent of significant $MnO_2(s)$ generation to oxidant transport distance than did increasing oxidant injection flow rate. These results suggest that low concentration injection at a high flow rate is the optimal method to deliver the required mass of oxidant so as to minimize unproductive oxidant consumption by NOD.

5.2   Introduction

Chlorinated solvents such as trichloroethylene (TCE) and tetrachloroethylene (PCE) are contaminants of concern in groundwater at many contaminated sites, ranking 16th and 30th respectively on the 2003 CERCLA Priority List of Hazardous Substances (ATSDR 2003). These chemicals have been used extensively since the early 20th century as cleaning solvents and as intermediate chemicals in production of pesticides, paints, refrigerants, and other chemicals (ATSDR 2004, USEPA 2004a, USHHS 2002). As contaminants, they are frequently present in the form of dense non-aqueous phase liquid (DNAPL) primary source zones, or as dissolved and/or sorbed contaminant in low

permeability media (LPM) secondary source regions (Johnson and Pankow 1992, Pankow and Cherry 1996, USEPA 1993, USEPA 2004b). Although they typically have solubilities in the parts-per-million range, the drinking water maximum contaminant levels (MCLs) are typically in the parts-per-billion range.

DNAPLs present a challenging source zone because of the complex nature of their movement through the subsurface. The interplay of viscous, gravitational, and capillary forces results in a non-uniform and unpredictable migration vertically and laterally. As the main body of DNAPL migrates, residual DNAPL is left behind as disconnected blobs and ganglia partially filling the pore space. Capillary forces hold this DNAPL residual in place, such that even relatively large hydraulic gradients can not further mobilize it (Kueper et al. 2003).

Chemical oxidation, specifically with permanganate, has been used to treat water and waste water for over 50 years. In the last fifteen years or so, chemical oxidation has become a promising in situ remediation technique for sites whose groundwater and soil are contaminated by chlorinated solvents, especially where contaminants are not present in DNAPL form. Field-scale pilot tests have shown encouraging results for sites contaminated with low levels of chlorinated solvents (Cline et al. 1997, Hood 2000, Lowe et al. 2002, Schnarr et al. 1998, Siegrist et al. 1999). A goal of ISCO is to speed up remediation of a contaminant source zone by inducing increased mass transfer (and subsequent destruction) from the source. Based on experimental results, Schnarr et al. (1998) suggest that NAPL dissolution and oxidation are processes that occur in parallel with increased mass transfer during oxidation occurring primarily as a result of an increased aqueous concentration gradient. Reitsma and Dai (2001) performed a theoretical study to estimate the maximum expected NAPL mass transfer enhancement resulting from chemical oxidation. They estimated a maximum five times increase in dispersive mass transport from a PCE NAPL pool resulting from the increased concentration gradient; however, they predict little enhancement in local-scale mass transfer from NAPL to aqueous phase suggesting no change in dissolution mass transfer

parameters. Further, they suggest that actual enhancement is likely to be less because permeability reduction and decreased interfacial contact area were not accounted for in the estimate. On the contrary, MacKinnon and Thomson (2002) calculated a ten times initial increase in PCE mass transfer from a DNAPL pool during a 2D oxidation experiment, with decreasing mass flux over time attributed to $MnO_2(s)$ formation.

Laboratory research has provided an understanding of many fundamental details of the technology. The reaction pathways and kinetics of permanganate oxidation of alkenyl halides, specifically chlorinated ethenes such as PCE and TCE have been elucidated (Huang et al. 1999, Huang et al. 2001, Huang et al. 2002, Schnarr et al. 1998, Yan and Schwartz 1999, Yan and Schwartz 2000). A number of researchers have also studied the impacts of water chemistry and porous media constituents on the reaction (Gates-Anderson et al. 2001, Glaze and Kang 1988, Li and Schwartz 2000, Urynowicz 2000, Vella and Veronda 1994).

Field soils and aquifer sediments typically contain natural organic matter (NOM) and other reductants that can be readily oxidized. These soil constituents are referred to collectively as natural oxidant demand (NOD), or sometimes soil oxidant demand (SOD), and compete with target contaminants for available oxidant. The original conceptual model of NOD oxidation proposed by Zhang and Schwartz (2000), in order to explain delayed breakthrough of MnO_4^- in column experiments by Schnarr et al. (1998), is that of an instantaneous sink (Figure 5.1a). Under this concept, all of the NOD must be oxidized before any PCE oxidation occurs; thus, in order to oxidize a given mass of PCE, the mass of MnO_4^- needed will be equal to the NOD plus the mass determined from the reaction stoichiometry. However, other studies provide evidence that not all NOD components are oxidized faster than the contaminant (Mumford et al. 2002, Mumford et al. 2005, Siegrist et al. 1999, Struse et al. 2002, Yan and Schwartz 1999). In light of these studies and because NOD is generally a complex mixture of components whose surface area available for oxidant contact varies, it is appropriate to treat NOD oxidation as a kinetic

process as depicted in Figure 5.1b. This means that oxidation of NOD and PCE occur simultaneously, with relative rates of oxidation controlling depletion of each.
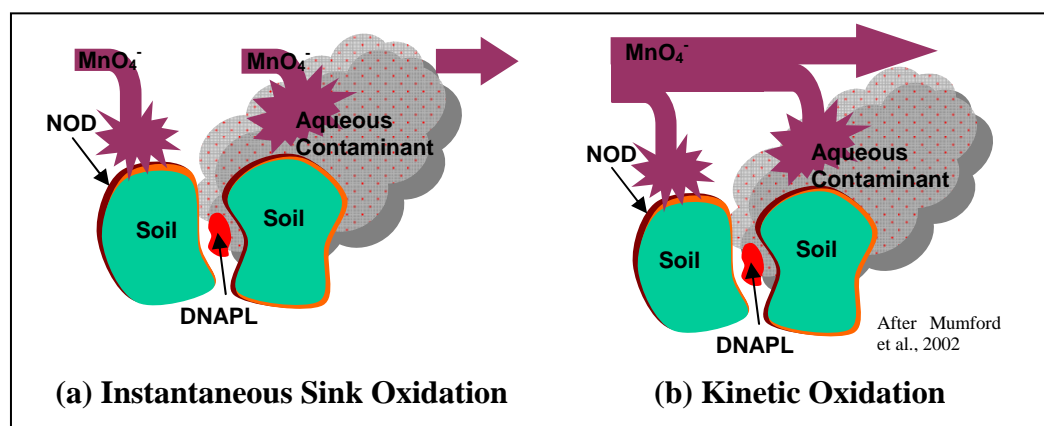
Figure 5.1: NOD Oxidation Conceptual Models

NOD is a critical parameter that must be considered when designing and implementing an ISCO system. If site aquifer materials have a substantial amount of NOD, the NOD can actually drive the ISCO design even more so than the contaminant. This is because the NOD is typically distributed through the entire site at mass levels greater than the DNAPL mass to be remediated, and at least some large portion of the NOD may have a much higher oxidation rate than the contaminant. As a result, oxidant delivery must be carefully designed to minimize the amount of oxidant unproductively consumed by NOD while maximizing the amount of oxidant that makes it to the contaminant. When using permanganate as the oxidant, NOD becomes even more critical; the oxidant consumption by NOD results in $MnO_2(s)$ formation that may alter the flow field decreasing the oxidant delivery to the source zone. In order to minimize the effect of NOD on oxidant delivery, the optimum oxidant concentration and delivery rate need to be selected. However, because of the complex interaction of oxidant consumption and $MnO_2(s)$ formation resulting from NOD, this is not easily determined.

Simulation provides a method of estimating NOD effects resulting from various injection flow rates and oxidant concentrations to assist in determining optimum delivery conditions.

Operable Unit 4 (OU4) of the former Naval Training Center (NTC) in Orlando, Florida (Figure 5.2), has groundwater contaminated with tetrachloroethylene (PCE). The contamination has been primarily attributed to dry-cleaning operations at the site. Initial site investigations identified the source area to be located beneath building 1100, and identified ISCO using permanganate as the remedial technology to be used to treat the contaminant source zone and subsequently reduce plume concentrations to acceptable levels (Tetra Tech NUS 2002). Subsequent pilot tests confirmed the viability of ISCO for the site and provided information for full-scale system design. However, problems were encountered with the full-scale system that may have been due to inaccurate estimation of the natural oxidant demand (NOD) of aquifer materials, and the impact of NOD on permanganate transport. Specifically, permanganate transport distances in the subsurface were found to be less than expected (CH2MHill 2003). The objective of this research was to evaluate the impact of NOD on oxidant transport and identify optimal oxidant delivery conditions for the high NOD levels (e.g., total organic carbon levels of 0.3-0.5%) of the NTC site.

Figure 5.2: Site Map, OU4, NTC, Orlando Florida (from Tetra Tech NUS 2002)

5.3   Methods

Simulations were performed, using the newly developed Chemical Oxidation Reactive Transport in 3D (CORT3D) computer model code, to look at the effect of NOD on permanganate transport under varied injection conditions.   The Groundwater Modeling System (GMS) 5.0 was used for pre- and post-processing of each simulation. The underlying groundwater flow solution used as input to the transport model came from the calibrated MODFLOW 2000 flow model provided by the Navy (Tetra Tech NUS 2002).

5.3.1 Description of CORT3D Numerical Model Code

CORT3D was developed to incorporate the processes listed in Table 3.1, which are important to simulation of ISCO. After development, the code was verified against analytical solutions or other verified numerical models, and then tested by modeling experiments of important ISCO processes. Refer to Chapter 3 for a full discussion of development and testing of CORT3D.

Table 5.1: Important Processes to be Captured by ISCO Model

Advection	2nd Order Contaminant Oxidation
Dispersion	Kinetic NOD oxidation
Sorption	Multiple NOD components
Diffusion	Permeability decrease due to $MnO_2(s)$ formation
DNAPL Dissolution	Permeability Increase due to DNAPL Dissolution

CORT3D is based on the existing 3D finite difference multi-component reactive contaminant transport code RT3D version 2.5 (Clement 1997, Clement 2002, Clement et al. 1998). It extends RT3D by expanding the diffusion process to handle each aqueous component independently, adding a chemical oxidation reaction package incorporating second-order contaminant and first-order NOD oxidation, and adding modules to simulate transient DNAPL dissolution and changing permeability from DNAPL dissolution and manganese oxide formation. The well-documented and commonly used groundwater flow code MODFLOW-2000, which can simulate the flow regime under both transient and steady-state conditions with a wide variety of boundary conditions and stresses (McDonald and Harbaugh 1988, Harbaugh et al. 2000), is used to generate the underlying spatial and temporal variations in groundwater head distribution.

The oxidation reaction package tracks a number of mobile and immobile species. The mobile species are: aqueous phase contaminant, permanganate (MnO_4^-), and chloride (Cl^-). Aqueous concentrations of MnO_4^- and Cl^- are calculated based on the reaction

stoichiometry. The stoichiometric ratios are adjustable to accommodate modeling oxidation of different contaminants. In addition to the specified mobile species, the model also tracks a number of immobile species, including: DNAPL phase contaminant, sorbed contaminant, $MnO_2(s)$, and NOD. NOD is broken into two components that can have different kinetic oxidation rates as suggested by a number of studies (Chambers et al. 2000, Crimi and Siegrist 2004, Jackson 2004, Mumford et al. 2005, Seitz 2004). $MnO_2(s)$ precipitates are assumed to be immobile, remaining at the location they are generated; however, permeabilities were not adjusted to account for the increase in solids occupying pore spaces as the permeability module had not been completed at the time of this study. Treating all the generated $MnO_2(s)$ as immobile provides a worst-case simulation of generated solids filling pore-space and potentially altering permeability.

5.3.2 Simulation of ISCO Injection

Simulation of the NTC site began by establishing a 3D rectangular model grid based on a MODFLOW flow model provided by the Navy. The grid covers an area 1600 feet (east-west) and 1200 feet (north-south), with boundaries sufficiently far from the actual site and injection/extraction well locations so that the wells do not impact the boundary conditions. The flow model consisted of a general head boundary to the east of the site based on extending the water table gradient to the eastern boundary, Lake Druid to the west, and no-flow boundaries along the north and south boundaries. The model included areal recharge at the surface (top), and leakage through the bottom of the lowest layer. The model domain was discretized into three layers (top layer 5' thick, middle layer 20' thick and bottom layer 40' thick, as provided). A horizontal grid cell size of 20' by 20' was used for most of the domain, with cell size further refined down to 4' by 4' at each well location. Figure 5.3 shows the model grid, boundary conditions, and steady-state groundwater head distribution for a total pumping rate of 15gpm. Note that groundwater head values are shown in cm H_2O, as units of feet resulted in too much roundoff error within the transport model.
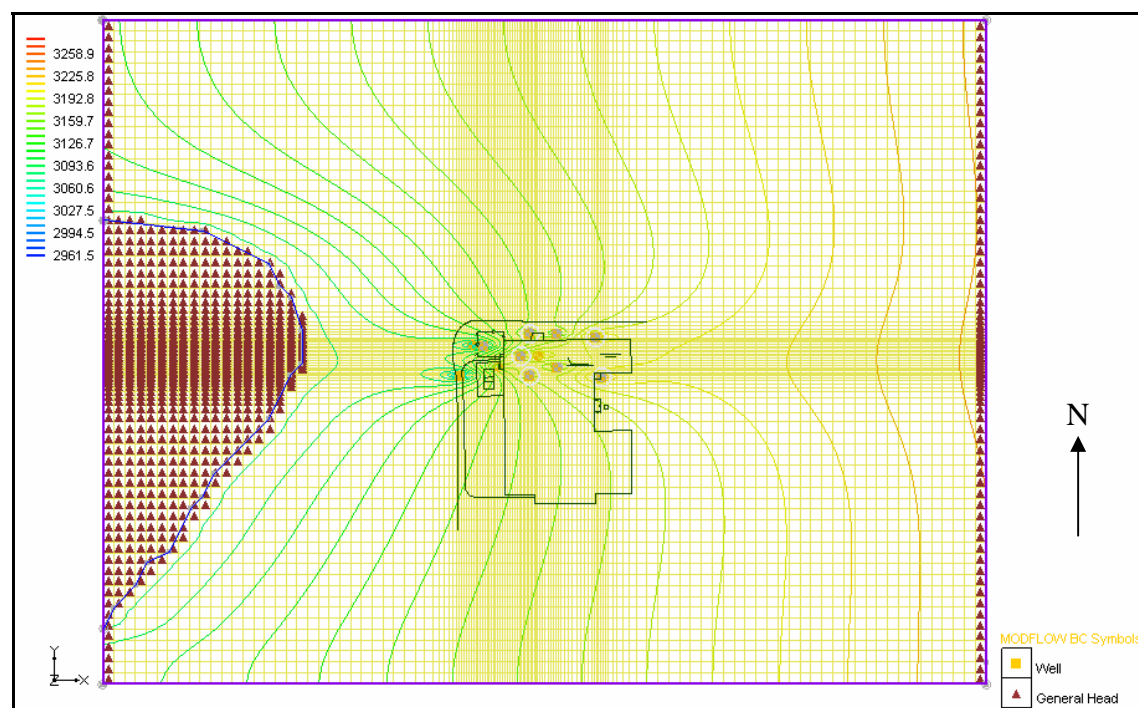
Figure 5.3: Model Grid and Groundwater Head Distribution (15gpm total well flow)

Transport simulations were run for a variety of conditions varying the injection/extraction well flow rates and injected oxidant concentration. An additional set of simulations was run keeping the well flow rates and oxidant concentration constant while varying the amount of NOD as well as the NOD oxidation rate. No contaminant was present for any of the simulations, as the goal was to compare oxidant transport under varying injection schemes and not to predict performance. Simulating conditions of no contamination kept the computer run time manageable, and provides a best case comparison of permanganate transport. See Table 5.2 for a summary of conditions used in each simulation.

Table 5.2: NTC Field Site Simulation Conditions

MnO$_4^-$ Conc (mg/mL)	Fast NOD fraction (mg/mg) Layer 1&2	Fast NOD fraction (mg/mg) Layer 3	Slow NOD fraction (mg/mg) Layer 1&2	Slow NOD fraction (mg/mg) Layer 3	Fast NOD Ox. Rate (1/sec)	Slow NOD Ox. Rate (1/sec)	Well Flow Rates (gpm) Total	Deep & Shallow Ext.	Deep Inj, Shallow Inj. 1 & 2	Shallow Inj. 3, 4, 5
0.25	0	0	0	0	5.56E-05	0	8	1.33	1.33	0.89
0.25	0.007	0.01	0	0	5.56E-05	0	5	0.83	0.83	0.56
0.25	0.007	0.01	0	0	5.56E-05	0	8	1.33	1.33	0.89
0.25	0.007	0.01	0	0	5.56E-05	0	10	1.67	1.67	1.11
0.25	0.007	0.01	0	0	5.56E-05	0	15	2.50	2.50	1.67
1.00	0.007	0.01	0	0	5.56E-05	0	5	0.83	0.83	0.56
1.00	0.007	0.01	0	0	5.56E-05	0	8	1.33	1.33	0.89
1.00	0.007	0.01	0	0	5.56E-05	0	10	1.67	1.67	1.11
1.00	0.007	0.01	0	0	5.56E-05	0	15	2.50	2.50	1.67
1.00	0.007	0.01	0	0	5.56E-05	0	48	8.00	8.00	5.33
4.00	0.007	0.01	0	0	5.56E-05	0	5	0.83	0.83	0.56
4.00	0.007	0.01	0	0	5.56E-05	0	8	1.33	1.33	0.89
4.00	0.007	0.01	0	0	5.56E-05	0	10	1.67	1.67	1.11
4.00	0.007	0.01	0	0	5.56E-05	0	15	2.50	2.50	1.67
4.00	0.007	0.01	0	0	5.56E-05	0	48	8.00	8.00	5.33
0.25	0.007	0.01	0	0	5.56E-06	0	8	1.33	1.33	0.89
0.25	0	0	0.0072	0.01	0	2.78E-05	8	1.33	1.33	0.89
0.25	0.011	0.015	0	0	5.56E-05	0	8	1.33	1.33	0.89
0.25	0.004	0.005	0	0	5.56E-05	0	8	1.33	1.33	0.89

Soil porosity (0.30) and initial mass fraction of NOD for soil within each layer were obtained from site investigation data provided by the Navy (CH2MHill 2003). NOD oxidation rates were estimated from batch tests (average of several runs with varied solids loading and mixing regimes) performed at Colorado School of Mines by Crimi and Siegrist (2004). Each simulation covers a one year period, and the figures show the distribution of the specified component after one year of continuous oxidant injection.

The 5, 10, and 15gpm flow rates, as well as the 1.0 and 4.0mg/mL oxidant concentrations were selected because they were used for the pilot tests and/or previous simulations. An additional flow rate of 8gpm was also initially selected for simulation, and for analyzing sensitivity to NOD mass fraction and kinetic oxidation rate. The

0.25mg/mL oxidant concentration was used because it was the concentration recommended as a result of the laboratory research done at Colorado School of Mines by Crimi and Siegrist (2004). That research indicated the lower oxidant concentrations result in slower oxidant depletion from NOD while still destroying PCE (for the NTC site soil). Further, 48gpm total flow simulations were added based on initial results suggesting higher flow rates would be better.

5.3.3   Comparing Extent of Oxidant Transport and Manganese Oxide Formation

The optimal oxidant delivery scenario was determined based on comparison of: distance of measurable MnO_4^-, distance of measurable NOD reduction, and extent of significant $MnO_2(s)$ generation. For the purpose of this study, significant $MnO_2(s)$ generation was considered to be a mass fraction of 1000 mg $MnO_2(s)$ /kg soil (shown on the graphs as 0.001 mg/mg). The selected cutoff represents a minimum 2.5% reduction in permeability based on a simple reduction in porosity using Equation 5.1 (Reis and Acock (1994).

$$k_{r,w} = \left(1 - \frac{\phi - \phi_{eff}}{\phi} \right)^{3.6}$$
(5.1)

where $k_{r,w}$ is relative water permeability, ϕ is the original porosity, and ϕ_{eff} is the effective porosity based on the volume of $MnO_2(s)$. Because the density of hydrous, porous $MnO_2(s)$ precipitates generated by oxidation in the subsurface is not known, it was assumed to be 1000mg/mL (20% of the density of dry, solid manganese oxide). However, actual permeability loss may be as much as 10-20 times higher at some locations due to $MnO_2(s)$ clogging of pore throats before significantly filling porespace volume. This was demonstrated by research described in Chapters 3 and 4, where the effective density of generated $MnO_2(s)$ was estimated to be less than 100mg/mL. Ideally, the MnO_4^- transport distance should be maximized while minimizing the $MnO_2(s)$

generation, as the $MnO_2(s)$ has the potential to decrease the permeability, thereby affecting the ability for oxidant to continue flushing through the desired region.

5.4   Results and Discussion

This study resulted in a large number of graphs, of which only the most significant are included here (Appendix E contains the full set of graphs from this study). Figure 5.4 shows the dramatic impact presence of NOD can have on oxidant transport. Both figures simulate the same conditions (groundwater flow, pumping rates, oxidant concentration), except that the bottom figure represents a system initially containing NOD at the mass fraction present at the NTC site and the top figure represents a system with no NOD.

Increasing the oxidant concentration from 0.25mg/mL to 4.0 mg/L resulted in a 1000% increase in the extent of significant $MnO_2(s)$ generation; however the oxidant transport distance only increased by 240% (Figure 5.5 top row compared to middle row). On the other hand, for a given oxidant concentration, increasing the flow rate from 5 to 15gpm increased the transport distance by 200% with only a 500% increase in the extent of significant $MnO_2(s)$ generation (Figure 5.5 middle row compared to bottom row). These results suggest that low concentration injection at a high flow rate is the optimal method to deliver the required mass of oxidant so as to minimize unproductive oxidant consumption by NOD.
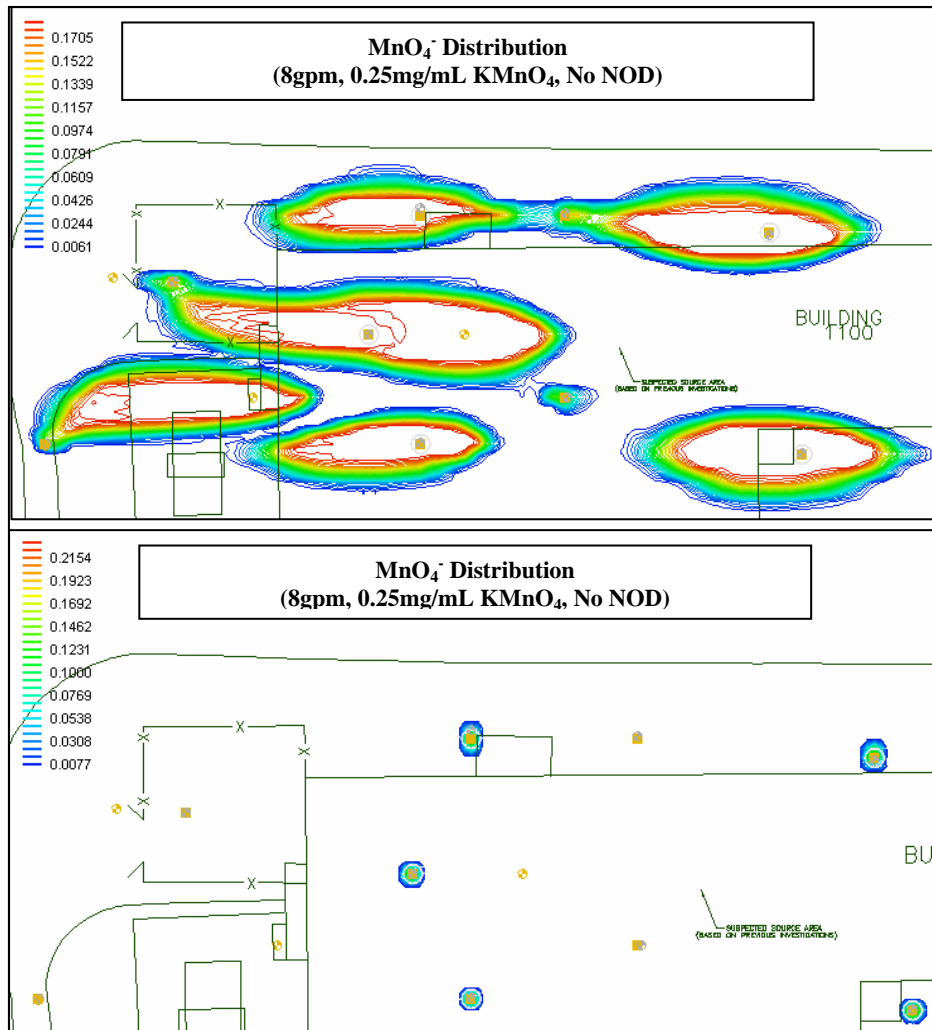
Figure 5.4: Comparison of Oxidant Transport Simulation Results, No NOD (top), with NOD (bottom)
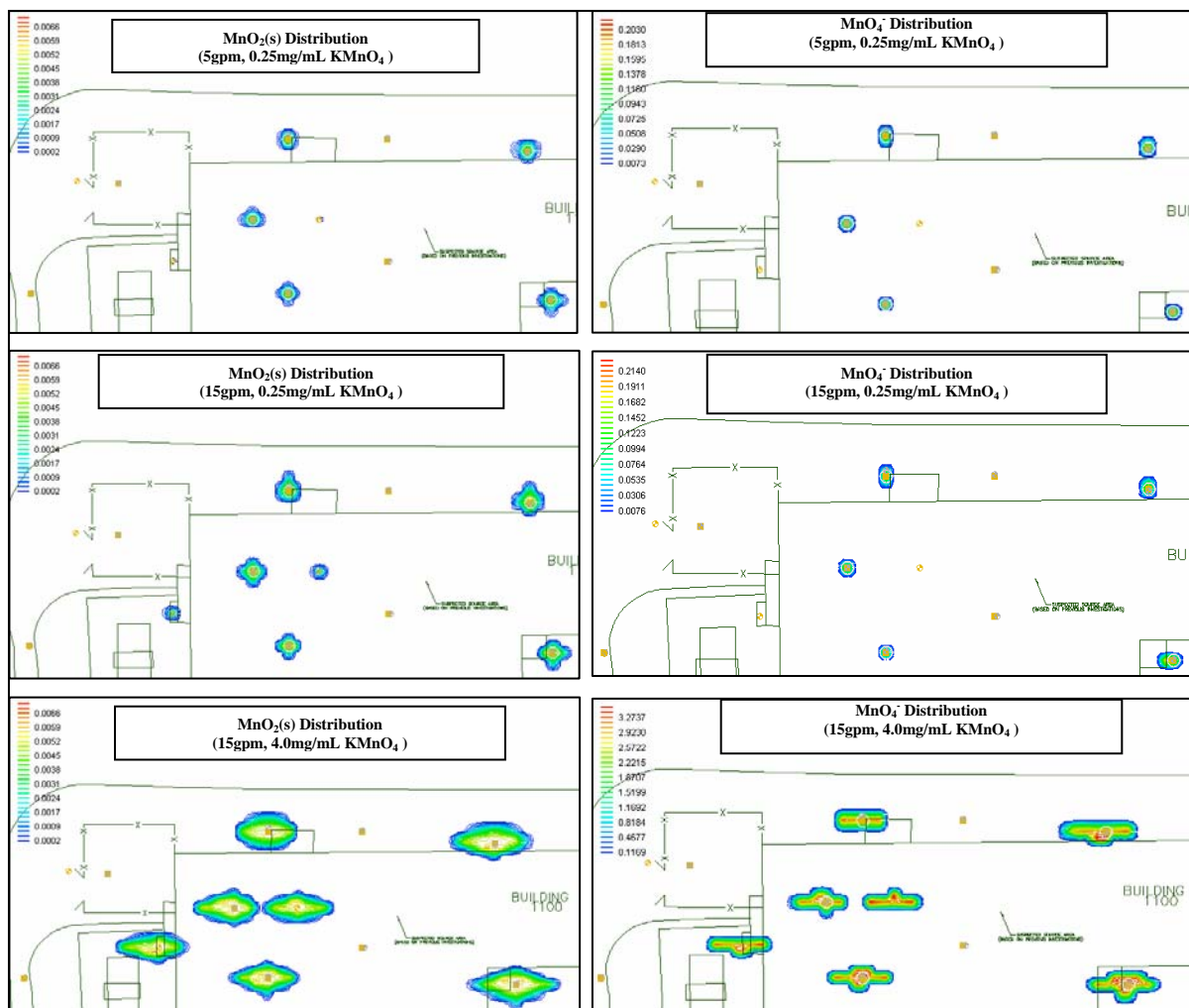
**Figure 5.5: Comparison of Oxidant Transport at NTC Site, $MnO_2(s)$ (left), MnO_4^- (right)
(middle row-base case, top-low flow rate, bottom-high oxidant concentration)**

Simulations were also run at a constant flow rate (8gpm) and oxidant concentration (0.25mg/mL) while varying the NOD mass fraction and kinetic rate to assess the sensitivity to these parameters. It was found that decreasing the NOD kinetic rate by a factor of 10 to simulate NOD with a much slower oxidation rate resulted in little or no change in transport distance. Presumably, this is because the fast NOD oxidation

rate was still so high as to be almost instantaneous. Similarly, increasing the mass fraction of fast NOD by 50% had little effect. On the other hand, decreasing the mass fraction of fast NOD by 50% resulted in a 50% increase in the oxidant transport distance (Figure 5.6, bottom right inset compared to bottom left).
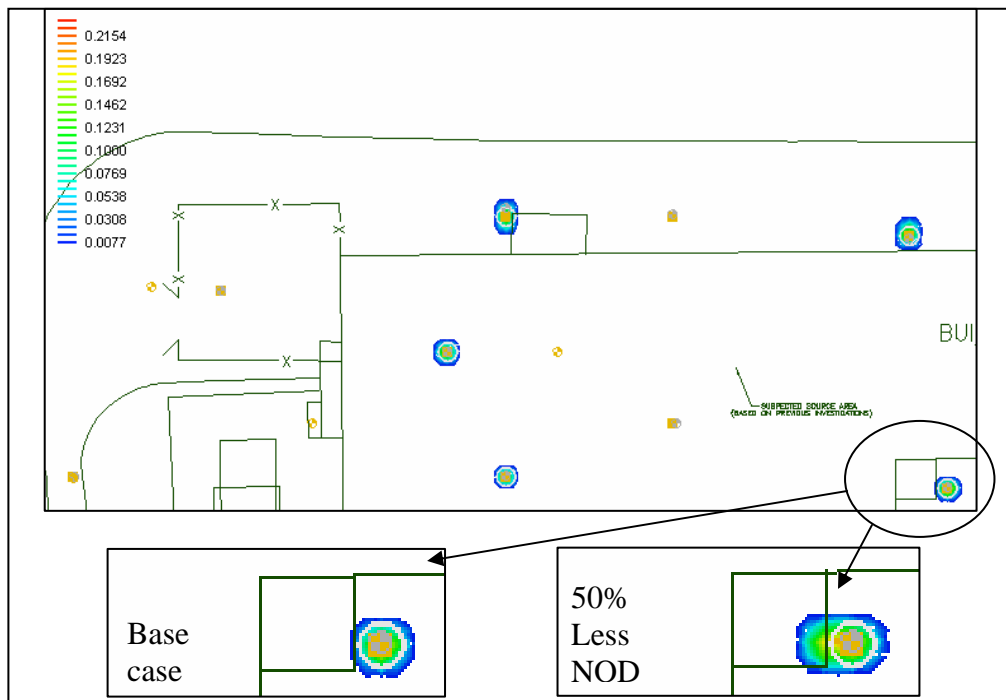
Figure 5.6: Effect of 50% reduction in NOD on MnO_4^- Distribution

Because initial results suggested that a low concentration delivered at a high flow rate may be optimal, two additional simulations were run at 48gpm total injection rate. One simulation utilized the higher 4.0mg/mL oxidant concentration; the other used the low 250 mg/L. As might be expected, for 48gpm oxidant injections, the permanganate transport is greater for 4000 mg/L (Figure 5.7a) than for 250 mg/L (Figure 5.7b) by a factor of approximately 2.7. However, the significant $MnO_2(s)$ generation increases by a

factor greater than 3 for the high concentration delivery (Figure 5.7a) compared to the low concentration delivery (Figure 5.7b).
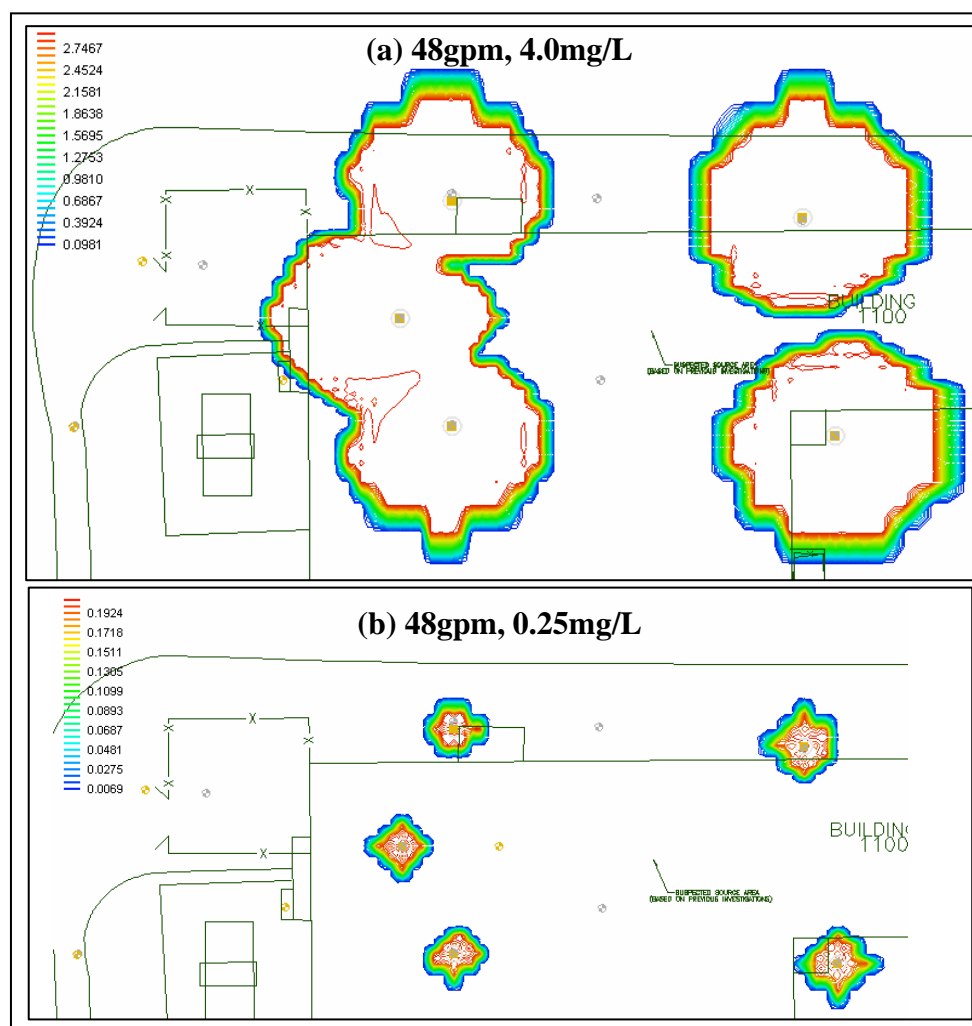
Figure 5.7: Comparison of Oxidant Transport for High Flow
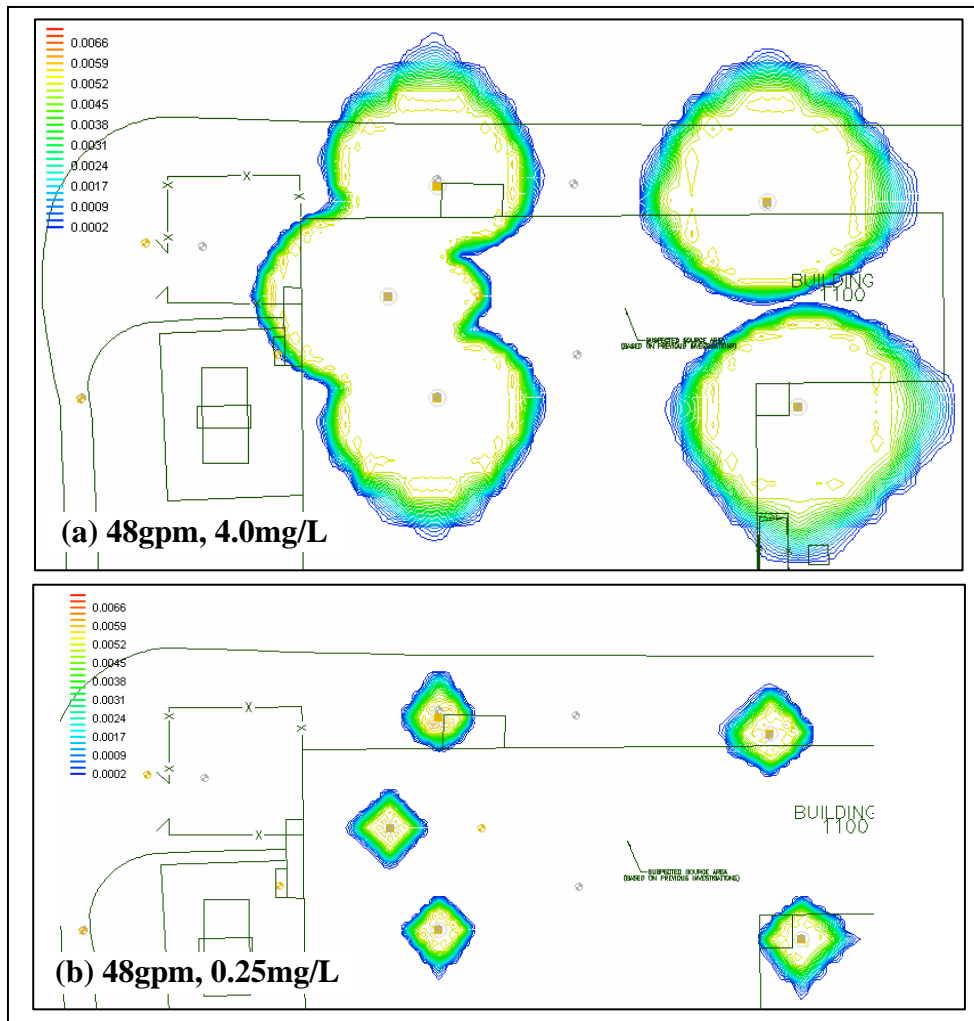
Figure 5.8: Comparison of MnO$_2$(s) Distribution for High Flow

These simulation results further support the conclusion that although a higher concentration may result in greater permanganate transport, it comes at the cost of even greater extent of MnO$_2$(s) generation. Although 1000 mg/kg of MnO$_2$(s) generation may result in as little as a 0.6% porosity reduction (depending on the actual density of the hydrous manganese oxide solids formed), the work of Chapters 3 and 4 demonstrate that the permeability reduction is likely to be as much as 10-20 times the 2.5% estimated

solely based on a porosity change using a density of 1000mg/mL. A large permeability reduction will result in greatly increased flow bypassing that may dramatically reduce the amount of oxidant reaching the desired source zone.

Figure 5.9 is a graph showing the number of source zone pore volumes and the duration of oxidant flushing necessary to destroy a hypothetical DNAPL source zone containing 10,000kg of PCE evenly distributed with a 20% DNAPL saturation. This comparison assumes all of the oxidant entering the source zone participates in PCE oxidation (no mass transfer limitations), and does not reflect NOD consumption of oxidant nor permeability reductions. Figure 5.9 shows that (as expected) decreasing the oxidant concentration inversely increases the number of pore volumes needed. On the other hand, while increasing the number of pore volumes and using a higher pumping rate will increase pumping costs, the higher flow rate minimizes the operational period. Sampling, analysis, and manpower costs are related to pumping duration and are likely to outweigh the increased pumping costs. Further, because simulation results suggested higher flow rate and lower oxidant concentration would be best, utilizing one of the lower flow rates or higher concentrations is going be less effective at ensuring the required oxidant reaches the source zone.
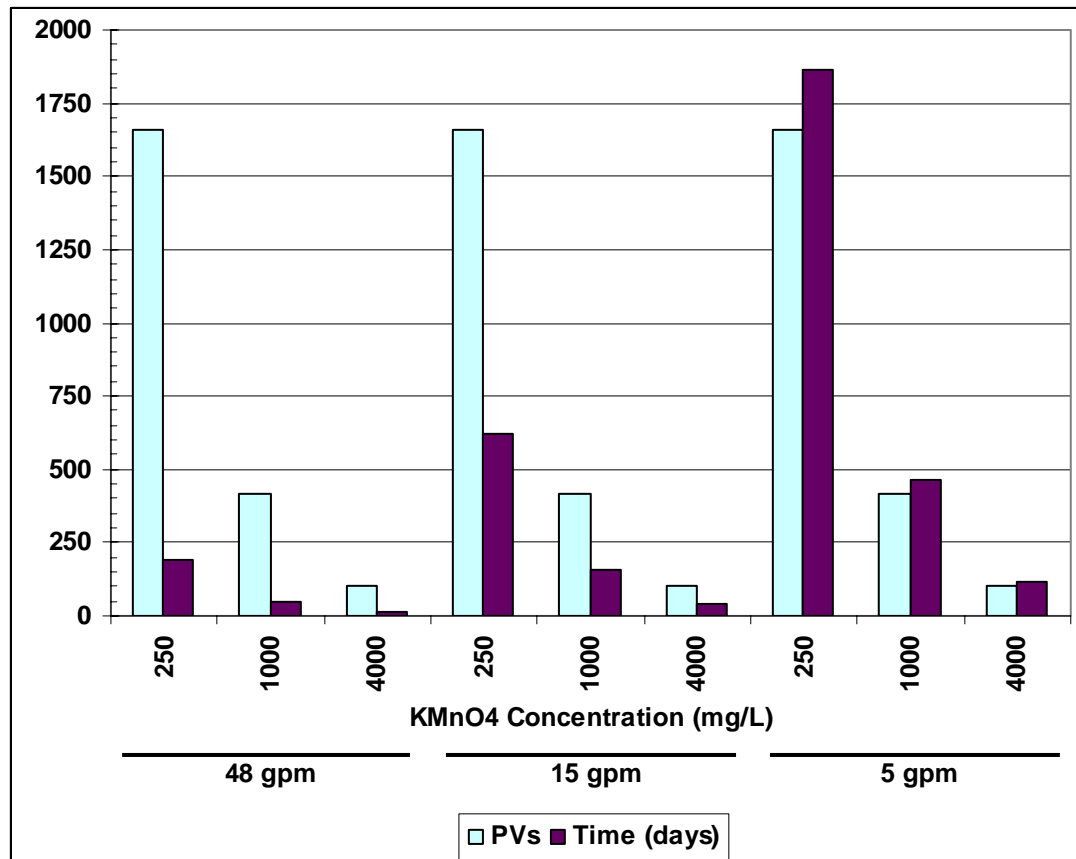
Figure 5.9: Comparison of Time and Pore Volumes Needed to Destroy Hypothetical 10,000kg PCE DNAPL Residual Source

A comparison of operational period and number of pore volumes required is useful information, but is not enough information upon which to base the design decision. Without considering the effects of NOD, an analysis like Figure 5.9 may suggest a high flow rate and high oxidant concentration as the best combination. However, simulation of NOD conditions at the specific site provides additional information which when taken into account with an analysis like in Figure 5.9 point to low oxidant concentration and high flow rate as a better design choice.

5.5   Conclusions

This research highlights the critical need to properly considering NOD when designing and implementing an ISCO system. It also demonstrates the importance of having a tool such as CORT3D to investigate various delivery schemes given particular site conditions. The optimal oxidant delivery design is not likely to be obvious, and this type of simulation study can help find it.

Based on the results of this study, a lower oxidant concentration delivered at a high injection/extraction well flow rate will provide optimal oxidant delivery effectiveness and limit unproductive oxidant consumption by the high NOD soil of the NTC site. This is based on comparison of: distance of measurable MnO_4^-, distance of measurable NOD reduction, and extent of $MnO_2(s)$ generation. Ideally, the MnO_4^- transport distance should be maximized while minimizing the $MnO_2(s)$ generation, as the $MnO_2(s)$ has the potential to decrease the permeability affecting the ability for oxidant to continue flushing through the desired region.

These simulation results provide a good qualitative comparison of different oxidation scenarios. Additionally, simulation results for an oxidant dose of 1 mg/mL at 15gpm generally agree with actual sampling results (CH2MHill 2003), further confirming the effectiveness of the model. The sampling results showed that MnO_4^- was generally measurable up to 18 feet from injection wells, while the simulation showed MnO_4^- up to about 10 feet from injection wells (Figure 5.10) and NOD reduction up to 16 feet from injection wells. Actual oxidant transport is expected to exceed simulation results for several reasons. First, the NOD mass fractions used in the simulation came from laboratory batch tests that provide an estimate of ultimate NOD; however, the actual NOD that is accessible to oxidant in situ is generally expected to be quite a bit less. This is supported well by the simulation results that showed a 50% increase in transport distance when the initial NOD present was reduced by half (Figure 5.6). Second, to represent the worst case scenario, the simulation was run considering the NOD to consist entirely of fast NOD (i.e., fast NOD oxidation rate), whereas the actual NOD is expected

to include some fraction that oxidizes at a slower rate. Additionally, the model was constructed with each layer being homogeneous, while the actual site may include some local-scale heterogeneities that result in regions of different transport velocities.

15 gpm, 1.0 mg/mL

Purple bar is 10 ft
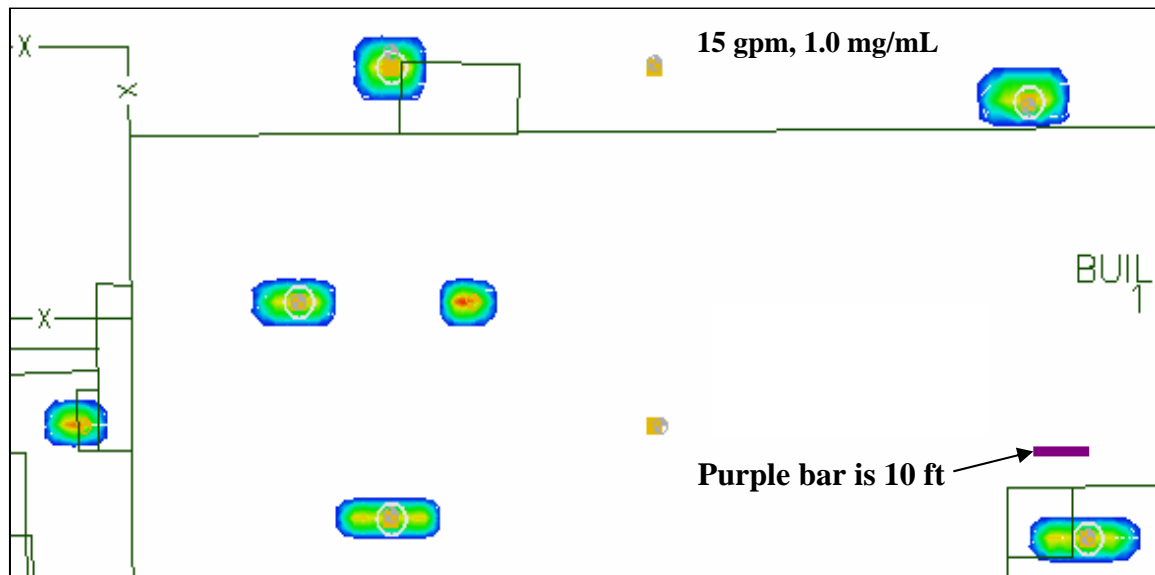
Figure 5.10: Simulated Permanganate Transport under Field Pilot Study Delivery Conditions

5.6   References

ATSDR. (2003). "2003 CERCLA Priority List of Hazardous Substances." Agency for Toxic Substances and Disease Registry, Division of Toxicology, U.S. Dept. of Health and Human Services. Oct. 2003. http://www.atsdr.cdc.gov/clist.html.

ATSDR. (2004). "Medical management guidelines (MMGs) for tetrachloroethylene." Agency for Toxic Substances and Disease Registry, Division of Toxicology, U.S. Dept. of Health and Human Services. May 2004. http://www.atsdr.cdc.gov/MHMI/mmg18.html.

CH2MHill, 2003. *Technical Memorandum: ISCO Injection Well Investigative Results, July-September 2003*. Atlanta, GA. 31 pp.

Clement, T.P. (1997). *A modular computer code for simulating reactive multi-species transport in 3-D groundwater systems*. PNNL-11720, Pacific Northwest National Laboratory, Richland WA, 1997. 59 pp.

Clement, T.P. (2002). *What's new in RT3D verstion 2.5*. Pacific Northwest National Laboratory, Richland WA, 2002. 20 pp.

Clement, T.P., Sun, Y., Hooker, B.S., and Petersen, J.N. (1998). "Modeling multispecies reactive transport in ground water." *Ground Water Monit. Rem*.; 18 (2): 79-92.

Cline, S.R., West, O.R., Korte, N.E., Gardner, F.G., Siegrist, R.L., and Baker, J.L. (1997). "KMnO4 chemical oxidation and deep soil mixing for soil treatment." *Geotech. News*, 15 (5): 25-28.

Crimi M. and Siegrist, R.L. (2004). *Experimental Evaluation of In Situ Chemical Oxidation Activities at the Naval Training Center (NTC) Site, Orlando, Florida*. Naval Facilities Engineering Command, Port Hueneme CA. 64 pp.

Delshad, M., Pope, G.A., and Sephrenoori, K. (1996). "A compositional simulator for modeling surfactant enhanced aquifer remediation: 1. Formulation." *J. Contam. Hydrol*., 23 (4): 303-327.

Doherty, J. (2003). *Manual for PEST 7.0*. Watermark Numerical Computing, Brisbane Australia, 279 pp. http://www.sspa.com/pest.

Gates-Anderson, D.D., Siegrist, R.L., and Cline, S.R. (2001). "Comparison of potassium permanganate and hydrogen peroxide as chemical oxidants for organically contaminated soils." *J. Environ. Eng.*, 127 (4): 337-347.

Glaze, W.H. and Kang, J.-W. (1988). "Advanced oxidation processes for treating groundwater contaminated with TCE and PCE: laboratory studies." *J. AWWA*, 88 (5): 57-63.

Harbaugh, A.W., Banta, E.R., Hill, M.C., and McDonald, M.G. (2000). *MODFLOW-2000, the U.S. Geological Survey modular ground-water model—User guide to modularization concepts and the ground-water flow process model*: U.S. Geological Survey Open-File Report 00-92, 130 pp.

Hood, E. (2000). *Permanganate Flushing of DNAPL Source Zones: Experimental and Numerical Investigation*. Ph.D. Dissertation, University of Waterloo, Waterloo, ON. 243 pp.

Huang, K., Hoag, G.E., Chheda, P., Woody, B.A., and Dobbs, G.M. (1999). "Kinetic study of oxidation of trichloroethylene by potassium permanganate." *Environ. Eng. Sci.*, 16 (4): 265-274.

Huang, K., Hoag, G.E., Chheda, P., Woody, B.A., and Dobbs, G.M. (2001). "Oxidation of chlorinated ethenes by potassium permanganate: a kinetics study." *J. Haz. Mater.*, 87 (1-3): 155-169.

Huang, K., Hoag, G.E., Chheda, P., Woody, B.A., and Dobbs, G.M. (2002). "Kinetics and mechanism of oxidation of tetrachloroethylene with permanganate." *Chemosphere*, 46 (6): 815-825.

Jackson, S. (2004). *Comparative evaluation of permanganate and catalyzed hydrogen peroxide during in situ chemical oxidation of DNAPLs.* Master's thesis, Colorado School of Mines, Golden, CO. 132 pp.

Johnson, R.L. and Pankow, J.F. (1992). "Dissolution of dense chlorinated solvents into groundwater. 2. Source functions for pools of solvent." *Environ. Sci. & Technol.*, 26 (5): 896-901.

Kueper, B.H., Wealthall, G.P., Smith, J.W.N., Leharne, S.A., and Lerner, D.N. (2003). *An illustrated handbook of DNAPL transport and fate in the subsurface.* Environment Agency R&D Publication 133, Environmental Agency, Almondsbury, Bristol, U.K. 67 pp.

Lenhard, R.J., Oostrom, M., and White, M.D. (1995). "Modeling fluid flow and transport in variably saturated porous media with the STOMP simulator. 2. Verification and validation exercises." *Adv. Water Resour.*, 18 (6): 365-373.

Li, X.D. and Schwartz, F.W. (2000). Efficiency problems related to permanganate oxidation schemes. In: Wickramanayake, G.B., Gavaskar, A.R., Chen, A.S.C. (Eds), *Chemical Oxidation and Reactive Barriers.* Battelle Press, Columbus, OH, pp. 41-48.

Lowe, K.S., Gardner, F.G., and Siegrist, R.L. (2002). "Field evaluation of in situ chemical oxidation through vertical well-to-well recirculation of NaMnO4." *Ground Water Monit. Rem.*, 22 (1): 106-115.

MacKinnon, L.L. and Thomson, N.R. (2002). "Laboratory-scale in situ chemical oxidation of a perchloroethylene pool using permanganate." *J. Contam. Hydrol.*, 56 (1-2): 49-74.

McDonald, M.G., and Harbaugh, A.W. (1988). A modular three-dimensional finite-difference ground-water flow model: U.S. Geological Survey Techniques of Water-Resources Investigations, book 6, chap. A1, 586 pp.

Mumford, K.G., Thomson, N.R., and Allen-King, R.M. (2002). "Investigating the kinetic nature of natural oxidant demand." In: Gavaskar, A.R. and Chen, A.S.,C (Eds), *Remediation of Chlorinated and Recalcitrant Compounds*. Battelle Press, Columbus, OH. 2C-37 (6 pp.).

Mumford, K.G., Thomson, N.R., and Allen-King, R.M. (2005). Bench-scale investigation of permanganate natural oxidant demand kinetics. *Environ. Sci. Technol.*, 39 (8): 2835-2840.

Pankow, J.F. and Cherry, J.A. (Eds). (1996). Dense Chlorinated Solvents and Other DNAPLs in Groundwater: History, Behavior, and Remediation. Waterloo Press, Portland, OR, 525 pp.

Pruess, K., Oldenburg, C., and Moridis, G. (1999). *TOUGH2 User's Guide, Version 2.0*, Lawrence Berkeley National Laboratory Report LBNL-43134, Berkeley, CA, November 1999.

Reitsma, S. and Dai, Q.L. (2001). Reaction-enhanced mass transfer and transport from non-aqueous phase liquid source zones. *J. Contam. Hydrol.*, 49: 49-66.

Schnarr, M., Truax, C., Farquhar, G., Hood, E., Gonully, T., and Stickney, B. (1998). "Laboratory and controlled field experimentation using potassium permangante to remediate trichloroethylene and perchloroethylene DNAPLs in porous media." *J. Contam. Hydrol.*, 29 (3): 205-224.

Seitz, S. (2004). *Experimental evaluation of mass transfer and matrix interactions during in situ chemical oxidation relying on diffusive transport*. MS Thesis, Colorado School of Mines, Golden, CO, 125 pp.

Siegrist, R.L., Lowe, K.S., Murdoch, L.C., Case, T.L., and Pickering, D.A. (1999). "In situ oxidation by fracture emplaced reactive solids." *J. Environ. Eng.*, 125 (5): 429-440.

Siegrist, R.L., Urynowicz, M.A., West, O.R., Crimi, M.L., and Lowe, K.S. (2001). *Principles and practices of in situ chemical oxidation using permanganate*. Battelle Press, Columbus, OH, 348 pp.

214

Struse, A.M., Siegrist, R.L., Dawson, H.E., and Urynowicz, M.A. (2002). "Diffusive transport of permanganate during in situ oxidation." *J. Environ. Eng*., 128(4): 327-334.

Tetra Tech NUS. (2002). *Remedial Design Report for the In Situ Chemical Oxidation System, NTC, Orlando, Florida*. February 2002. Pittsburgh, PA. 278 pp.

Urynowicz, M.A. (2000). *Dense non-aqueous phase trichloroethene degradation with permanganate ion*. Ph.D. Dissertation, Colorado School of Mines, Golden CO. 166 pp.

USEPA. (1993). *Evaluation of the likelihood of DNAPL presence at NPL sites*. U.S. EPA Rep. No. EPA/540/R-93/073, Office of Solid Waste and Emergency Response, Washington D.C. 114 pp., http://www.epa.gov/superfund/resources/remedy/pdf/540r-93073-s.pdf.

USEPA. (2004a). *Contaminant focus-trichloroethylene*. U.S. EPA, Technology Innovation Program, Washington D.C. http://www.clu-in.org/ contaminantfocus/default.focus/sec/Trichloroethylene_(TCE)/cat/Overview/.

USEPA. (2004b). *Discussion paper--Cleanup goals appropriate for DNAPL source zones*. U.S. EPA, Office of Solid Waste and Emergency Response, Washington D.C., 16 pp., http://gwtf.cluin.org/docs/options/dnapl_goals_paper.pdf.

USHHS. (2002). *Report on Carcinogens, Tenth Edition*. U.S. Department of Health and Human Services, Public Health Service, National Toxicology Program, December 2002. http://ehp.niehs.nih.gov/roc/toc10.html.

White, M.D., Oostrom, M., and Lenhard, R.J. (1995). "Modeling fluid flow and transport in variably saturated porous media with the STOMP simulator. 1. Nonvolatile three-phase model description." *Adv. Water Resour*., 18 (6): *353-364*.

Yan, E.Y. and Schwartz, F.W. (1999). "Oxidative degradation and kinetics of chlorinated ethylenes by potassium permanganate." *J. Contam. Hydrol*., 37 (3): 343-365.

Yan, E.Y. and Schwartz, F.W. (2000). "Kinetics and mechanisms for TCE oxidation by permanganate." *Environ. Sci. Technol*., 34 (12): 2535-2541.

Zhang, H. and Schwartz, F.W. (2000). "Simulating the in situ oxidative treatment of chlorinated ethylenes by potassium permanganate." *Water Resour. Res*., 36 (10): 3031-3042.

Zheng, C. and Wang, P.P. (1999). *MT3DMS: A modular three-dimensional multispecies transport model for simulation of advection, dispersion, and chemical reactions of contaminants in groundwater systems; documentation and user's guide*. Contract Report SERDP-99-1, U.S. Army Engineer Research and Development Center, Vicksburg, MS.

Chapter 6

CONCLUSIONS

6.1   Summary

In situ chemical oxidation using permanganate is a promising remedial technology for dealing with groundwater contamination from dense non-aqueous phase liquid (DNAPL) sources of chlorinated ethenes. While research has advanced the understanding of fundamental processes of ISCO using permanganate, questions remain about oxidant delivery and effects on DNAPL source zone depletion performance. Previous research has shown that manganese oxide solids formed at the DNAPL-water interface can diminish the magnitude of enhanced mass transfer from the DNAPL into the aqueous phase (and subsequent destruction by oxidation). However, additional research was needed to investigate the effects of oxidation using permanganate on a complex DNAPL source zone at field sites using intermediate-scale experiments.

Because of potential permeability and mass transfer effects from generation of manganese oxides, successful field implementation of the technology requires optimal design of oxidant delivery rate, concentration, location, and duration. These parameters interact in a complex manner, affected by site and source conditions such as DNAPL configuration and natural oxidant demand of the aquifer material. A numerical model code, capable of simulating the complex interaction of site, source, and delivery conditions will provide a design and decision tool for more effectively implementing ISCO using permanganate. The decision tool can be used to help screen site conditions and determine if ISCO using permanganate is feasible. If ISCO using permanganate is found to be feasible, the tool can be used to assess different oxidant delivery scenarios and identify the optimal scheme. Such a model code will also be useful for quantifying and understanding the interaction of factors affecting ISCO using permanganate

including: NOD, soil heterogeneity, source morphology (e.g., ganglia versus pool), groundwater velocity, oxidant concentration, and oxidant delivery location.

This dissertation focused on two areas. First, was the development and testing of a numerical model code for simulating ISCO using permanganate that can be used to investigate the interaction of factors controlling the effective implementation of the technology. Next, an intermediate-scale 2D experiment was conducted to investigate the effects of ISCO using permanganate on a complex DNAPL source zone containing multiple sources of various configurations.

6.1 Conclusions

Chapter 3 described the development of the Chemical Oxidation Reactive Transport in 3D (CORT3D) numerical tool.

- The tool was able to reproduce and predict results of 1D experiments highlighting ISCO processes including NOD oxidation, DNAPL PCE oxidation, DNAPL TCE oxidation.

- A power law relation was able to capture the reduction of permeability due to manganese oxide formation in 1D column experiments.

- Simulations of PCE oxidation experiments highlighted the importance of incorporating multiple NOD fractions, kinetic NOD oxidation, and permeability effects.

- For 1D conditions, simulations confirmed that oxidation can increase the intrinsic mass transfer coefficient for dissolution of DNAPL PCE into the aqueous phase.

Chapter 4 described an intermediate-scale 2D experiment conducted to investigate the performance of ISCO using permanganate on mass depletion of a complex PCE DNAPL source zone.

- The configuration and location of sources appeared to determine whether a source experienced increased mass transfer when oxidation began.

- All sources underwent a gradual decline in mass depletion rate as oxidation continued, likely due to manganese oxide formation.

- Several sources returned to pre-oxidation mass depletion rates or higher, apparently as a result of increased mixing through the source zone from manganese oxide buildup altering the flow field.

- For the conditions of this 2D tank, manganese oxide formation did not noticeably affect permeability until the mass fraction in the soil exceeded 0.1mg $MnO_2(s)$/kg soil.

- Use of a much more coarse sand than the surrounding sand resulted in low ganglia mass and high velocities in sources, possibly limiting mass depletion. A similar situation is possible at field sites if DNAPL migrating through a fine subsurface soil encounters a lens of more coarse sand where DNAPL will accumulate as a pool similar to sources used in this study. Under these conditions, ISCO using permanganate may not be suited to full depletion of the DNAPL source; however, a substantial reduction in mass loading from the DNAPL into the groundwater may be still be achieved.

- It appeared that a different flow rate and oxidant concentration could have resulted in optimal mass depletion during oxidation for the conditions of this 2D tank.

- The power law permeability relation of CORT3D was able to capture the permeability effects of manganese oxide formation in this 2D experiment.

In Chapter 5, the CORT3D tool was used to investigate the interaction of aquifer NOD, oxidant delivery rate, and oxidant concentration on delivery of oxidant at the Navy Training Center field site in Orlando, Florida.

- Results indicated that for this site, a lower oxidant concentration delivered at a higher flow rate will provide more optimal oxidant delivery effectiveness limiting the unproductive oxidant consumption (and accompanying permeability reduction) by NOD.

6.2   Recommendation for Future Work

This research improved the understanding of ISCO using permanganate on mass depletion of complex DNAPL PCE sources, and provided a useful numerical decision-making tool.   However, several avenues for future research have been identified to further enhance the understanding of ISCO and to expand the capabilities of the decision tool.

- Additional intermediate- and large-scale 2D experiments should utilize source zones with less hydraulic property contrast.
- Repeat the experiment performed in this research using optimal oxidant concentration and flow rates as suggested by the 1D research of Petri (2005) to investigate whether those conditions decrease negative impacts on mass transfer and permeability.
- Determine if the second Damkohler number can be used to help determine the optimum flow rate and oxidant concentration for a particular site.
- Further research should be performed to determine the reaction order for NOD for a variety of soils and aquifer solids from field sites.
- Additional research is recommended to determine if the mass transfer rate enhancement by ISCO can be quantitatively predicted.
- A 3D experiment with sufficient instrumentation and sampling to observe mass transfer and permeability effects in the source zone would permit investigation of ISCO effects in a more realistic flow field.

- Test the CORT3D tool against a 3D data set to determine if the power law implementation of permeability effects still captures the process under 3D flow conditions.

- Perform a formal, independent sensitivity analysis on the CORT3D model code.

- Use CORT3D to perform 3D simulations under a variety of conditions varying site heterogeneity, source configuration, NOD amount and rate, and oxidant delivery to assess the impact each condition has on ISCO effectiveness.

- Make the CORT3D code more efficient by modifying it to solve the coupled flow and transport equation as opposed to the current method of solving them separately.

- Modify the CORT3D code to accommodate higher order NOD oxidation (if necessary) and increase of mass transfer rate during oxidation (if possible to predict).

NOTATIONS

Acronyms and Abbreviations

1D	-	one dimensional
2D	-	two dimensional
3D	-	three dimensional
ATSDR	-	Agency for Toxic Substances and Disease Registry
Br^-	-	bromide ion
^oC	-	degrees Celsius
Cl^-	-	chloride ion
cm	-	centimeter
CORT3D	-	Chemical Oxidation Reactive Transport in 3D
CSM	-	Colorado School of Mines
DI	-	deionized water
DNAPL	-	dense non-aqueous phase liquid
ECD	-	electron capture detector
EPA	-	Environmental Protection Agency
ESTCP	-	Environmental Security Technology Certification Program
FID	-	flame ionization detector
g	-	gram
G	-	gravity
GAC	-	granular activated carbon
GC	-	gas chromatography
GTP	-	ganglia-to-pool ratio
hr	-	hour
IC	-	ion chromatography
ICP-AES	-	inductively-coupled plasma-atomic emissions spectroscopy

ID	-	internal diameter
ISCO	-	in situ chemical oxidation
kg	-	kilogram
$KMnO_4$	-	potassium permanganate
L	-	liter
LPM	-	low permeability media
m	-	meter
M	-	molar
MCL	-	maximum contaminant level
MDL	-	method detection limit
mg	-	milligram
min	-	minute
mL	-	milliliter
mm	-	millimeter
mM	-	millimolar
$MnO_2(s)$	-	manganese oxides solids
MnO_4^-	-	permanganate anion
Mn^{+2}	-	manganese ion
NOD	-	natural oxidant demand
NOM	-	natural organic matter
NPL	-	national priorities list
NRC	-	National Research Council
PCE	-	tetrachloroethylene
ppb	-	parts per billion
ppm	-	part per million
PTT	-	partitioning tracer test
PV	-	pore volume
RCRA	-	Resource Conservation and Recovery Act

rpm	-	revolutions per minute
s	-	second
SD	-	Standard deviation
SERDP	-	Strategic Environmental Research and Development Program
SOD	-	soil oxidant demand
T	-	time
TCE	-	trichlorethylene
TDS	-	total dissolved solids
TOC	-	total organic carbon
TSS	-	total suspended solids
VOC	-	volatile organic compound
wt	-	weight

Symbols

The M, L, T, and Mol appearing as units of the following symbols represent mass, length, time, and moles, respectively.

α_n	-	empirical constants (n=1 - 4) [-]
δ	-	theoretical stagnant film thickness for DNAPL dissolution [L]
ϕ	-	soil porosity [-]
ϕ_{eff}	-	effective soil porosity [-]
λ	-	linear sorption coefficient [L^3M^{-1}]
μ_w	-	aqueous dynamic viscosity [$ML^{-1}T^{-1}$]
θ_n	-	volumetric DNAPL content [-]
θ_w	-	volumetric water content [-]
ρ_B	-	soil bulk density [ML^{-3}]
ρ_w	-	water density [ML^{-3}]
τ	-	soil tortuosity factor [-]

τ_f	-	characteristic time of fluid motion [T]
τ_m	-	characteristic time of DNAPL mass transfer [T]
τ_r	-	characteristic time of chemical reaction [T]
ξ	-	rate-limiting mass transfer coefficient [T^{-1}]
A_{nw}	-	DNAPL-water interfacial surface area [L^2]
c_∞	-	steady-state bulk solution concentration of contaminant [ML^{-3}]
c^*	-	aqueous solubility limit of contaminant [ML^{-3}]
C_i	-	concentration of species i [ML^{-3}]
d_{50}	-	median grain size diameter [L]
dc/dx	-	concentration gradient [ML^{-4}]
dc/dt	-	change in concentration per time [ML^{-3}T^{-1}]
$Da(I)$	-	First Damkohler number [-]
$Da(II)$	-	Second Damkohler number [-]
D_e	-	effective aqueous phase diffusion coefficient [L^{2}T^{-1}]
D_m	-	molecular diffusion coefficient in water [L^{2}T^{-1}]
D_x	-	longitudinal dispersion coefficient [L^{2}T^{-1}]
D_y	-	transverse dispersion coefficient [L^{2}T^{-1}]
i	-	component i [-]
j	-	component j [-]
J_a	-	mass flux per unit area [ML^{-2}T^{-1}]
k_1	-	1st-order reaction rate constant [T^{-1}]
k_2	-	2nd-order oxidation reaction rate constant [L^{3}Mol^{-1}T^{-1}]
k_L	-	intrinsic mass transfer coefficient [LT^{-1}]
k_L^*	-	intrinsic mass transfer coefficient with chemical reaction [LT^{-1}]
k_{La}	-	lumped mass transfer (NAPL dissolution) coefficient [T^{-1}]
k_{nod_f}	-	1st-order oxidation rate constant for fast NOD [T^{-1}]
k_{nod_s}	-	1st-order oxidation rate constant for slow NOD [T^{-1}]
$k_{r,w}$	-	relative aqueous permeability [-]

K_s	-	saturated hydraulic conductivity [LT^{-1}]
MW_i	-	molecular weight of component i [$MMol^{-1}$]
q	-	Darcy groundwater velocity [LT^{-1}]
Re	-	Reynolds number [-]
Sc	-	Schmidt number [-]
Sh	-	Sherwood number [-]
S_{mno2}	-	$MnO_2(s)$ pseudo-saturation
S_n	-	DNAPL saturation
$S_{r,w}$	-	irreducible water saturation
t	-	time [T]
$t_{1/2}$	-	reaction half life [T]
U_{in}	-	soil uniformity index [-]
$\bar{v}$	-	linear pore groundwater velocity [LT^{-1}]
$\bar{v}_x$	-	linear pore groundwater velocity in the x-direction[LT^{-1}]
V	-	volume of interest [L^3]
X^0_i	-	initial mass fraction of component i in soil [MM^{-1}]
X_i	-	mass fraction of component i in soil [MM^{-1}]
X_{sorb}	-	mass fraction of sorbed contaminant in the soil [MM^{-1}]
$Y_{i/j}$	-	stoichiometric ratio of component i to component j

APPENDIX A

DETAILS OF MATERIALS AND METHODS

A.1   Materials

Experiments were conducted using clean white silica sands and bentonite. Table A.1 lists properties of the sands and bentonite. The saturated hydraulic conductivities, K_s, of the sands are approximate values, because the hydraulic conductivity can vary greatly depending on packing procedure. The parameters d_{50} and U are the median grain diameter and uniformity index, respectively. $S_{r,w}$ is the residual or irreducible saturation of water, ρ_B is the dry bulk density, and TOC is the total organic carbon. Table A.2 lists the typical chemical analysis for silica sands obtained from Unimin and Wedron. Natural oxidant demand (NOD) for the silica sands, measured by batch studies, was found by S. Jackson to be below detection levels (personal communication, Oct 2003).

Table A.1: Properties of Porous Media Used in Experiments

Property	#8 sand	#16 sand	#30 sand	#50 sand	#70 sand	#110 sand	#140 sand[4]	Clay[5]
Material	silica	silica	silica	silica	silica	silica	silica	bentonite
K_s (cm/min)[1]	101.3	37.500	11.800	2.267	1.458	0.383	0.126	n/a
d_{50} (cm)[1]	0.125	0.088	0.049	0.030	0.019	0.010	0.010	0.0045
U (-)[1]	1.56	1.72	1.50	1.94	1.86	2.00	1.92	n/a
$S_{r,w}$ (-)[2]	0.11	0.070	0.260	0.290	0.30	0.260	0.26	n/a
pH[3]	7.39	7.39	7.39	7.39	7.39	7.39	7.39	9.1
TOC[3]	0.019	0.019	0.019	0.019	0.019	0.019	0.019	n/a
ρ_B (g/mL)	1.6	1.6	1.6	1.8	1.6	1.8	1.6	0.83
Grain density (g/mL)	2.65	2.65	2.65	2.65	2.65	2.65	2.65	2.55
Supplier	Unimin	Unimin	Unimin	Wedron	Unimin	U.S. Silica	Manley Bros.	Wyo-Ben

[1]Saenton et al. (2001), [2]Barth et al. (2001), [3]Seitz (2004) , [4]Wilking (2004), [5]Wyo-Ben (1999)

**Table A.2: Average Chemical Analysis of Porous Media Used in Experiments (%
by weight)**

Mineral	#8 & #16 sand	#30 & #70 sand	#50 sand
Silicon Dioxide (SiO_2)	90.484	87.263	99.88
Iron Oxide (Fe_2O_3)	0.095	0.113	0.025
Aluminum Oxide (Al_2O_3)	5.451	7.244	0.050
Calcium Oxide (CaO)	0.358	0.609	0.010
Titanium Dioxide (TiO_2)	0.016	0.018	-
Magnesium Oxide (MgO)	0.021	0.024	0.003
Potassium Oxide (K_2O)	2.536	2.819	0.003
Sodium Oxide (Na_2O)	0.714	1.672	0.007
Loss on Ignition (LOI)	0.325	0.238	0.15

Table A.3 lists the chemicals used and what they were used for. See Table A.4 for PCE properties. All aqueous solutions, except oxidant, were prepared using DI water (>18.2MΩ-cm). Oxidant was mixed in tap water instead of DI water, so that background chloride levels in the tank remained constant during the oxidation flush and subsequent post-oxidation phase. If DI water was used during oxidation, the background chloride levels would vary with spatially and temporally as flushing was changed from the oxidant (in DI water) back to tap water; this would make it difficult to account for background chloride levels when estimating PCE destruction based on chloride concentrations. See Table A.5 for tap water properties.

Table A.3: Chemicals Used in Experiments

Chemical	Formula	Supplier	Grade	Used for	Comment
Potassium Permanganate	$KMnO_4$	Carus Chemical	Technical	Oxidant	
PCE	C_2Cl_4	Mallinckrodt Chemicals	Analytical	DNAPL	Dyed with 50mg/L Sudan IV
Sudan IV	-	Aldrich Chemicals	Analytical	Organic dye	
Sodium Bromide	NaBr	Fisher Scientific	Analytical	Conserv-ative tracer	
Hexane	$CH_3(CH_2)_4CH_3$	Mallinckrodt Chemicals	HPLC	Solvent	
Hydroxylamine Hydrochloride	$NH_2OH \bullet OH$	J.T. Baker	Reagent	Reduce $MnO_2(s)$	
Sodium Bisulfate	$NaHSO_3$	Fisher Scientific	Certified ACS	Reduce MnO_4^-	
Nitric Acid	HNO3	Mallinckrodt Chemicals	70%	Acidify samples	
n-Hexanol	$CH_3(CH_2)_5OH$	GFS Chemicals	Reagent	Partitioning tracer	$k_p = 8.49$
2,2-dimethyl-3-pentanol	$C_2H_5CH(OH)C(CH_3)_3$	Aldrich Chemicals	97%	Partitioning tracer	a.k.a. DMP, $k_p = 27.51$
6-methyl-2-heptanol	$(CH_3)_2CH(CH_2)_3CH(OH)CH_3$	Aldrich Chemicals	99%	Partitioning tracer	a.k.a. 6M2H, $k_p = 71.92$

Table A.4: PCE Properties

Property	Value
Density (mg/mL)	1620.0
Solubility (mg/L)	200.0
Diffusion Coefficient (cm^2/s)	8.7×10^{-6}
Molecular Weight (g/mol)	165.83
2nd Order Oxidation Rate (L/mol-sec)[*]	4.5×10^{-2}

[*](Zhang and Schwartz, 2000)

Table A.5: Tap Water Properties

pH: 7.41	Cations
Conductivity: 348 *u*S at T=22.6 ∘C	Ca: 27.39 mg/L
Alkalinity: 35.2 mg/L as CaCO3	S: 25.53 mg/L
TOC: 1.14 mg/L	Na: 25.45 mg/L
Anions:	Mg: 7.85 mg/L
Fluoride: 1.5 +/- 0.2 mg/L	K: 5.66 mg/L
Chloride: 25.0 +/- 1.3 mg/L	Si: 4.50 mg/L
Bromide: below detection	P: 1.01 mg/L
Nitrate: 0.89 +/- 0.16 mg/L	B: 0.21 mg/L
Phosphate: below detection	Zn: 0.19 mg/L
Sulfate: 75.3 +/- 1.0 mg/L	Sr: 0.18 mg/L
Solids	Fe: 0.04 mg/L
Total: 200 mg/L	Cu: 0.03 mg/L
Suspended: 15 mg/L	Mn: 0.02 mg/L
Dissolved: 185 mg/L	Li: 0.02 mg/L
	Ba: 0.01 mg/L

A.2 Sampling and Analytical Methods

This section describes how samples were obtained, followed by how they were analyzed.

A.2.1 Aqueous Sampling

Aqueous samples were collected at multiple locations within the tank as well as from the effluent. Sampling locations consisted of a permanently installed stainless steel needle reaching to the tank centerline and a valve on the tank exterior. Before collecting an aqueous sample, approximately 0.1mL was purged from the sampling port to eliminate stagnant water from the last sampling episode. All aqueous samples were collected by opening the sampling port valve and catching liquid (typically for 1-15 seconds) in a 1.5mL glass vial. The vials were immediately capped with a Teflon-lined septa cap and then analyzed immediately if possible, or refrigerated until analytical equipment was available. In all cases, samples held for volatile organic analysis by GC were analyzed

within seven days. Samples held for inorganic analysis by IC and ICP were analyzed within 30 and 90 days, respectively.

A.2.2   Aqueous Sample Analysis

Bromide tracer samples were analyzed on a Dionex AS50 ion chromatograph/high performance liquid chromatograph (IC/HPLC) with Dionex IonPac AS-14A ion exchange analytical (4mm x 150mm) and IonPac AG-14A (4mm x 50mm) guard columns, AS50 auto-sampler, AS50 gradient pump, and CD25 conductivity detector. A sodium carbonate (8.0 mM) and sodium bicarbonate (1.0 mM) eluent, at a flow rate of 1.2mL/min, was used with this carbonate-selective anion exchange column.

Aqueous PCE samples during the natural dissolution and post-oxidation phases were collected with zero-headspace and capped. Samples were analyzed on a Hewlett-Packard (HP) 6890 gas chromatograph (GC) equipped with an HP7683 auto-sampler/injector and DB-624 column, utilizing a flame ionization detector (FID), see Table A.4 for method summary.

Aqueous PCE samples during partitioning tracer tests (PTTs) were collected with zero-headspace and capped. Samples were analyzed on a Hewlett-Packard (HP) 6890 gas chromatograph (GC) equipped with an HP7683 auto-sampler/injector and DB-624 column, utilizing a flame ionization detector (FID), see Table A.4 for method summary.

During oxidation, aqueous samples were collected and then sub-sampled for a variety of analyses. Immediately after collection, 0.1mL was placed into 1.0mL of hexane and capped, shaken for one minute, and allowed to settle for at least 60 minutes prior to analysis for PCE using an HP GC equipped with an HP7683 auto-sampler/injector and DB-5 GC column, utilizing an electron capture detector (ECD) , see Table A.4 for method summary. Another 0.1mL was placed into a 15mL glass tubes (Hach) containing 4.5mL of DI water, capped, shaken, and analyzed on a HACH DR/4000 spectrophotometer for MnO_4^- at an absorbance of 525 nm within three hours. A third 0.1mL sub-sample was added to 1.0mL of sodium bisulfite (to stop oxidation by

reducing any permanganate in the sample), capped, shaken, and manganese oxides allowed to settle out for six hours prior to analysis for chloride using the same IC method described for bromide samples. Next, (for select aqueous samples obtained during the intermediate-scale 2D experiments), a 0.75mL sub-sample was added to a 15mL polypropylene conical vial containing 4.5mL of DI water and acidified with nitric acid to pH<2, capped, shaken, and analyzed for Mn^{+2} using inductively coupled plasma-atomic emission spectroscopy (Perkin Elmer Optima 3000 ICP-AES). It was assumed that Mn(II) was initially present as either MnO_4^- or $MnO_2(s)$, so Mn^{+2} concentrations determined by ICP-AES were reduced by the amount of MnO_4^- measured in the sample by spectrophotometry and then converted to $MnO_2(s)$ concentrations. Finally, pH was measured, during oxidation phases, in remaining original sample using an Orion 98-63BN micro-pH probe and Orion 420A+ meter. A 3-point calibration was performed daily.

Table A.6: GC Method Summary

Parameter	Aqueous PCE and Partitioning Tracers	Aqueous PCE during Dissolution	Aqueous PCE during Oxidation	PCE in Soil Cores
Initial Oven Temp ($^\circ$C)	55	55	120	55
Oven Ramp ($^\circ$C/min)	12	12	45	26
Final Oven Temp ($^\circ$C)	150	100	200	120
Injector Mode	Splitless	Splitless	Split (50:1 ratio)	Splitless
Injection Volume (µL)	1.0	1.0	0.2	1.0
Detector	FID	FID	ECD	FID
Detector Temp ($^\circ$C)	250	250	250	250

A.2.3 Soil Cores

Upon completion of the experiment, soil cores were obtained from throughout the tank (for the 3rd and 4th intermediate scale 2D experiments) using the equipment shown in Figure A.1. The soil coring grids were used to core the source zones such that the entire

source could be extracted while subdividing it into rectangular cores 2.0cm x 2.6cm. The cylindrical samplers were used to obtain 1.3cm diameter cores at representative locations, along the tank centerline, through the rest of the tank. When obtaining a core, the water level was lowered to the desired core level, and the tank was excavated to that point. The coring device was then pushed into the soil at the desired location and sand was excavated around the device. The device was then removed and the soil sample pushed out into a 50mL polypropylene conical vial containing hexane (36mL for source zone cores, 18mL for other cores). The vial was capped and shaken for 30 seconds, then let sit quiescently for 24 hours.

Figure A.1: Soil Coring Devices

A.2.4   Soil Core Analysis

Approximately 1mL of the hexane was transferred into a glass vial for GC analysis using the FID detector on the GC, see Table A.4 for method summary. After analyzing for PCE, the hexane remaining in the soil core vials was allowed to evaporate

for 48 hours under an exhaust hood. Then 30mL of hydroxylamine hydrochloride (0.2M) and nitric acid (0.1M) were added to the vials to reduce and dissolve any $MnO_2(s)$ (this was assumed to be the dominant species of manganese present so other extractions to identify exchangeable cations were not performed). This is reasonable as there was no visible MnO_4^- present in the pore water from the cores, so MnO_4^- was less than 1mg/L and would be negligible compared to the concentrations of Mn^{+2} in ICP-AES samples from $MnO_2(s)$. The vials were placed on a wrist-action shaker (60rpm) for two hours and then centrifuged for 10min at 1150G before transferring 6mL of liquid into 15mL polypropylene conical vials to be analyzed for Mn^{+2} by ICP-AES. Following ICP-AES analysis, the remaining liquid was drained and the core dried at 103°C for four hours before determining the dry weight, so PCE and $MnO_2(s)$ content could be expressed as mass fractions.

APPENDIX B

CORT3D COMPUTER MODEL USER DOCUMENTATION

B.1   Program Operation

The program operates similar to running MODFLOW 2000 for a flow simulation followed by RT3D v2.5 for a transport simulation. However, a user-specified reaction package is used, and several additional executables are utilized to incorporate changing permeability and DNAPL dissolution rate as the simulation progresses.

Because dissolution and oxidation are transient processes where NAPL saturation decreases with time and manganese oxide solids (a byproduct of the chemical oxidation process when using permanganate) increases with time (i.e. effective porosity and permeability change), the groundwater flow pattern needs to be updated over time. The more frequent the update of the flow solution (through changes of effective hydraulic conductivity, porosity, NAPL saturation, and manganese oxide volume), the closer the simulation approaches transient solution. That is, long (time) simulations are broken down to a number of short steady-state runs that are executed in sequence. In each run, there are a number of executables and input files. The CORT3D perl script automates the sequential executions to arrive at the target simulation time. Table B.1 lists the executables and briefly describes what each one is used for and Table B.2 lists the required input files for each executable program. Table B.3 lists the files generated by various modules or executables, and subsequently used by another module during a simulation. The fort.yxx files pertain to a specific simulation parameter, as described in Table B.3, with one such file for each model layer (described in more detail later).

Table B.1: Executable Files and Their Functions.

Program	Function(s)
file_gen.exe	Generate a file series of a single value (e.g. concentration) for all model cells.
c_modk.exe	Read saturated K, NAPL saturation, residual saturation, and return the output of effective K (Fort.06xxx series) for MODFLOW simulation.
c_dss.exe	Read initial porosity, NAPL saturation, layer thickness, residual saturation, surfactant concentration, and return input parameters for CORT3D simulation (see Table 3).
c_update.exe	Extract observations (i.e. concentrations) at specified locations, Re-calculate the new NAPL saturation and NAPL mass based on outputs from pm.exe.
mf2k.exe	MODFLOW 2000 executable – generates flow solution
rt3dv41j.exe	Modified RT3D executable, including chemical oxidation – generates transport/reaction solution
pm.exe	Process outputs from RT3D by reading unformatted concentration outputs and re-write in text files.
perl.exe	Perl interpreter that processes CORT3D script
cort3d	Script file that automates the iterative running of the model

Table B.2: Input Files Required By Executables.

Program	Required Input Filename	
file_gen.exe	file_gen.7000 file_gen.8000 file_gen.9000 file_gen.10000 file_gen.12000 file_gen.13000 file_gen.14000	Note: read below for explanation of when to change these files from default.
c_modk.exe	cort3d.inp phi0.dat init_k.dat srw.dat smn.dat	
c_dss.exe	cort3d.inp phi0.dat smn.dat d50.dat	
c_update.exe	cort3d.inp phi0.dat	
cort3d	cort3d.inp sn.dat.ini	
pm.exe	pm.conc7 pm.conc8 pm.conc9 pm.mfrac10 pm.mfrac11 pm.mfrac12 pm.mfrac13 pm.mfrac14	Note: these input files only need to be changed if different RT3D output filenames are used.

The 'file_gen.y000' files are necessary to ensure initial concentrations (or mass fractions for immobile components) are established for each component, except DNAPL contaminant, at every model cell; generally these will be used to set initial concentrations and mass fractions to zero. The 'y' in the 'file_gen.y000' filenames y represents the series number of the parameter or component (see Table B.3). The FILE_GEN program

will set the initial concentration (or mass fraction) for the given component to the same value at every model location. Initial DNAPL contaminant is designated using the 'sn.dat.ini' file; this file contains the initial DNAPL contaminant saturation value for every cell in the model.

If it is desired to have the initial concentration (or mass fraction) of one or more components vary spatially, this can be done by creating 'fort.yxxx.ini' files. It is only necessary to create 'fort.yxxx.ini' files for those components whose initial concentration (or mass fraction) varies spatially, and only for those layers within which the initial concentration (or mass fraction) varies. In the 'fort.yxxx.ini' filenames, the 'y' again represents the series number of the parameter or component (see Table 3), and 'xxx' represents the model layer number with preceeding zeros. For example, initial concentrations of chloride in layer 1 would be specified using the 'fort.9001.ini' file.

Table B. 3: Program Generated Input/Output Files

File Type/Name	Function (Layerwise)	Generated by Program
fort.1xxx	Cell thickness, Δz	c_dss.exe
fort.2xxx	Bulk density	c_dss.exe
fort.3xxx	Lumped mass transfer coefficient, T^{-1}	c_dss.exe
fort.4xxx	Effective porosity	c_dss.exe
fort.5xxx	Initial porosity	c_dss.exe
fort.6xxx	Effective hydraulic conductivity, K	c_modk.exe
fort.7xxx	Starting concentration of contaminant (PCE)	file_gen.exe c_update.exe
fort.8xxx	Starting concentration of oxidant (MnO_4^-)	file_gen.exe c_update.exe
fort.9xxx	Starting concentration of chloride (Cl^-)	file_gen.exe c_update.exe
fort.10xxx	Starting mass fraction of manganese oxide solids ($MnO_2(s)$)	file_gen.exe c_update.exe
fort.11xxx	Starting mass fraction of DNAPL	c_dss.exe c_update.exe
fort.12xxx	Starting mass fraction of sorbed contaminant	file_gen.exe c_update.exe
fort.13xxx	Starting mass fraction of fast natural oxidant demand (NOD)	file_gen.exe c_update.exe
fort.14xxx	Starting mass fraction of slow NOD	file_gen.exe c_update.exe
mass.out	Total mass of each immobile component in simulated aquifer at end of each iteration	c_update.exe
obs_c.out	Concentration of each mobile component at designated observation points and effluent, along with total aqueous flow rate at effluent, at end of each iteration	c_update.exe
obs_m.out	Mass fraction of each immobile component at designated observation points at end of each iteration	c_update.exe
obs_h.out	Hydraulic head at each observation point at end of each iteration	c_update.exe

Table B.4: Overall Program Sequence

c_modk.exe
MODFLOW.exe
c_dss.exe
RT3Dv42j.exe
pm.exe
c_update.exe

In normal operation, the individual programs are executed by the CORT3D perl script. This is accomplished by entering 'perl cort3d' at the command prompt.

B.1   User Instructions

The first step in setting up a CORT3D simulation is to develop a steady-state flow model in MODFLOW 2000, using the layer property flow (LPF) package. However, horizontal hydraulic conductivities need to be entered to be read free-format from external files with one file per layer. Below is an example entry for layer 1.

OPEN/CLOSE fort.6001   1.0 (free) 0 HK layer 1

Subsequent layers are entered the same manner, except that 6001 is incremented for each layer so it becomes 6002 for layer 2, 6003 for layer 3, and so on. This modification allows MODFLOW to read the hydraulic conductivities calculated by the "c_modk" module of CORT3D.   The "c_modk" module calculates the effective hydraulic conductivity as a result of DNAPL and manganese oxide within the porespace using a modification of Wyllie's (1962) power law relation for estimating relative permeability.

Next, the transport simulation is set up just as if setting up an RT3D simulation, except that the BTN file is modified to specify external files for cell thickness, effective porosity, starting concentrations of mobile aqueous components, and starting mass fractions of immobile components as shown in bold in Figure B.1. The number in the first column (e.g., 1001) specifies the external fort.yxxx file corresponding to the

appropriate parameter and model layer (see Table B.3 for descriptions). For 2D and 3D simulations, enter a line for each layer, for each parameter. Additionally, the length of the transport simulation (PERLEN) should be set to the desired length of one CORT3D iteration, so the number of iterations times the period length is equal to the simulation length.

```
GMS MT3D Simulation
08 November 2004
         1          1         40          1          8          3
  hr   cm   mg
 T T T T T F F F F F
 1          LAYCON
         0 1.0000000
         0 4.5000000
         0 4.5000000
      1001        1.0                              0    DZ(K)DZ(K)
      4001        1.0                              0    PRSTY_EFF
         0          1
      7001        1.0                              0    CONC FOR CONT (M/L3)
      8001        1.0                              0    CONC FOR MNO4 (M/L3)
      9001        1.0                              0    CONC FOR CL (M/L3)
     10001        1.0                              0    MASSFRAC FOR MNO2 (M/M)
     11001        1.0                              0    MASSFRAC FOR NAPL CONT (M/M)
     12001        1.0                              0    MASSFRAC FOR SORBED CONT (M/M)
     13001        1.0                              0    MASSFRAC FOR FAST NOD (M/M)
     14001        1.0                              0    MASSFRAC FOR SLOW NOD (M/M)
-999.0000
         1          0          0          0          T
         0
         0
         T
  6.00000           1 1.0000000                         PERLEN
      0.0        1000 1.0000000          0.0
```

Figure B.1: BTN Input File Structure (differences from traditional RT3D input shown in bold).

The RCT reaction package input file is set up as shown in Figure B.2, following RT3D instructions, for a user-defined reaction. Specifically, the second entry in row 1 is set to 10 (for user-defined reaction), the third item in row 1 is set to 15 (15 constant reaction data), and the fourth item in row 1 is set to 2 (two variable reaction data). Row 2 specifies the external file(s) containing soil dry bulk density (enter as many lines as model layers). Reaction data entered are shown in bold in Figure B.2, although values

will vary according to the conditions being simulated. Just as in the BTN file, variable reaction parameters are read from external files with the number in the first column (e.g., 3001) specifying the external fort.yxxx file corresponding to the appropriate parameter and model layer. For 2D and 3D simulations, enter a line for each layer, for each parameter. See Table B.5 for a description of each of the reaction parameters.

```
         0        10       15        2        1        2
      2001       1.0                          2  RHOB (M/M)
1.0e-010 1.0e-009
1.0e-010 1.0e-009
1.0e-010 1.0e-009
1.0e-010 1.0e-009
1.0e-010 1.0e-009
1.0e-010 1.0e-009
1.0e-010 1.0e-009
1.0e-010 1.0e-009
0.03132                                       rc(1):Dm_cont   (L2/T)
0.0588                                        rc(1):Dm_mno4   (L2/T)
0.07308                                       rc(1):Dm_cl     (L2/T)
1.3333                                        rc(1):Y_mno4_cont (mol/mol)
4.0                                           rc(1):Y_cl_cont    (mol/mol)
1.0                                           rc(1):Y_mno2_mno4 (mol/mol)
3000.0                                        rc(1):rho_mno2 (M/L3)
165830.0                                      rc(1):MW_cont   (M/mol)
1630.0                                        rc(1):rho_cont (M/L3)
262000.0                                      rc(1):k2_cont   (L3/mol-T)
0.200                                         rc(1):C_c_star (M/L3)
0.0                                           rc(1):eta       (1/T)
150.0                                         rc(1):lambda_c (L3/M)
52152.35                                      rc(1):k_nod_f   (1/T)
3.36e-005                                     rc(1):k_nod_s   (1/T)
      3001       1.0                          2  vrc(1):k_La (1/T)
      5001       1.0                          2  vrc(2):initial porosity
```

Figure B.2: RCT Input File Structure (CORT3D specific items shown in bold).

Table B.5: Reaction Variables for RCT Input File

Parameter	Type	Description[1]
Dm_cont	Constant	Molecular diffusion coefficient for aqueous contaminant (L^2T^{-1})
Dm_mno4	Constant	Molecular diffusion coefficient for permanganate (L^2T^{-1})
Dm_cl	Constant	Molecular diffusion coefficient for chloride (L^2T^{-1})
Y_mno4_cont	Constant	Stoichiometric mole ratio, moles permanganate consumed to destroy one mole of contaminant $(MolMol^{-1})$
Y_cl_cont	Constant	Stoichiometric mole ratio, moles chloride created by destroying one mole of contaminant $(MolMol^{-1})$
Y_mno2_mno4	Constant	Stoichiometric mole ratio, moles manganese oxide created from consumption of one mole permanganate $(MolMol^{-1})$
rho_mno2	Constant	Effective density of manganese oxide solids (ML^{-3})
MW_cont	Constant	Molecular weight of contaminant $(MMol^{-1})$
rho_cont	Constant	Density of contaminant (ML^{-3})
k2_cont	Constant	Second-order kinetic rate constant for oxidation of contaminant by permanganate $(L^3Mol^{-1}T^{-1})$
C_c_star	Constant	Aqueous solubility limit for contaminant (ML^{-3})
eta	Constant	(T^{-1})
lambda_c	Constant	(L^3M^{-1})
k_nod_f	Constant	First-order kinetic rate constant for oxidation of the fraction of NOD with a faster rate (T^{-1})
k_nod_s	Constant	First-order kinetic rate constant for oxidation of the fraction of NOD with a slower rate (T^{-1})
k_La	Variable	Lumped mass transfer coefficient (T^{-1})
porosity	Variable	Effective porosity of porous media (-)

[1]Variables M, L, T, and Mol shown as units for these parameters denote mass, length, time, and moles, respectively

Next, the CORT3D-specific input file <u>CORT3D.INP</u> needs to be constructed. This file is used by each of the CORT3D modules (CORT3D.PL, C_MODK.EXE, FILE_GEN.EXE, C_DSS.EXE, and C_UPDATE.EXE) in carrying out the simulation. Figure B.3 shows a sample CORT3D.INP input file.

```
ex2.mfn        / MODFLOW name (NAM or MFN) file
ex2.rts        / MODFLOW RT3D super (RTS) file
56             / number of iterations to perform
n              / is this a continuation of another run (Y/N)?
ex2.dis        / MODFLOW discretization (DIS) file
ex2.ftl        / MODFLOW flow-transport link file (binary)
ex2.hed        / file containing heads from MODFLOW (binary)
ex2.btn        / RT3D basic transport (BTN) file
ex2.rct        / RT3D reaction parameters file
init_K.dat     / input file containing hydraulic conductivity for all layers
phi0.dat       / input file containing porosity for all layers (w/  no napl)
d50.dat        / input file containing d50 for all layers
srw.dat        / input file containing residual water saturation for all layers
sn.dat         / input file containing napl saturation for all layers
smn.dat        / input file containing MnO2 pseudo-saturation for all layers
conc7.out      / output file containing contaminant concentration
conc8.out      / output file containing permanganate concentration
conc9.out      / output file containing chloride concentration
mfrac10.out    / output file containing MnO2 mass fraction
mfrac11.out    / output file containing NAPL mass fraction
mfrac12.out    / output file containing Sorbed contaminant mass fraction
mfrac13.out    / output file containing Fast NOD mass fraction
mfrac14.out    / output file containing Slow NOD mass fraction
mass.out       / output file containing mass of immobile species within model
obs_c.out      / output file containing mobile species conc. at obs. points
obs_m.out      / output file containing immobile species mass frac. at obs points
obs_h.out      / output file containing heads at observation points
4200.0         / density of the solid phase
1.008801779    / tortuosity factor (tau)
75.50161425    / alpha_1 - empirical parameter for natural dissolution
.6878052435    / alpha_2 - empirical parameter for natural dissolution
1.991786E-4    / alpha_3 - empirical parameter for natural dissolution
.5942657302    / alpha_4 - empirical parameter for natural dissolution
3              / number of obs pts.
30  1   1      / col row lay (j,i,k) for obs. pts.
35  1   1
40  1   1
39             / effluent concentration measured at this column
```

Figure B.3: Example <u>CORT3D.INP</u> Input File

The input instructions for <u>CORT3D.INP</u> are listed below. Each record refers to a line of the input file. A comment can be included on the line, following the required input, by preceding the comment with a "/" and a space.

Record #1:   File name of MODFLOW name (NAM or MFN) file

Record #2:   File name of RT3D super (RTS) file

Record #3:   Number of iterations the simulation time has been broken down to

Record #4:   Indicate whether this is a continuation of a previous run. This is used when the simulation is divided up into phases to accommodate different boundary conditions or stresses.

Record #5:   File name of MODFLOW discretization (DIS) file

Record #6:   File name of MODFLOW flow-transport link file (binary)

Record #7:   File name of binary file containing heads, output by MODFLOW

Record #8:   File name of RT3D basic transport (BTN) file

Record #9:   File name of RT3D reaction parameters (RCT) file

Record #10:   File name of input file containing initial (saturated) hydraulic conductivity for all layers

Record #11:   File name of input file containing initial (fully) water saturated porosity for all layers (with no DNAPL or manganese oxide)

Record #12:   File name of input file containing median soil grain size (d50)

Record #13:   File name of input file containing residual water saturation

Record #14:   File name of input file containing DNAPL saturation

Record #15:   File name of input file containing $MnO_2(s)$ pseudo-saturation

Record #16:   File name of output file to write contaminant concentration

Record #17:   File name of output file to write permanganate concentration

Record #18:   File name of output file to write chloride concentration

Record #19:   File name of output file to write $MnO_2(s)$ mass fraction

Record #20:   File name of output file to write DNAPL mass fraction

Record #21:   File name of output file to write Sorbed contaminant mass fraction

Record #22:   File name of output file to write Fast NOD mass fraction

Record #23:   File name of output file to write Slow NOD mass fraction

Record #24:   File name of output file to write mass of immobile species remaining within model

Record #25:   File name of output file to write mobile species concentrations, at observation points

Record #26:   File name of output file to write immobile species mass fraction, at observation points

Record #27:   File name of output file to write hydraulic heads at observation points

Record #28:   Density of the solid phase (soil grain density)

Record #29: Soil tortuosity factor (τ); used in Gilland-Sherwood relationship for natural dissolution

Record #30: Pre-multiplier (α_1) in Gilland-Sherwood relationship for natural dissolution

Record #31: Exponent (α_2) of Reynolds number in Gilland-Sherwood relationship for natural dissolution

Record #32: Exponent (α_3) of Schmidt number in Gilland-Sherwood relationship for natural dissolution

Record #33: Exponent (α_4) of $\left(\dfrac{\theta_n d_{50}}{\tau L} \right)$ term in Gilland-Sherwood relationship for natural dissolution

Record #34: Number of observations points at which to record concentration, mass fraction, and hydraulic head for each iteration

Record #35: column, row, layer (j,i,k) of each observation point. Enter one observation point per line. Enter as many lines as there are observation points specified in Record #34.

Record 36: Enter column number to use for calculating and recording effluent concentrations and flow rate

Additionally, input files are needed to define several additional simulation parameters. These are: D50.DAT, INIT_K.DAT, PHI0.DAT, SRW.DAT, SN.DAT.INI, and SMN.DAT.INI. These are text files contain an entry for every model cell; entries can be specified using free format. When read, they are read sequentially such that all of the model columns (x=1…j) in model row 1 of model layer 1 are read first, followed by all the columns of row 2 of layer 1 through all the columns of row j in layer 1. Then the same sequence is repeated for layer 2 through layer k.

After generating all input files, open a "Command Prompt" window and change to the folder containing all the input files. Ensure all executable files (including "PERL.EXE" and "PERL58.DLL") are either in a location included in the PATH environment variable of your computer, or located in the same folder as the data files. Then type "PERL CORT3D.PL" to start the simulation.

The output files (MASS.OUT, OBS_C.OUT, OBS_M.OUT, and OBS_H.OUT) will contain the remaining mass in the model domain for each immobile species, concentration of mobile species at each observation point and effluent, mass fraction of immobile species at each observation point, and hydraulic head at each observation point, respectively. These files will contain an entry for each simulation iteration, and can be easily imported into Microsoft Excel for data analysis.

B.2   Example Simulations

Example simulation inputs are provided for both a 2D and a 1D example.

B.2.1   ISCO (Using Permanganate) of Entrapped DNAPL PCE in 2-D Aquifer

This simulation includes transient dissolution and chemical oxidation of stably entrapped dense non-aqueous phase liquid (DNAPL) PCE in a *confined* hypothetical 2-D aquifer. The aquifer has a dimension of 25 m long, 5 m high, and 0.05 m wide. The saturation distribution of a NAPL source zone is shown in Figure B.4. In order to simulate transient dissolution of PCE and the transport of the dissolved constituent, groundwater velocity must be calculated using MODFLOW. Then, the *reactive* contaminant transport program RT3D takes over to simulate mass transfer. Additional pre- and post-processor software are run before or after MODFLOW and RT3D, as appropriate, to generate or format input parameters and conditions. In the example simulation, the aquifer is discretized into 25 columns, 10 layers, and 1 row. The simulation covers five days, broken down into 40 three-hour intervals. The injection well array is located upstream of the source zone to drive groundwater containing oxidant through aquifer. An injection rate of 0.25 m^3/day, corresponding to a Darcy velocity of 1.0 m/day, is used in this simulation. The oxidant is permanganate (MnO_4^-) at a concentration of 10,000mg/L (1.0% by weight). The hydraulic head at the end of the test

aquifer is kept constant at 5m. The LPF, BTN, RCT, and CORT3D.INP input files for this example are shown in Figures B.5, B.6-B.8, B.9, and B.10, respectively.
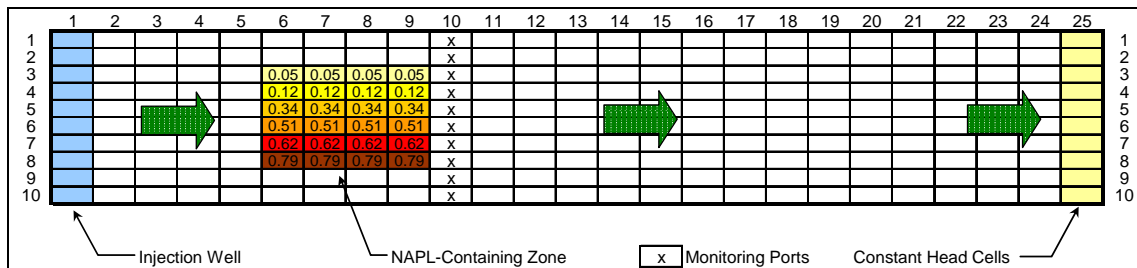
Figure B.4: Test Aquifer for Example Problem 1.

```
       62    -888.00          0   ILPFCB,HDRY,NPLPF
 0 0 0 0 0 0 0 0 0 0
 0 0 0 0 0 0 0 0 0 0
  1.00E+00   1.00E+00   1.00E+00   1.00E+00   1.00E+00   1.00E+00   1.00E+00   1.00E+00
  1.00E+00   1.00E+00
 1 1 1 1 1 1 1 1 1 1
 0 0 0 0 0 0 0 0 0 0
OPEN/CLOSE  fort.6001   1.0  (free) 0  HK layer  1
CONSTANT   1.000000E+00  VKA layer  1
OPEN/CLOSE  fort.6002   1.0  (free) 0  HK layer  2
CONSTANT   1.000000E+00  VKA layer  2
OPEN/CLOSE  fort.6003   1.0  (free) 0  HK layer  3
CONSTANT   1.000000E+00  VKA layer  3
OPEN/CLOSE  fort.6004   1.0  (free) 0  HK layer  4
CONSTANT   1.000000E+00  VKA layer  4
OPEN/CLOSE  fort.6005   1.0  (free) 0  HK layer  5
CONSTANT   1.000000E+00  VKA layer  5
OPEN/CLOSE  fort.6006   1.0  (free) 0  HK layer  6
CONSTANT   1.000000E+00  VKA layer  6
OPEN/CLOSE  fort.6007   1.0  (free) 0  HK layer  7
CONSTANT   1.000000E+00  VKA layer  7
OPEN/CLOSE  fort.6008   1.0  (free) 0  HK layer  8
CONSTANT   1.000000E+00  VKA layer  8
OPEN/CLOSE  fort.6009   1.0  (free) 0  HK layer  9
CONSTANT   1.000000E+00  VKA layer  9
OPEN/CLOSE  fort.6010   1.0  (free) 0  HK layer 10
CONSTANT   1.000000E+00  VKA layer 10
```

Figure B.5: LPF Input File for 2D Example

```
DISSOLUTION OF PCE: 2D TEST PROBLEM                         COMMENT1
DISSOLUTION & CHEMOX MODELING                               COMMENT2
        10            1        25        1        8        3
 day   m  kg                                                TUNIT,LUNIT,MUNIT
 T T T T T F F F F F                                        TRNOP
 0 0 0 0 0 0 0 0 0 0                                        LAYCON
         0         1.0                            0         DELR
         0         0.05                           0         DELC
         0         5.0                            0         HTOP
      1001         1.0                            0         DZ(K)
      1002         1.0                            0
      1003         1.0                            0
      1004         1.0                            0
      1005         1.0                            0
      1006         1.0                            0
      1007         1.0                            0
      1008         1.0                            0
      1009         1.0                            0
      1010         1.0                            0
```

Figure B.6: BTN Input File for 2D Example (part 1)

```
4001      1.0                              0        PRSTY_EFF
4002      1.0                              0
4003      1.0                              0
4004      1.0                              0
4005      1.0                              0
4006      1.0                              0
4007      1.0                              0
4008      1.0                              0
4009      1.0                              0
4010      1.0                              0
   0        1                              0        ICBUND
   0        1                              0
   0        1                              0
   0        1                              0
   0        1                              0
   0        1                              0
   0        1                              0
   0        1                              0
   0        1                              0
7001      1.0                              0        CONC FOR CONT (M/L3)
7002      1.0                              0
7003      1.0                              0
7004      1.0                              0
7005      1.0                              0
7006      1.0                              0
7007      1.0                              0
7008      1.0                              0
7009      1.0                              0
7010      1.0                              0
8001      1.0                              0        CONC FOR MNO4 (M/L3)
8002      1.0                              0
8003      1.0                              0
8004      1.0                              0
8005      1.0                              0
8006      1.0                              0
8007      1.0                              0
8008      1.0                              0
8009      1.0                              0
8010      1.0                              0
9001      1.0                              0        CONC FOR CL (M/L3)
9002      1.0                              0
9003      1.0                              0
9004      1.0                              0
9005      1.0                              0
9006      1.0                              0
9007      1.0                              0
9008      1.0                              0
9009      1.0                              0
9010      1.0                              0
10001     1.0                              0        MASSFRAC FOR MNO2 (M/M)
10002     1.0                              0
10003     1.0                              0
10004     1.0                              0
10005     1.0                              0
10006     1.0                              0
10007     1.0                              0
10008     1.0                              0
10009     1.0                              0
10010     1.0                              0
```

Figure B.7: BTN Input File for 2D Example (part 2)

```
   11001       1.0                                  0        MASSFRAC FOR NAPL CONT (M/M)
   11002       1.0                                  0
   11003       1.0                                  0
   11004       1.0                                  0
   11005       1.0                                  0
   11006       1.0                                  0
   11007       1.0                                  0
   11008       1.0                                  0
   11009       1.0                                  0
   11010       1.0                                  0
   12001       1.0                                  0        MASSFRAC FOR SORBED CONT (M/M)
   12002       1.0                                  0
   12003       1.0                                  0
   12004       1.0                                  0
   12005       1.0                                  0
   12006       1.0                                  0
   12007       1.0                                  0
   12008       1.0                                  0
   12009       1.0                                  0
   12010       1.0                                  0
   13001       1.0                                  0        MASSFRAC FOR FAST NOD (M/M)
   13002       1.0                                  0
   13003       1.0                                  0
   13004       1.0                                  0
   13005       1.0                                  0
   13006       1.0                                  0
   13007       1.0                                  0
   13008       1.0                                  0
   13009       1.0                                  0
   13010       1.0                                  0
   14001       1.0                                  0        MASSFRAC FOR SLOW NOD (M/M)
   14002       1.0                                  0
   14003       1.0                                  0
   14004       1.0                                  0
   14005       1.0                                  0
   14006       1.0                                  0
   14007       1.0                                  0
   14008       1.0                                  0
   14009       1.0                                  0
   14010       1.0                                  0
   -999.0      0.01                                          CINACT, (THKMIN)
       1        0         0         0        T
     IFMTCN,IFMTNP,IFMTRF,IFMTDP,SAVUCN
       0                                                     NPRS    {save/print results
at: 0=end only, <0=NPRS multiples, >0=specified times listed below (TIMPRS)}
       0                                                     NOBS,(NPROBS)
       T         1                                           CHKMAS,(NPRMAS)
   0.125         6       1.0                                      PERLEN,NSTP,TSMULT
     0.0     100000     1.0         0.0                      DT0,MXSTRN,TTSMULT,TTSMAX
```

Figure B.8: BTN Input File for 2D Example (part 3)

```
        0          10         15          2          1          2
     2001      1.0                                   2                      RHOB
     2002      1.0                                   2
     2003      1.0                                   2
     2004      1.0                                   2
     2005      1.0                                   2
     2006      1.0                                   2
     2007      1.0                                   2
     2008      1.0                                   2
     2009      1.0                                   2
     2010      1.0                                   2
1.0e-010 1.0e-009                                                           ATOL,RTOL
1.0e-010 1.0e-009
1.0e-010 1.0e-009
1.0e-010 1.0e-009
1.0e-010 1.0e-009
1.0e-010 1.0e-009
1.0e-010 1.0e-009
1.0e-010 1.0e-009
0.000075168                                                    rc(1):Dm_cont    (L2/T)
0.00014112                                                     rc(2):Dm_mno4    (L2/T)
0.000175392                                                    rc(3):Dm_cl      (L2/T)
1.3333                                                         rc(4):Y_mno4_cont (mol/mol)
4.0                                                            rc(5):Y_cl_cont   (mol/mol)
1.0                                                            rc(6):Y_mno2_mno4 (mol/mol)
1000.0                                                         rc(7):rho_mno2   (M/L3)
0.165875                                                       rc(8):MW_cont    (M/mol)
1630.0                                                         rc(9):rho_cont   (M/L3)
3.888                                                          rc(10):k2_cont   (L3/mol-T)
0.200                                                          rc(11):C_c_star (M/L3)
0.0                                                            rc(12):eta       (1/T)
0.15                                                           rc(13):lambda_c (L3/M)
4.8                                                            rc(14):k_nod_f   (1/T)
0.48                                                           rc(15):k_nod_s   (1/T)
     3001      1.0                                   2         vrc(1):k_La      (1/T)
     3002      1.0                                   2
     3003      1.0                                   2
     3004      1.0                                   2
     3005      1.0                                   2
     3006      1.0                                   2
     3007      1.0                                   2
     3008      1.0                                   2
     3009      1.0                                   2
     3010      1.0                                   2
     5001      1.0                                   2         vrc(2):initial porosity
     5002      1.0                                   2
     5003      1.0                                   2
     5004      1.0                                   2
     5005      1.0                                   2
     5006      1.0                                   2
     5007      1.0                                   2
     5008      1.0                                   2
     5009      1.0                                   2
     5010      1.0                                   2
```

Figure B.9: RCT Input File for 2D Example

```
EX1.nam          / MODFLOW name (NAM or MFN) file
EX1.rts          / MODFLOW RT3D super (RTS) file
40               / number of iterations to perform
N                / is this a continuation of another run (Y/N)?
Ex1.dis          / MODFLOW discretization (DIS) file
Ex1.ftl          / MODFLOW flow-transport link file (binary)
Ex1.hed          / file containing heads from MODFLOW (binary)
Ex1.btn          / RT3D basic transport (BTN) file
Ex1.rct          / RT3D reaction parameters file
init_K.dat       / input file containing hydraulic conductivity for all layers
phi0.dat         / input file containing porosity for all layers (w/ no napl)
d50.dat          / input file containing d50 for all layers
srw.dat          / input file containing residual water saturation for all layers
sn.dat           / input file containing dnapl saturation for all layers
smn.dat          / input file containing MnO2 pseudo-saturation for all layers
conc7.out        / output file containing contaminant concentration
conc8.out        / output file containing permanganate concentration
conc9.out        / output file containing chloride concentration
mfrac10.out      / output file containing MnO2 mass fraction
mfrac11.out      / output file containing NAPL mass fraction
mfrac12.out      / output file containing Sorbed contaminant mass fraction
mfrac13.out      / output file containing Fast NOD mass fraction
mfrac14.out      / output file containing Slow NOD mass fraction
mass.out         / output file containing mass of immobile species within model
obs_c.out        / output file containing mobile species conc. at obs. points
obs_m.out        / output file containing immobile species mass frac. at obs. points
obs_h.out        / output file containing heads at observation points
2710.0           / density of the solid phase
2.0              / tortuosity factor (tau)
9.170            / alpha_1 - empirical parameter for natural dissolution
0.216            / alpha_2 - empirical parameter for natural dissolution
0.5              / alpha_3 - empirical parameter for natural dissolution
1.071            / alpha_4 - empirical parameter for natural dissolution
10               / number of obs pts.
8  1   1         / col row lay (j,i,k) for obs. pts.
8  1   2
8  1   3
8  1   4
8  1   5
8  1   6
8  1   7
8  1   8
8  1   9
8  1  10
24               / effluent concentration measured at column #
```

Figure B.10: <u>CORT3D.INP</u> Input File for 2D Example

B.2.2 <u>ISCO (Using Permanganate) of Entrapped DNAPL PCE in 1-D Column</u>

This simulation includes transient dissolution and chemical oxidation of stably entrapped, residual dense non-aqueous phase liquid (DNAPL) PCE in a hypothetical 1-D column. The column has a dimension of 40 cm long, 4.5 cm high, and 4.5 cm wide. The residual PCE (1.0% saturation) is distributed in the column as shown in Figure B.11. In

this example simulation, the column is discretized into 40 columns, 1 layer, and 1 row. The simulation covers 14 days, broken down into 56 six-hour intervals. The injection is located upstream of the source zone to drive groundwater containing oxidant through column. An injection rate of 0.886 mL/min, corresponding to a Darcy velocity of 63.0 cm/day, is used in this simulation. The oxidant is permanganate (MnO_4^-) at a concentration of 7,500mg/L (0.75% by weight). The hydraulic head at the end of the test column is kept constant at 4.5 cm. The BTN, RCT, and CORT3D.INP input files for this example are shown in Figures B.12, B.13, B.14 and B.15, respectively.
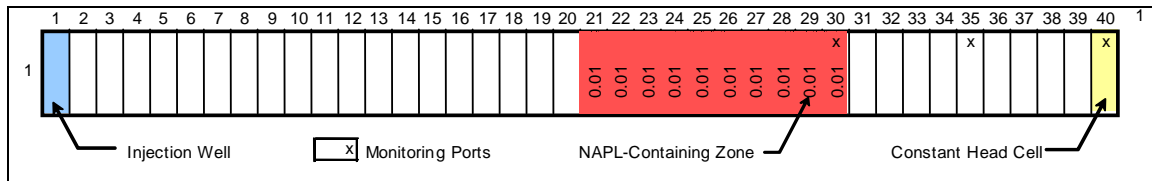
Figure B.11: Test Column for Example Problem 2.

```
40   -888.0   0
1
0
-1.0
1
0
OPEN/CLOSE  fort.6001  1.0  (free) 0  HK layer  1
CONSTANT 1.0
CONSTANT 1.0
```

Figure B.12: LPF Input File for 1D Example

```
GMS MT3D Simulation                                     COMMENT1
08 November 2004                                        COMMENT2
         1          1         40          1          8          3
 hr   cm   mg        TUNIT,LUNIT,MUNIT
 T T T T T F F F F F         TRNOP(ADV,DSP,SSM,RCT,GCG,NA,NA,NA,NA,NA)
 1         LAYCON
         0 1.0000000                                    DELR
         0 4.5000000                                    DELC
         0 4.5000000                                    HTOP
      1001       1.0                              0     DZ(K)
      4001       1.0                              0     PRSTY_EFF
         0         1                                    ICBUND
      7001       1.0                              0     CONC FOR CONT (M/L3)
      8001       1.0                              0     CONC FOR MNO4 (M/L3)
      9001       1.0                              0     CONC FOR CL (M/L3)
     10001       1.0                              0     MASSFRAC FOR MNO2 (M/M)
     11001       1.0                              0     MASSFRAC FOR NAPL CONT (M/M)
     12001       1.0                              0     MASSFRAC FOR SORBED CONT (M/M)
     13001       1.0                              0     MASSFRAC FOR FAST NOD (M/M)
     14001       1.0                              0     MASSFRAC FOR SLOW NOD (M/M)
 -999.0000                                              CINACT, (THKMIN)
         1         0         0         0          T     IFMTCN,IFMTNP,IFMTRF,IFMTDP,SAVUCN
         0                                              NPRS
         0                                              NOBS,(NPROBS)
         T                                              CHKMAS,(NPRMAS)
  6.00000        12 1.0000000                           PERLEN,NSTP,TSMULT
     0.0       1000 1.0000000            0.0            DT0,MXSTRN,TTSMULT,TTSMAX
```

Figure B.13: BTN Input File for 1D Example

```
        0          10         15         2         1         2
      2001       1.0                                2              RHOB
1.0e-010 1.0e-009
1.0e-010 1.0e-009
1.0e-010 1.0e-009
1.0e-010 1.0e-009
1.0e-010 1.0e-009
1.0e-010 1.0e-009
1.0e-010 1.0e-009
1.0e-010 1.0e-009
0.03132                                            rc(1):Dm_cont   (L2/T)
0.0588                                             rc(2):Dm_mno4   (L2/T)
0.07308                                            rc(3):Dm_cl     (L2/T)
1.3333                                             rc(4):Y_mno4_cont (mol/mol)
4.0                                                rc(5):Y_cl_cont   (mol/mol)
1.0                                                rc(6):Y_mno2_mno4 (mol/mol)
3000.0                                             rc(7):rho_mno2 (M/L3)
165830.0                                           rc(8):MW_cont   (M/mol)
1630.0                                             rc(9):rho_cont (M/L3)
262000.0                                           rc(10):k2_cont  (L3/mol-T)
0.200                                              rc(11):C_c_star (M/L3)
0.0                                                rc(12):eta  (1/T)
150.0                                              rc(13):lambda_c (L3/M)
52152.35                                           rc(14):k_nod_f  (1/T)
3.36e-005                                          rc(15):k_nod_s  (1/T)
      3001       1.0                                2      vrc(1):k_La (1/T)
      5001       1.0                                2      vrc(2):initial porosity
```

Figure B.14: RCT Input File for 1D Example

```
ex2.mfn           / MODFLOW name (NAM or MFN) file
ex2.rts           / MODFLOW RT3D super (RTS) file
56                / number of iterations to perform
n                 / is this a continuation of another run (Y/N)?
ex2.dis           / MODFLOW discretization (DIS) file
ex2.ftl           / MODFLOW flow-transport link file (binary)
ex2.hed           / file containing heads from MODFLOW (binary)
ex2.btn           / RT3D basic transport (BTN) file
ex2.rct           / RT3D reaction parameters file
init_K.dat        / input file containing hydraulic conductivity for all layers
phi0.dat          / input file containing porosity for all layers (w/ no napl)
d50.dat           / input file containing d50 for all layers
srw.dat           / input file containing residual water saturation for all layers
sn.dat            / input file containing napl saturation for all layers
smn.dat           / input file containing MnO2 pseudo-saturation for all layers
conc7.out         / output file containing contaminant concentration
conc8.out         / output file containing permanganate concentration
conc9.out         / output file containing chloride concentration
mfrac10.out       / output file containing MnO2 mass fraction
mfrac11.out       / output file containing NAPL mass fraction
mfrac12.out       / output file containing Sorbed contaminant mass fraction
mfrac13.out       / output file containing Fast NOD mass fraction
mfrac14.out       / output file containing Slow NOD mass fraction
mass.out          / output file containing mass of immobile species within model
obs_c.out         / output file containing mobile species conc. at obs. points
obs_m.out         / output file containing immobile species mass frac. at obs. points
obs_h.out         / output file containing heads at observation points
4200.0            / density of the solid phase
1.008801779       / tortuosity factor (tau)
75.50161425       / alpha_1 - empirical parameter for natural dissolution
.6878052435       / alpha_2 - empirical parameter for natural dissolution
1.991786E-4       / alpha_3 - empirical parameter for natural dissolution
.5942657302       / alpha_4 - empirical parameter for natural dissolution
3                 / number of obs pts.
30   1    1       / col row lay (j,i,k) for obs. pts.
35   1    1
40   1    1
39                / effluent concentration measured at this column
```

Figure B.15: <u>CORT3D.INP</u> Input File for 1D Example

APPENDIX C

PRELIMINARY INTERMEDIATE-SCALE 2D EXPERIMENTS

C.1   Introduction

Several intermediate-scale 2D tank experiments were performed prior to the main experiment described in Chapter 4. The first experiment involved only dissolution of a PCE source (known mass at near residual saturation) located at the bottom of a homogenous (#70 silica sand) layer. The second experiment involved dissolution of the PCE source as well as diffusion of aqueous-phase PCE into a LPM layer. The experiment consisted of a two-layer system (#70 silica sand over #140 silica sand). In this case a residual PCE source of the same size as experiment 1 was placed at the bottom of the #70 sand layer, sitting directly on top of the #140 layer. The PCE was again dissolving but was also be able to diffuse into the LPM region (#140 sand). A third experiment (with the same configuration as the second) was conducted where permanganate was injected.

C.2   Methodology

The experiments were done in a tank that is 240cm long x 46cm high x 8cm deep (Figure C.1), using a PCE source zone (at residual saturation) that is 8cm long x 3cm high x 8 cm deep. The source zone was a coarse sand lens within the finer sand of the primary flow region, to create a capillary barrier effect allowing a well-defined spatial limit to the source zone. See Figures C.1 and C.2.
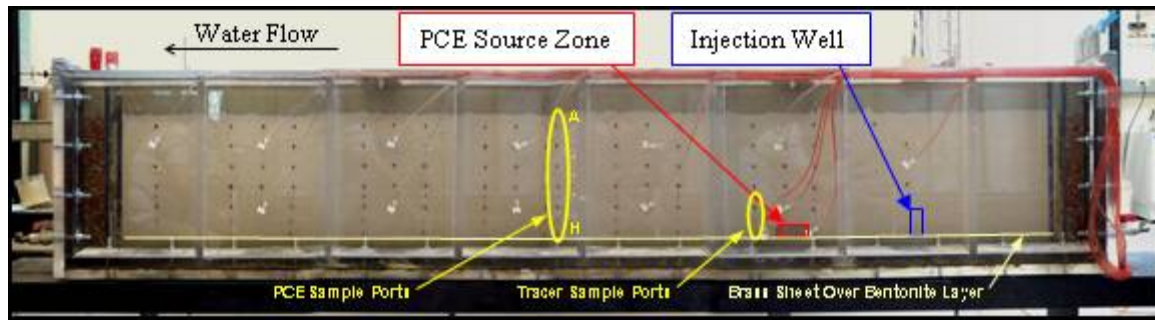
Figure C.1: Experiment 1 - Intermediate 2-D Tank
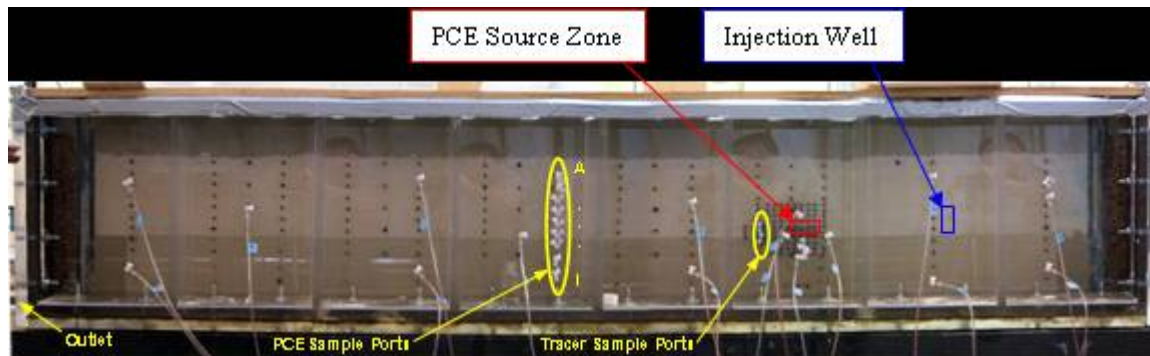
Figure C.2: Experiment 2 & 3 - Intermediate 2-D Tank with Layer of LPM

For each experiment, the tank was wet-packed without PCE and then flushed with de-aired water for 14 days (approx 10 pore volumes) to ensure no air was trapped within the porous media. Then a dye tracer test was performed by injecting water with red food dye into the inlet to verify that flow was uniform with no preferential flow paths or stagnant zones. Once the flow was verified to be uniform, the steady-state head distribution within the tank was obtained from a series of manometers or pressure transducers located horizontally and vertically throughout the tank. The head distribution and volumetric flow rate at the tank outlet were used to obtain values for the hydraulic conductivities by inverse modeling. The estimated hydraulic conductivities were used to obtain a steady-state flow field for input into the transport model. Next, both transient

and steady-state conservative (bromide) tracer tests were performed prior to source emplacement. The results were used along with the steady-state flow field to determine the porosity and dispersivities through inverse modeling.

Bromide tracer samples were collected and analyzed as described in Appendix A. Following the bromide tracer tests, water flow in the tank was stopped and the PCE source was emplaced. A glass syringe was used to inject PCE (dyed with 44 mg/L Sudan IV) into the bottom of the source zone, over approximately a 30-minute period, until the PCE filled the source zone without breaching the capillary barrier. Once the source zone appeared fully saturated (Figure C.3a), PCE was slowly withdrawn over approximately 60-minutes, until PCE could no longer be extracted. The mass of PCE emplaced was the difference between what was injected and what was removed. This resulted in a source zone that was approximately at residual saturation through the top 75% of the zone, and near full saturation in the bottom 25% (Figure C.3b). The source zone for experiment 1 had 13.9 mL of PCE with an average PCE saturation of 18.3%. The source zone for experiment 2 had 10.3 mL of PCE with an average PCE saturation of 13.4%.
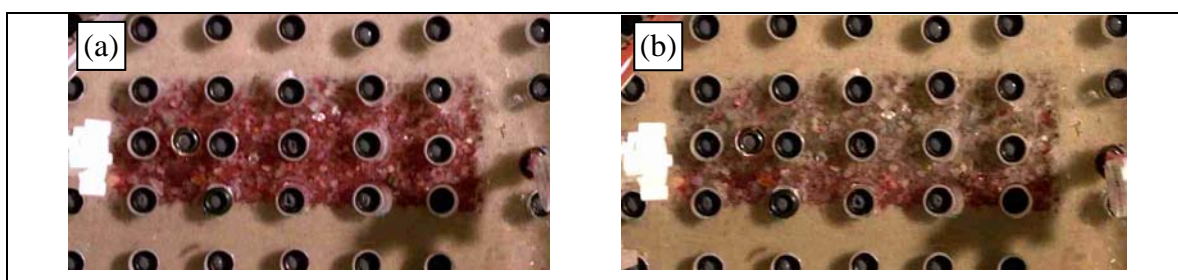
Figure C.3: Experiment 2 Source Zone - (a) after Injection, (b) after Withdrawal

Once the source was emplaced, water flow was resumed and frequent sampling was performed down-gradient of the source zone and at the tank outlet every 15-30 min for 9.5 hours, then every 3-8 hours for the next 62 hours, followed by every 1-4 days after

that. Once aqueous PCE concentrations reach a steady-state, a partitioning tracer test (PTT) was performed. Bromide was used as the conservative tracer. The three partitioning tracers used (and their partitioning coefficients for PCE) were: 2-2-dimethyl-3-pentanol (k_p=27.51), n-hexanol (k_p=8.49), and 6-methyl-2-heptanol (k_p=71.92). Sampling for the PTT occurred at the tank outlet as well as at ports located down-gradient of the leading edge of the source zone (Figures C.1 and C.2).

PTT samples (and aqueous PCE samples during the dissolution phase of the experiment) were collected and analyzed as described in Appendix A. Following the first PTT, the experiment progressed with routine sampling, as well as head and flow measurements. Upon completion, another PTT was performed, followed by destructive coring of the source zone.

C.3   Experiment 1

For experiment one, there were three down-gradient ports (covering bottom 9 cm of tank). Port A was 8 cm above tank bottom (tracer was injected across bottom 6 cm of tank), port B was 4.5 cm above tank bottom, port C was 1.5 cm above tank bottom. Breakthrough curves for PTT 1 are shown in Figure C.4. Note that no breakthrough curve is shown for the tank outlet. This is because sampling at the outlet started too late, missing the tracer peaks. Based on moment analysis of the tracer breakthrough curves, the PTT estimated an initial PCE volume of 4.5 mL (3.2 mL in bottom of source as seen by port C, and 1.3 mL in top of source as seen by port B). Clearly the tracers missed a great deal of the PCE; however, this is not surprising because a great deal of the PCE mass was present at high saturation at the bottom of the source zone. It is estimated that the PCE was initially distributed through the source zone with approximately 1.0 mL (~2% saturation) in the top ¾ of the source zone and approximately 12.9 mL (~68% saturation) in the bottom ¼, and the high PCE saturation appears to have resulted in flow bypassing. It appears that port B did a fair job of estimating PCE volume in the residually saturated portion of the source zone.
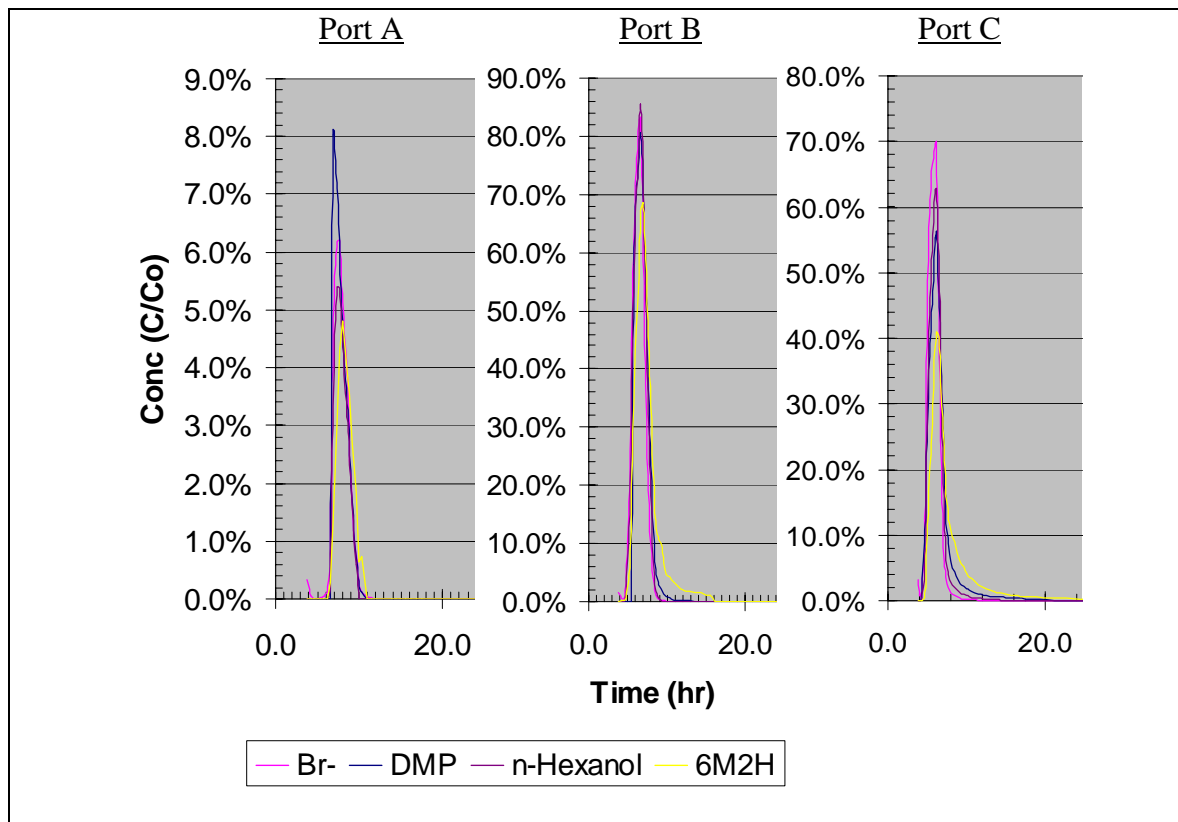
Figure C.4: Experiment 1 - Initial Partitioning Tracer Breakthrough Curves

PCE dissolution continued for six weeks after PTT 1. Then, when approximately 40% of the PCE was estimated to have dissolved, based upon volumetric flow rate and outlet aqueous concentration, a second PTT was performed (Figure C.5). The same tracers and sampling ports were used. The sampling at ports B and C resulted in an estimated remaining PCE volume of 0.7 mL (0.2 mL in bottom of source as seen by port C, and 0.5 mL in top of source as seen by port B). The results for ports B and C show significant source reduction (~85%) since PTT 1, but continue to severely underestimate the PCE volume in the source zone. Based upon effluent concentrations and volumetric

flow rates through the tank, there was an estimated 11.3 mL of PCE still in the source zone at the time of PTT 2 (an actual source reduction of ~19%). This time outlet sampling captured the peaks so analysis could be done. Moment analysis of the outlet breakthrough curve resulted in an estimated PCE source volume of 3.8 mL. Although the estimate using the outlet sampling data is higher than that from ports B and C, it is still quite low. Although no photos were taken of the source zone, visually it appeared that virtually all the residual PCE in the upper ¾ of the source were gone and remaining PCE was present at fairly high saturation in the bottom of the source zone.
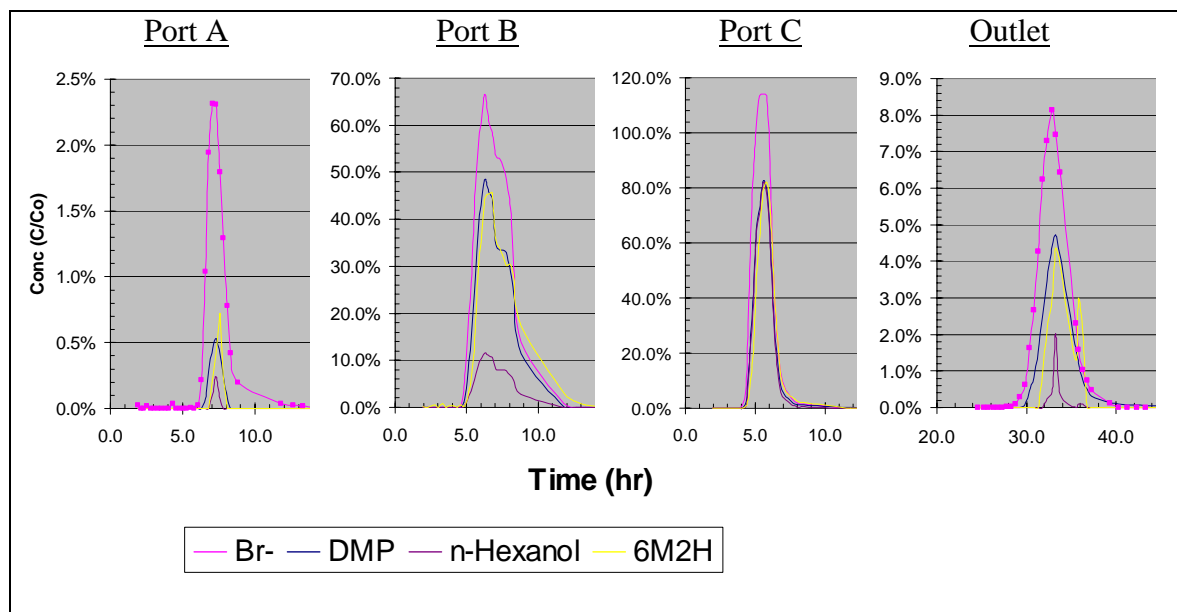
Figure C.5: Experiment 1 - Final Partitioning Tracer Breakthrough Curves

Following PTT 2, experiment 1 was stopped and the tank cored in three locations through the entire height of the tank, two locations above and through the source zone, one location up-gradient of the source, and one location directly down-gradient of the source. Continuous cores were obtained by draining the tank, driving 7 mm diameter

drinking straws into the soil, digging them out, freezing them, cutting them into ~1 cm lengths, performing hexane extractions on the soil, and analyzing the hexane on a gas chromatograph (GC) using an electron capture detector (ECD). The coring included cores of the bentonite clay layer in the bottom of the tank at three locations. Although a layer of brass sheeting had been installed between the bentonite and silica sand, to eliminate or minimize diffusion of aqueous PCE into the bentonite, coring of the bentonite was needed to determine if diffusion had occurred.

The tank was drained after experiment 1 (except for the bottom layer of bentonite which was below the tank outlet) prior to coring, so the coring results represent aqueous PCE in residual water or sorbed to sand grains. Less than 2.5 mg/L of PCE were found throughout the sand of the tank, corresponding to the effluent concentration at the end of the experiment, indicating that essentially no PCE was sorbed to sand grains. This was not unexpected because the silica sand being used had virtually no total organic carbon. On the other hand, the bentonite layer contained a fairly significant level of PCE (from 9-32 mg/L with an average of 17.6 mg/L). This high level of PCE was present all the way through the bentonite clay with the highest concentrations near the center vertically. Despite being almost completely cut off from the sand layer by brass sheeting, diffusion of PCE into this LPM was substantial. Only 1% of the source zone was cored, with resulting PCE mass for the source zone estimated at 1.5 mg (far less than the 18,000 mg expected). This suggests the remaining PCE may not have been evenly distributed even at the highly saturated bottom of the source zone. Alternately, a possibly large mass of PCE may have been lost during the soil coring process. As a result, the soil coring process was modified to that described in Appendix A for subsequent experiments.

Figure C.6 shows the aqueous PCE concentrations during experiment 1, at the outlet as well as ports E through H (bottom 10.4 cm). The inset shows the first 200 hours to provide better resolution. The tank outlet concentrations reached a steady value after two days, drop to a new steady value after about four days, and yet a third steady value after about 26 days. The first steady condition likely represents the dissolution of PCE in

the residually saturated portion of the source zone. The middle steady condition occurs once a significant portion of the upper residual PCE zone is essentially gone. The third steady condition is likely a result of the entire residually saturated PCE being gone and remaining dissolution occurs from the highly saturated region—high saturation results in decreased permeability to flow as well as less surface area for dissolution. An average mass transfer coefficient (k_{La}) can be estimated from the volumetric flow rate through the tank (Q), the tank volume (V_o), the maximum aqueous solubility (c^*), and the steady-state effluent concentration (c^∞) using

$$k_{La} = -\frac{Q}{V_o * \left(1 - \dfrac{c^*}{c^\infty}\right)} \tag{C.1}$$

Based on the flow rate maintained during the experiment (10 mL/min), tank volume (54,000 mL), and a maximum aqueous solubility for PCE of 200 mg/L, the initial average mass transfer rate is 2.06×10^{-5} min^{-1} or 2.96×10^{-2} day^{-1} during dissolution of the residual zone. The average mass transfer rate decreases to 7.72×10^{-6} min^{-1} or 1.11×10^{-2} day^{-1} during the middle phase, and 1.87×10^{-6} min^{-1} or 2.69×10^{-3} day^{-1} during the final phase.
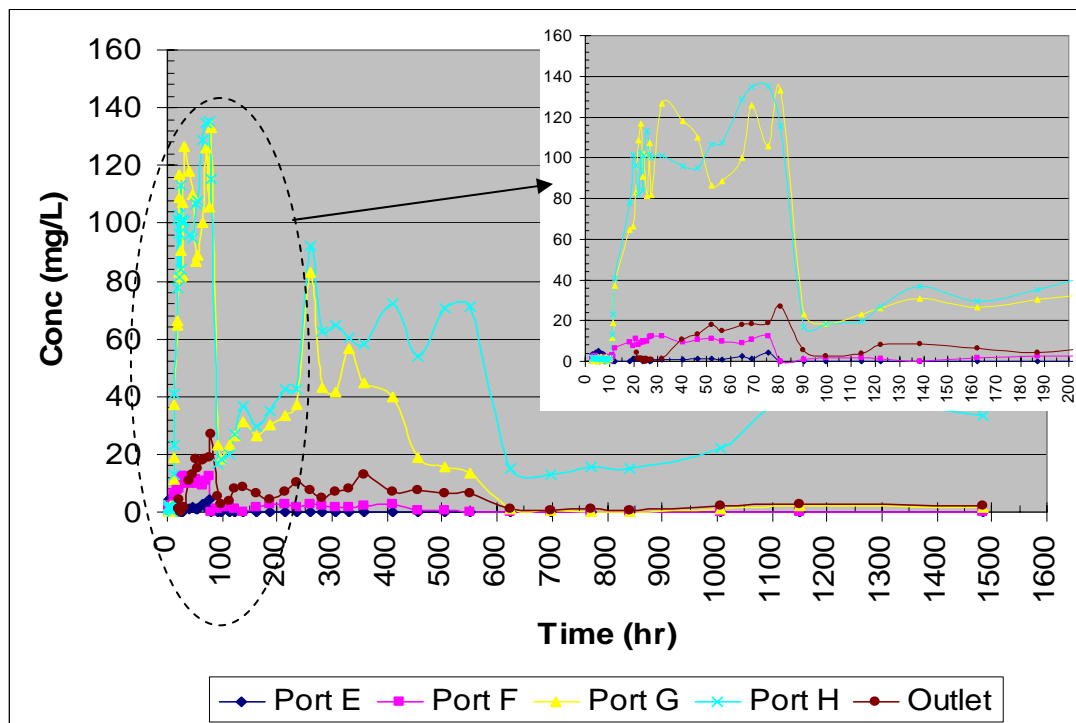
Figure C.6: Experiment 1 - Aqueous PCE Breakthrough Curves

C.4   Experiment 2

The second experiment placed a similarly configured PCE source on top of a low permeability material (LPM) consisting of #140 silica sand, and incorporated both natural dissolution as well as diffusion of aqueous PCE into the LPM. Two actual field soils were considered along with the #140 sand for use as LPM—one a silty soil, the other a loamy sand. Both field soils have significant organic carbon content as well as natural oxidant demand (NOD), while the #140 sand has neither. While the field soils would provide realistic conditions, it was determined that the increased complexity would prevent quantification of PCE and oxidant lost to various processes. For example, with field soils PCE mass would be lost to sorption as well as dissolution and oxidation, and oxidant would be lost to oxidation of NOD as well as PCE. Additionally, during oxidation the sorptive characteristics of the LPM would likely change as organic matter is

mineralized. On the other hand, #140 sand has a slightly higher permeability than either of the field soils making it more difficult to restrict transport within the LPM to diffusion. In hopes of limiting the advective transport through the #140 sand LPM, bentonite clay was used at the up- and down-gradient boundaries of the LPM region.

The source emplacement technique was improved for experiment 2 (by injecting and withdrawing through 5 ports instead of 3), so the source zone had 10.3 mL of PCE emplaced with an average PCE saturation of 13.4%. Ten days after source emplacement (one week after dissolution reached steady-state conditions), the initial PTT was performed to estimate the amount of PCE within the source zone. By this time, based on effluent concentrations, approximately 1.7 mL of PCE was estimated to have dissolved leaving 8.6 mL in the source zone. This time there were four down-gradient sampling ports (covering bottom 5 cm of higher permeability flow region—from bottom of source zone to 2cm above source zone). Port A was 3.8 cm above source bottom (tracer is injected from source bottom to 3cm above source), port B was 2.4 cm above source bottom, port C was 1.3 cm above source bottom, and Port D was 0.1 cm above source bottom.

Breakthrough curves for PTT 1 are shown in Figure C.7. Based on moment analysis of the tracer breakthrough curves, PTT 1 estimated an initial PCE volume of 1.8 mL (1.1 mL in bottom of source as seen by ports C and D, and 0.7 mL in top of source as seen by ports A and B). Clearly the tracers missed a great deal of the PCE; however, this is not surprising because a great deal of the PCE mass was present at high saturation at the bottom of the source zone. It is estimated that the PCE was initially distributed through the source zone with approximately 1.0 mL (~2% saturation) in the top ¾ of the source zone and approximately 9.3 mL (~65% saturation) in the bottom ¼. This estimation was done by visually estimating the amount of visible pore space present with dyed PCE in the top ¾ of the source zone and computing the remaining amount of injected PCE that would need to be present in the bottom ¼. The high PCE saturation

likely resulted in flow bypassing. It appears that combined ports A and B did a fair job of estimating PCE volume in the residually saturated portion of the source zone.
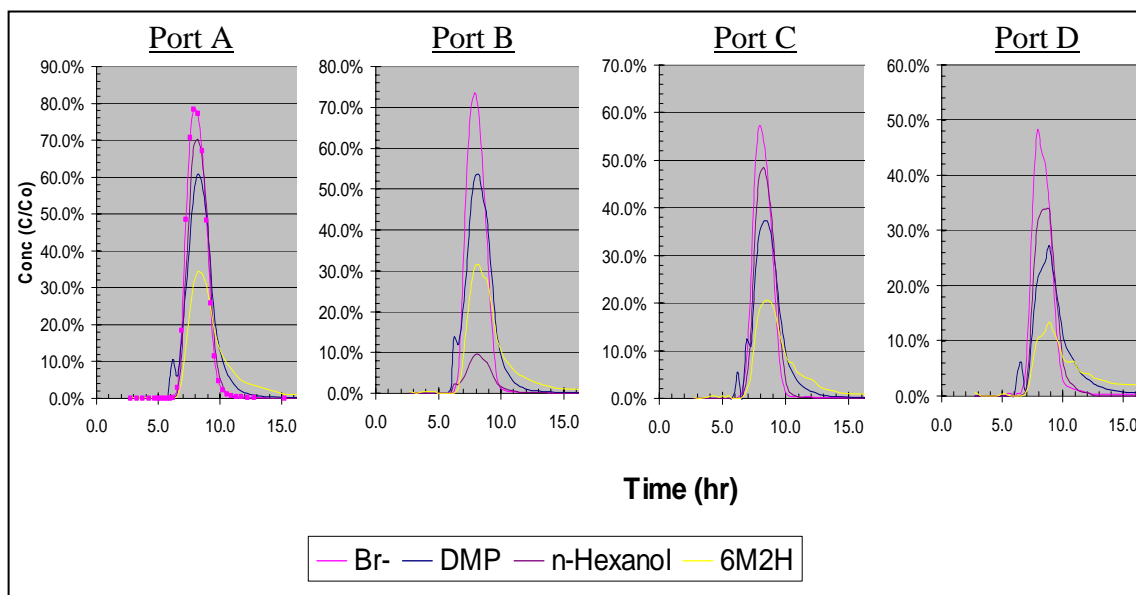
Figure C.7: Experiment 2 - Initial Partitioning Tracer Breakthrough Curves

PCE dissolution continued for seven weeks after PTT 1 and then a second PTT was performed. Breakthrough curves are shown in Figure C.8. The same tracers and sampling ports were used. The results of PTT 2 indicated a remaining PCE volume of 0.4mL (0.4 mL in bottom of source as seen by ports C & D, and 0.0 mL in top of source as seen by ports A & B). These results indicate significant source reduction (~95%) since PTT 1, but continue to severely underestimate the PCE volume in the source zone—especially in the bottom pool region. Based upon effluent concentrations and volumetric flow rates through the tank, there was an estimated 5.4 mL of PCE still in the source zone at the time of PTT 2 (an actual source reduction of ~37% since PTT 1). While partitioning tracer results for experiment two once again greatly underestimated PCE

saturation, the estimated source reduction for experiment two was quite a bit better than for experiment one, likely due to the smaller vertical spacing and increased number of sampling ports down-gradient of the source. Additionally, the decreased mass of PCE initially emplaced in experiment 2 likely resulted in less mass configured as a pool.
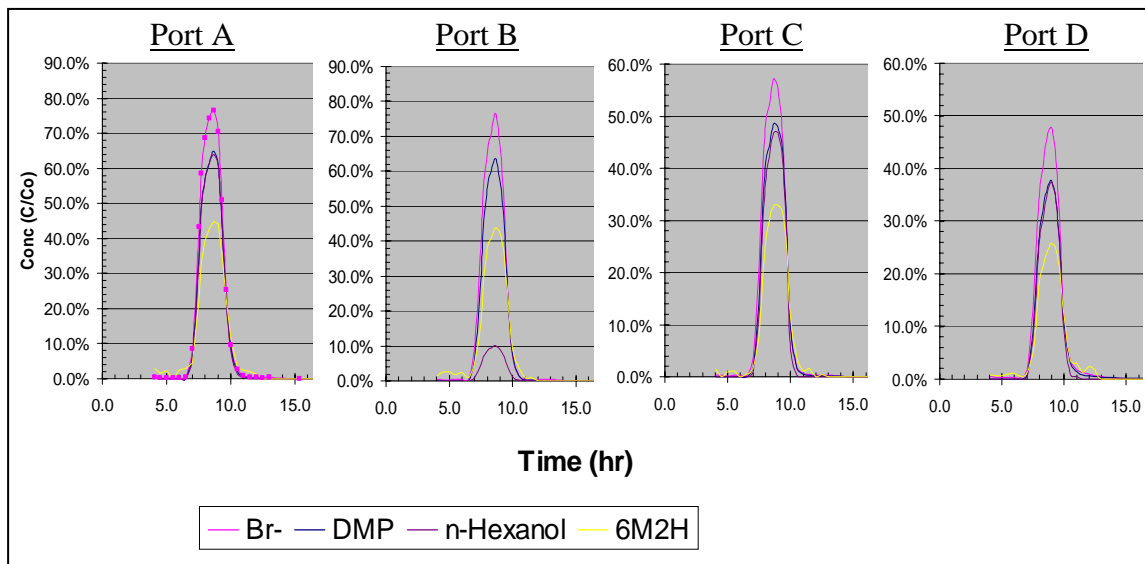
Figure C.8: Experiment 2 - Final Partitioning Tracer Breakthrough Curves

Tank outlet concentrations over time exhibited three distinct pseudo-steady-state regions on the breakthrough curve (Figure C.9). Tank outlet concentrations reached a steady value after three days, dropped to a new steady value after about 15 days, and decreased to a third steady value after about 35 days. Just as with experiment 1, the first steady condition likely represented the dissolution of PCE in the residually saturated portion of the source zone. The middle steady condition occurred once a significant portion of the upper residual PCE zone was essentially gone. The third steady condition was likely a result of the entire residually saturated PCE being gone and remaining

dissolution occurring from the highly saturated region—high saturation results in decreased permeability to flow as well as less surface area for dissolution.
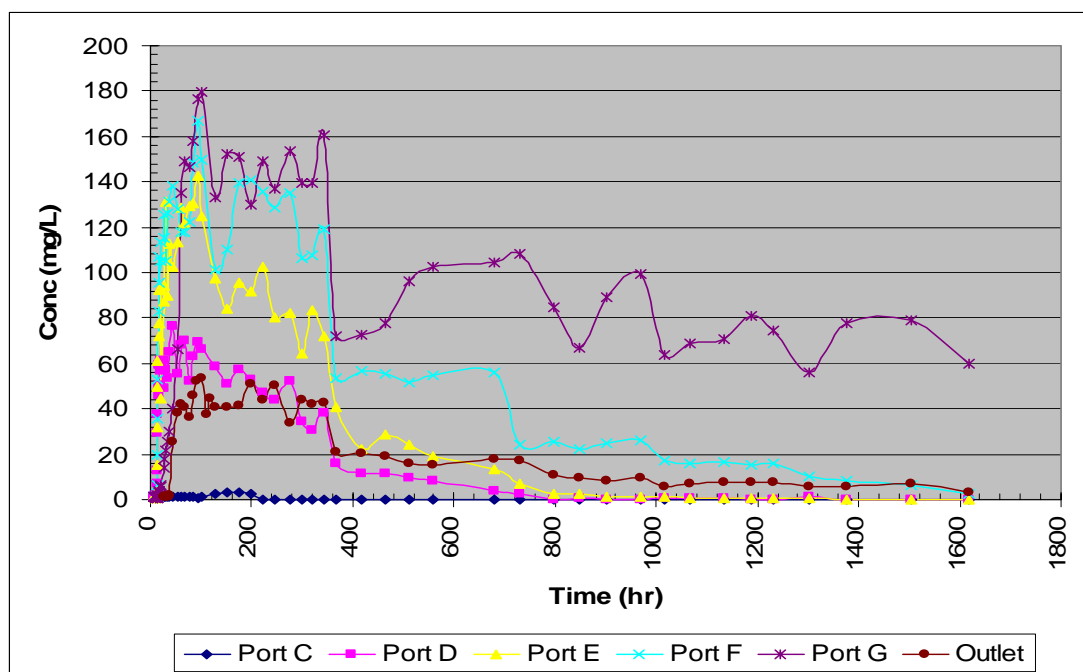
Figure C.9: Experiment 2 - Aqueous PCE Breakthrough Curves

Again, average mass transfer coefficients (k_{La}) were computed based on the flow rate maintained during the experiment (5.3 mL/min), tank volume (55,800 mL), and a maximum aqueous solubility for PCE of 200 mg/L, the initial average mass transfer rate was 2.38×10^{-5} min^{-1} or 3.42×10^{-2} day^{-1} during dissolution of the residual zone. The average mass transfer rate decreased to 9.39×10^{-6} min^{-1} or 1.35×10^{-2} day^{-1} during the middle phase, and 2.44×10^{-6} min^{-1} or 3.51×10^{-3} day^{-1} during the final phase. The estimated mass transfer coefficients for experiments 1 and 2 differ little (from 16% in the residually saturated region to 31% in the pool region). This is encouraging because the source zones for the two experiments were constructed so as to be similar. The slight

differences likely resulted from variations in source morphology within the source zone block.

C.5   Experiment 3

Instead of coring the tank after experiment 2 was finished, the source zone was flushed with potassium permanganate to look at oxidation of a simple PCE DNAPL pool source. The tank is shown in Figure C.10. Permeability changes around the source zone, down-gradient plume changes, and changes in DNAPL mass transfer rate were monitored. It is estimated the source zone contained about 4 mL (6500mg) of PCE at the time of oxidant delivery. Potassium permanganate (1250 mg/L as permanganate) was injected approximately 28 cm up-gradient of the source zone. Oxidant injection continued for 48 hours, at 1.5mL/min (increasing the flow rate through the tank from 5 to 6.5 mL/min). Before, during, and after the oxidant flush, samples were taken throughout the tank as well as in and around the source area. Samples were collected and analyzed as described in Appendix A.
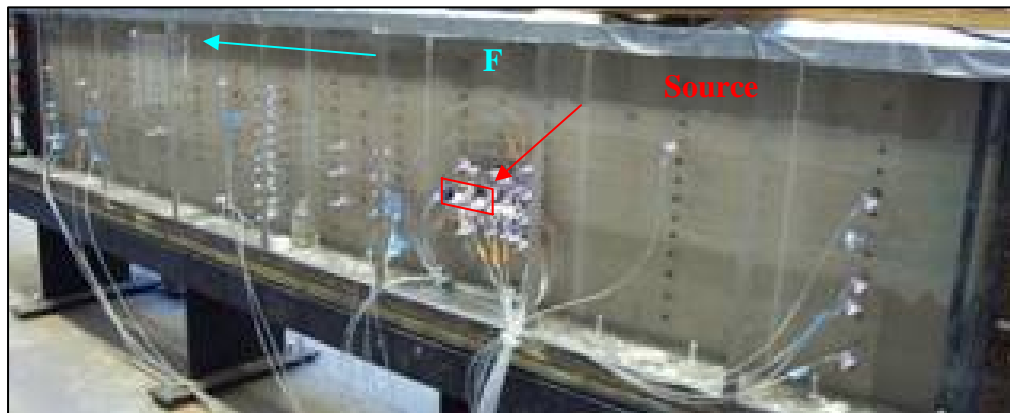
Figure C.10: Intermediate-Scale 2D Tank

Figure C.11 shows the PCE mass removed from the tank via dissolution and oxidation, as measured at the effluent. The mass of PCE oxidized was estimated based on the chloride concentration, because the only source of chloride in the system (after subtracting background levels obtained from influent samples) is from oxidization of PCE. From the figure, it can be seen that PCE dissolution increased as expected when flow rate through the tank was increased during oxidant injection. During the last fourth of the oxidant injection, the dissolved PCE drops off significantly as the oxidized PCE was increasing. This indicates that PCE was being oxidized as it dissolved. Further, the slope of the "Total PCE" line becomes greater than the slope of the dissolved PCE line prior to oxidant arrival, indicating that mass-transfer from the DNAPL was enhanced by the presence of oxidant. This enhancement continues to be visible after oxidant injection stops, and PCE and oxidant finish traveling through the tank.
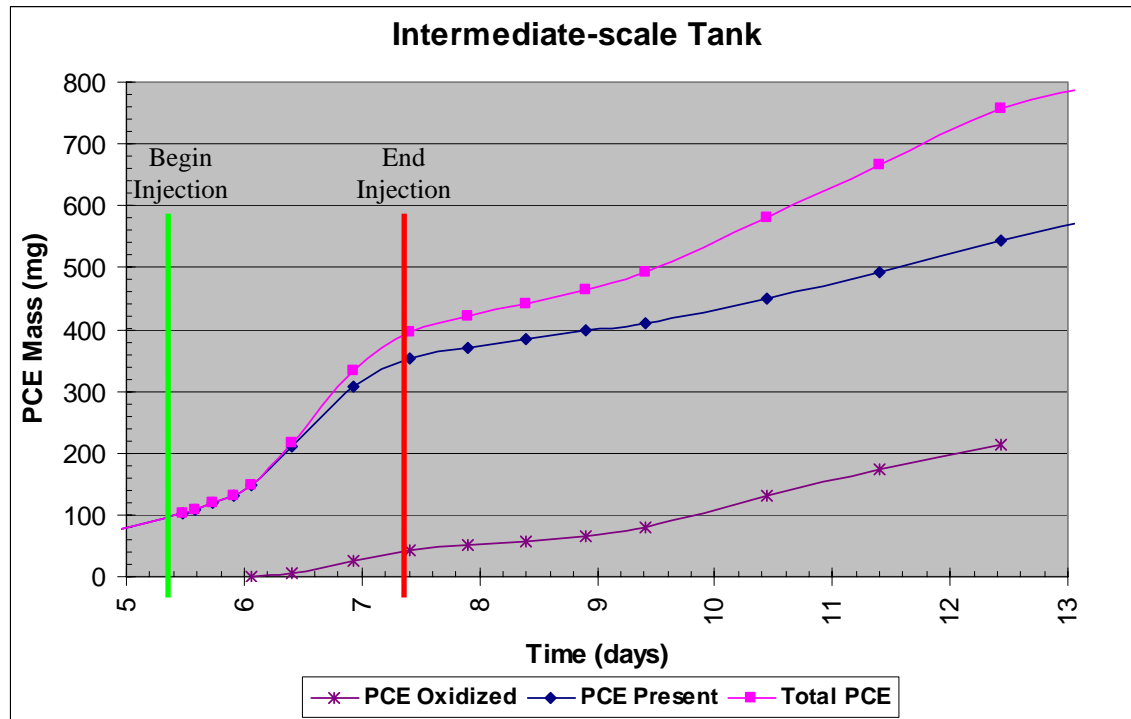
Figure C.11: Cumulative PCE Mass Removed from Intermediate 2D Tank

As oxidant flushed through the source zone, the silica sand in and down-gradient of the source zone was observed to turn brown. This suggests that some manganese oxides generated during oxidation became immobile. Hydraulic head was also monitored continuously throughout the tank and extensively around the source area. Figure C.12 shows the head measurements around the source zone prior to, during, and following oxidation. The inset is a graphic of the source zone, green dots represent head measurement locations. For clarity, only measurements from column "a" (up-gradient) and column "g" (down-gradient) are shown. During oxidant flushing, total flow through the tank increased from 5 mL/min to 6.5 mL/min, causing the drastic jump in head measurements between 5.4 days to 7.4 days. Additionally, the daily sinusoidal-like fluctuations are apparently a result of daily temperature fluctuations in the lab of 4-5°C. The low points occur overnight when lab temps are lowest; this is when the water density

will be increased, presumably decreasing its volume and therefore its pressure. In any case, it can be seen that the head drop across the source zone at the end of oxidation is twice what it was at the beginning of oxidation. This suggests permeability was substantially reduced through the source zone as a result of oxidation.
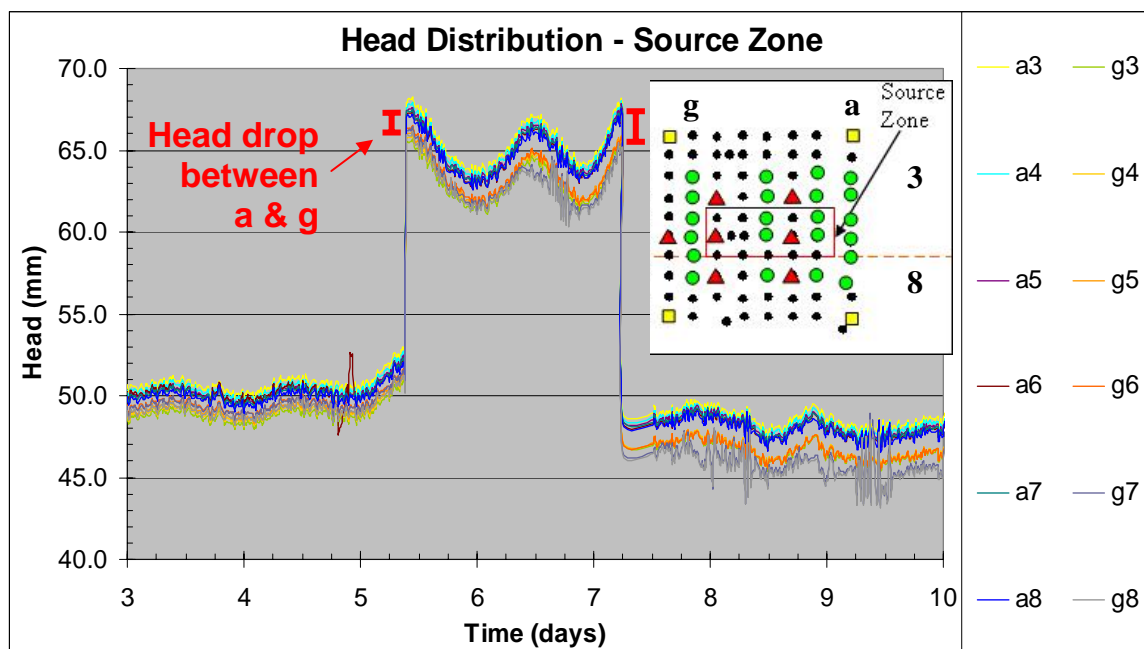
Figure C.12: Head Change across Source Zone due to Oxidation

While the hydraulic head drop across the source zone increased as a result of oxidation, the change was too small to utilize in inverse modeling of the experiment to quantify changes in hydraulic conductivity by location. Inverse modeling was able to match observed values to simulated values to within ±0.4mm; however, the increase in head drop was less than 0.8mm so inverse modeling was not able to determine a unique solution to the change in hydraulic conductivities. The use of a single small DNAPL pool relative to the cross-sectional area of the tank, combined with the small mass of

oxidant applied resulted in less $MnO_2(s)$ formation than desired. Additionally, it was found that the rectangular source cell resulted in considerable vertical flow out of the down-gradient end of the source cell due to the abrupt change in hydraulic conductivity. As a result, these experiments served to refine tank assembly and sampling protocols, as well as pointing out the value of using a larger, complex, constructed source zone for this experiment. They also demonstrated the need to have tapered ends on the sources to prevent abrupt hydraulic conductivity changes resulting in significant vertical flow.

APPENDIX D

LARGE-SCALE 2D HETEROGENEOUS EXPERIMENTS

D.1   Introduction

Two large-scale 2D, heterogeneous, complex DNAPL PCE source zone experiments were conducted investigating in situ chemical oxidation (ISCO) using permanganate. ISCO was just a portion of each of these experiments. Prior to oxidation, both experiments involved a surfactant enhanced aquifer remediation (SEAR) remedial flush as well as several partitioning tracer tests (PTT). The experiment was a combined effort of several researchers each looking primarily at one aspect of the overall experiment. Data analysis is still underway, and must be completed before the entire experiment can be formally written up. However, the general experimental methodology is summarized here along with a summary of preliminary results relating to the chemical oxidation portion.

D.2   Experimental Design

The experimental design for this research involved performing two PCE DNAPL dissolution and oxidation experiments in a large-scale 2D tank, packed with a different degree of soil heterogeneity for each experiment. PCE was injected into the designated source zone to simulate a spill forming a complex PCE DNAPL source zone with regions ranging from high saturation pools to residual saturation. The first experiment utilized a high degree of soil heterogeneity; the second had a low degree of soil heterogeneity. These experiments incorporated a number of phases to look at natural dissolution, surfactant enhanced remediation, and chemical oxidation. Before and after each remedial phase, partitioning tracer tests were conducted, and the PCE DNAPL source zone was

scanned using a dual-energy gamma attenuation system to determine the distribution and saturation of remaining DNAPL. The chemical oxidation phase occurred last, after several weeks of flushing with water to minimize surfactant still in the system. The surfactant and partitioning tracer portions of the experiment will not be covered here.

D.2.1 Materials

The experiment was conducted using clean white #16, #30, #50, #70 and #110 silica sand. Refer to Table A.1 in Appendix A for sand properties.

Table D.1: Properties of Porous Media Used in Experiment

Properties	#16 sand	#30 sand	#50 sand	#70 sand	#110 sand
K_s **(cm/min)**[1]	37.500	11.800	2.267	1.458	0.383
d_{50} **(cm)** [1]	0.088	0.049	0.030	0.019	0.010
U **(-)**[1]	1.72	1.50	1.94	1.86	2.00
$S_{r,w}$ **(-)**[2]	0.070	0.260	0.290	0.30	0.260
pH (in DI water) [3]	7.39	7.39	7.39	7.39	7.39
TOC (dry wt. %)[3]	0.019	0.019	0.019	0.019	0.019
ρ_B **(g/mL)**	1.6	1.6	1.8	1.6	1.8
Grain density (g/mL)	2.65	2.65	2.65	2.65	2.65

[1]Barth et al. (2001), Saenton et al. (2001), [3]Seitz (2004)

Technical grade potassium permanganate (Carus Chemical) was the oxidant used. Analytical grade PCE (>99% purity) from Mallinckrodt Chemicals, colored with 160mg/L Sudan IV hydrophobic organic red dye (analytical grade, Aldrich Chemicals) was used as the DNAPL. The surfactant was Tween-80 (polyoxyethylene sorbitan monoleate). See Table A.2 in Appendix A for partitioning tracers and other chemicals used. See Table A.3 in Appendix A for PCE properties. All aqueous solutions were prepared using DI water (>18.2MΩ-cm). Ordinary tap water was de-aired and provided flow through the tank. See Table 5.3 for tap water properties.

Table D.2: Properties of Tap Water

Property	Value
pH	7.41
Alkalinity (mg/L as $CaCO_3$)	35.2
TOC (mg/L)	1.14
Chloride (mg/L)	32.6
Total Dissolved Solids (mg/L)	185

D.2.2   2D Large-scale Tank Assembly

A 2D large-scale tank was constructed (L x W x H = 480cm x 5.0cm x 120cm). The up-gradient half of the tank, that would contain the DNAPL source zone, had an aluminum back panel and a glass lined clear acrylic front panel. The down-gradient half had clear acrylic front and back panels. Six vertical arrays of sampling ports (1.5mm diameter, sealed with rubber septa) were located down-gradient of the source. Each array contained two vertical rows (spaced 5cm apart) of ports spaced 2.5cm apart vertically- one row was used for taking aqueous samples, the other for measuring hydraulic head. Another array of ports was located 30cm up-gradient of the designated source zone for injection of remedial agent (oxidant in this case). The injection array was in the center of a homogeneous section (#16 sand) to facilitate mixing and uniform vertical distribution of oxidant injected through 32 of the ports. The tank included influent and effluent endwells connected to constant head reservoirs to maintain a specified hydraulic gradient through the tank. Figure D.1 shows a schematic of experiment 1, Figure D.2 shows a schematic of experiment 2. Figure D.3 shows a photo of the tank as packed for experiment 1.
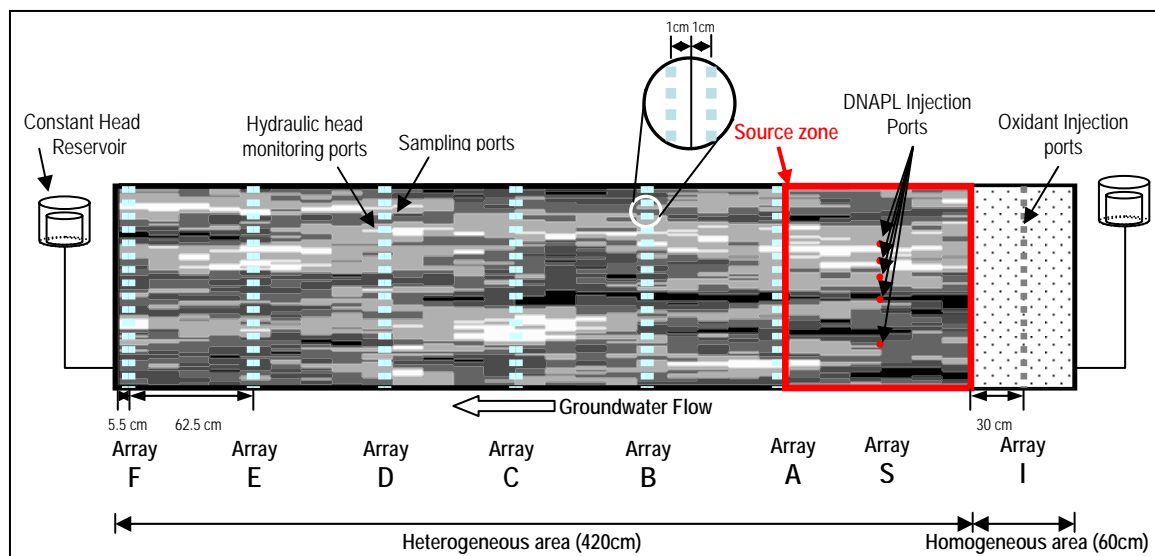
Figure D.1: Schematic of Large-Scale 2D Experiment 1
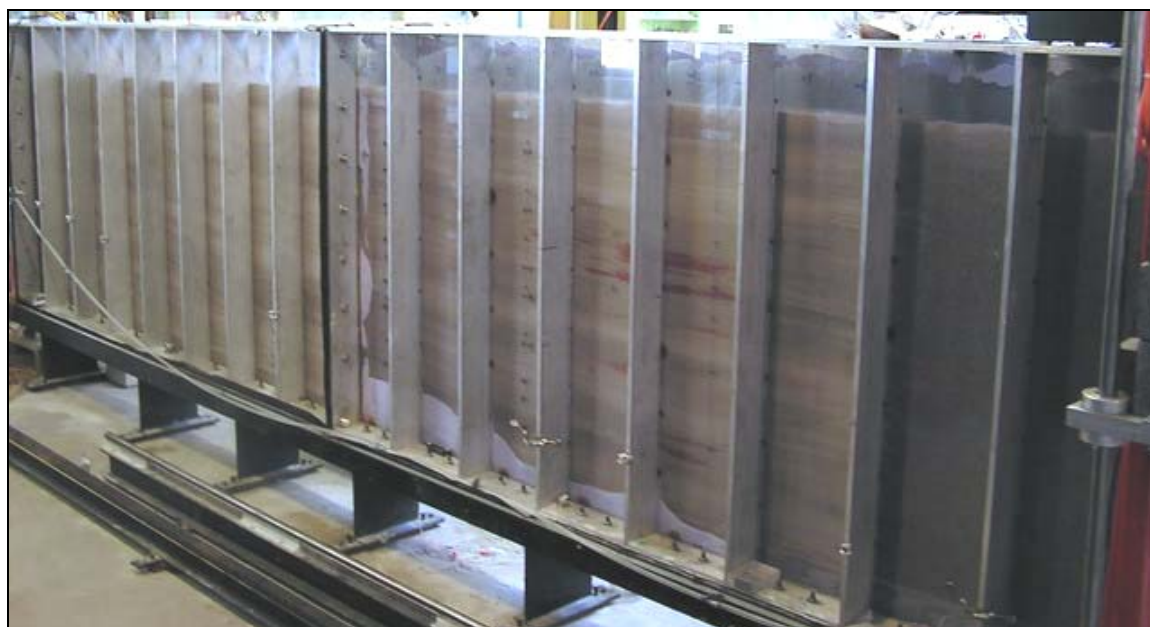
Figure D.2: Photo of Packed Tank for Large-Scale 2D Experiment 1
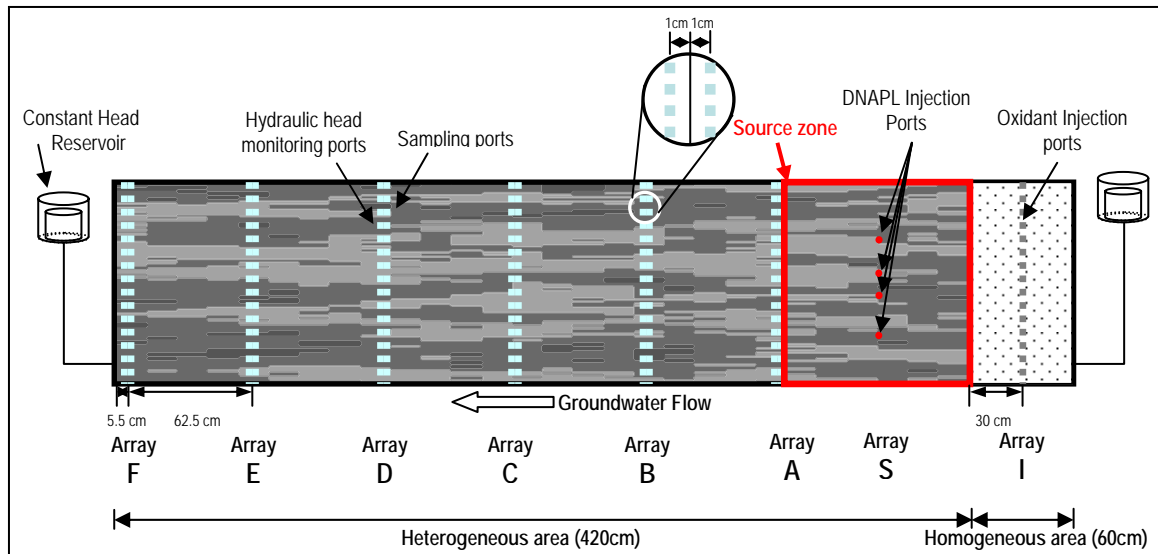
Figure D.3: Schematic of Large-Scale 2D Experiment 2

Prior to packing the tank, a spatially correlated random field was generated using the turning bands algorithm, producing a continuous distribution of lognormally distributed hydraulic conductivity values (ln K_s). This distribution of ln K_s values was then discretized into five ranges correlating to the properties of the five silica sands being used in the experiment, such that the theoretical average ($\mu_{ln\ K}$) and variance ($\sigma^2_{ln\ K}$) of ln K used to generate the continuous distribution were preserved. Table D.3 summarizes the heterogeneity used for each experiment. Figure D.4 shows diagrams of the discretized heterogeneity field for (a) experiment 1 and (b) experiment 2.

Table D.3: Heterogeneity Description for Experiment

Parameter	Experiment 1	Experiment 2
$\mu_{ln\ K}$ (m/day)	4.18	4.18
$\sigma^2_{ln\ K}$ (m/day)	1.22	0.25
Horizontal correlation length (m)	0.50	0.50
Vertical correlation length (m)	0.05	0.05
Anisotropy Ratio	10	10

284
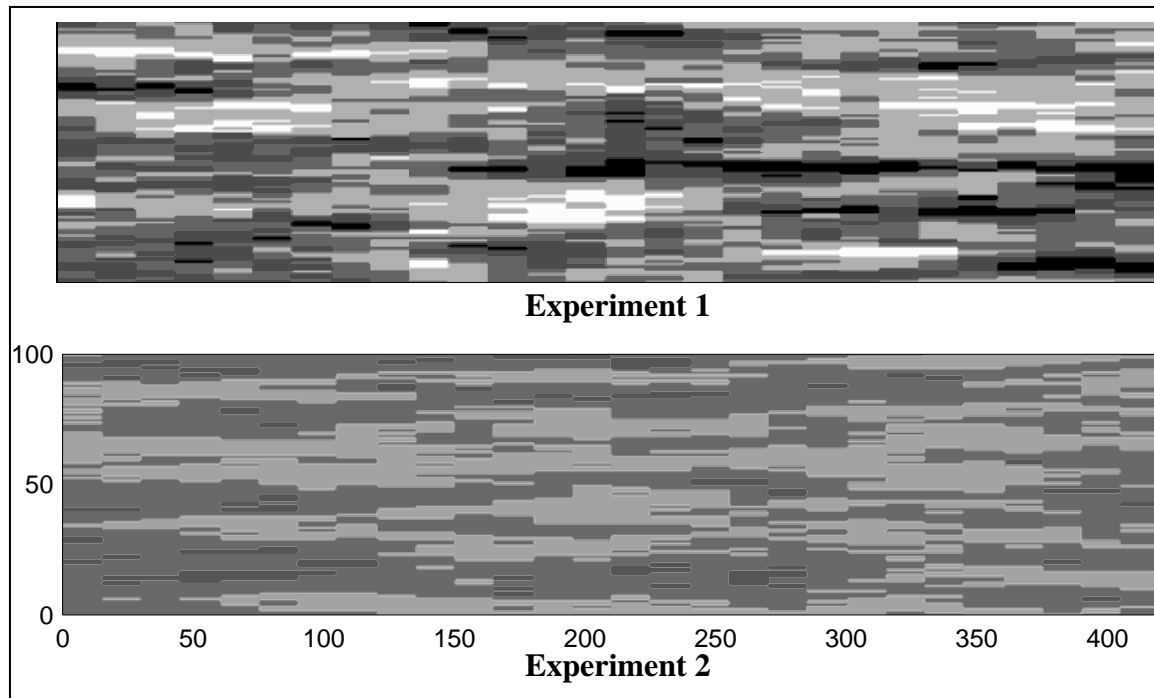
Figure D.4: Diagram of Soil Heterogeneity for Each Experiment

Once the heterogeneity field had been determined, the tank was wet-packed by hand in an effort to eliminate trapped air. Packing was performed in 1cm lifts, keeping the water level approximately 2cm above the current sand level. Water was added as needed, by raising the inlet constant head reservoir 1-2cm. Each layer was filled one sand lens at a time, progressing from one end of the tank to the other. Approximately 80cm^3 of the appropriate sand was placed for each lens to dimensions of about 15cm long by 1cm high. Placement was accomplished by dropping the sand through a 5cm diameter PVC pipe while moving the pipe back and forth along the lens location. This back and forth movement maintained a slow and even sand deposition rate as the sand settled through the water layer. Further, this method resulted in each sand lens having realistic, tapered ends instead of 'blocky' geometry with sharp vertical fronts.

Ambient air temperature of the lab was $22 \pm 3^{\circ}C$. Flow into and out of the tank was through constant head reservoirs to maintain a constant head difference resulting in the desired flow rate. Several periods of different flow rates were utilized during the natural dissolution, surfactant flush, and partitioning tracer phases. For experiment 1, during chemical oxidation the flow rate was initially 61.9mL/min. During chemical oxidation of experiment 2, the flow rate was initially 50.4mL/min. The flow rates dropped approximately 30% off during the chemical oxidation phase of each experiment, apparently due to manganese oxide buildup in the tank. Before entering the tank, water passed through a 5gal holding tank, sediment and carbon filters, a Degassit A6342 inline de-gassing unit from Varian, Inc, and finally an ultraviolet water purifier (Bio-Logic). The tank was flushed with approximately 20 pore volumes of water before PCE emplacement, to ensure removal of any fines or air bubbles that may have been trapped despite wet-packing.

Prior to emplacing PCE (and again after), the source zone of the tank was scanned using a dual-energy gamma attenuation system. Each scan took approximately eight days, but the difference between the two scans provides a quantitative measurement of the spatial DNAPL saturation through the source zone. Between gamma scans, flow through the tank was stopped and PCE was slowly injected into the source zone through multiple injection ports (Figure D.1 for experiment 1 and Figure D.2 for experiment 2). PCE injection was performed under constant head conditions using a Marriott bottle. Multiple injection locations (five for experiment 1, four in experiment 2) were used to ensure the PCE stayed within the defined source zone without migrating too far laterally and that the source zone was composed of a combination of residual and pool regions. Table D.4 lists the volume of PCE injected into each of the ports.

Table D.4: Initial PCE Volume Emplaced

Injection Port	PCE Volume (mL)	
	Experiment 1	**Experiment 2**
1	272.0	61.0
2	71.9	103.1
3	41.4	60.0
4	93.3	60.0
5	93.2	-
Total	586.7	284.1

Following PCE emplacement, both experiments underwent gamma scans of the source zone, partitioning tracer tests, natural dissolution, and surfactant flushing. Surfactant flushing was performed by flushing 50g/L Tween-80 through the tank (at approximately 53.0mL/min for 10 hours during experiment 1 and approximately 57.0mL/min for 11.75hours in experiment 2). After the surfactant flush, the source zone was gamma scanned again, along with natural dissolution and another partitioning tracer test. Several weeks (five for experiment 1 and 3 for experiment 2) elapsed between the surfactant flushing and commencement of the chemical oxidation phase. This was intended to provide sufficient time to ensure little or no residual surfactant remained in the tank; however, surfactant was still present up to 1000 mg/L. Tween-80 is readily oxidized by permanganate, so exerts a non-productive oxidant demand similar to NOD. As a result, increased manganese oxide generation was expected beyond that from oxidation of PCE alone.

D.2.3   2D Large-scale PCE Oxidation

Gamma scan data was used to determine the beginning PCE DNAPL distribution in the source zone as well as the initial PCE DNAPL mass for the chemical oxidation phase of each experiment. Figure D.5 is a plot of the PCE DNAPL distribution at the

beginning of the chemical oxidation phase of experiment 1 and Figure D.6 is a plot of the PCE DNAPL distribution at the beginning of experiment 2.
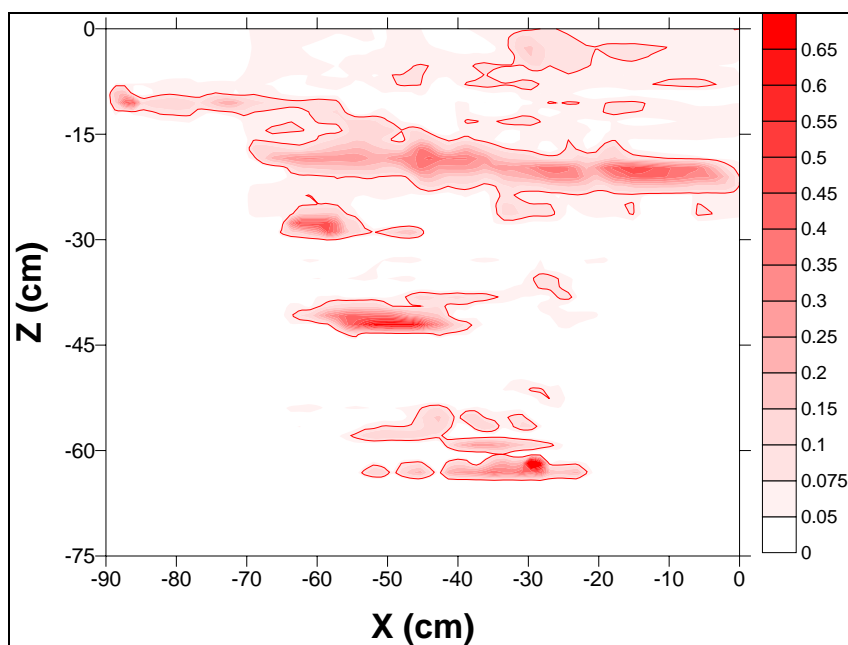
Figure D.5: DNAPL PCE Saturation Distribution Prior to Chemical Oxidation, Experiment 1 (axes are distance from origin of gamma scan)
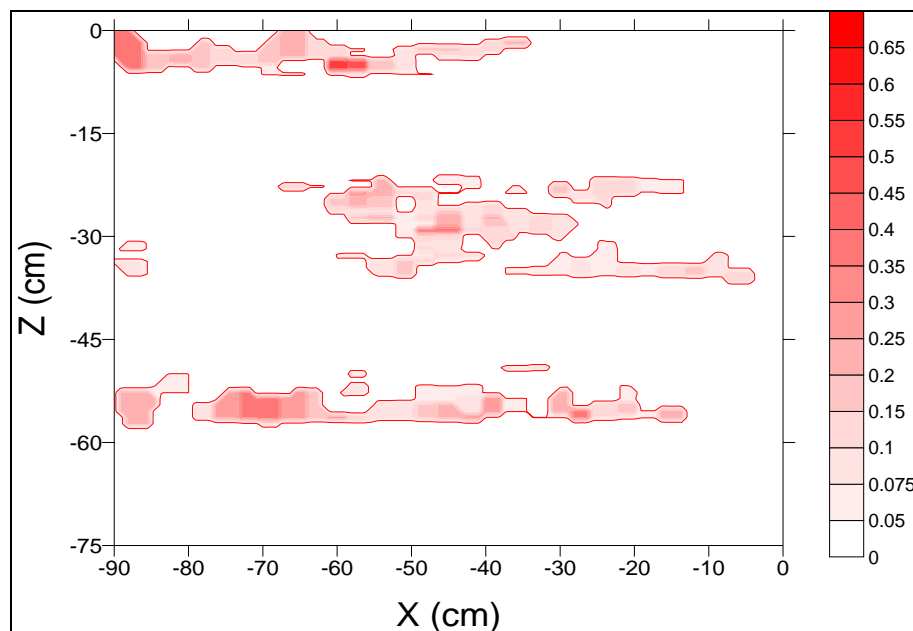
Figure D.6: DNAPL PCE Saturation Distribution Prior to Chemical Oxidation, Experiment 2 (axes are distance from origin of gamma scan)

Potassium permanganate was injected into the homogeneous region up-gradient of the source zone (see Figures D.2 and D.3) per Table D.5 during each experiment. The total injection rate (divided among 32 injection ports evenly spaced vertically through the tank) was approximately 1/8 the ambient flow rate through the tank, so the concentration flowing in the tank was expected to be approximately 1/8 of that injected. Aqueous samples were obtained frequently from sampling arrays A and C, as well as the effluent. Figure D.8 is a representative photo of the oxidation flush, taken during experiment 1. No photos were taken during experiment 2.

Table D.5: Oxidant Injection Summary

Parameter	Experiment 1	Experiment 2
$KMnO_4$ Concentration (mg/L)	8000.0	5000.0
Injection Duration (hrs)	48.5	24.5
Total Injection Rate (mL/min)	8.0	8.0
$KMnO_4$ Mass Injected (g)	186.24	58.8
Approximate PCE Mass at Start of Oxidation (g)	509.2	273.3
Maximum PCE Oxidation Possible (g)	146.6	46.3

Figure D.7: Oxidation of Large-Scale 2D Tank, Experiment 1

Despite the build-up of manganese oxides, mass transfer from the DNAPL was enhanced for both experiment 1 and experiment 2 as suggested by Figures D.8 and D.9, respectively. These figures show the mass of PCE removed from the tank via dissolution and oxidation, as measured at the effluent. Oxidant injection began at time 0, and ended at 1 day. The slope of the dissolved PCE line decreases as a result of oxidation, while the slopes of the oxidized and total PCE lines are much greater than the dissolved PCE line was originally, indicating mass-transfer from the DNAPL has been enhanced by the presence of oxidant. The enhancement is much more dramatic in the first experiment,

likely because of the much higher oxidant concentration and longer injection period. It may also be due to differences in the source configuration or flow field heterogeneity.
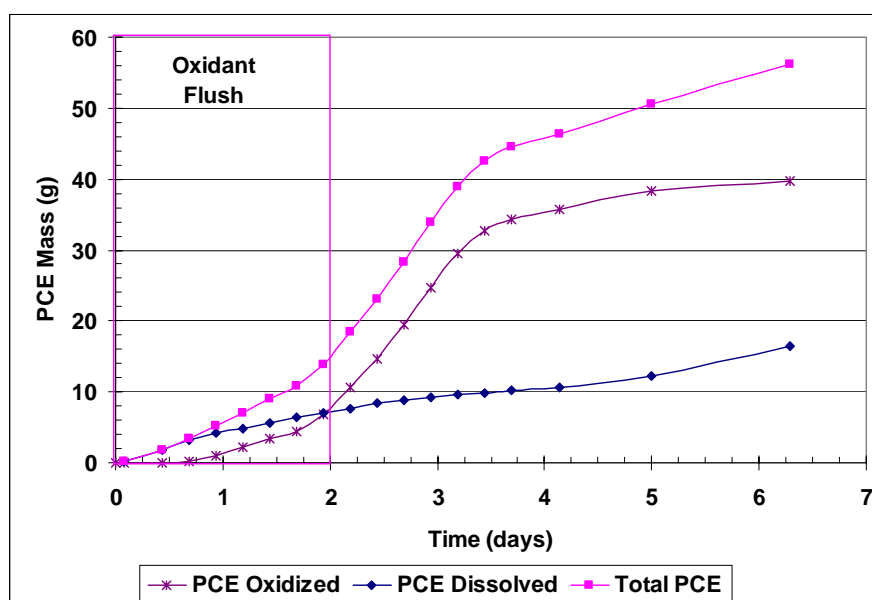
Figure D.8: Oxidation of Large-Scale 2D Tank, Experiment 1
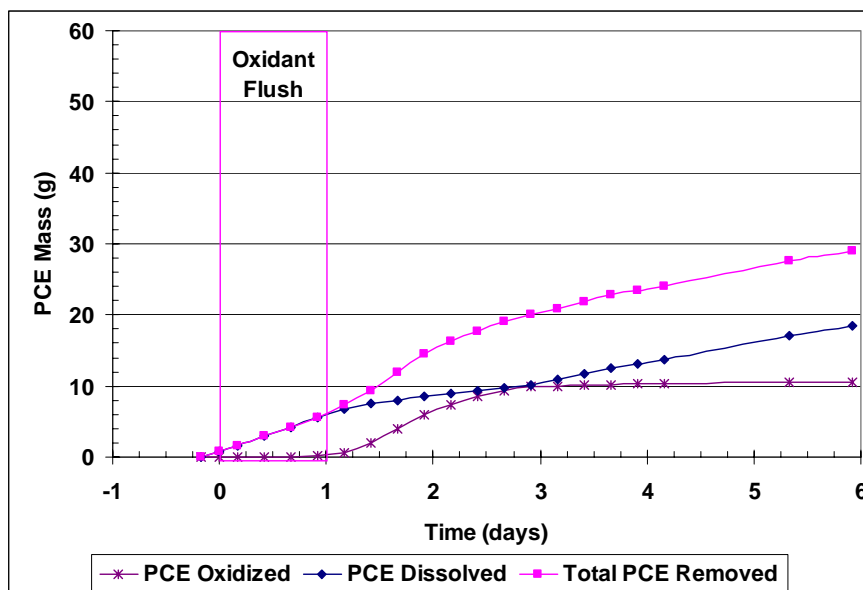
Figure D.9: Oxidation of Large-Scale 2D Tank, Experiment 2

Table D.6 summarizes the overall oxidation performance. The first experiment resulted in more effective oxidation, based on the percent of oxidant added that actually oxidized PCE. However, as discussed in Chapter 4, in a flushing scheme there is sure to be some portion of oxidant that does not pass through the source zone due to the flow heterogeneity and/or the size of the source zone relative to the cross-sectional area of the flush. In these experiments, the flush was distributed from the bottom of the tank to the top. Comparing the approximate cross-sectional areas of the sources (transverse to water flow), the sources of experiment 1 were about twice as large as experiment 2. As a result, it is not surprising to see that experiment 1 had a higher percentage of oxidant participate in destroying PCE. However, experiment 1 had a significantly larger mass of DNAPL PCE in the sources, as well as a more heterogeneous flow field, as a result a larger percentage of oxidant may have bypassed the source. In short, additional analysis is necessary to determine which experiment better utilized oxidant (i.e., which experiment had a higher percentage of oxidant, which contacted sources, destroy PCE).

Table D.6: Oxidation Performance Summary

Parameter	Experiment 1	Experiment 2
Approximate PCE Mass at Start of Oxidation (g)	509.2	273.3
Ganglia-to-pool Ratio	TBD	TBD
Approx. Cross-sectional Area of All Sources (cm)	225	150
Maximum PCE Oxidation Possible (g)	146.6	46.3
PCE Oxidized (measured as Cl- at effluent) (g)	40.2	10.6
Percent of Possible PCE Oxidized	27.4	22.9

PCE DNAPL distribution following chemical oxidation for experiments 1 and 2, is shown in Figures D.10 and D.11, respectively. Comparing these images to the pre-oxidation ones (Figures D.5 and D.6), it appears that PCE was destroyed fairly uniformly throughout the source zone of both experiments. However, further data analysis is necessary to confirm this.
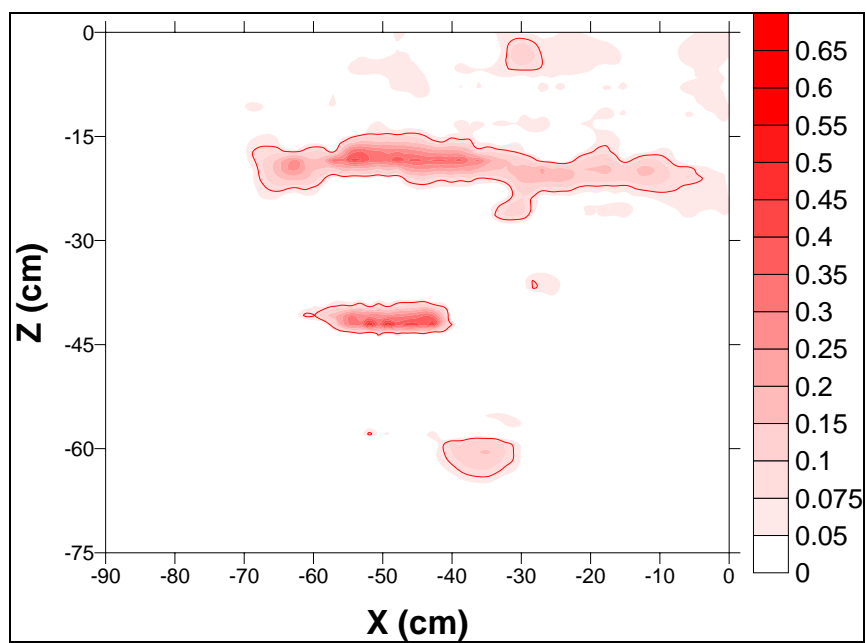
Figure D.10: DNAPL PCE Saturation Distribution Following Chemical Oxidation, Experiment 1 (axes are distance from origin of gamma scan)
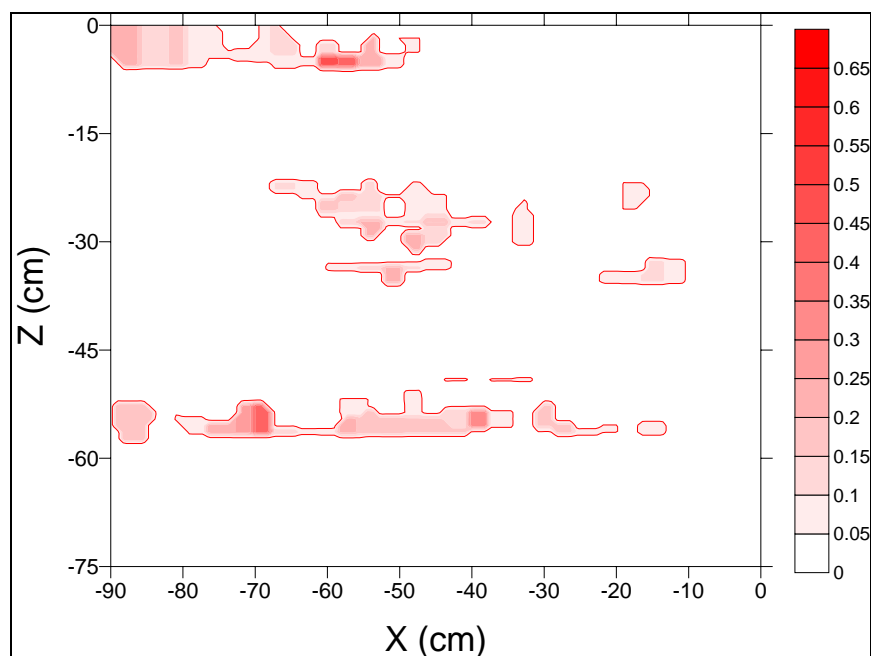
Figure D.11: DNAPL PCE Saturation Distribution Following Chemical Oxidation, Experiment 2 (axes are distance from origin of gamma scan)

Although more data analysis is needed, chemical oxidation using permanganate shows potentially significant enhancement of mass-transfer from a complex DNAPL sources in heterogeneous flow fields, even in the presence of non-productive oxidant demand.

APPENDIX E

NTC SITE SIMULATION RESULTS

E.1 Simulation Results
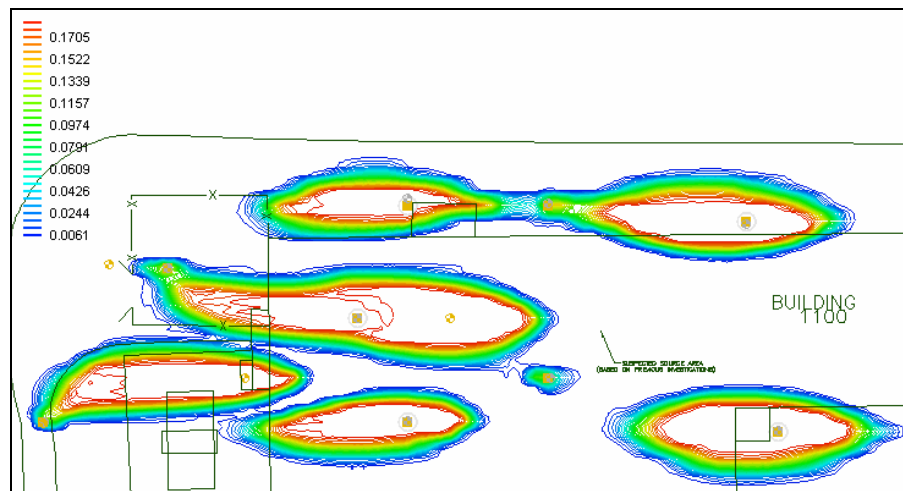
Figure E.1: MnO_4^- Distribution, 8gpm, 0.25mg/mL $KMnO_4$, Layer 2, no NOD present
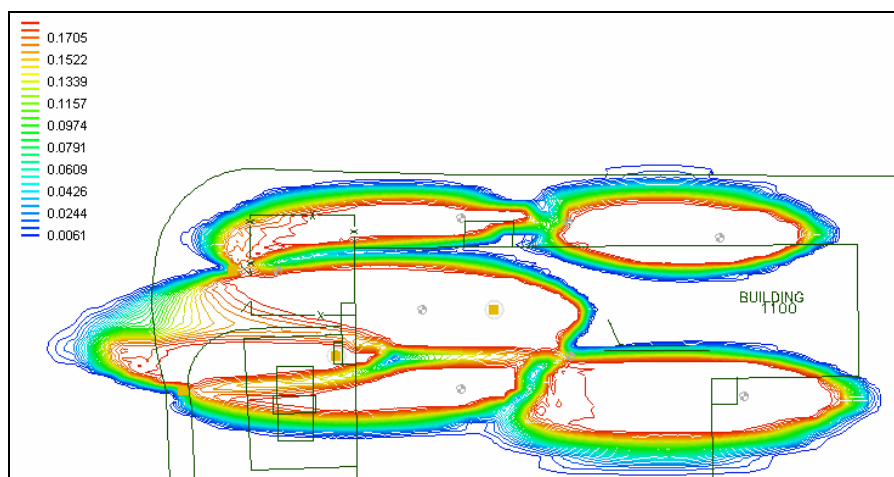
Figure E.2: 8gpm, 0.25mg/mL $KMnO_4$, Layer 3, no NOD present
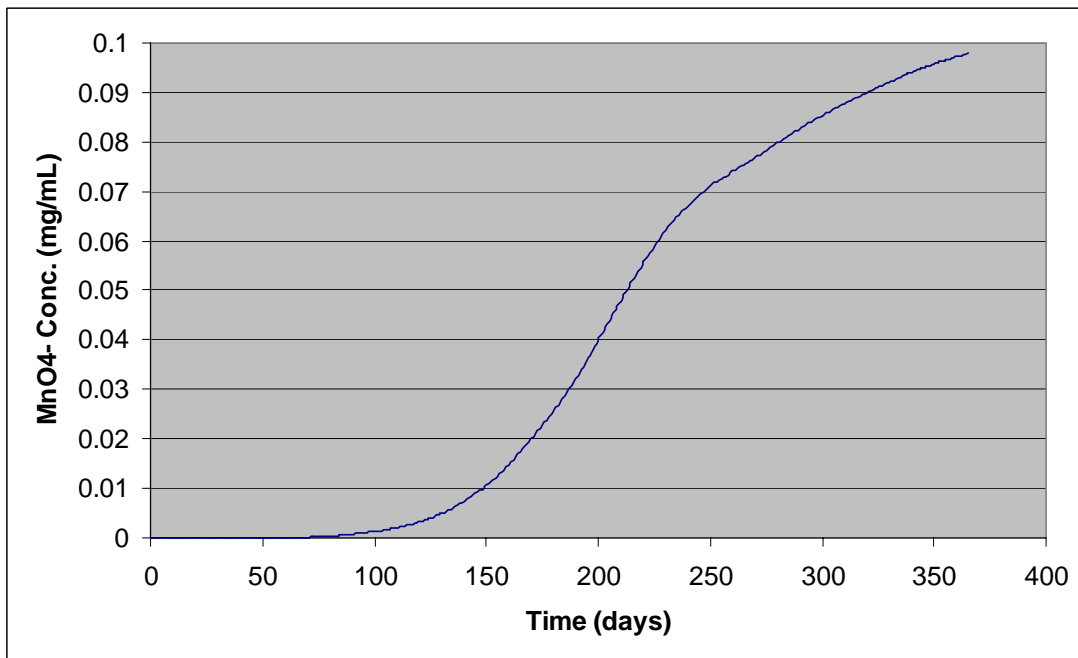
Figure E.3: MnO$_4^-$ Breakthrough at Shallow Extraction Well 2 (no NOD)
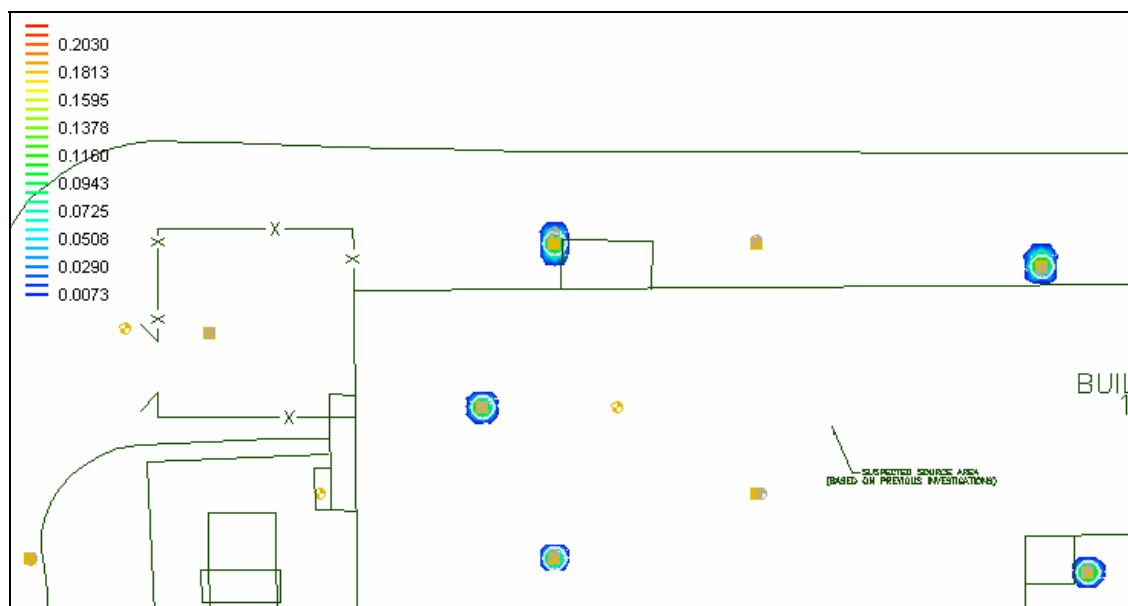
Figure E.4: MnO$_4^-$ Distribution, 5gpm, 0.25mg/mL KMnO$_4$, Layer 2, fast NOD present
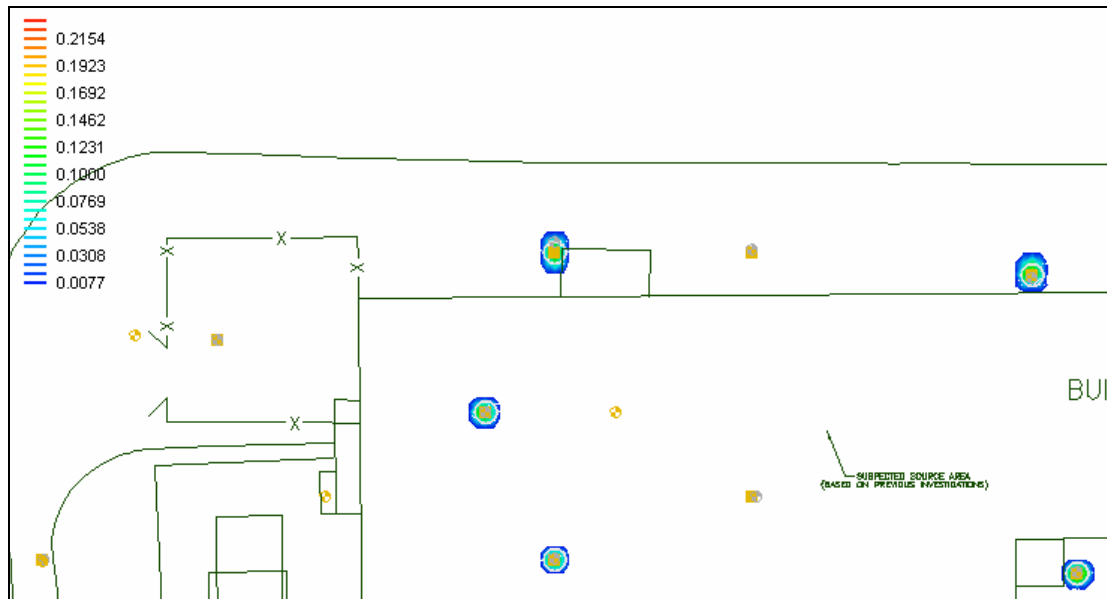
Figure E.5: MnO$_4^-$ Distribution, 8gpm, 0.25mg/mL KMnO$_4$, Layer 2, fast NOD present
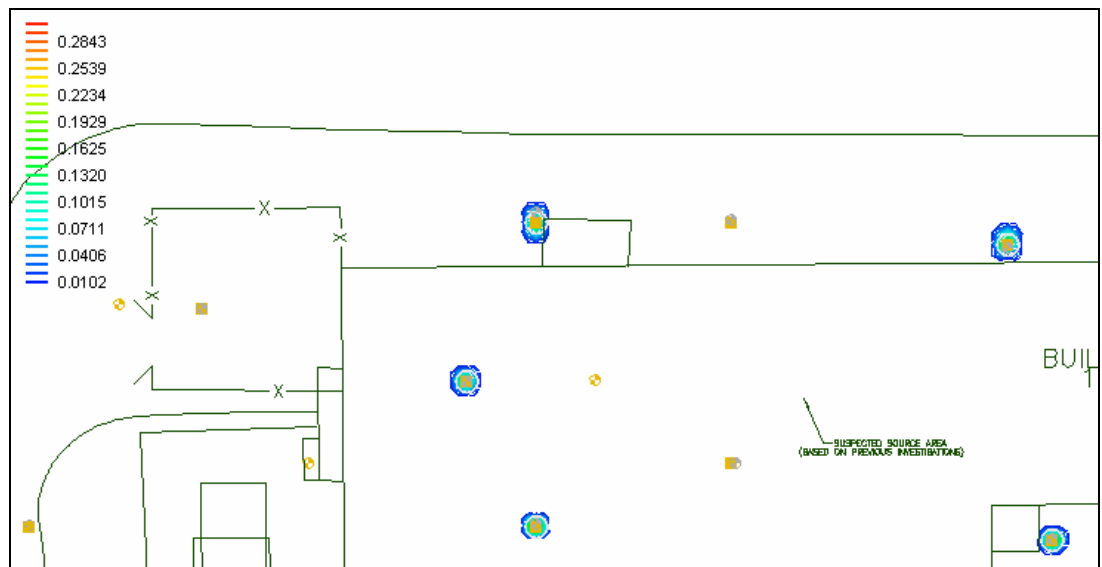
Figure E.6: MnO$_4^-$ Distribution, 10gpm, 0.25mg/mL KMnO$_4$, Layer 2, fast NOD present
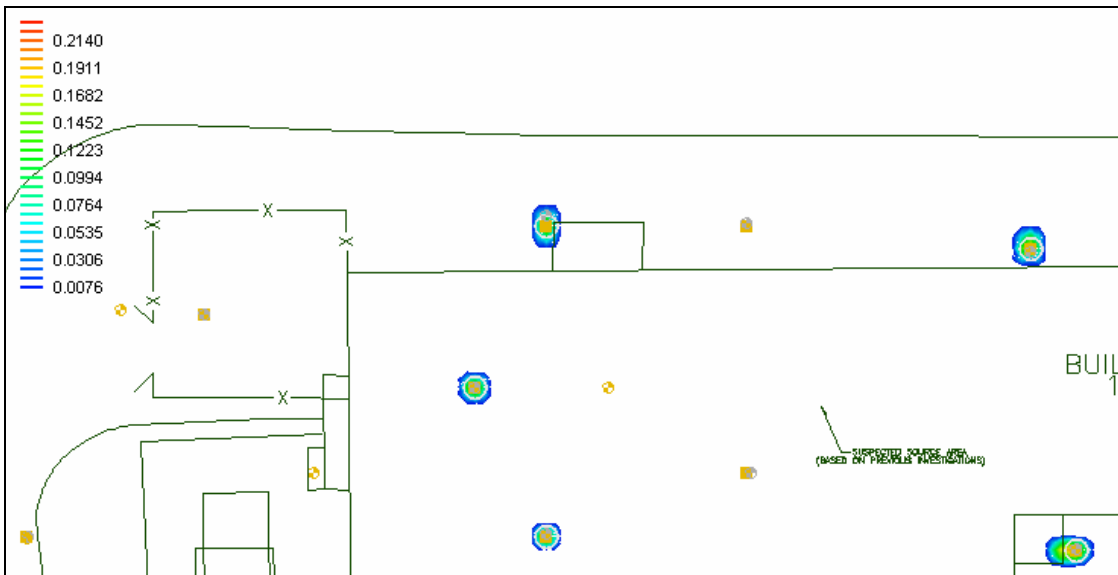
Figure E.7: MnO$_4^-$ Distribution, 15gpm, 0.25mg/mL KMnO$_4$, Layer 2, fast NOD present
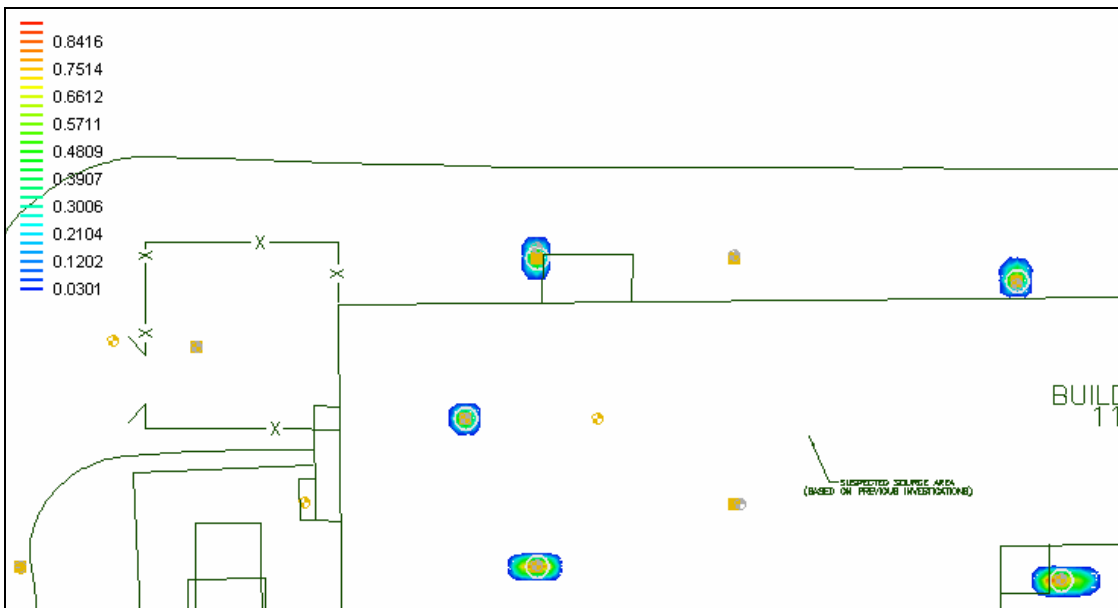
Figure E.8: MnO$_4^-$ Distribution, 5gpm, 1.0mg/mL KMnO$_4$, Layer 2, fast NOD present
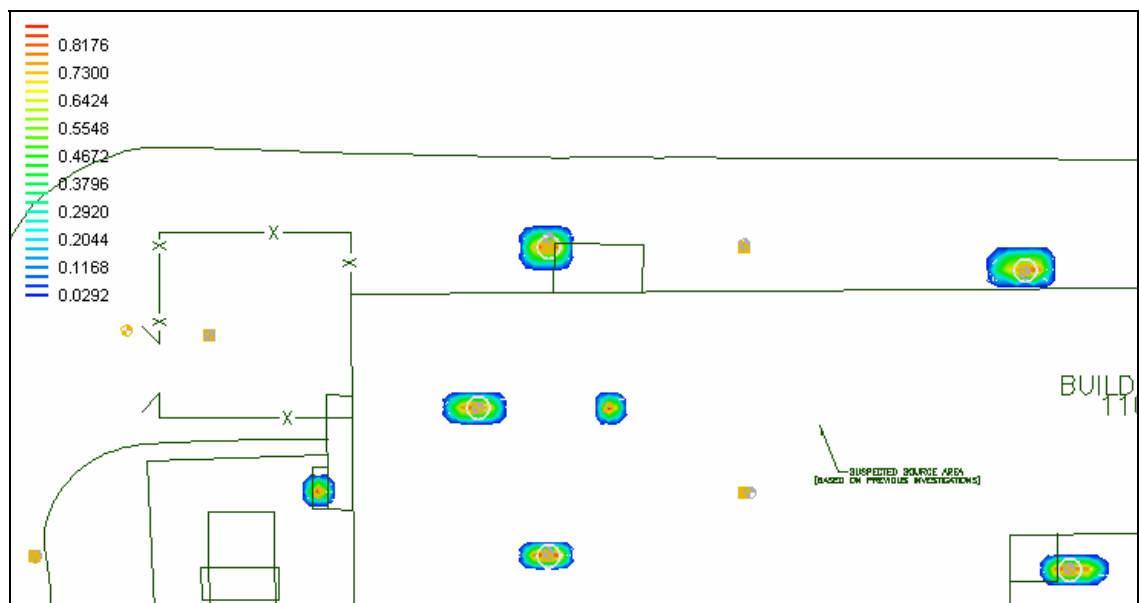
Figure E.9: MnO_4^- Distribution, 8gpm, 1.0mg/mL $KMnO_4$, Layer 2, fast NOD present
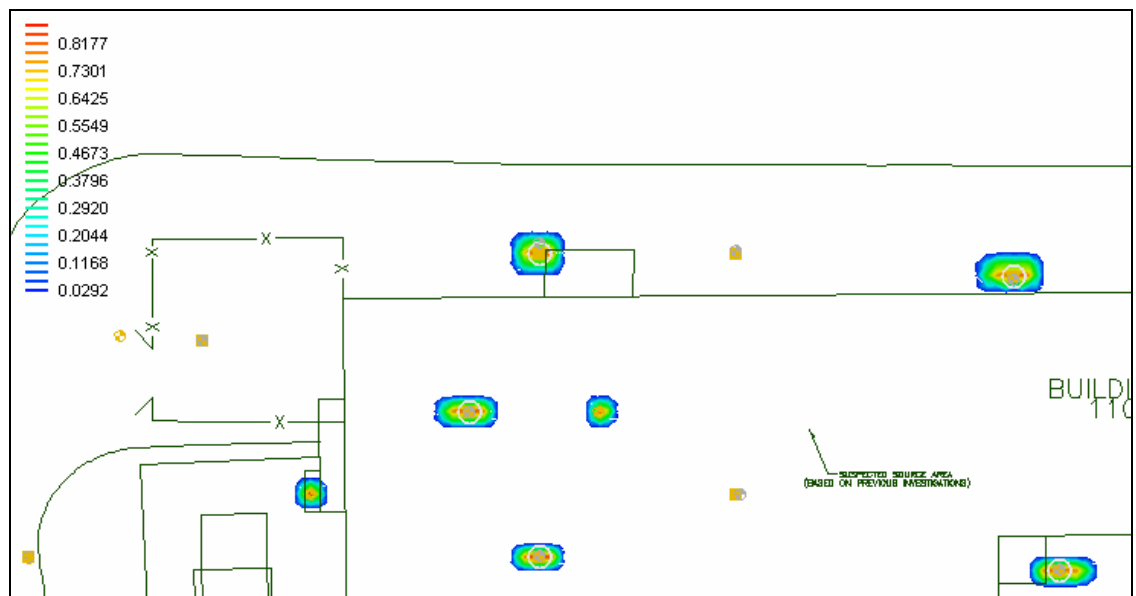
Figure E.10: MnO_4^- Distribution, 10gpm, 1.0mg/mL $KMnO_4$, Layer 2, fast NOD present
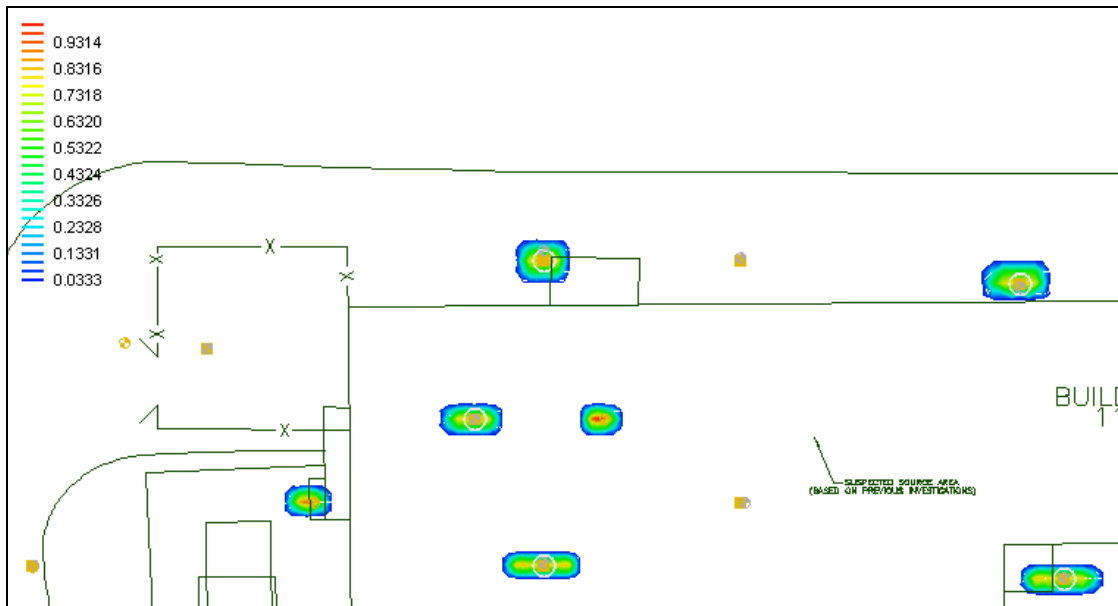
Figure E.11: MnO$_4^-$ Distribution, 15gpm, 1.0mg/mL KMnO$_4$, Layer 2, fast NOD present

Figure E.12: MnO$_4^-$ Distribution, 5gpm, 4.0mg/mL KMnO$_4$, Layer 2, fast NOD present
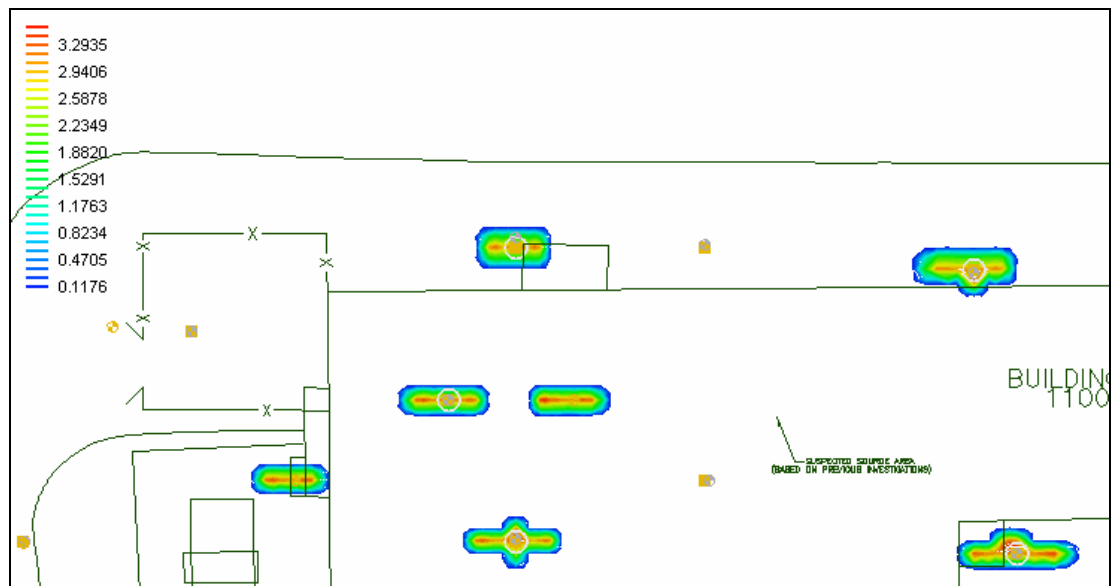
Figure E.13: MnO$_4^-$ Distribution, 8gpm, 4.0mg/mL KMnO$_4$, Layer 2, fast NOD present
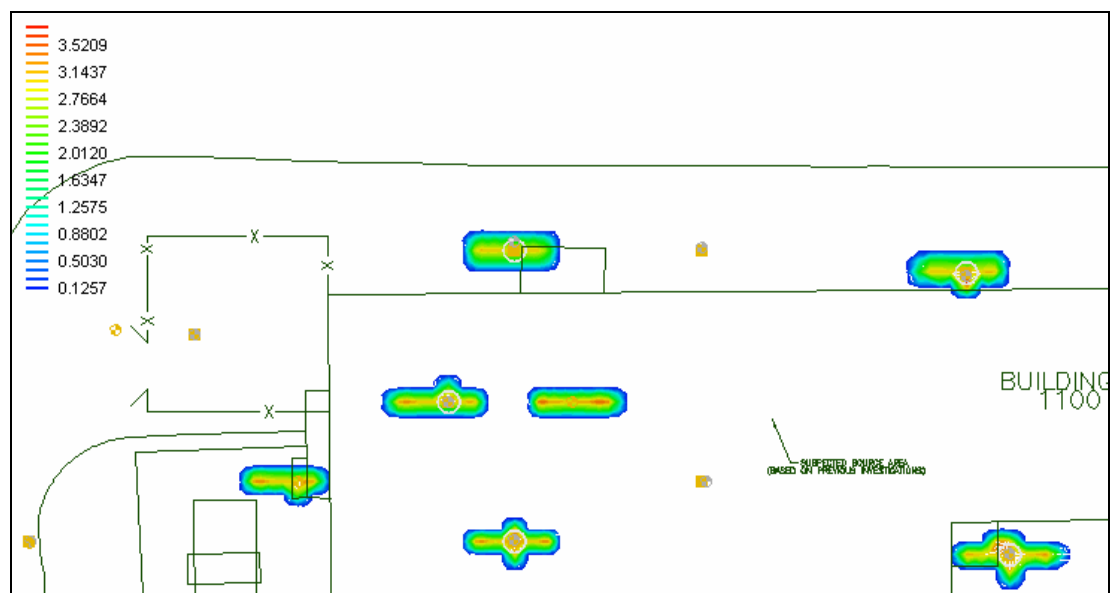
Figure E.14: MnO$_4^-$ Distribution, 10gpm, 4.0mg/mL KMnO$_4$, Layer 2, fast NOD present
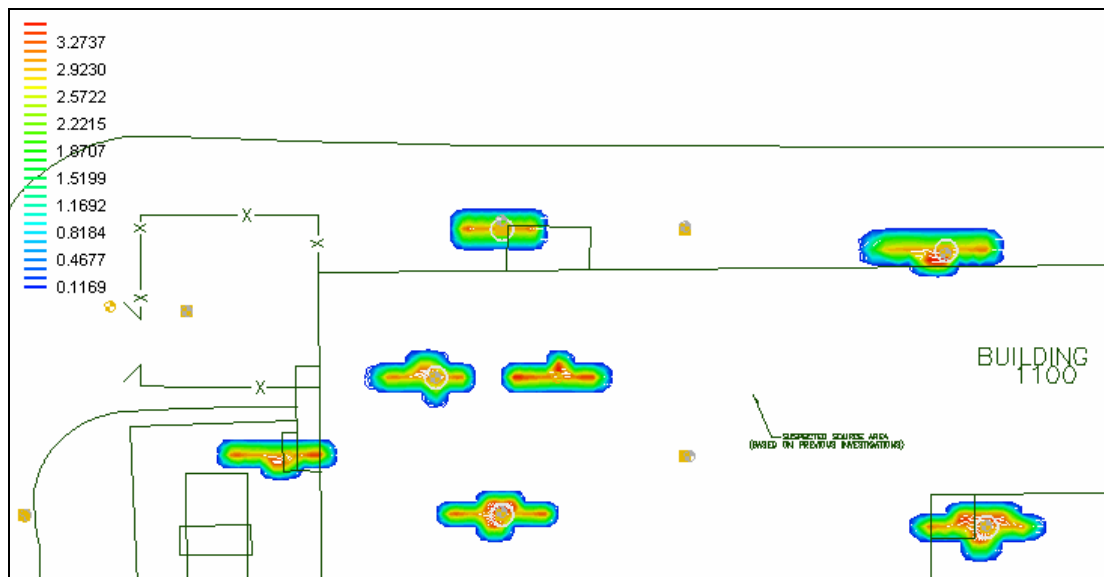
Figure E.15: MnO$_4^-$ Distribution, 15gpm, 4.0mg/mL KMnO$_4$, Layer 2, fast NOD present
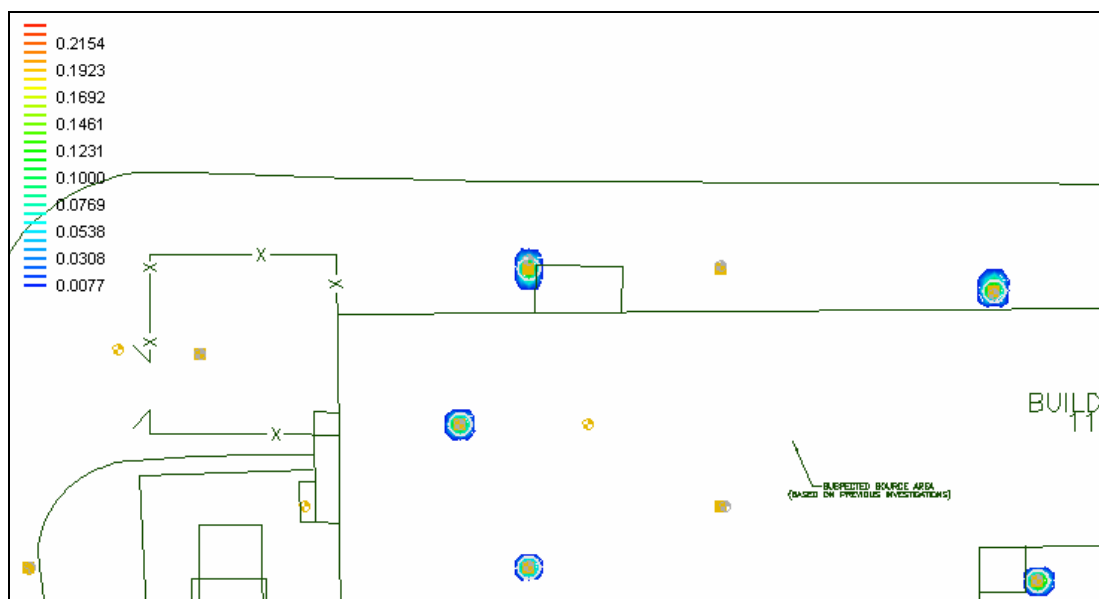
Figure E.16: MnO$_4^-$ Distribution, 8gpm, 0.25mg/mL KMnO$_4$, Layer 2, fast NOD present (decreased k)

Figure E.17: MnO$_4^-$ Distribution, 8gpm, 0.25mg/mL KMnO$_4$, Layer 2, slow NOD present
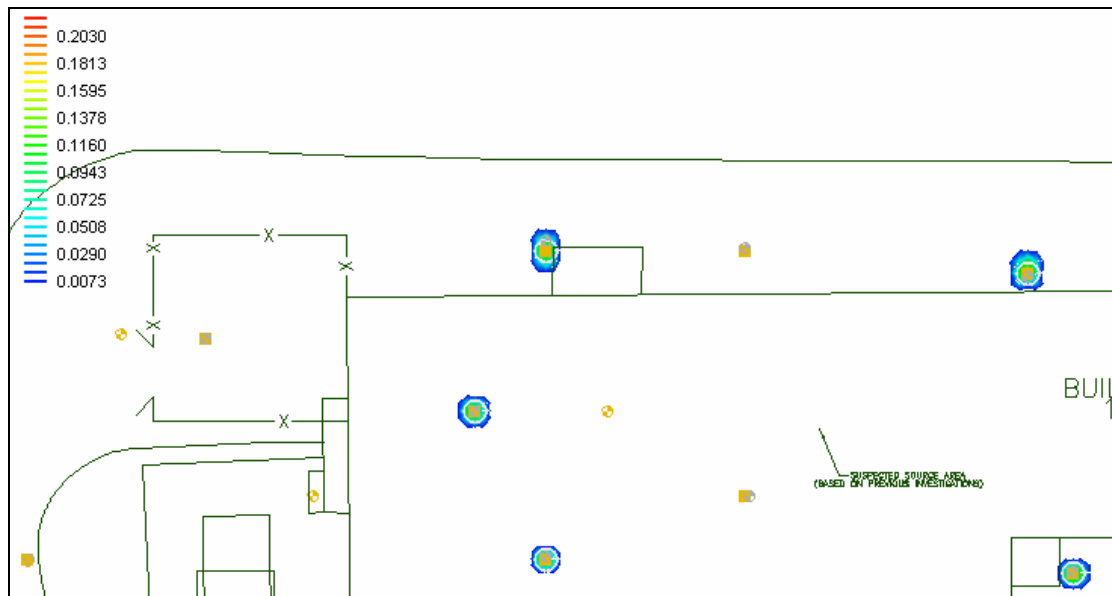
Figure E.18: MnO$_4^-$ Distribution, 8gpm, 0.25mg/mL KMnO$_4$, Layer 2, qty fast NOD increased
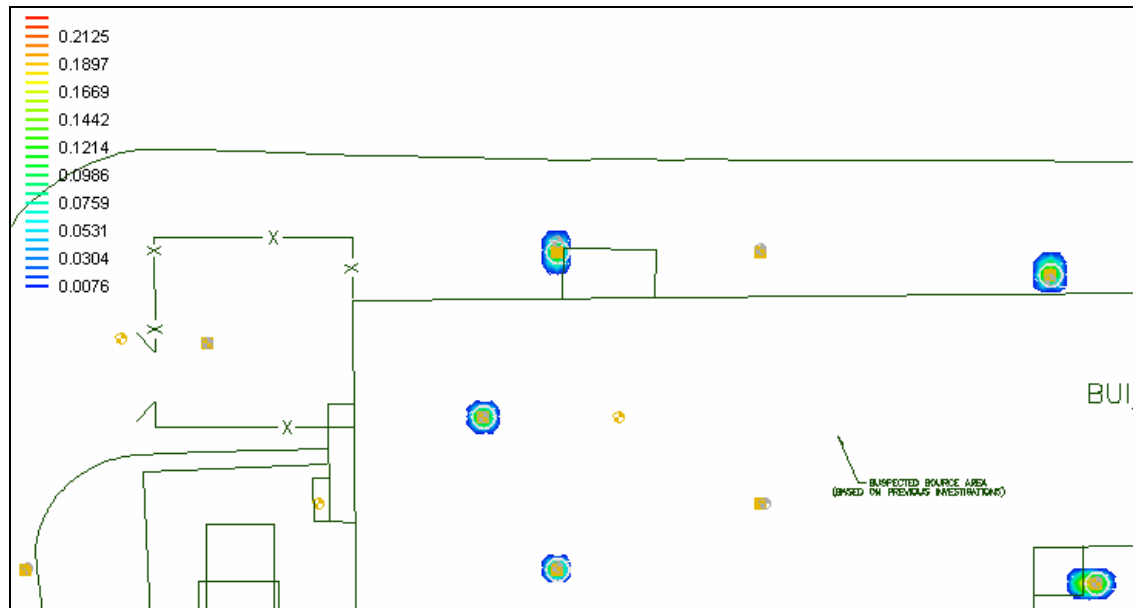
Figure E.19: MnO$_4^-$ Distribution, 8gpm, 0.25mg/mL KMnO$_4$, Layer 2, qty fast NOD reduced
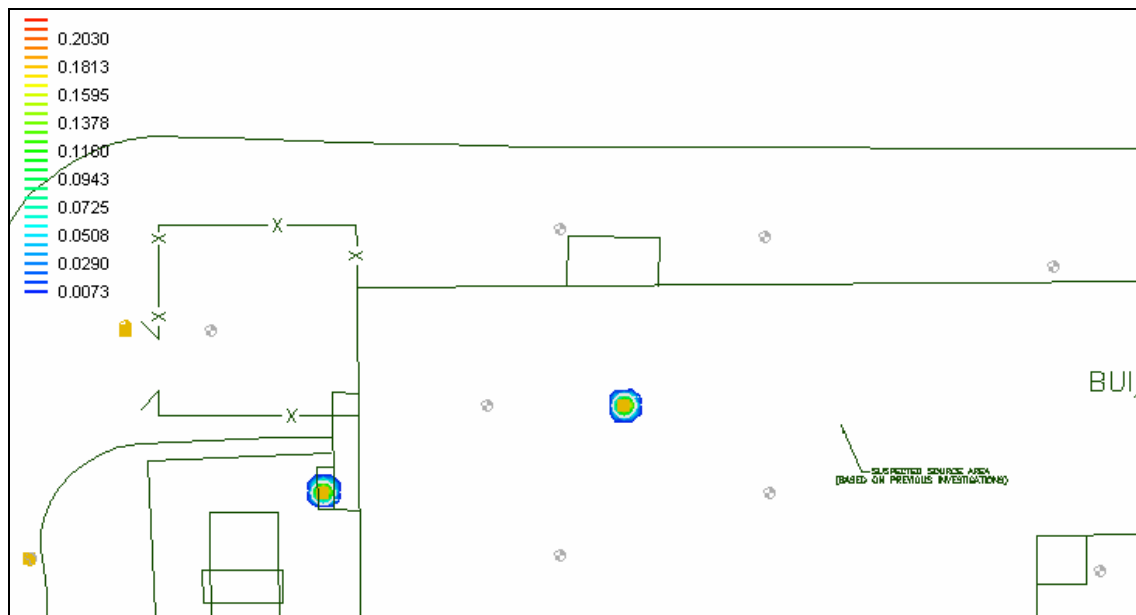
Figure E.20: MnO$_4^-$ Distribution, 5gpm, 0.25mg/mL KMnO$_4$, Layer 3, fast NOD present
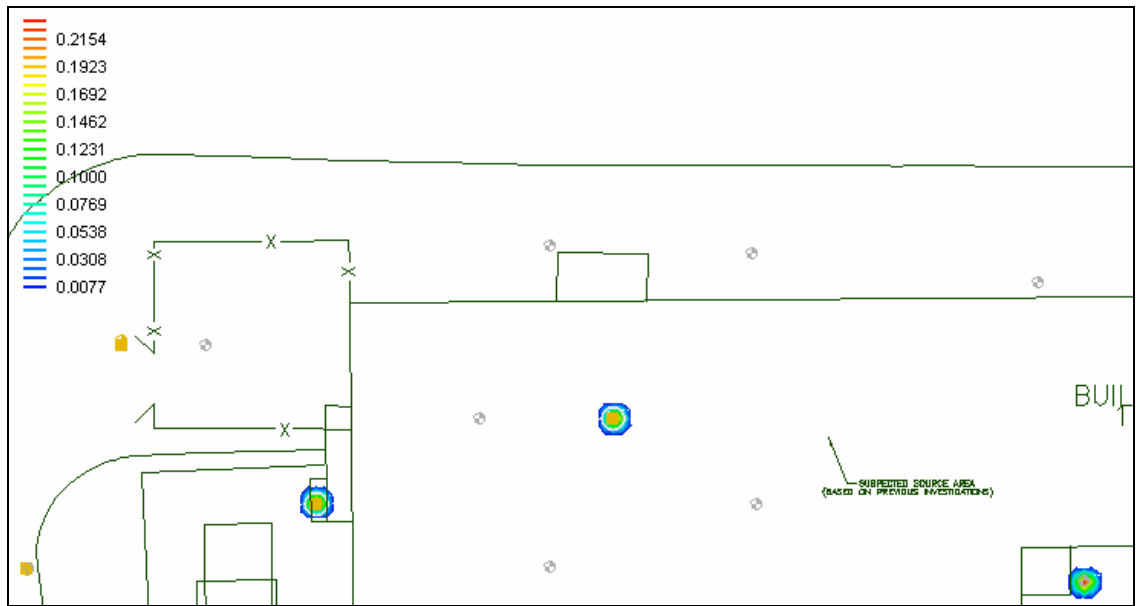
Figure E.21: MnO$_4^-$ Distribution, 8gpm, 0.25mg/mL KMnO$_4$, Layer 3, fast NOD present
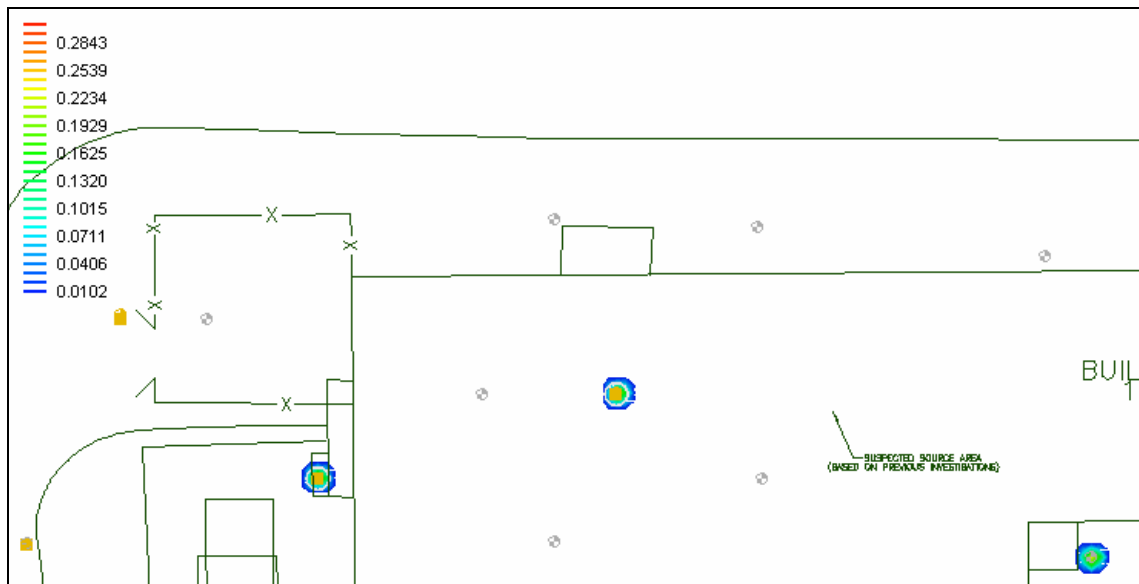
Figure E.22: MnO$_4^-$ Distribution, 10gpm, 0.25mg/mL KMnO$_4$, Layer 3, fast NOD present
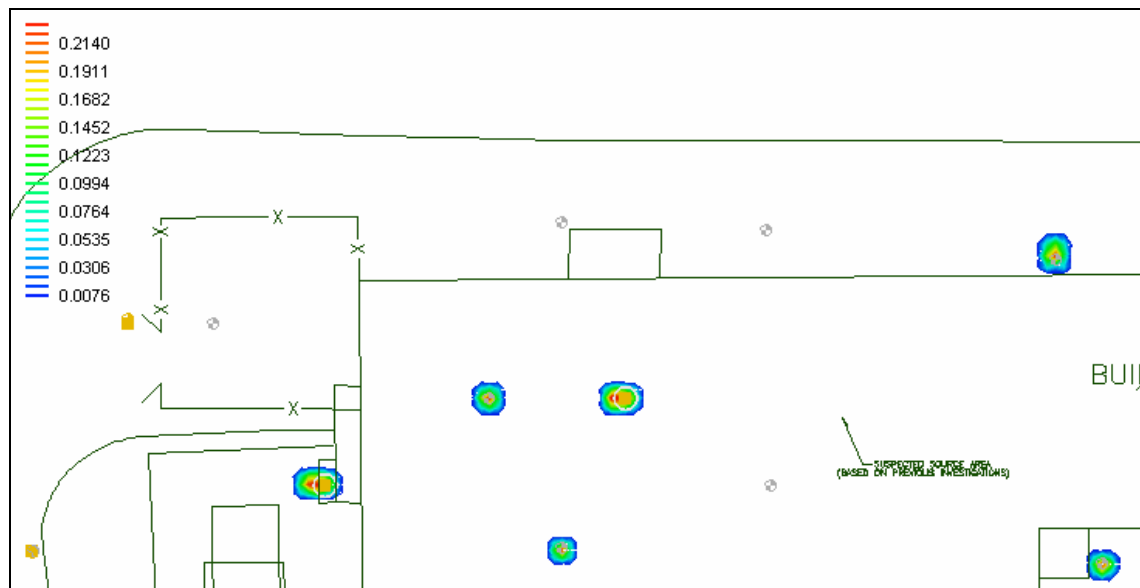
Figure E.23: MnO$_4^-$ Distribution, 15gpm, 0.25mg/mL KMnO$_4$, Layer 3, fast NOD present
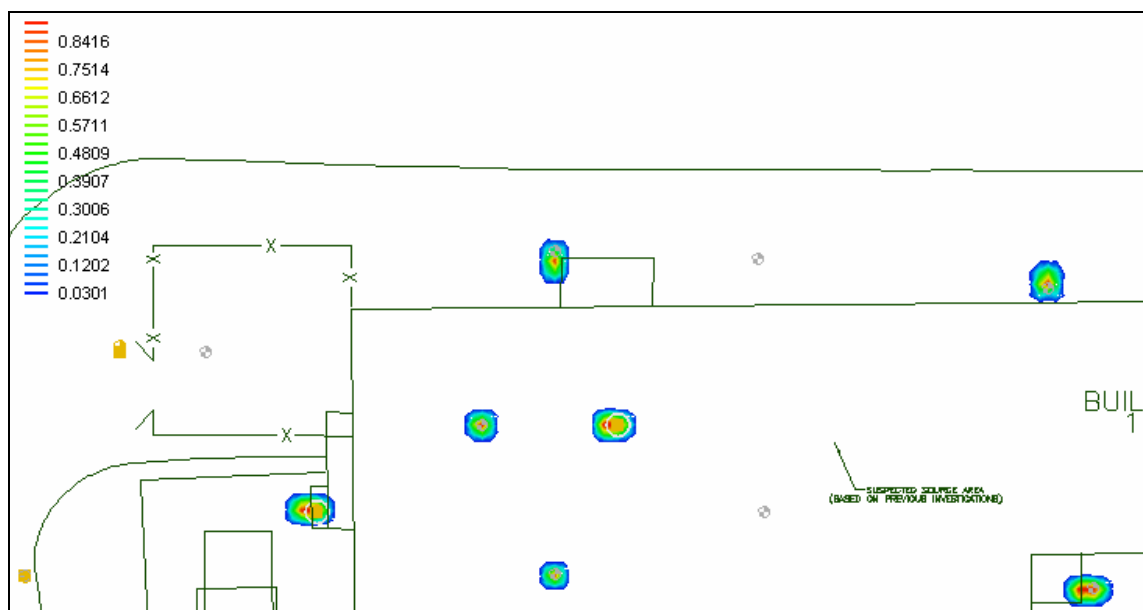
Figure E.24: MnO$_4^-$ Distribution, 5gpm, 1.0mg/mL KMnO$_4$, Layer 3, fast NOD present
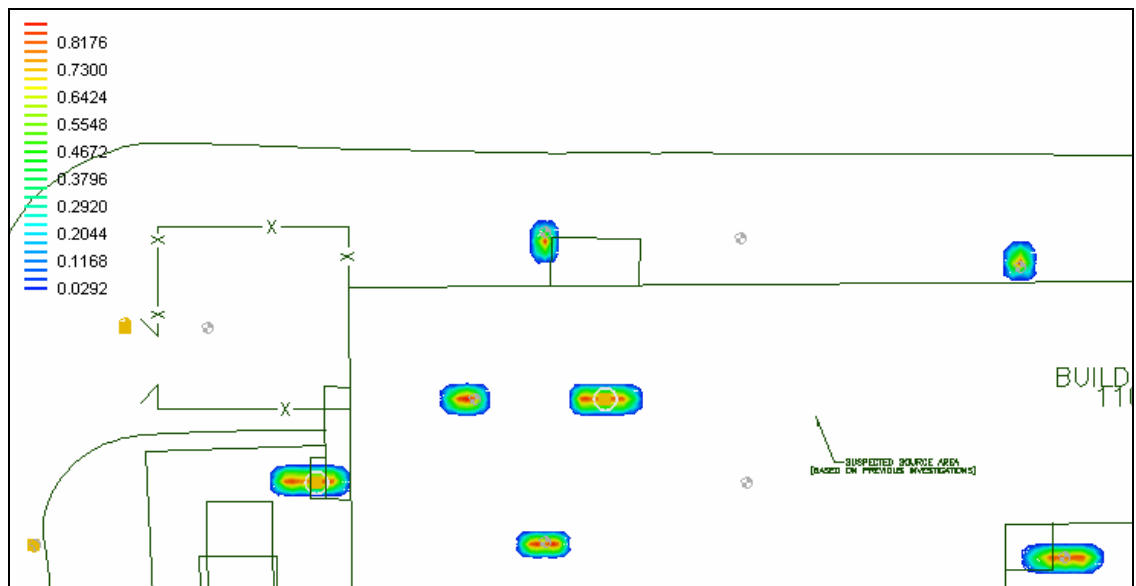
Figure E.25: MnO$_4^-$ Distribution, 8gpm, 1.0mg/mL KMnO$_4$, Layer 3, fast NOD present
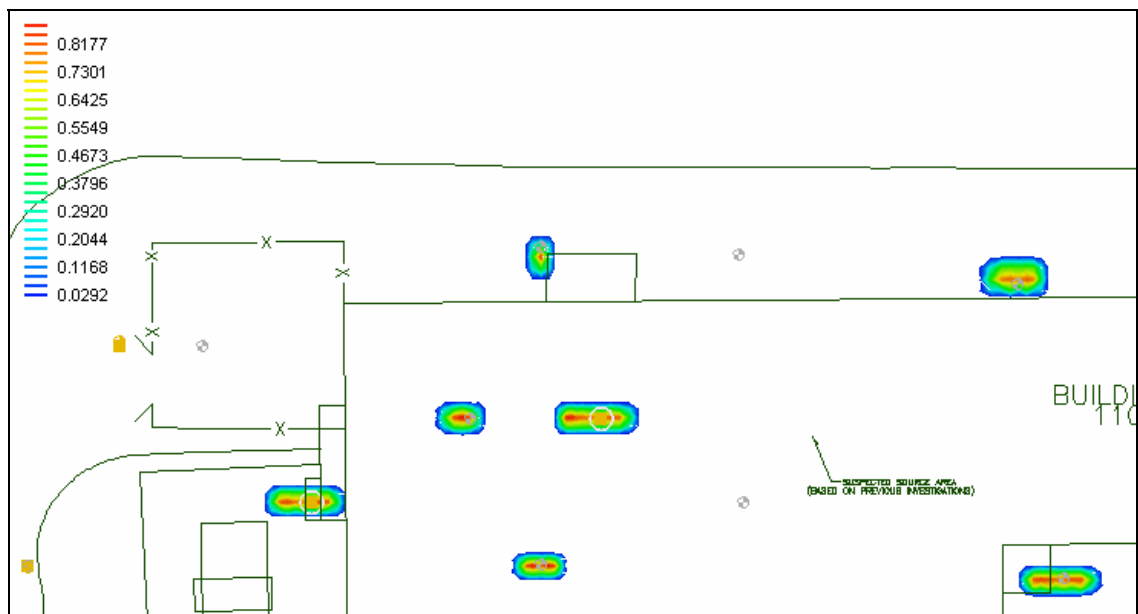
Figure E.26: MnO$_4^-$ Distribution, 10gpm, 1.0mg/mL KMnO$_4$, Layer 3, fast NOD present
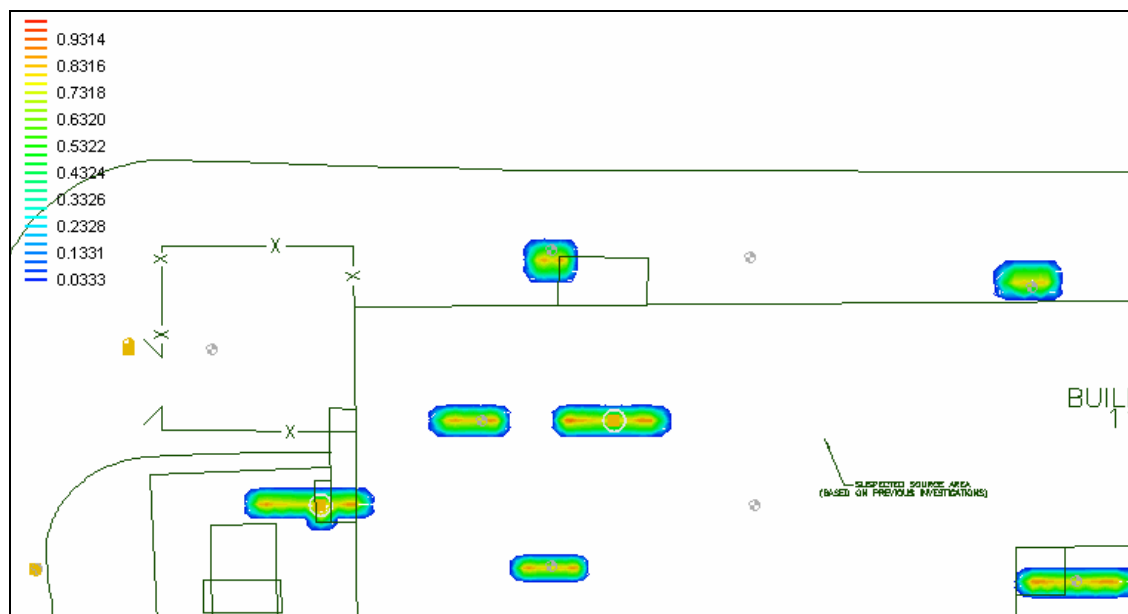
Figure E.27: MnO$_4^-$ Distribution, 15gpm, 1.0mg/mL KMnO$_4$, Layer 3, fast NOD present
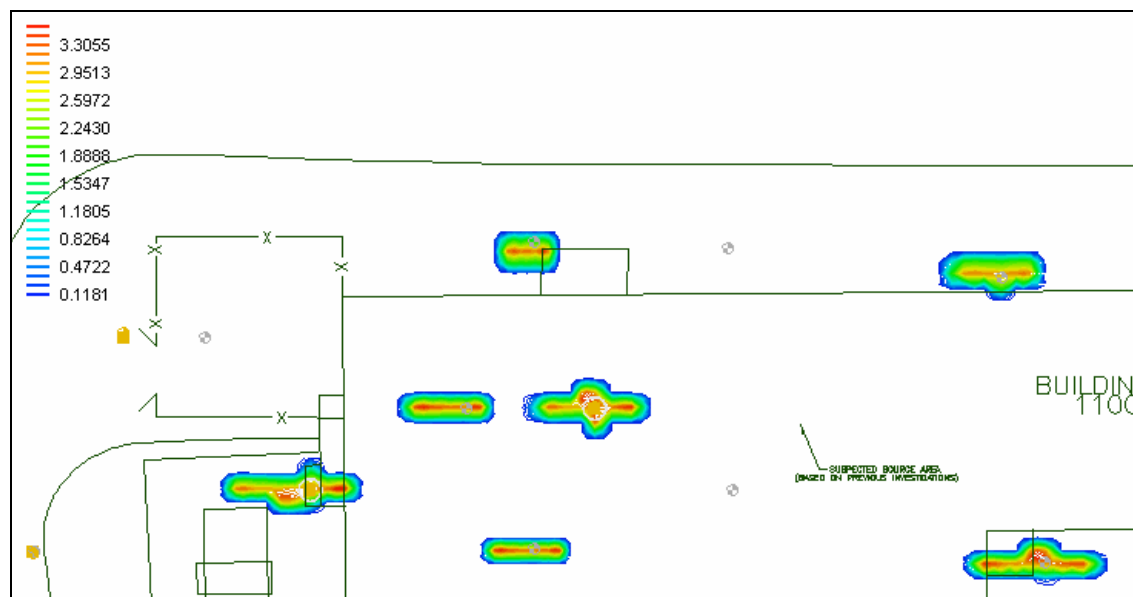
Figure E.28: MnO$_4^-$ Distribution, 5gpm, 4.0mg/mL KMnO$_4$, Layer 3, fast NOD present
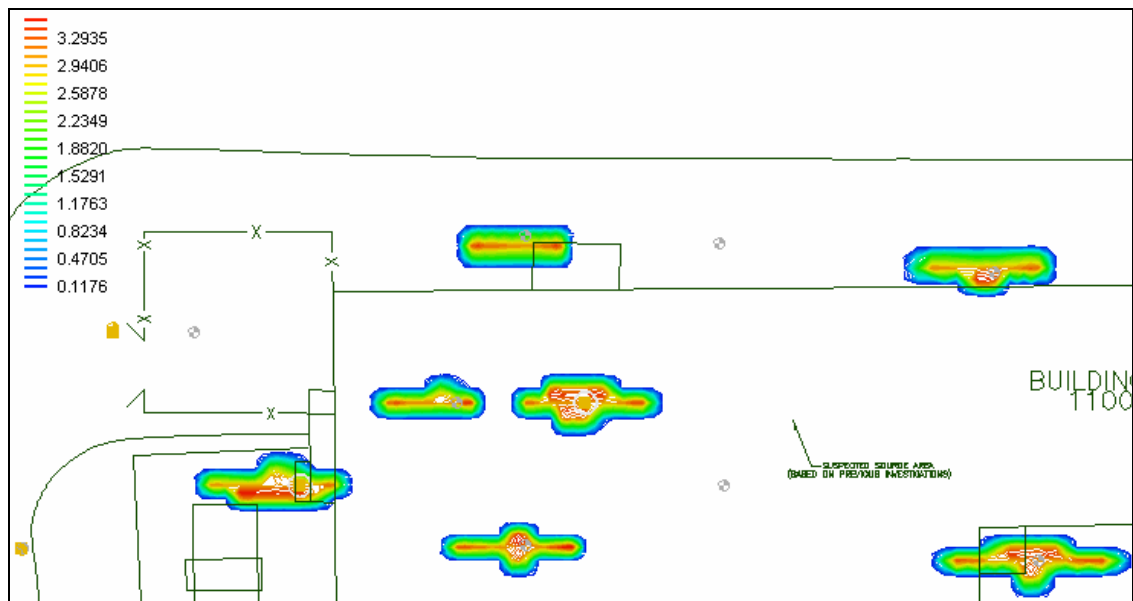
Figure E.29: MnO₄⁻ Distribution, 8gpm, 4.0mg/mL KMnO₄, Layer 3, fast NOD present
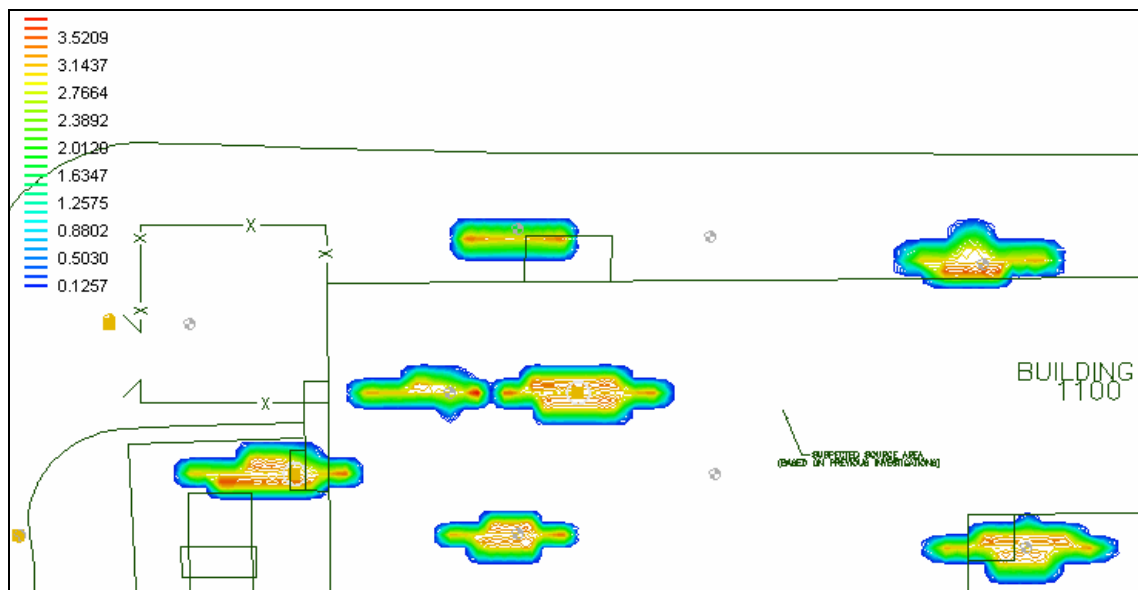
Figure E.30: MnO₄⁻ Distribution, 10gpm, 4.0mg/mL KMnO₄, Layer 3, fast NOD present
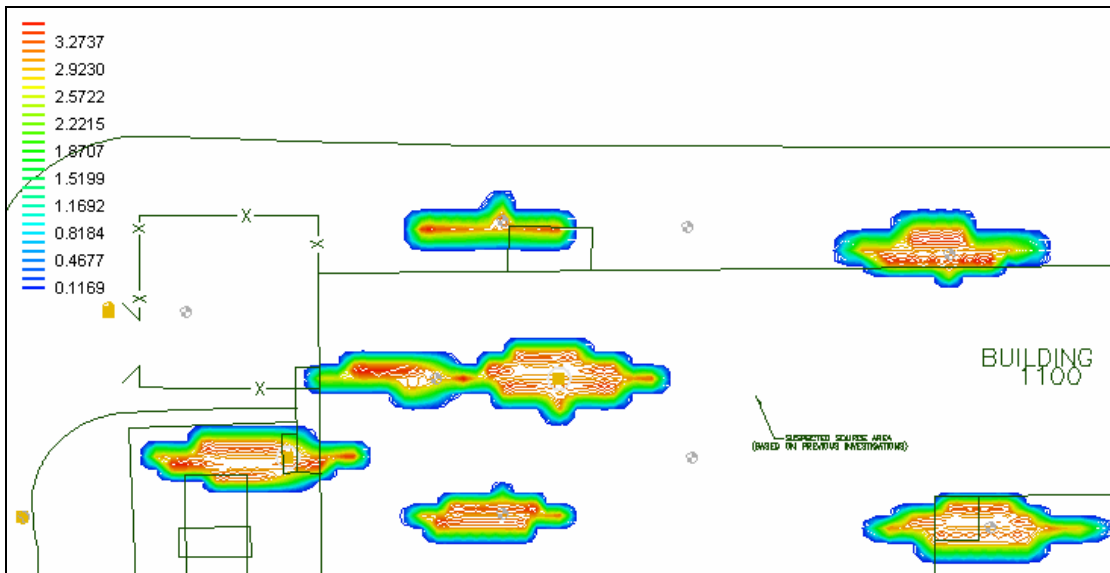
Figure E.31: MnO$_4^-$ Distribution, 15gpm, 4.0mg/mL KMnO$_4$, Layer 3, fast NOD present
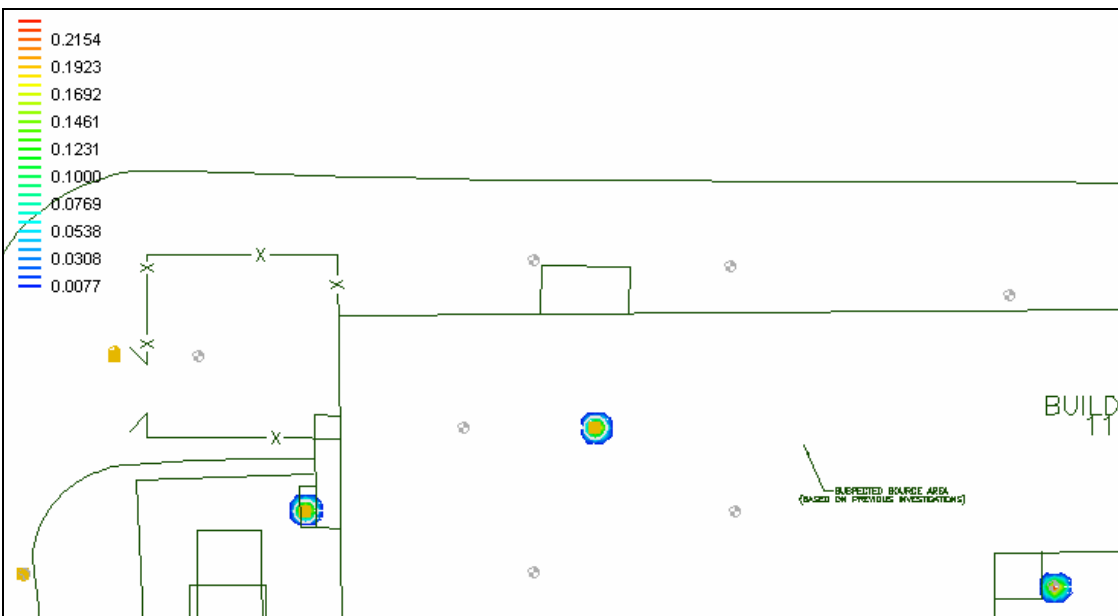
Figure E.32: MnO$_4^-$ Distribution, 8gpm, 0.25mg/mL KMnO$_4$, Layer 3, fast NOD present (decreased k)
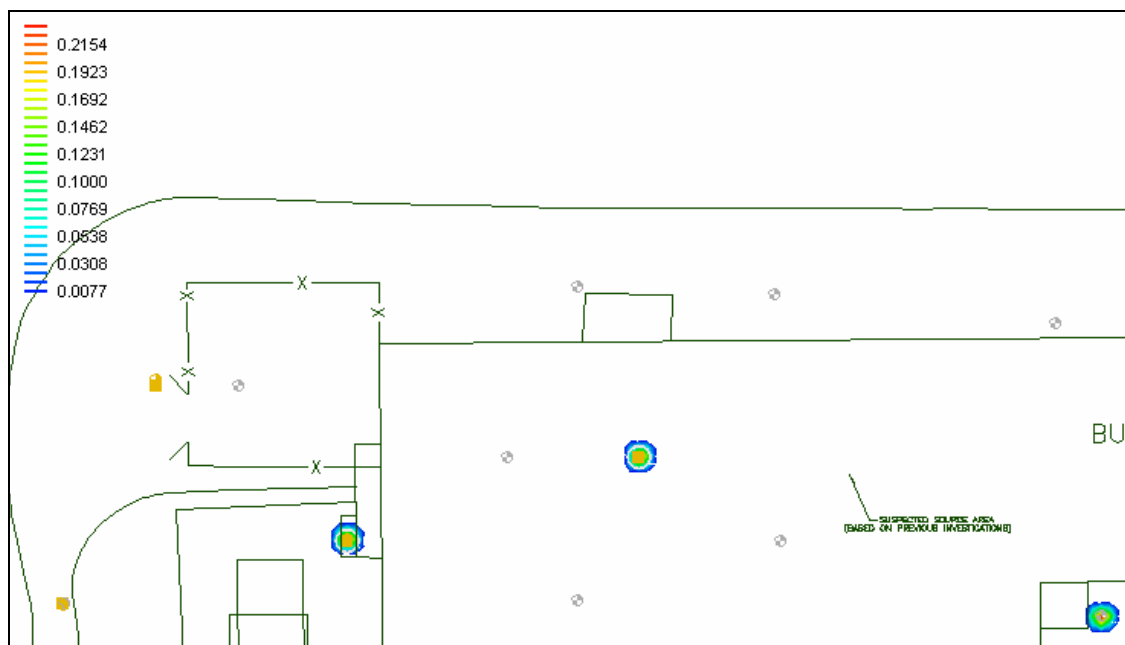
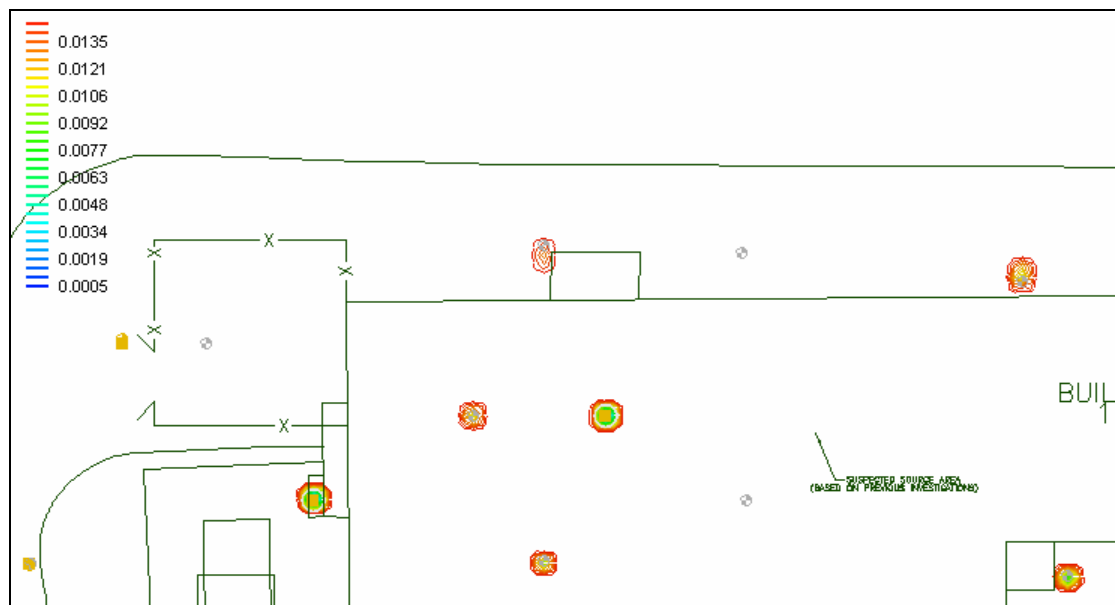**Figure E.33: MnO$_4^-$ Distribution, 8gpm, 0.25mg/mL KMnO$_4$, Layer 3, slow NOD present**
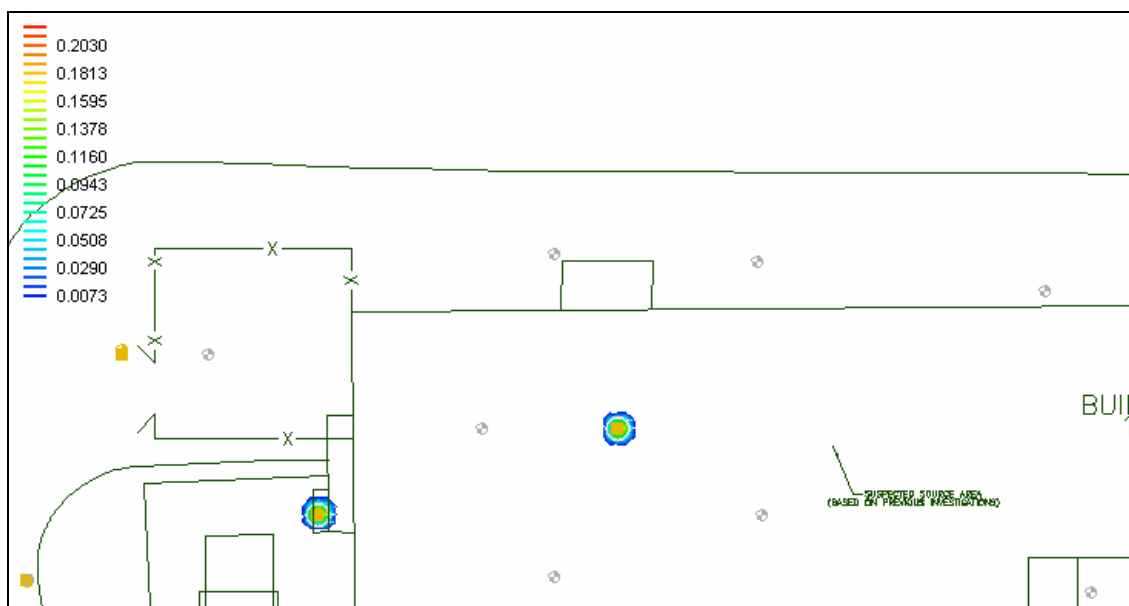
Figure E.34: MnO$_4^-$ Distribution, 8gpm, 0.25mg/mL KMnO$_4$, Layer 3, qty fast NOD increased
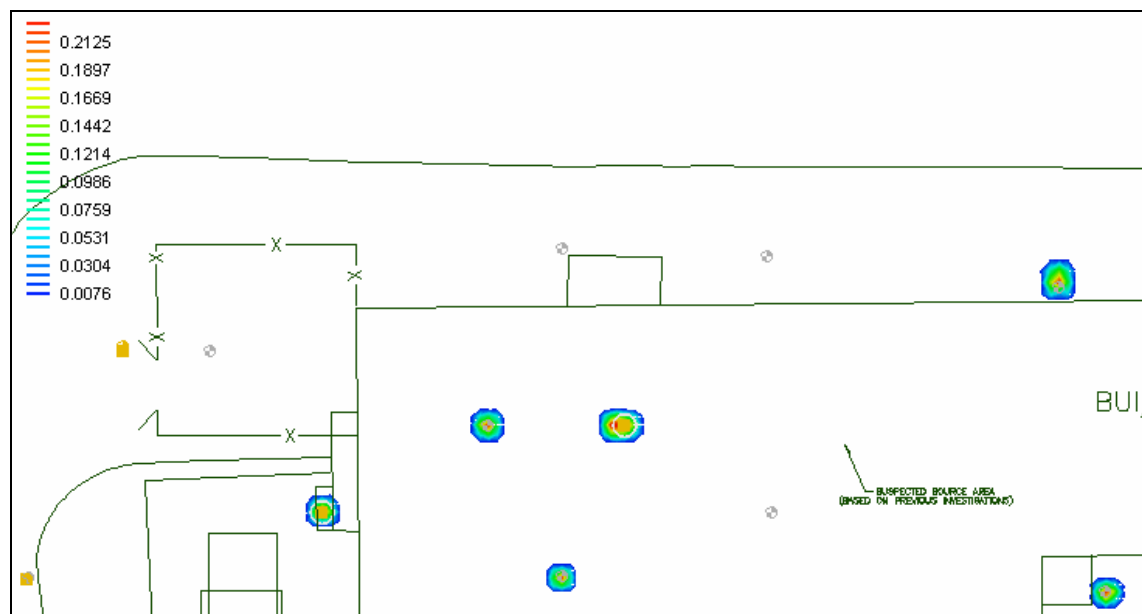
Figure E.35: MnO$_4^-$ Distribution, 8gpm, 0.25mg/mL KMnO$_4$, Layer 3, qty fast NOD reduced
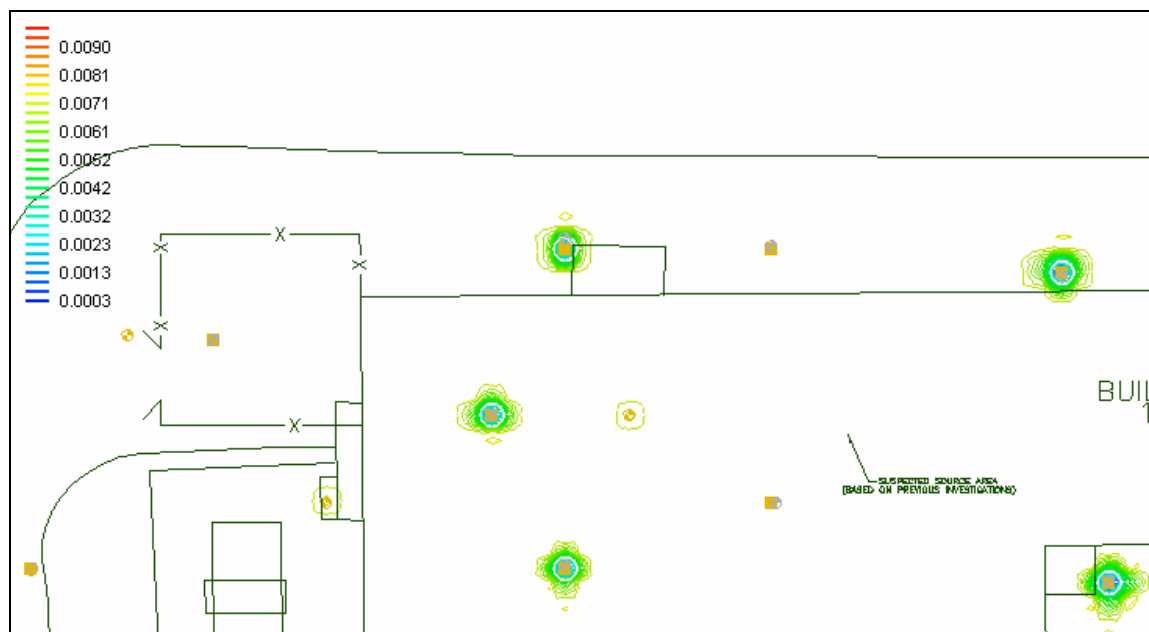
Figure E.36: Fast NOD Distribution, 5gpm, 0.25mg/mL KMnO$_4$, Layer 2
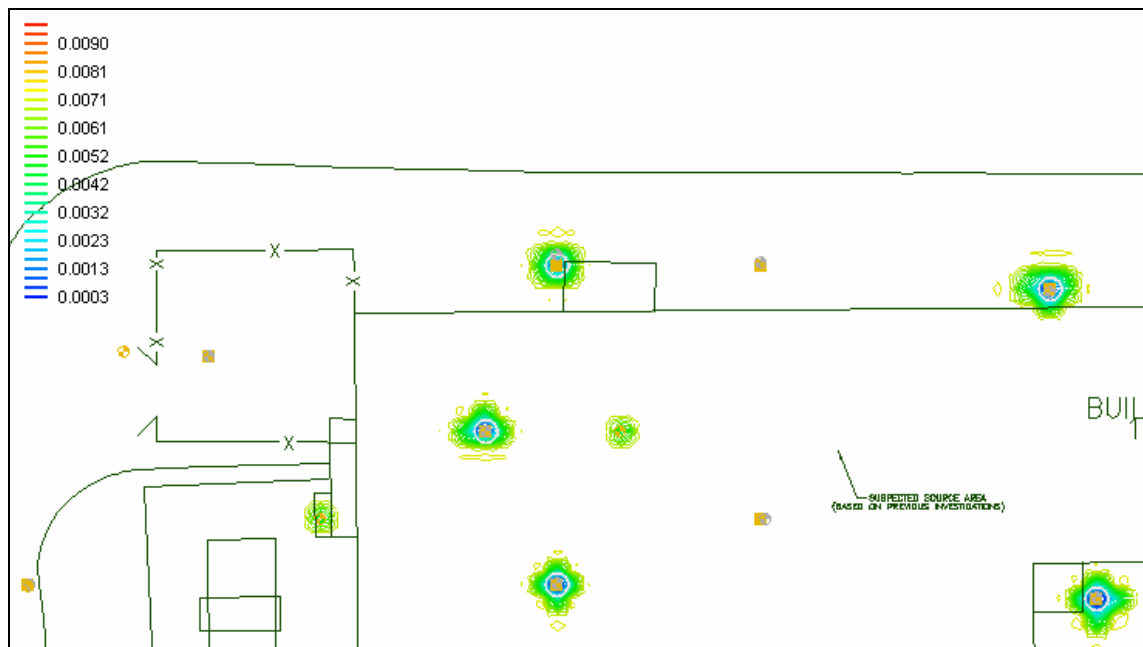
Figure E.37: Fast NOD Distribution, 8gpm, 0.25mg/mL KMnO$_4$, Layer 2
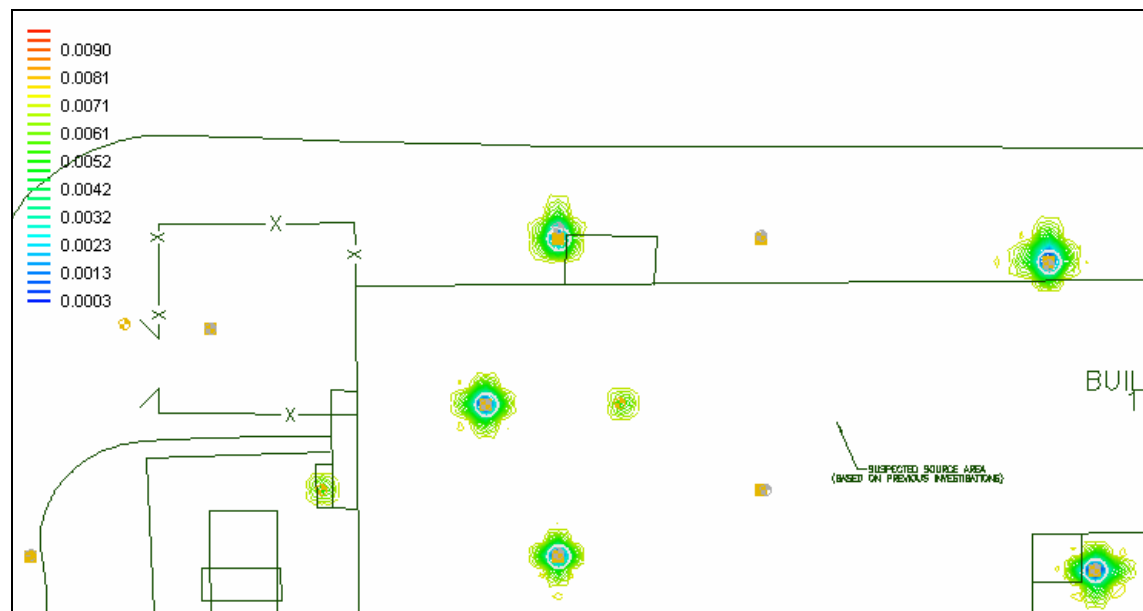
Figure E.38: Fast NOD Distribution, 10gpm, 0.25mg/mL KMnO$_4$, Layer 2
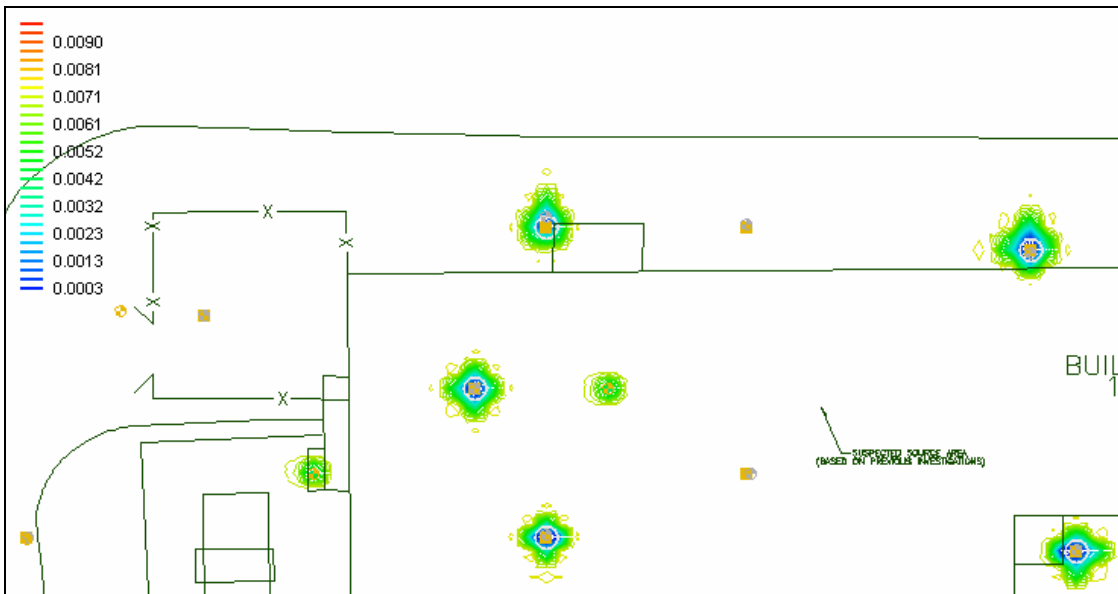
Figure E.39: Fast NOD Distribution, 15gpm, 0.25mg/mL KMnO$_4$, Layer 2
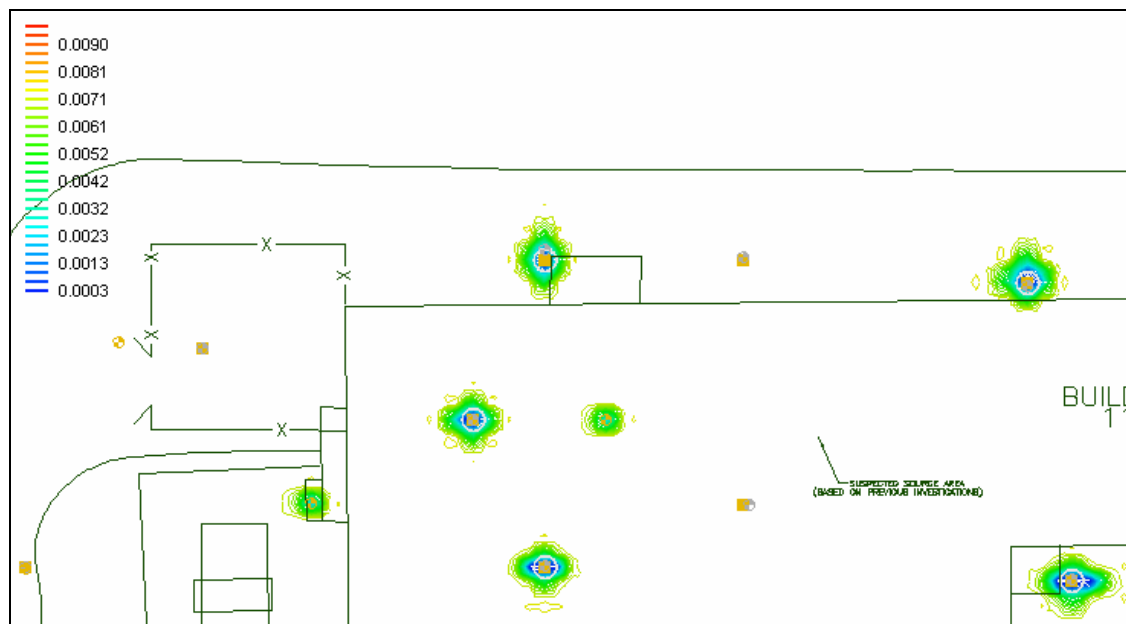
Figure E.40: Fast NOD Distribution, 5gpm, 1.0mg/mL KMnO$_4$, Layer 2
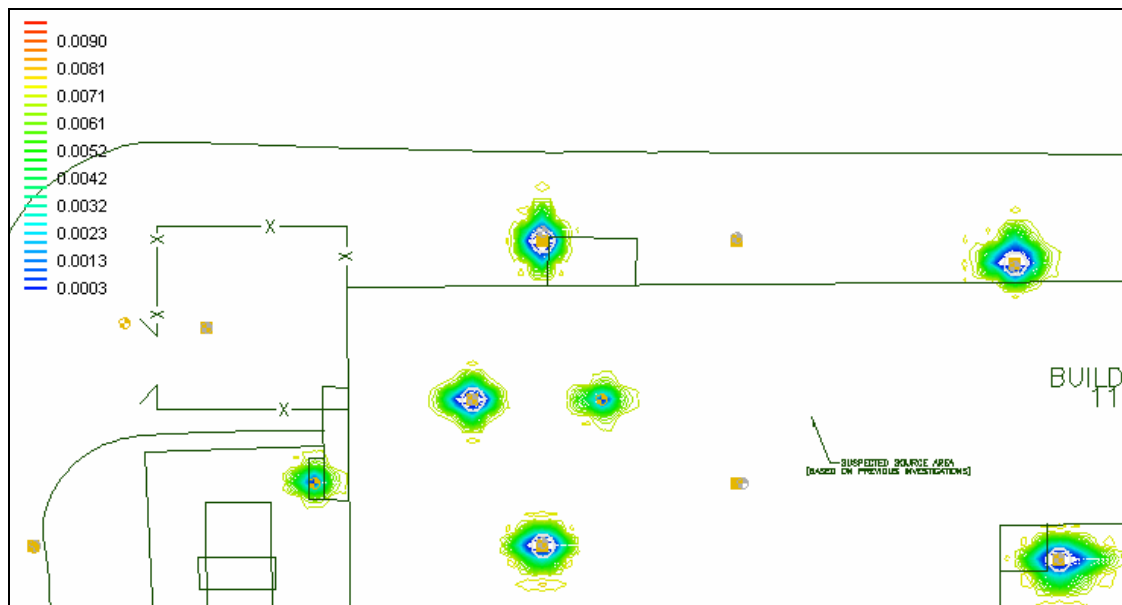
Figure E.41: Fast NOD Distribution, 8gpm, 1.0mg/mL KMnO$_4$, Layer 2
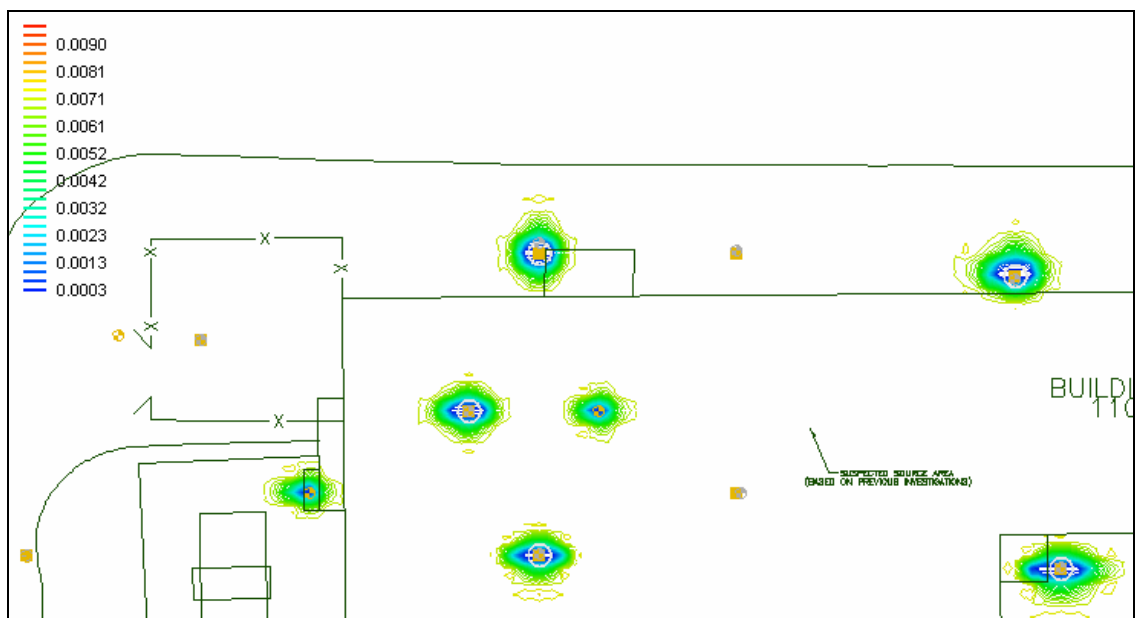
Figure E.42: Fast NOD Distribution, 10gpm, 1.0mg/mL KMnO$_4$, Layer 2
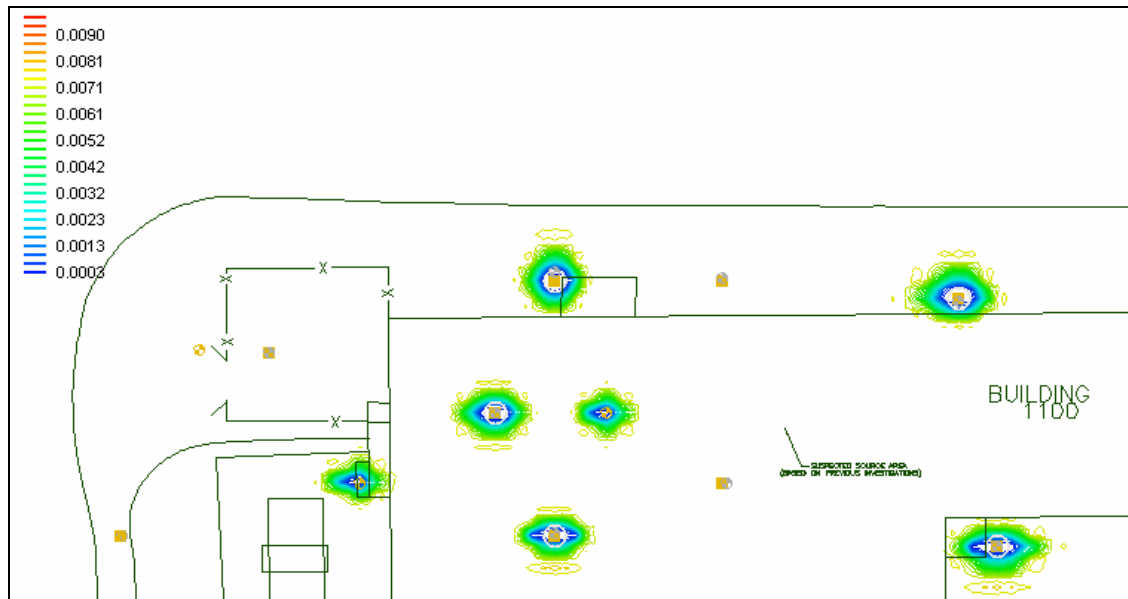
Figure E.43: Fast NOD Distribution, 15gpm, 1.0mg/mL KMnO₄, Layer 2
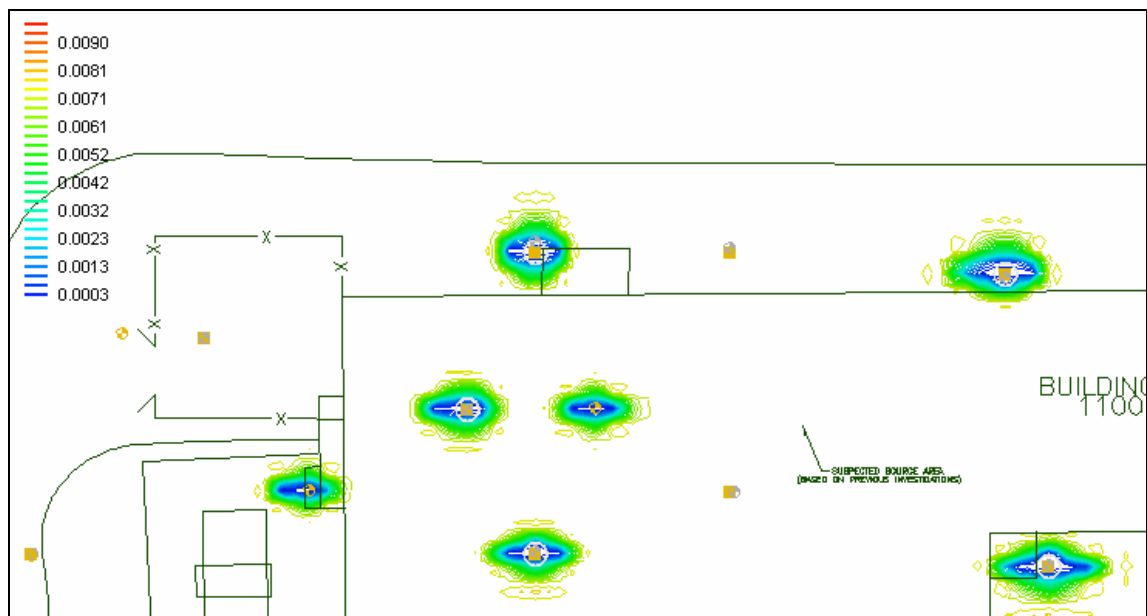
Figure E.44: Fast NOD Distribution, 5gpm, 4.0mg/mL KMnO₄, Layer 2
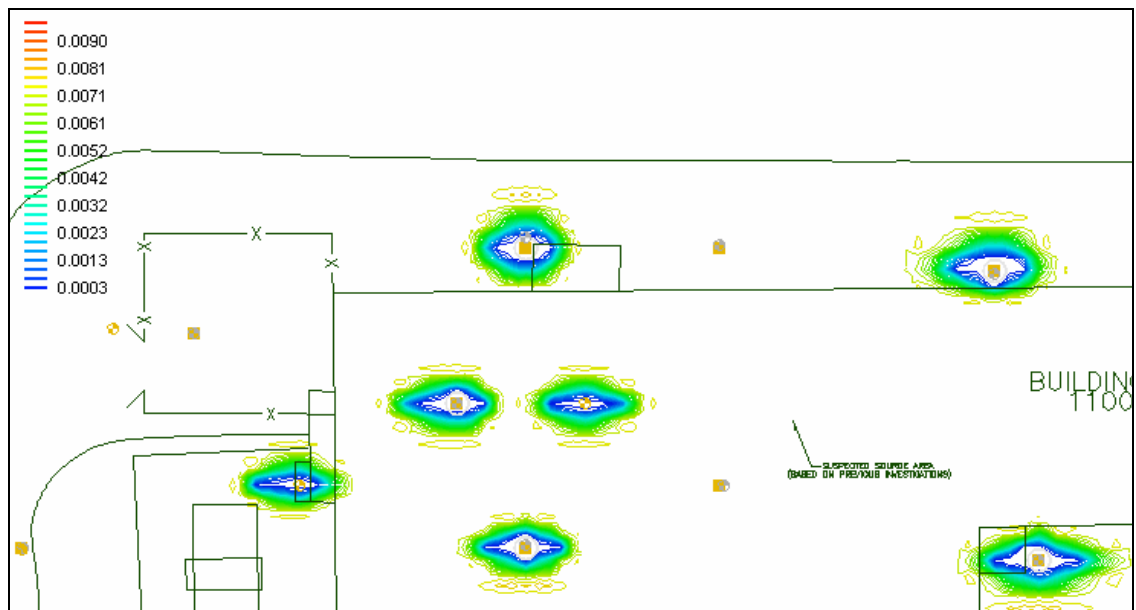
Figure E.45: Fast NOD Distribution, 8gpm, 4.0mg/mL KMnO$_4$, Layer 2
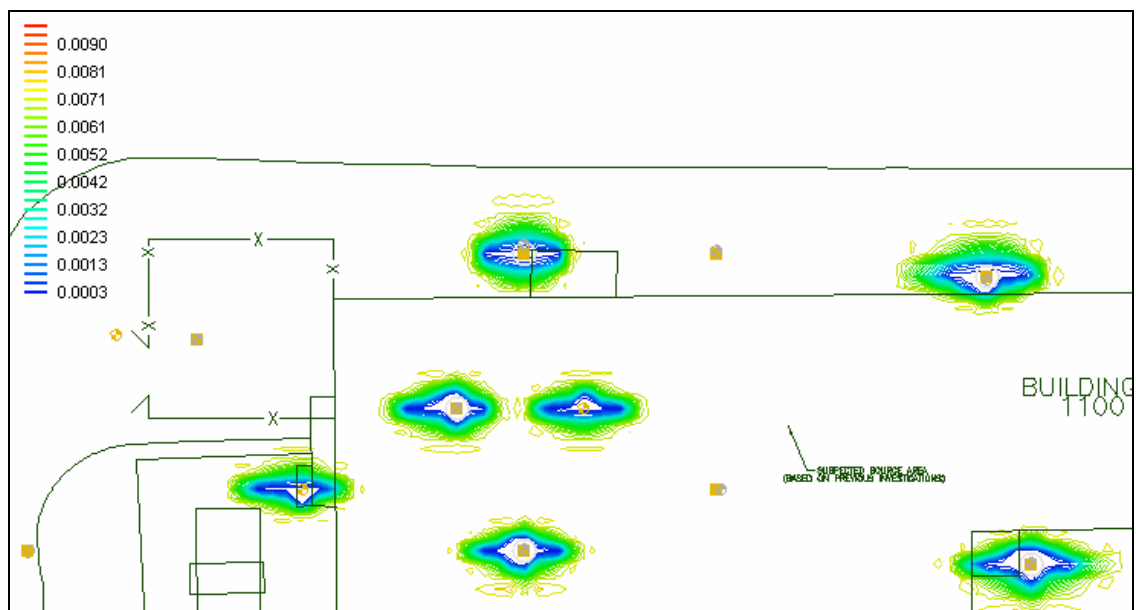
Figure E.46: Fast NOD Distribution, 10gpm, 4.0mg/mL KMnO$_4$, Layer 2
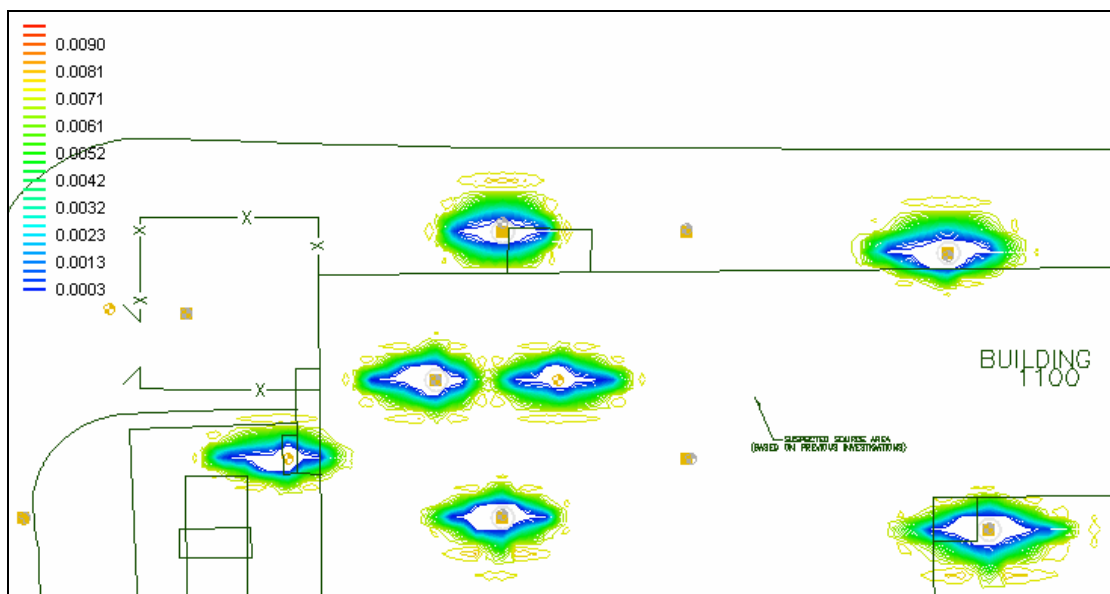
Figure E.47: Fast NOD Distribution, 15gpm, 4.0 mgm/L KMnO$_4$, Layer 2

Figure E.48: Fast NOD Distribution, 8gpm, 0.25mg/mL KMnO$_4$, Layer 2, fast NOD present (decreased k)
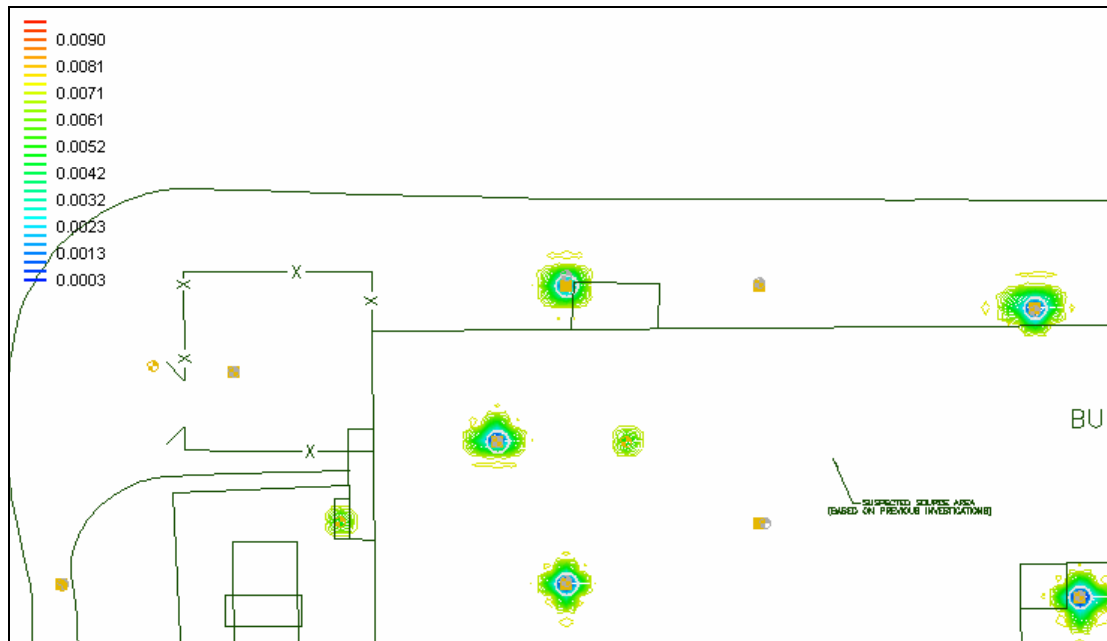
Figure E.49: Slow NOD Distribution, 8gpm, 0.25mg/mL KMnO$_4$, Layer 2
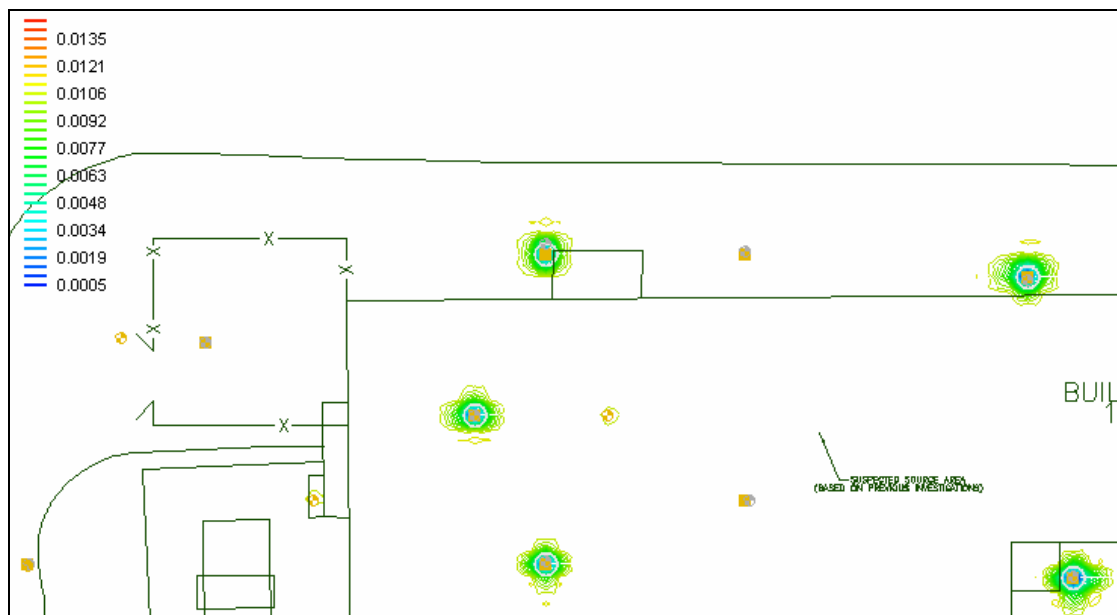
Figure E.50: Fast NOD Distribution, 8gpm, 0.25mg/mL KMnO$_4$, Layer 2, more fast NOD initially
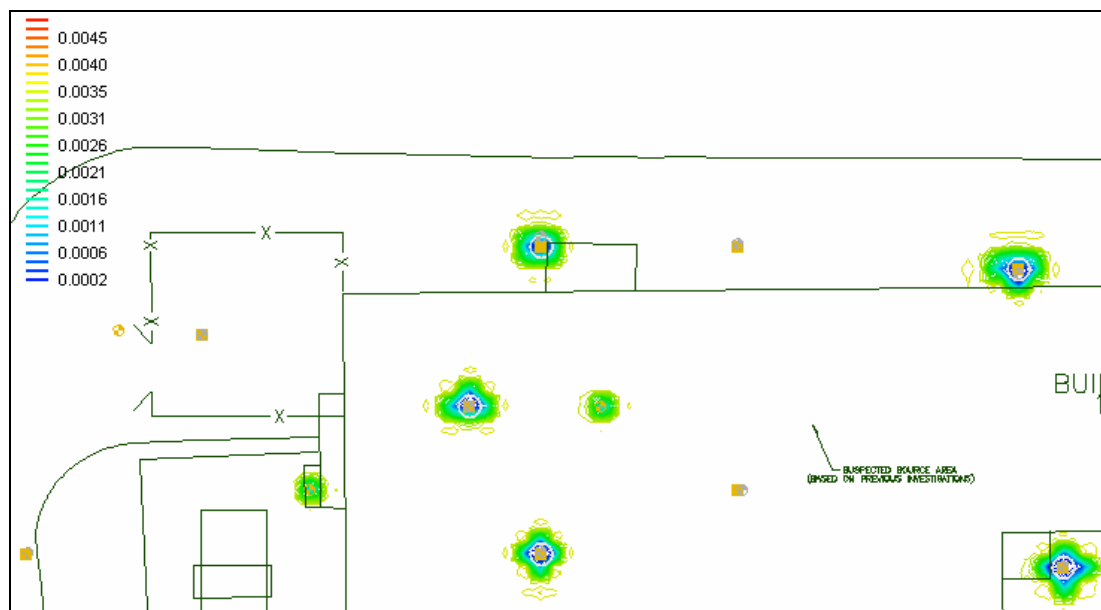
Figure E.51: Fast NOD Distribution, 8gpm, 0.25mg/mL KMnO₄, Layer 2, less fast NOD initially
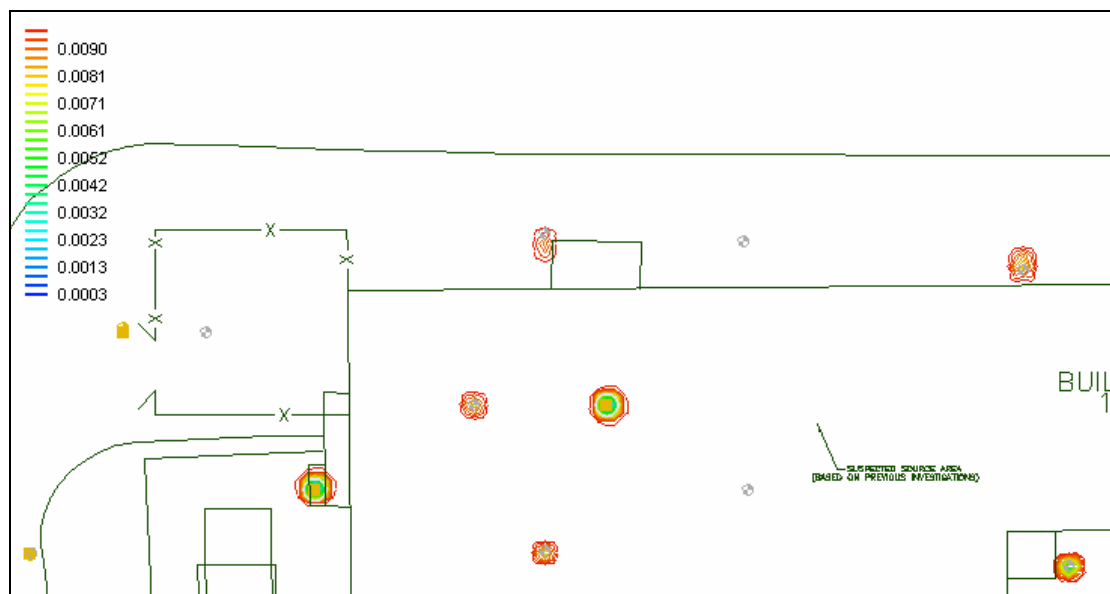
Figure E.52: Fast NOD Distribution, 5gpm, 0.25mg/mL KMnO₄, Layer 3
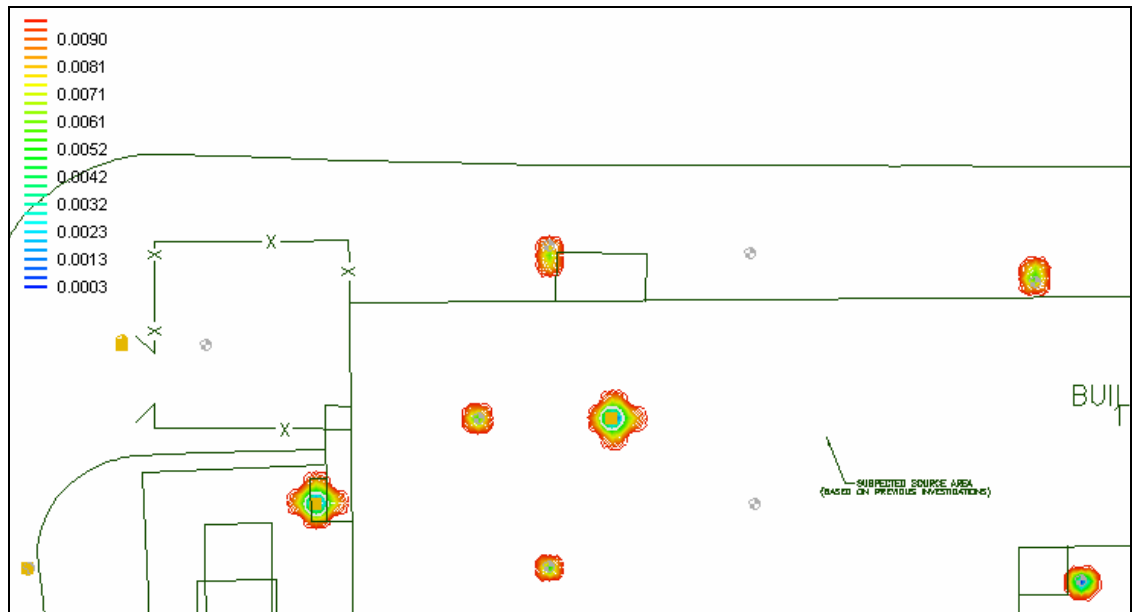
Figure E.53: Fast NOD Distribution, 8gpm, 0.25mg/mL KMnO$_4$, Layer 3
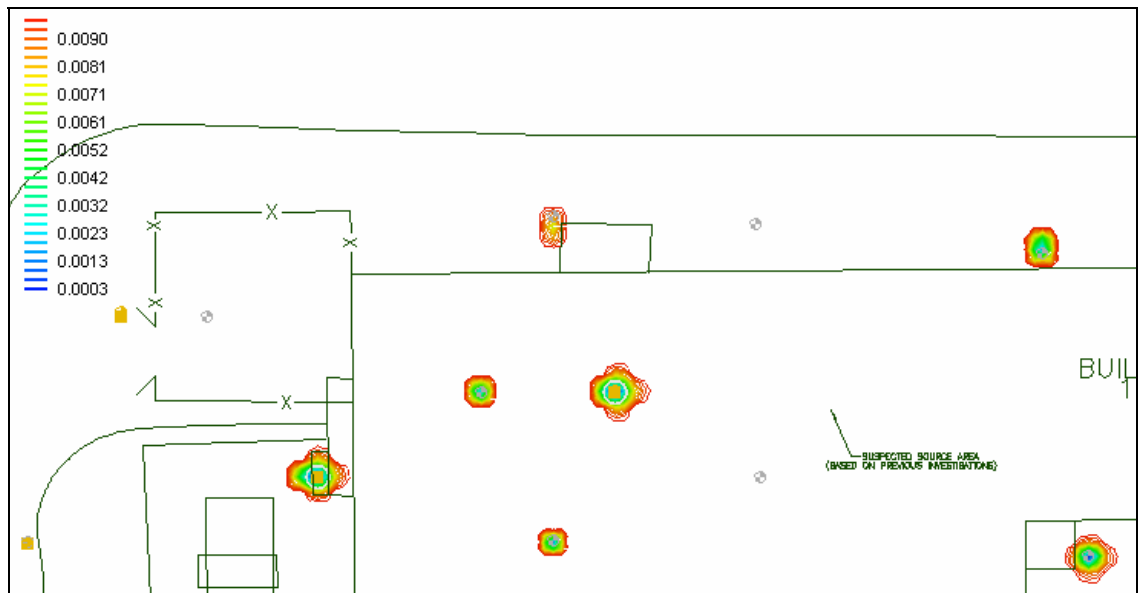
Figure E.54: Fast NOD Distribution, 10gpm, 0.25mg/mL KMnO$_4$, Layer 3
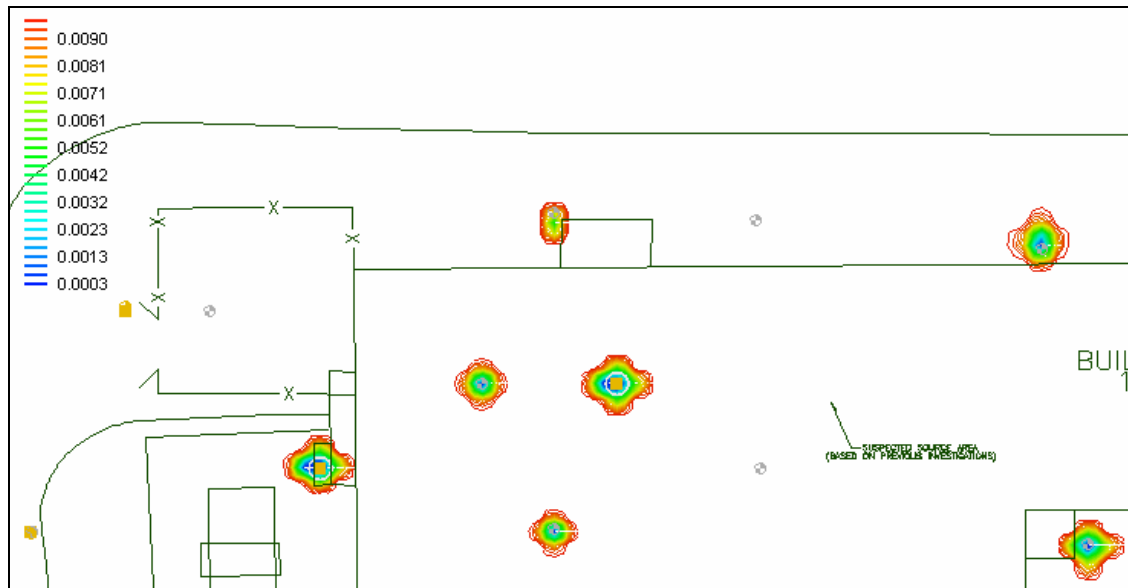
Figure E.55: Fast NOD Distribution, 15gpm, 0.25mg/mL KMnO₄, Layer 3

Figure E.56: Fast NOD Distribution, 5gpm, 1.0mg/mL KMnO₄, Layer 3
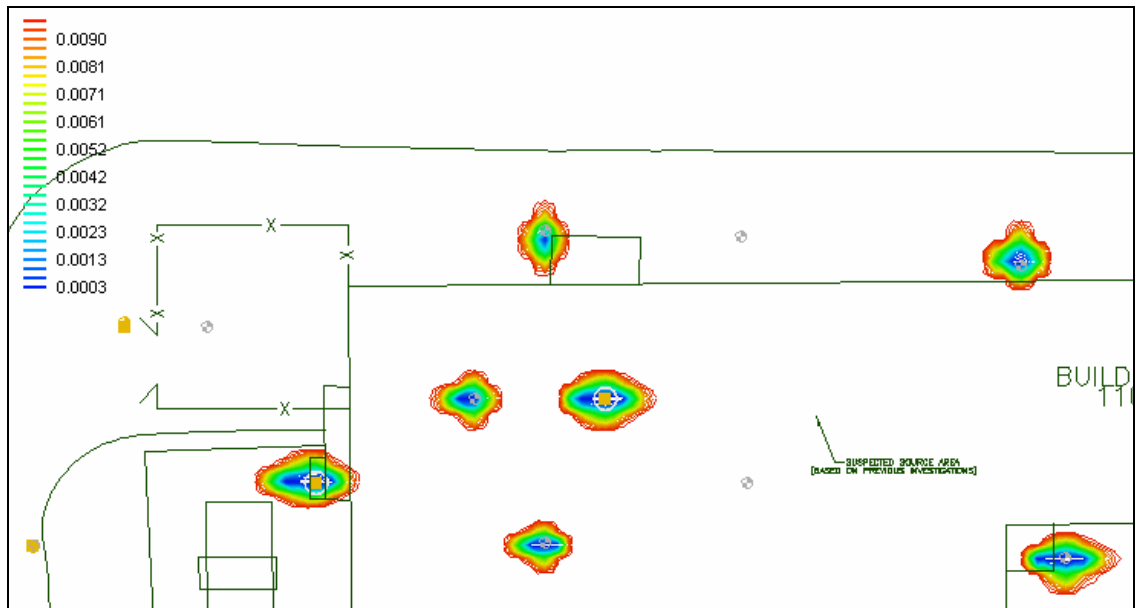
Figure E.57: Fast NOD Distribution, 8gpm, 1.0mg/mL KMnO₄, Layer 3
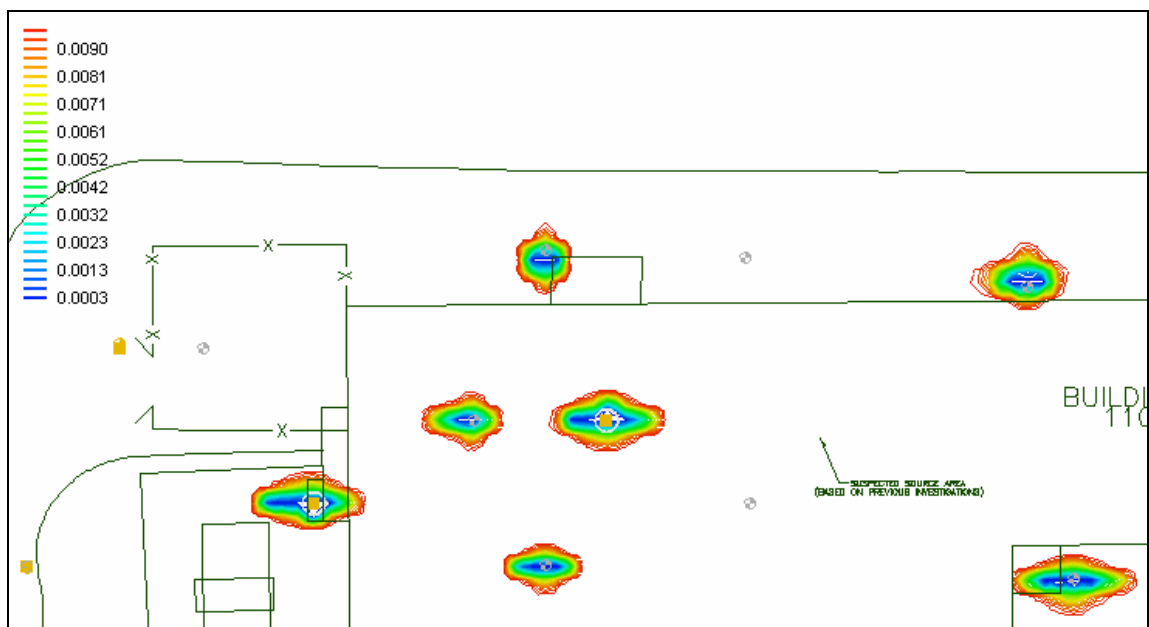
Figure E.58: Fast NOD Distribution, 10gpm, 1.0mg/mL KMnO₄, Layer 3
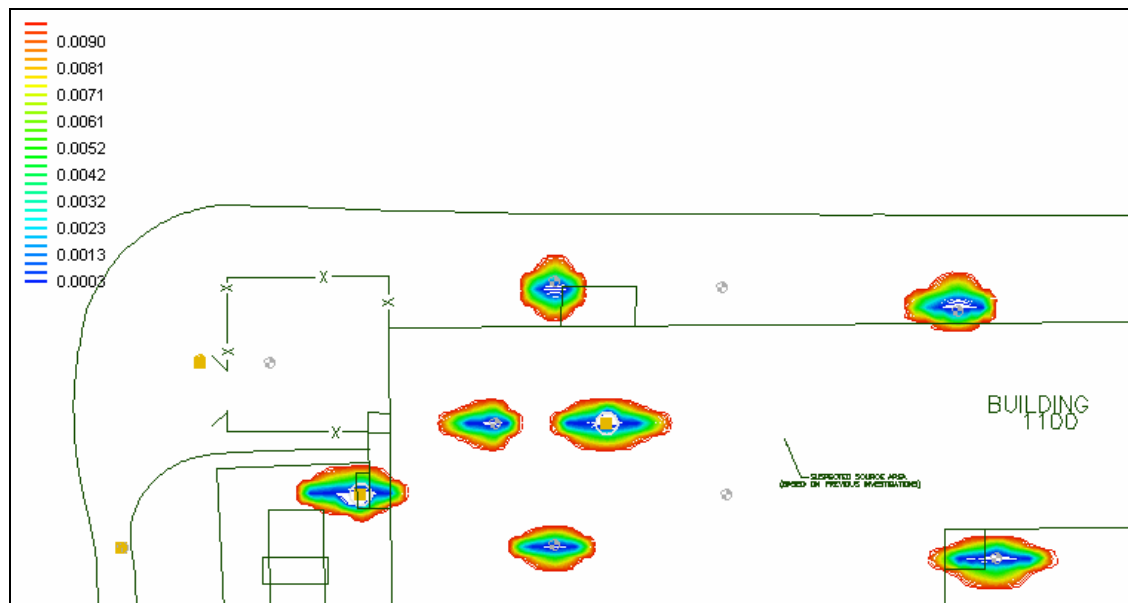
Figure E.59: Fast NOD Distribution, 15gpm, 1.0mg/mL KMnO$_4$, Layer 3
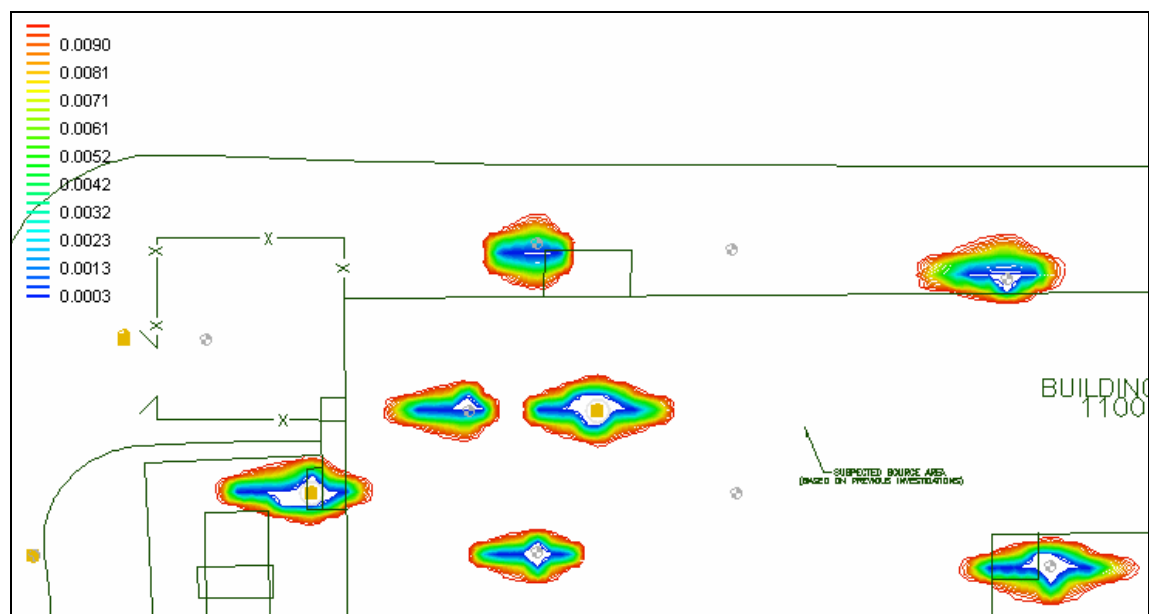
Figure E.60: Fast NOD Distribution, 5gpm, 4.0mg/mL KMnO$_4$, Layer 3
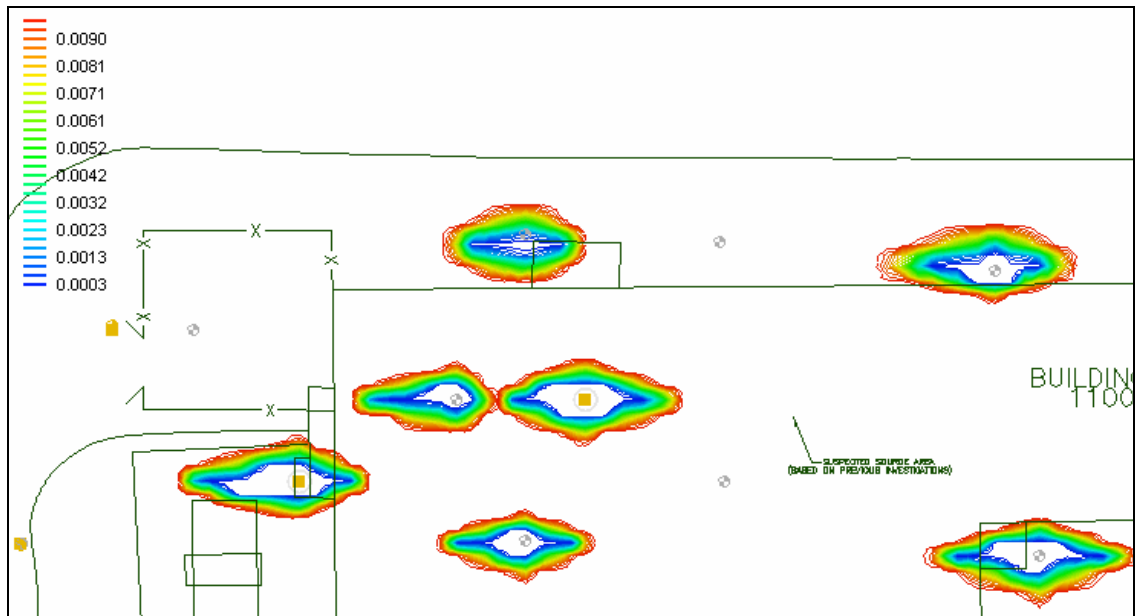
Figure E.61: Fast NOD Distribution, 8gpm, 4.0mg/mL KMnO$_4$, Layer 3
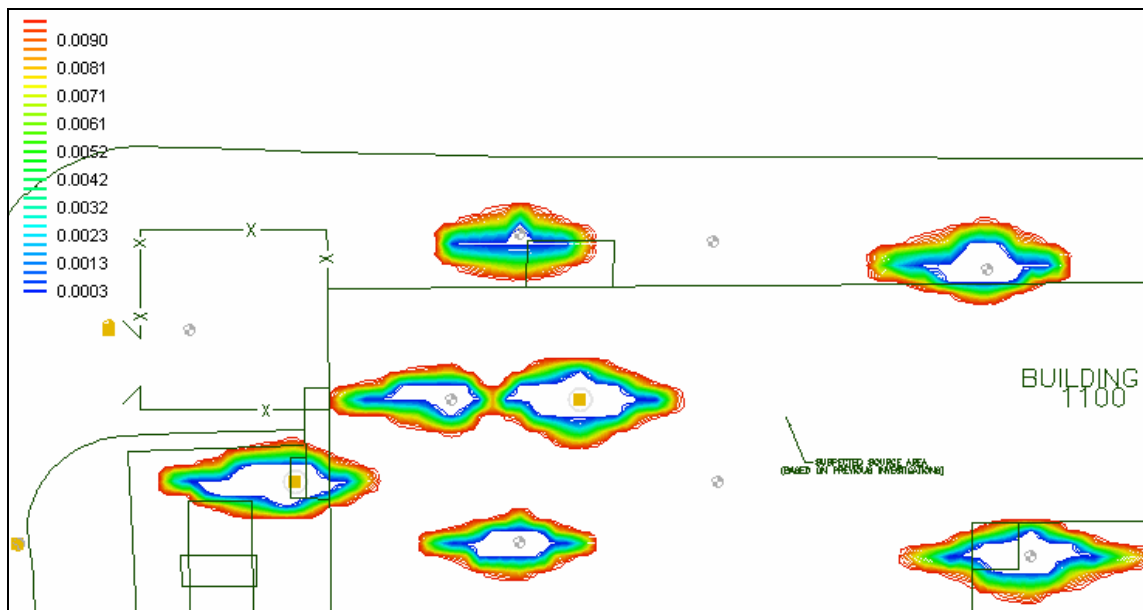
Figure E.62: Fast NOD Distribution, 10gpm, 4.0mg/mL KMnO$_4$, Layer 3
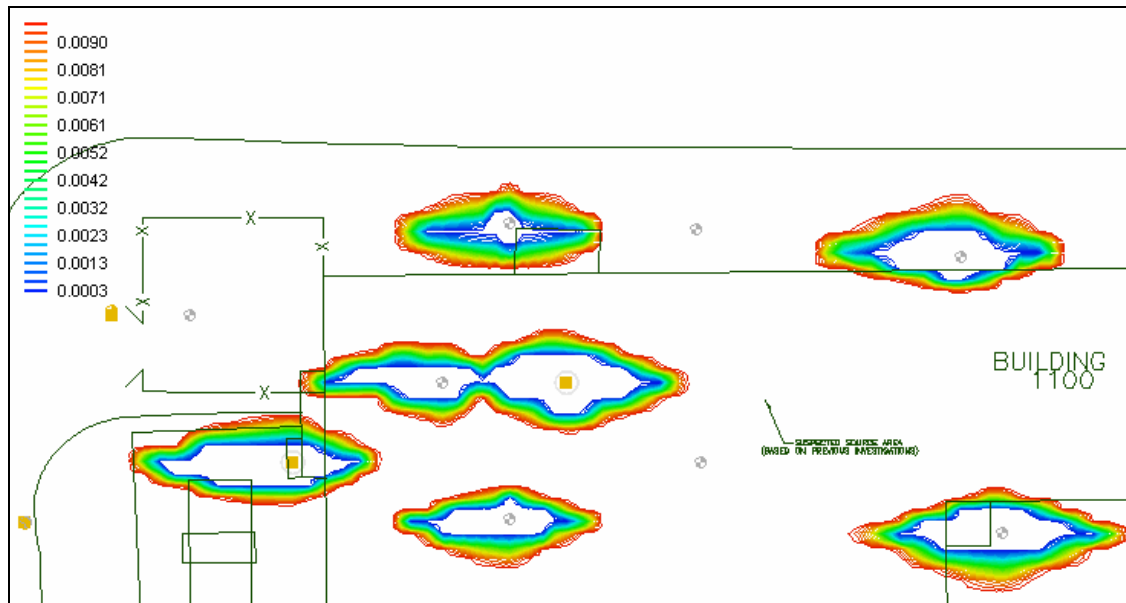
Figure E.63: Fast NOD Distribution, 15gpm, 4.0mg/mL KMnO$_4$, Layer 3
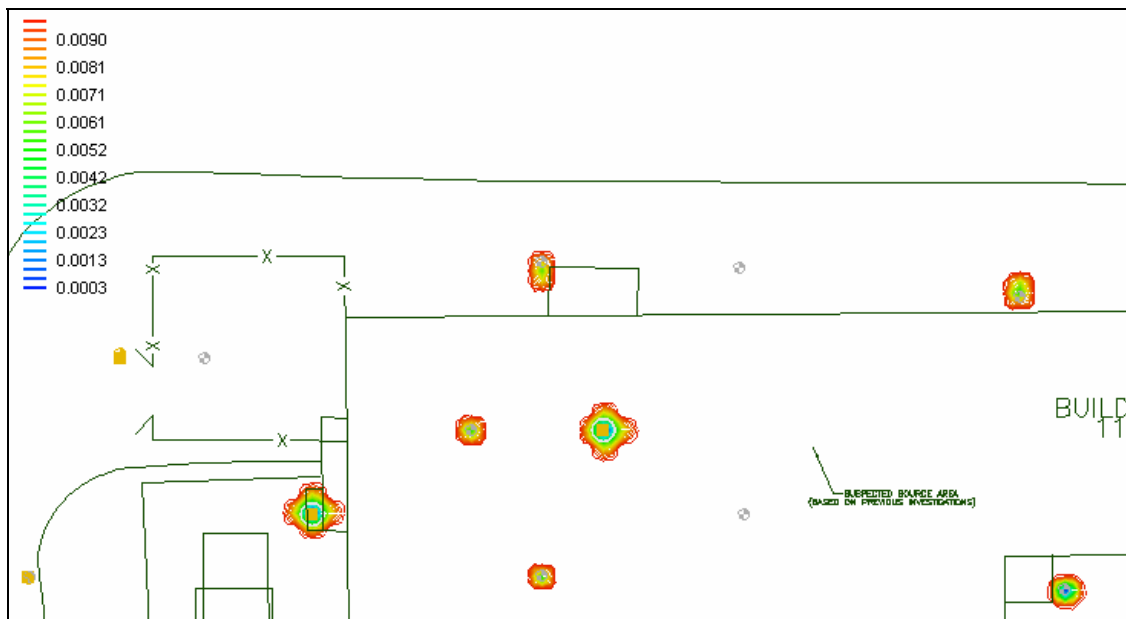
Figure E.64: Fast NOD Distribution, 8gpm, 0.25mg/mL KMnO$_4$, Layer 3, fast NOD present (decreased k)
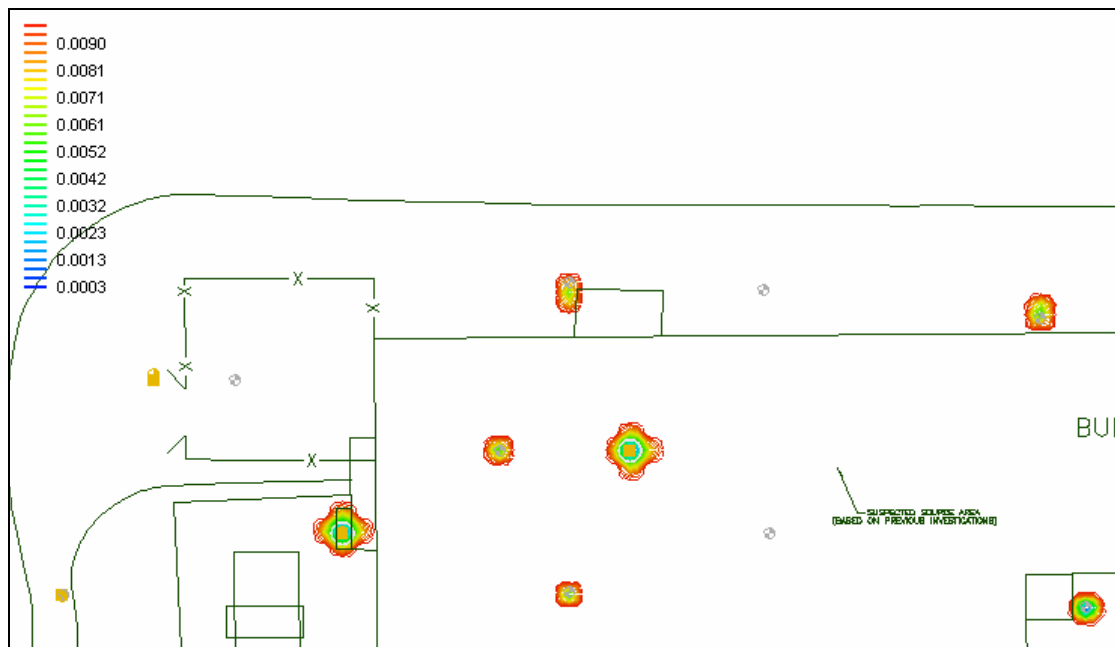
Figure E.65: Slow NOD Distribution, 8gpm, 0.25mg/mL KMnO$_4$, Layer 3

Figure E.66: Fast NOD Distribution, 8gpm, 0.25mg/mL KMnO$_4$, Layer 3 (more fast NOD initially)
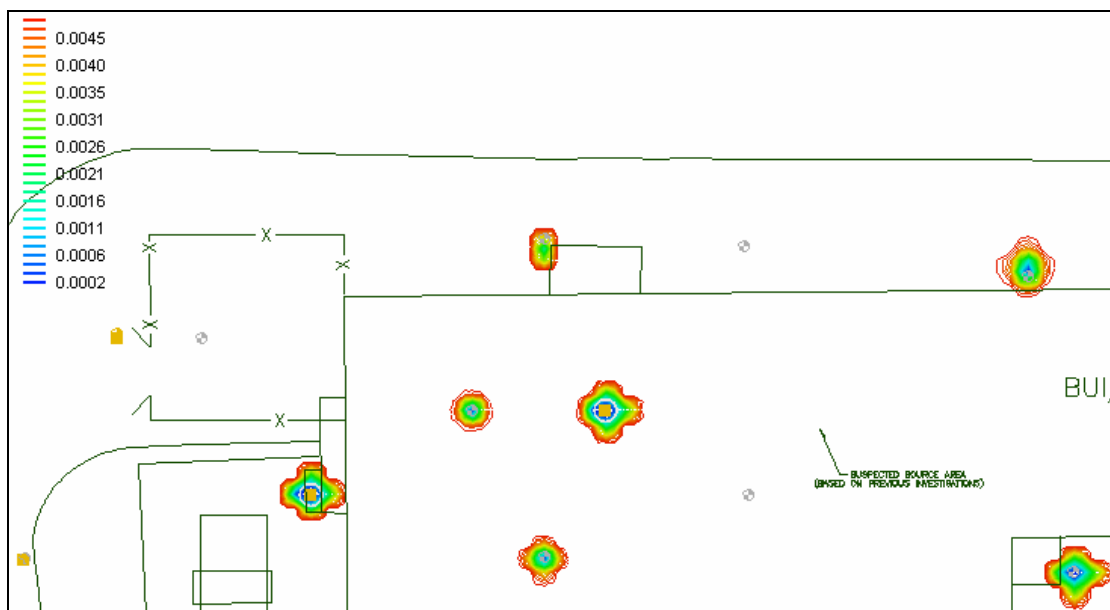
Figure E.67: Fast NOD Distribution, 8gpm, 0.25mg/mL KMnO₄, Layer 3 (less fast NOD initially)
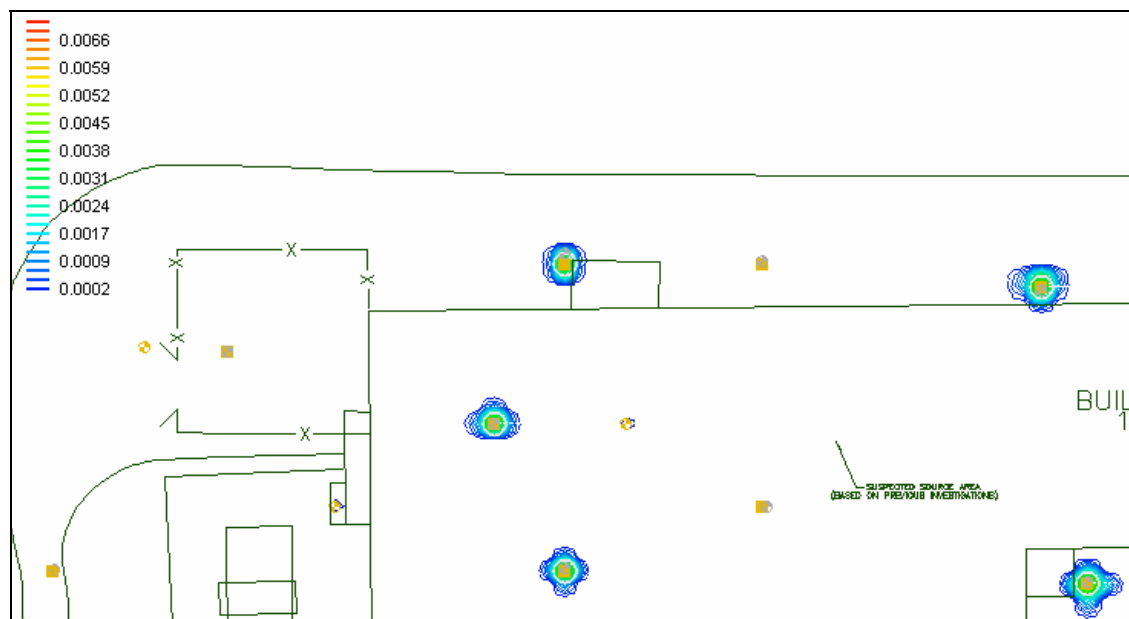
Figure E.68: MnO₂(s) Distribution, 5gpm, 0.25mg/mL KMnO₄, Layer 2, fast NOD present
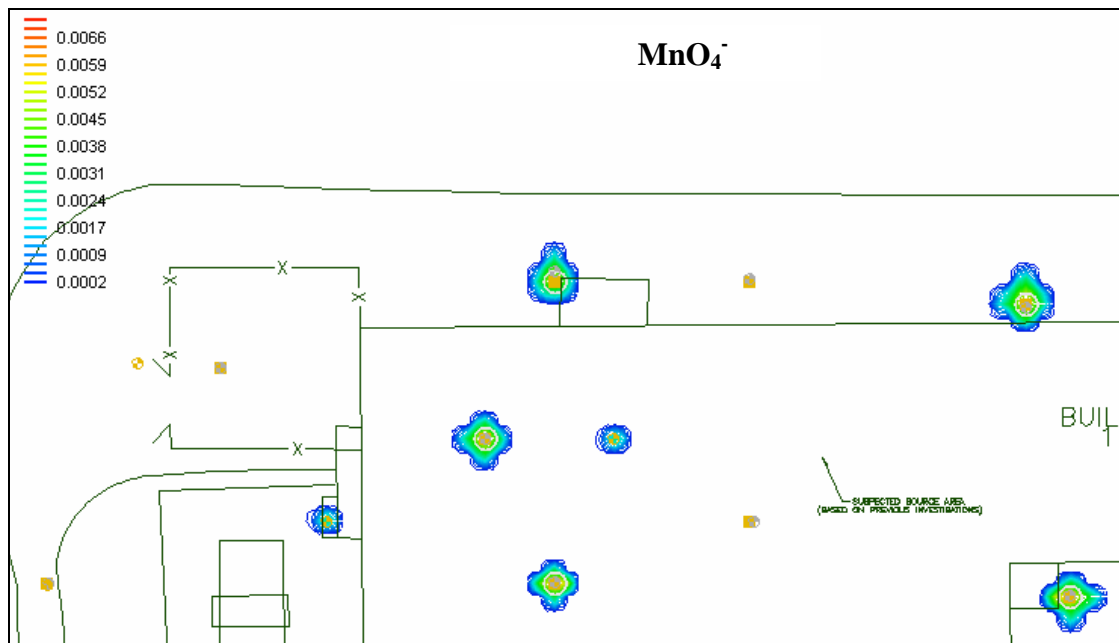
Figure E.69: MnO$_2$(s) Distribution, 15gpm, 0.25mg/mL KMnO$_4$, Layer 2, fast NOD present
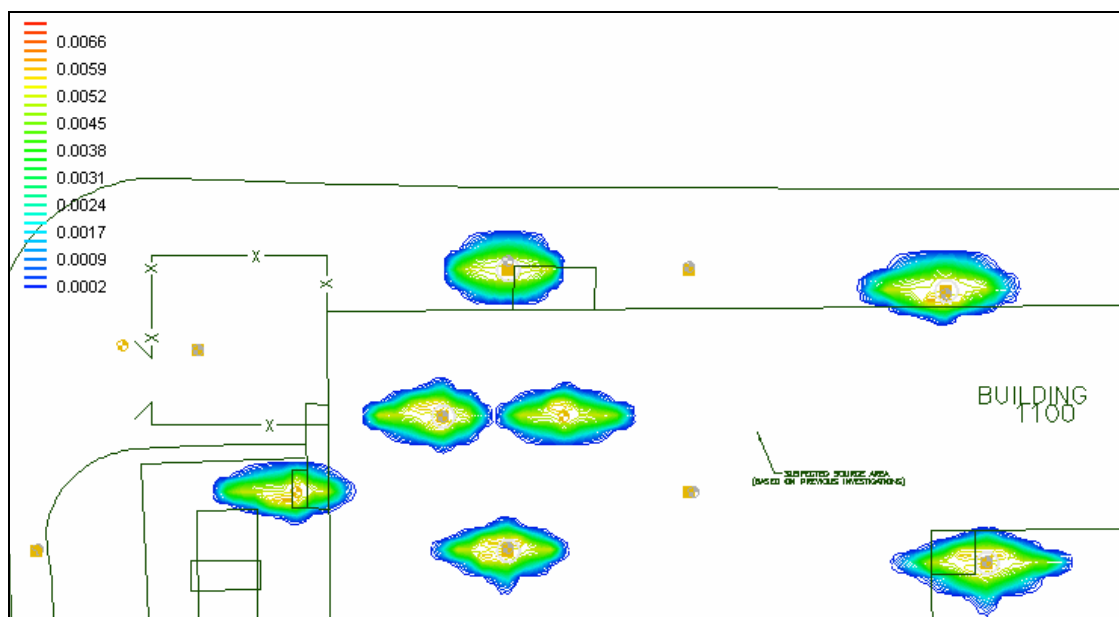
Figure E.70: MnO$_2$(s) Distribution, 15gpm, 4.0mg/mL KMnO$_4$, Layer 2, fast NOD present
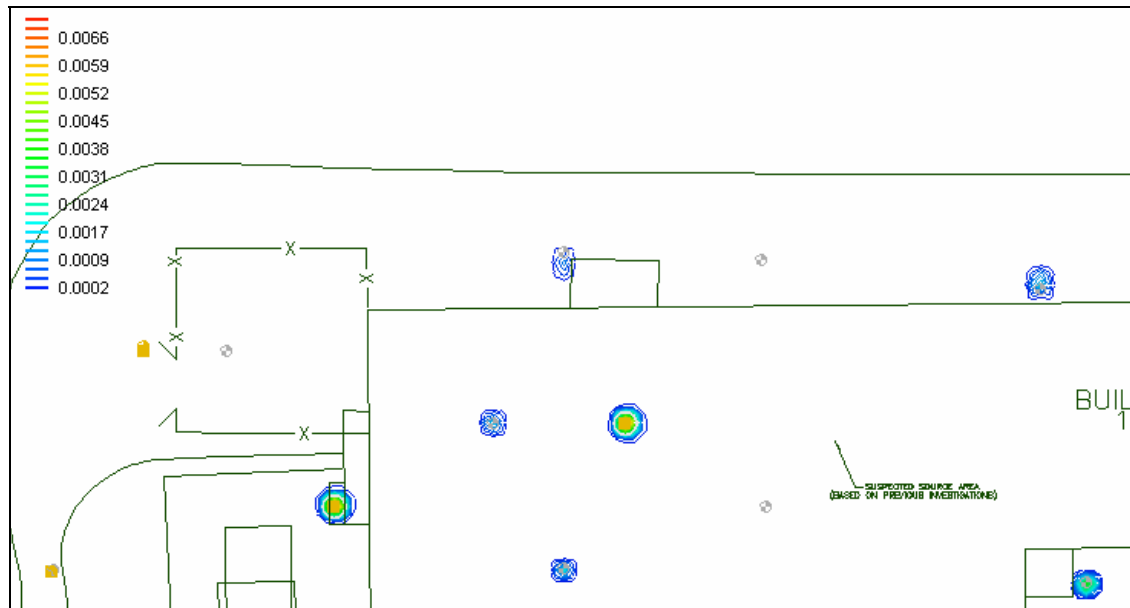
Figure E.71: MnO$_2$(s) Distribution, 5gpm, 0.25mg/mL KMnO$_4$, Layer 3, fast NOD present
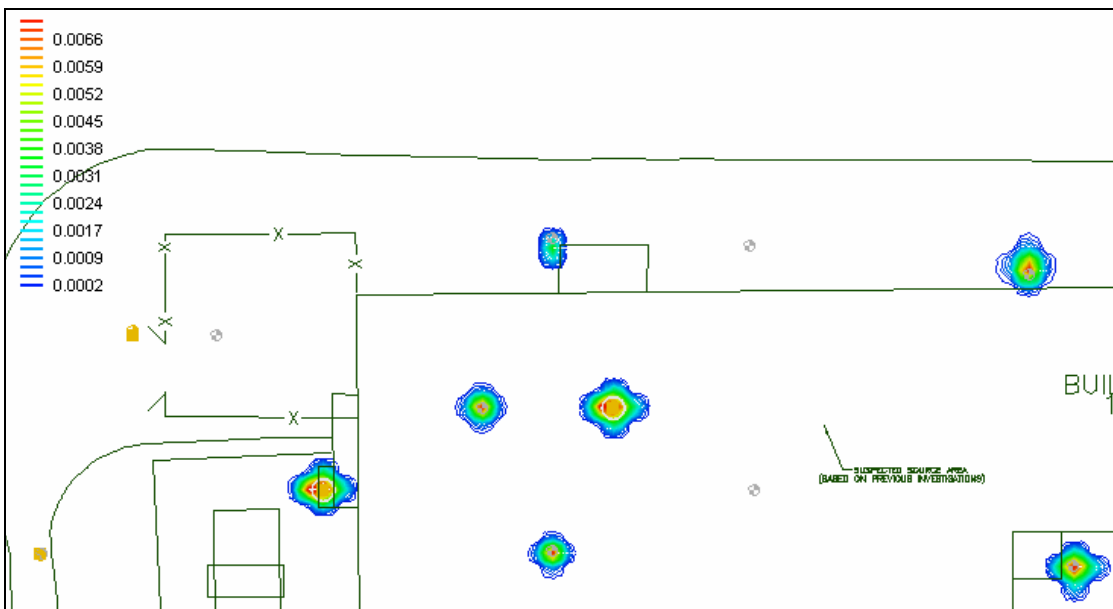
Figure E.72: MnO$_2$(s) Distribution, 15gpm, 0.25mg/mL KMnO$_4$, Layer 3, fast NOD present
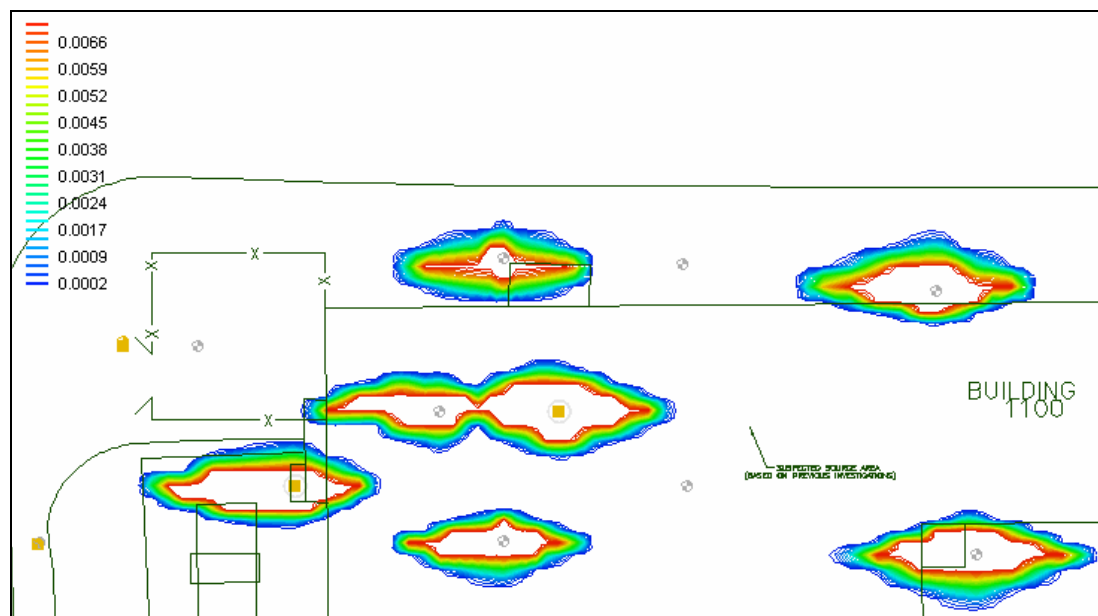
Figure E.73: MnO$_2$(s) Distribution, 15gpm, 4.0mg/mL KMnO$_4$, Layer 3, fast NOD present
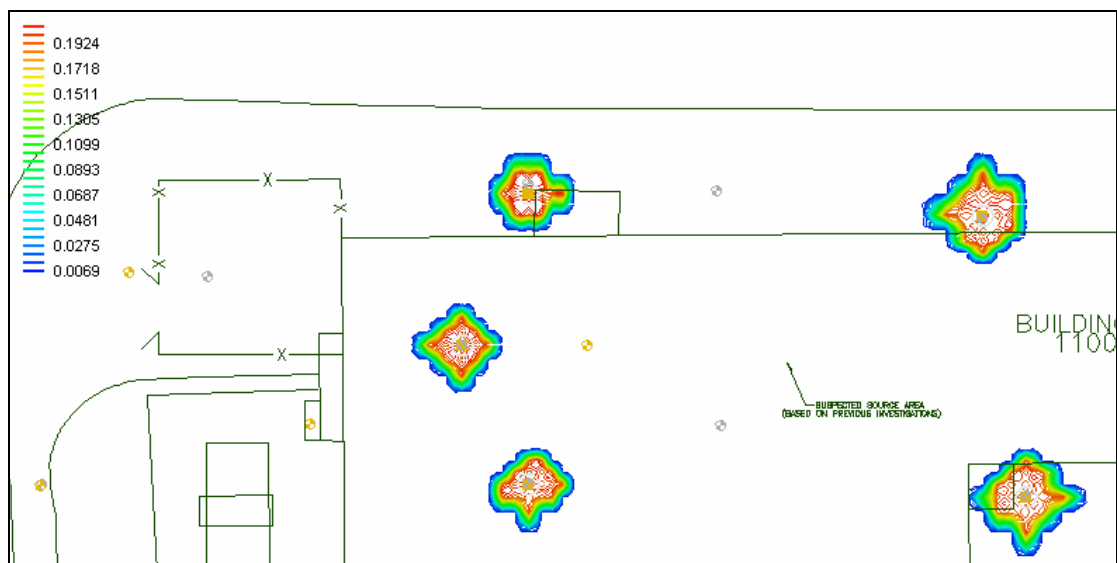
Figure E.74: MnO$_4^-$ Distribution, 48gpm, 0.25mg/mL KMnO$_4$, Layer 2
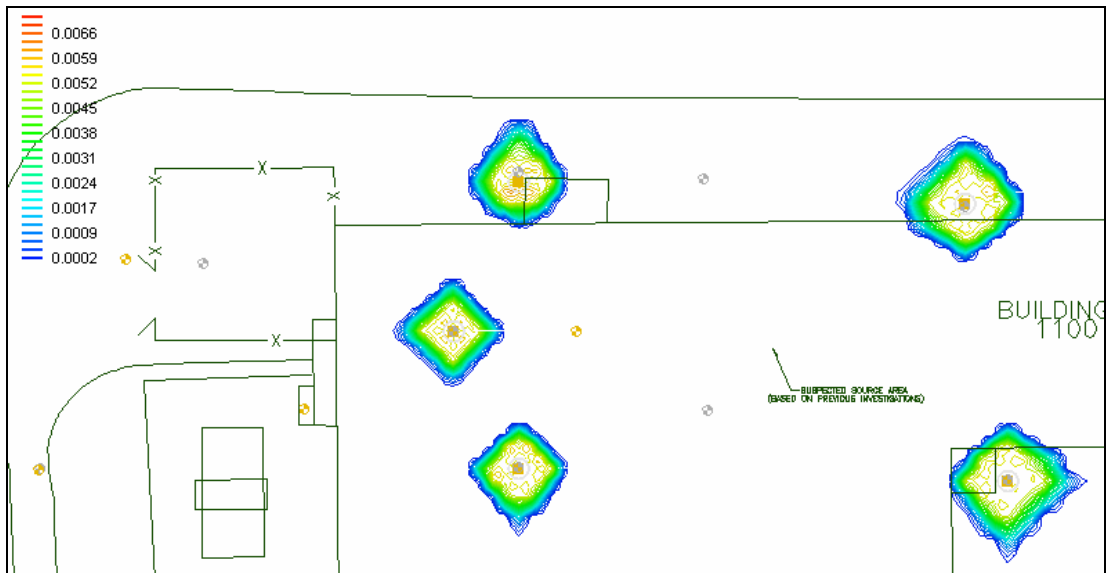
Figure E.75: MnO$_2$(s) Distribution, 48gpm, 0.25mg/mL KMnO$_4$, Layer 2
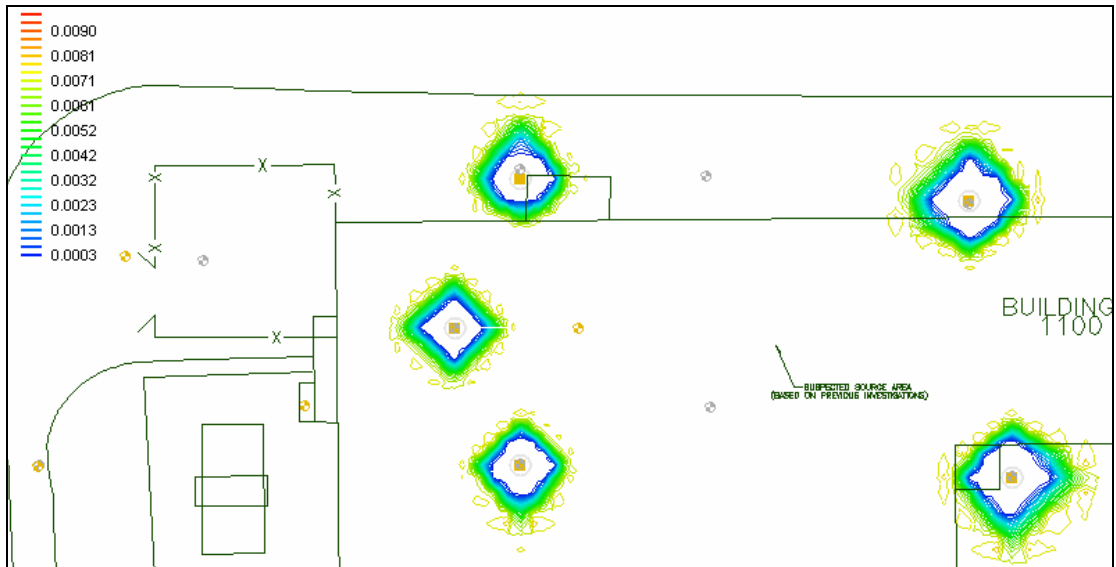
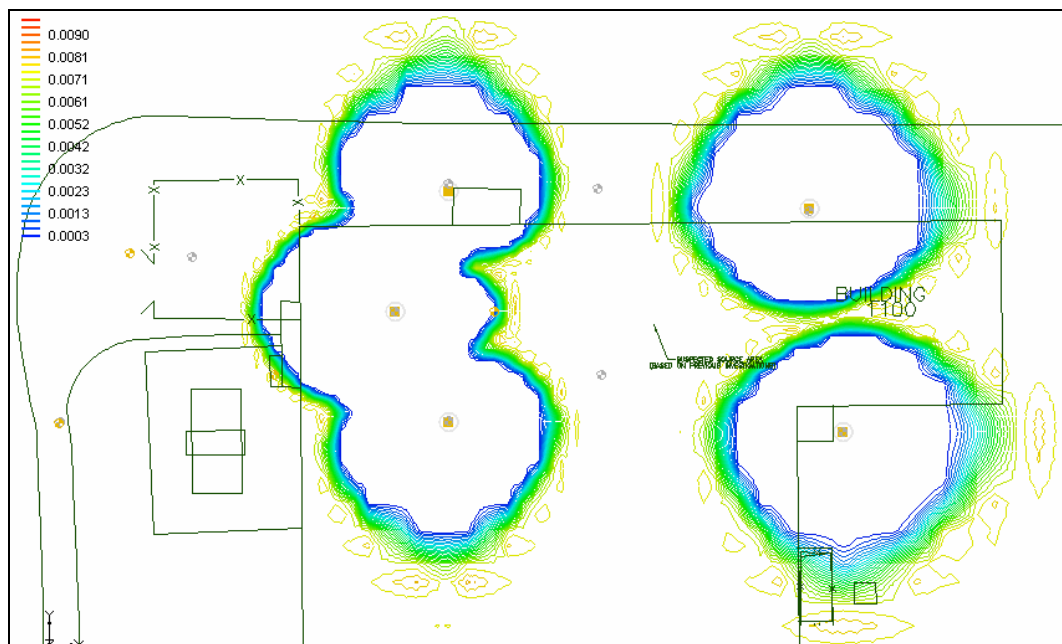**Figure E.76: Fast NOD Distribution, 48gpm, 0.25mg/mL KMnO$_4$, Layer 2**
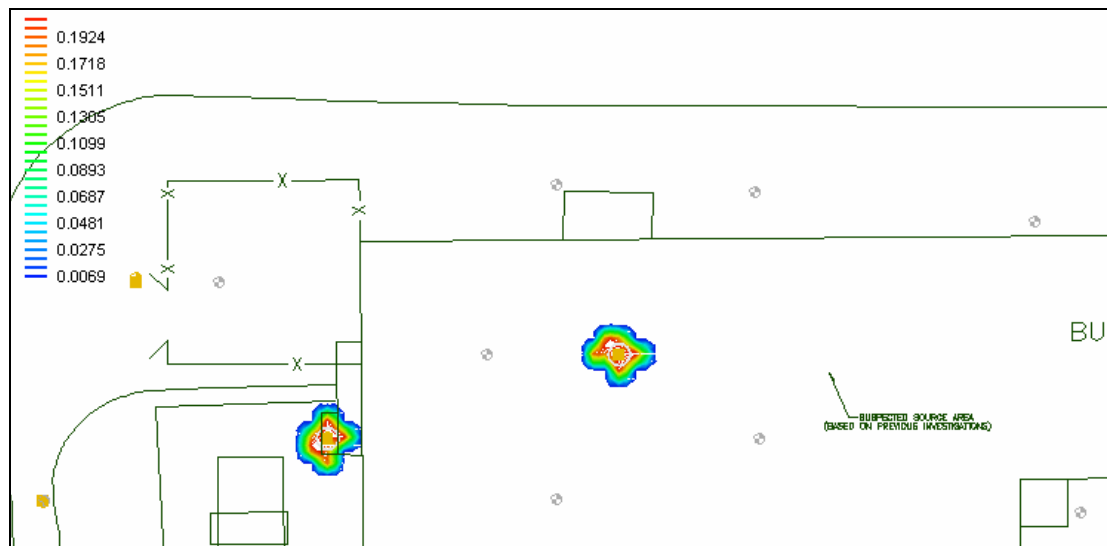
Figure E.77: MnO_4^- Distribution, 48gpm, 0.25mg/mL $KMnO_4$, Layer 3
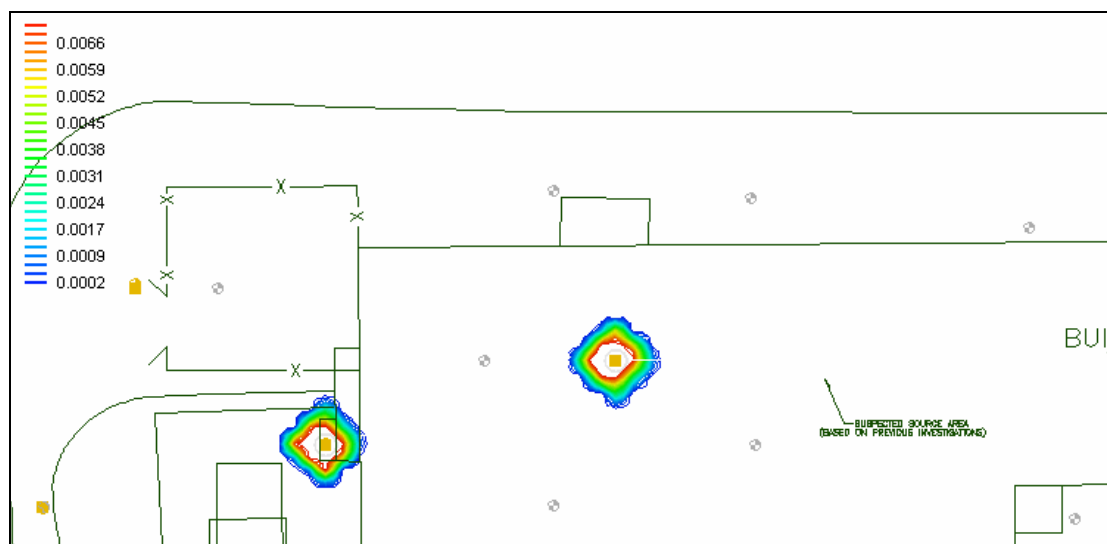
Figure E.78: $MnO_2(s)$ Distribution, 48gpm, 0.25mg/mL $KMnO_4$, Layer 3
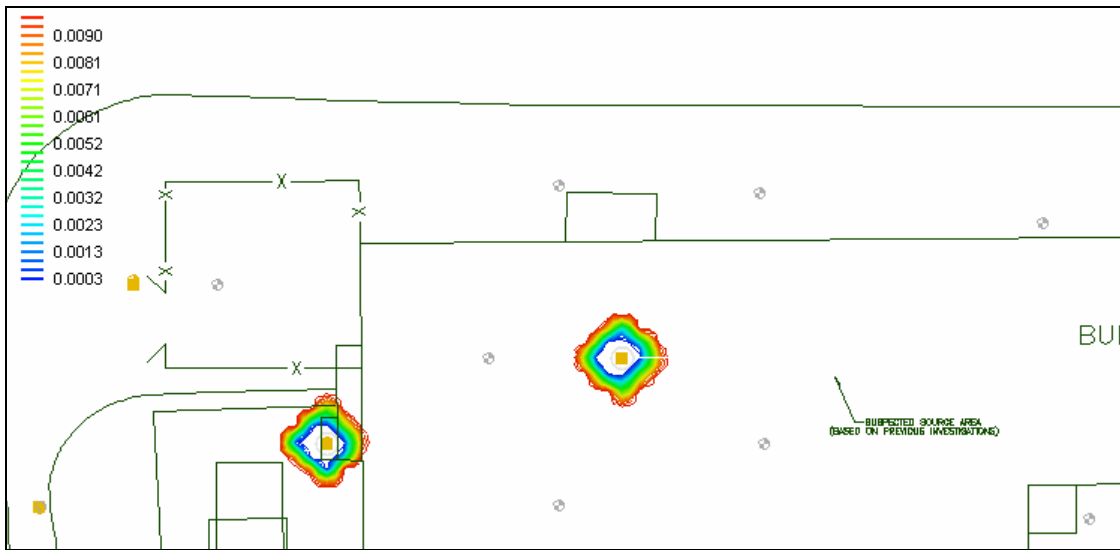
Figure E.79: Fast NOD Distribution, 48gpm, 0.25mg/mL KMnO4, Layer 3
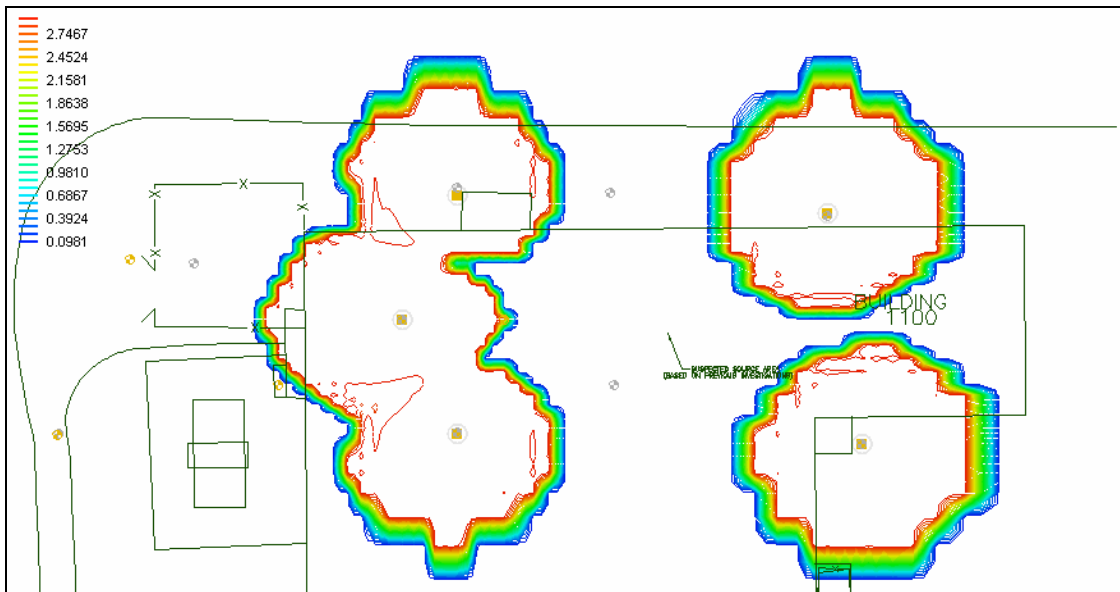
Figure E.80: MnO$_4^-$ Distribution, 48gpm, 4.00 mg/mL KMnO4, Layer 2
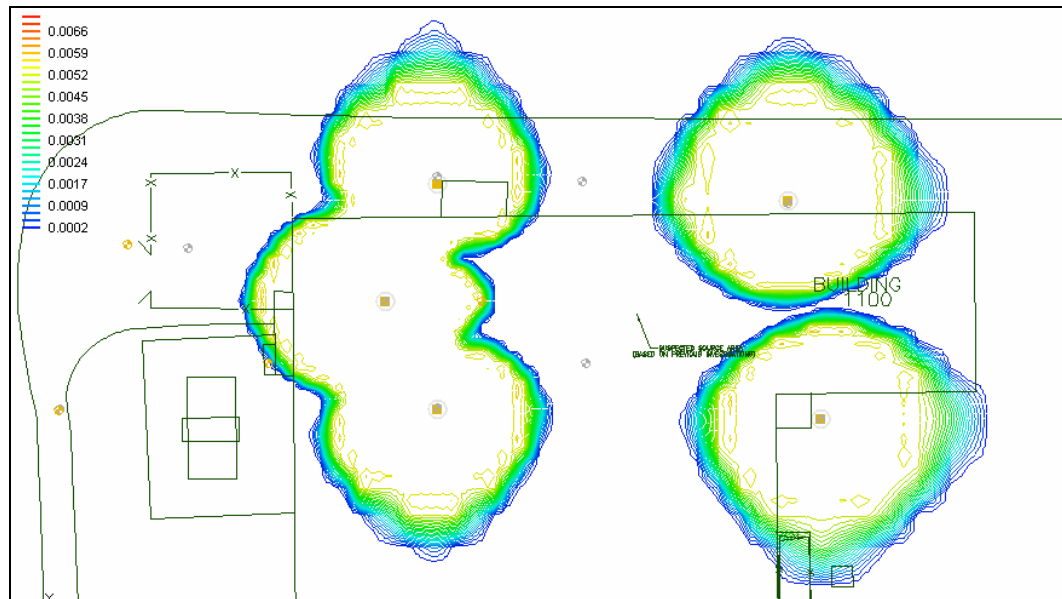
Figure E.81: MnO$_2$(s) Distribution, 48gpm, 4.00mg/mL KMnO$_4$, Layer 2

Figure E.82: Fast NOD Distribution, 48gpm, 4.00mg/mL KMnO$_4$, Layer 2

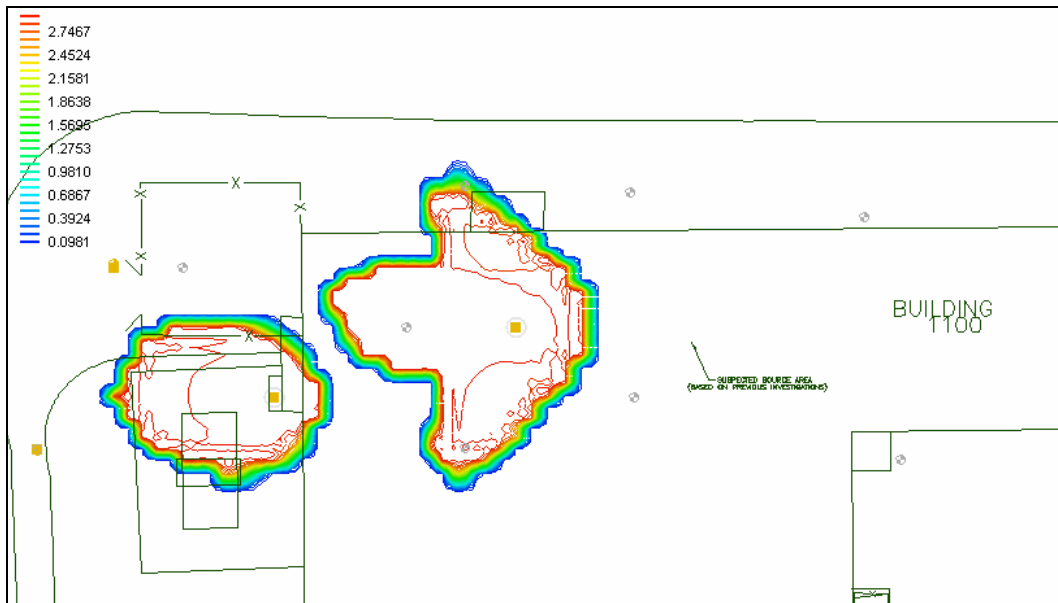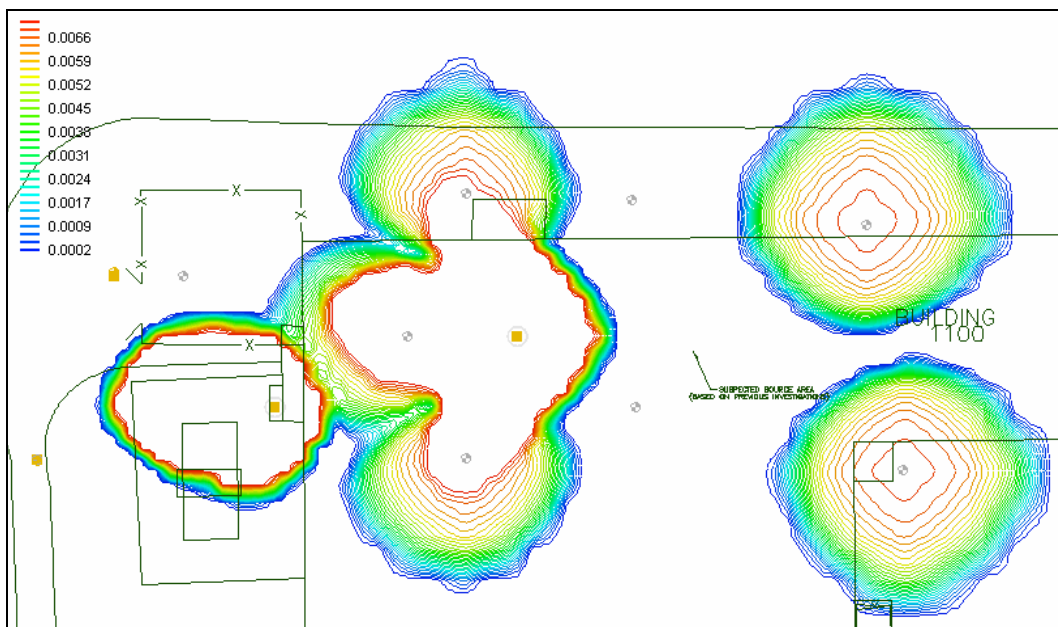**Figure E.83: MnO$_4^-$ Distribution, 48gpm, 4.00mg/mL KMnO$_4$, Layer 3**

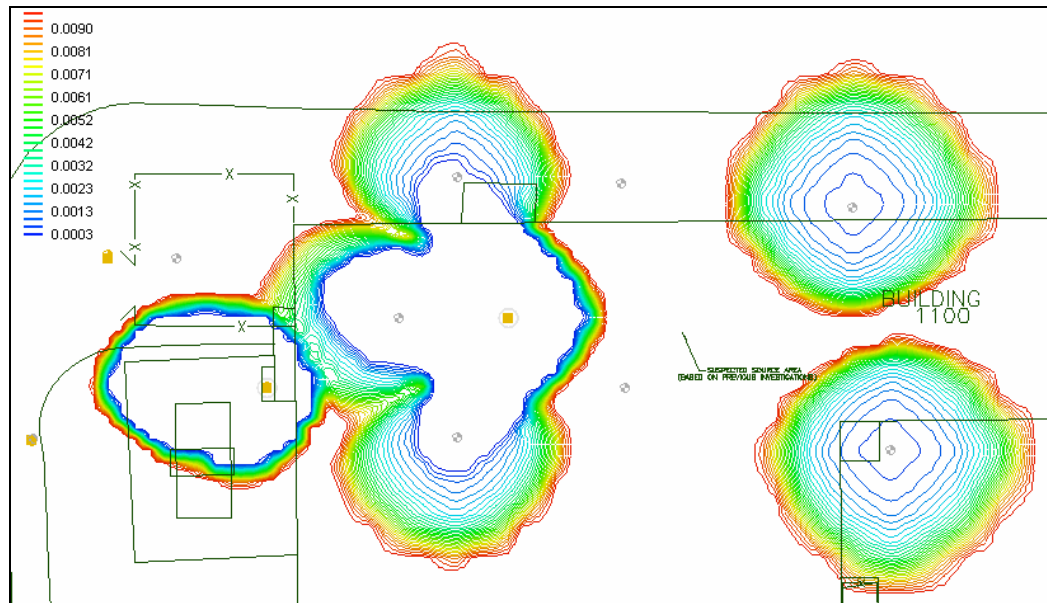**Figure E.84: MnO$_2$(s) Distribution, 48gpm, 4.00mg/mL KMnO$_4$, Layer 3**

Figure E.85: Fast NOD Distribution, 48gpm, 4.00mg/mL KMnO$_4$, Layer 3